

Development and Application of a Fully Coupled Eulerian Thin Film/Discrete Phase Approach to a Simplified Aeroengine Bearing Chamber

Andrew Nicoli

MEng

Submitted to the University of Nottingham for the degree of *Doctor of Philosophy*, February 2020.

Abstract

With a global drive to reduce emissions and improve fuel efficiency, aeroengine manufacturers are challenged with the significant task of developing more efficient engines. In order to achieve improved propulsion and thermal efficiencies, the desire to operate at both higher temperatures and shaft speeds requires sufficient understanding of the engine systems for design optimisation.

In aeroengines, the shafts are supported by bearings and these bearings are supplied with oil for lubrication and cooling. The bearings are housed in bearing chambers that are sealed, typically with labyrinth seals at present, creating a highly rotating two-phase environment. It is important that oil from the bearings is collected and returned to the tank to avoid unnecessary working of the oil, as this increases heat to the oil and may lead to its decomposition. Traditionally, to prevent over-heating, a surplus of oil is supplied to these rotating elements, therefore, through proper dimensioning of the oil system, a more light-weight and efficient design can be achieved.

The use of Computational Fluid Dynamics (CFD) to accurately model components of the aeroengine is seen as key to improving efficiencies and optimising design. Previous work at the Gas Turbine and Transmissions Research Centre (G2TRC) has highlighted the need for a sophisticated computational model including the capability to appropriately capture the oil shedding behaviour from bearings. Oil can breakup, generating droplets and ligaments, subsequently forming thin and thick films driven by both gravity and shear. At the G2TRC, experimental investigations into the oil shedding behaviour from a ball bearing within a simplified aeroengine bearing chamber have been previously published. This work has generated flow field images obtained using a high-speed camera configuration and derived film thickness data is presented. The experimental data provides vital validation resources for this current research.

To date, for aeroengine bearing chamber applications, there is still considerable uncertainty regarding the best practice computational modelling approach and, more specifically, the selection of a suitable turbulence model. Therefore, an objective of the work is to provide closure to this problem and recommendations are made for a turbulence model that is applicable to aeroengine bearing chamber simulations. However, to begin with, the capability to accurately model fluid flow within a rotating Taylor-Couette systems is seen as a necessary first step for informing the subsequent bearing chamber computational investigations carried out here.

Within recent aeroengine bearing chamber investigations, one of the areas yet to be properly explored is the behaviour of oil shed from the bearing into the bearing chamber; moreover, up to now, minimal progress has been made in order to quantify these droplets and the disintegration

process. Historically, attempts to model this phenomenon has been demonstrated utilising a Eulerian Thin Film Model (ETFM) coupled with a Discrete Phase Model (DPM). However, these prior computational modelling approaches have been limited by the state-of-the-art capability and many challenges still need to be overcome. As such, within the scope of this thesis, the requirement for a more appropriate computational methodology, has led to the development of *sprayParcelFilmFoam*, a fully coupled two-way ETFM-DPM solver within OpenFOAM. In addition, two new thin film sub-models are included, based on empirical models for both a film stripping and an edge separation criteria. The newly developed *sprayParcelFilmFoam* solver is validated against an experimental study for a liquid jet injected into a high velocity crossflow. The fidelity of both the solver and the novel film sub-models are evaluated against both experimental film thickness measurements as well as particle diameters and velocities. Compared to the existing state-of-the-art techniques available, the results achieved within *sprayParcelFilmFoam* demonstrate a significant improvement and, overall, represents an advance in bearing chamber modelling capability.

Subsequently, *sprayParcelFilmFoam* is applied to a simplified aeroengine bearing chamber and has, for the first time, demonstrated a fully coupled two-way ETFM-DPM investigation into the droplet generation process. Numerical investigations are conducted for three different shaft speeds namely 5,000, 7,000 and 12,000 rpm, at two different oil flow rates: 5.2 and 7.3 l/min. CFD results are validated against the G2TRC experimental data for the two lower shaft speeds. Evaluation of computed mean film thickness results shows excellent agreement with the experimental measurements. Overall, there is a diminishing reduction in film thickness with each increase in shaft speed. Good qualitative agreement of the film development is found, whereby, upstream of the separation edge a fully shear driven flow regime is observed. However, immediately before the separation edge, a gravity dominated flow regime persists, even at 12,000 rpm. A comprehensive investigation into the oil disintegration process is performed. A detailed analysis of droplet statistics is presented, including: particle trajectories, diameters, velocities and residence times. For these droplets, an understanding of solution sensitivity to both operational parameters and initial conditions is provided. Predominately, the most notable quantities that influence the droplet shedding behaviour are the shaft speed and angular location.

The work presented in this thesis demonstrates a significant improvement in bearing chamber modelling capability through the use of the developed coupled ETFM-DPM approach. The results obtained within the simplified bearing chamber have provided a greater understanding of the underlying mechanisms and new flow physics. Overall, *sprayParcelFilmFoam*, will support future research activities, helping to improve bearing chamber design optimisation and, ultimately, better inform the heat and oil management process based on required functionality.

List of Publications

1. A. Nicoli, R. Jefferson-Loveday and K. Simmons, "A New OpenFOAM Solver Capable of Modelling Oil Jet-Breakup and Subsequent Film Formation for Bearing Chamber Applications," *Proceedings of the ASME Turbo Expo 2019, Phoenix, Arizona, 2019.*

2. A. Nicoli, K. Johnson and R. Jefferson-Loveday, "Computational Modelling of Turbulent Taylor-Couette Flow for Bearing Chamber Applications: A Comparison of Unsteady Reynolds-Averaged Navier-Stokes (URANS) Models," *Submitted for publication, 2020.*

3. A. Nicoli, K. Johnson and R. Jefferson-Loveday, "Simulation of A Simplified Aeroengine Bearing Chamber Using A Fully Coupled Two-Way Eulerian Thin Film/Discrete Phase Approach: Film Behaviour Near the Bearing," *Submitted for publication, 2020.*

4. A. Nicoli, K. Johnson and R. Jefferson-Loveday, "Simulation of A Simplified Aeroengine Bearing Chamber Using A Fully Coupled Two-Way Eulerian Thin Film/Discrete Phase Approach: Droplet Behaviour in the Chamber," *Submitted for publication, 2020.*

Acknowledgements

I would like to thank my supervisors, Dr Kathy Johnson and Dr Richard Jefferson-Loveday for their invaluable support and dedication throughout the whole course of this research; not only in supervision meetings, but also in their contributions, mentoring and motivation that I have received. I have benefited a great deal and thoroughly enjoyed working with both of you.

I am also grateful for having the opportunity to further my studies at the University of Nottingham, who also sponsored my PhD. I would like to thank my internal examiner, Dr Antonino La Rocca, for his constructive input and detailed reviews. Additionally, I would like to sincerely acknowledge the technical and financial support provided by Rolls-Royce.

I have been very fortunate to have met many great individuals in my time at the Gas Turbine and Transmissions Research Centre (G2TRC). I would like to thank the friends and colleagues I have made in the G2TRC, for the help along the way and making this a memorable experience.

Finally, I wish to thank my family for their constant support and encouragement during my studies. A great thanks goes to Maria, for always being supportive and understanding throughout the whole process.

Contents

Abstract ..... **II**

List of Publications ..... **IV**

Acknowledgements ..... **V**

Contents ..... **VI**

List of Figures ..... **XI**

List of Tables ..... **XVIII**

Nomenclature ..... **XX**

Acronyms XX

Characteristic Numbers XXII

Greek Symbols XXII

Latin Symbols XXIII

Derivatives XXV

Subscripts and Superscripts XXVI

Chapter 1 Introduction **1**

1.1 Background 1

1.2 Aeroengine Oil Systems 4

1.3 Aeroengine Rotor Support Structures 6

1.4 Aeroengine Bearing Chambers 7

1.5 Aims and Objectives 10

1.6 Thesis Outline 11

Chapter 2 Literature Review **14**

2.1 Couette Flow 15

2.2 Taylor-Couette Flow 16
2.2.1 Experimental Investigations 18
2.2.1.1 Velocity Distributions 20
2.2.2 Numerical Investigations 22
2.2.3 Small Aspect Ratio Chambers 25
2.3 Bearing Chamber Experimental Studies 27
2.3.1 Early Experimental Investigations 27
2.3.2 Airflow Measurements 27
2.3.3 Film Thickness Measurements 28
2.3.4 Droplet Characteristics 30
2.3.4.1 G2TRC Bearing Oil Shedding Rig 33
2.3.5 Oil Jet Systems 38
2.3.6 Gas-Sheared Liquid Films 39
2.4 Bearing Chamber Numerical Studies 42
2.4.1 The Volume of Fluid Method 43
2.4.1.1 VOF Mesh Requirements 46
2.4.1.2 Additional Aeroengine VOF Applications 47
2.4.2 The Eulerian Thin Film Model 48
2.4.3 Coupled VOF-ETFM 50
2.4.4 Coupled VOF-DPM 52
2.4.5 Coupled ETFM-DPM 54
2.5 Summary of Literature Reviews 57
Chapter 3 Validation: Taylor-Couette Turbulence Modelling Study 59
3.1 Introduction 60
3.2 Objectives 61
3.3 Taylor-Couette Geometrical and Flow Field Parameters 62
3.4 Numerical Modelling 64
3.4.1 Governing Equations 64
3.4.1.1 Continuity Equation 64

3.4.1.2 Momentum Equation 65
3.4.2 Discretisation and Solution Method 65
3.4.2.1 Spatial Discretisation 65
3.4.2.2 Temporal Discretisation 66
3.4.2.3 Solution Algorithms 67
3.4.2.4 Numerical Approach 68
3.4.3 URANS Turbulence Modelling 70
3.4.4 Wall Function Approach 72
3.4.4.1 Standard Wall Functions 73
3.4.4.2 Enhanced Wall Treatment 73
3.4.4.3 Insensitive Near-Wall Treatment 74
3.5 Axisymmetric Configuration 75
3.5.1 Axisymmetric Results 77
3.5.1.1 Start-up Procedure 77
3.5.1.2 URANS Turbulence Modelling 79
3.6 Three-Dimensional Configuration 85
3.6.1 Three-Dimensional Results 86
3.6.1.1 Start-up Procedure 87
3.6.1.2 Rotational-Periodicity Study 87
3.6.1.3 Full 360° Domain 89
3.6.1.4 SST k-ω Turbulence Model 92
3.7 Taylor-Couette Recommendations 94
3.8 Aeroengine Bearing Chamber Investigations 96
3.8.1 Computational Set-up 97
3.8.1.1 Boundary Conditions and Mesh 97
3.8.1.2 Numerical Methods and Solution Procedure 98
3.8.1.3 URANS Turbulence Modelling 98
3.8.2 Bearing Chamber Results 99
3.8.2.1 Rotational Speed Driven Mode 100

3.8.2.2 Sealing Air Driven Mode 104
3.9 Single-Phase Bearing Chamber Modelling Conclusions 109
Chapter 4 Development: sprayParcelFilmFoam 110
4.1 Introduction 111
4.2 Objectives 115
4.3 OpenFOAM 116
4.3.1 Single-Phase Validation 117
4.3.1.1 Rotational Speed Driven Mode 118
4.3.1.2 Sealing Air Driven Mode 119
4.3.1.3 Single-Phase Study Conclusions 121
4.4 Validation Case Study: Jet-Breakup and Film Formation 122
4.5 Coupled Euler-Lagrange and Eulerian Thin Film Method (ETFM-DPM) 124
4.5.1 The Newly Developed Solver: sprayParcelFilmFoam 124
4.5.1.1 Discrete-Phase Modelling 125
4.5.1.2 Surface Film Modelling 131
4.6 Parametric Study: Jet-Breakup and Film Formation 136
4.6.1 Mesh 138
4.6.1.1 Hex-Dominant Meshing 139
4.6.2 Numerical Settings 141
4.6.2.1 DPM Injection Configuration 142
4.6.3 Results 143
4.6.3.1 Momentum Source Terms 147
4.6.3.2 Particle Diameters and Velocities 149
4.7 Conclusions 152
Chapter 5 Application: Aeroengine Bearing Chamber Modelling 153
5.1 Objectives 154
5.2 Bearing Oil Shedding Rig 155
5.2.1 Computational Setup 159
5.2.1.1 Numerical Settings 161

5.3 ETFM Results 163
5.3.1 Qualitative Oil Distribution 163
5.3.2 Quantitative Oil Distribution 169
5.3.3 Oil Residence Time 173
5.4 Comprehensive Film Inlet Boundary Condition 176
5.4.1 Results: Comprehensive Boundary Condition 177
5.5 DPM Results 180
5.5.1 Oil Residence Mass 180
5.5.2 Qualitative Oil Distribution 182
5.5.3 Quantified Particle Trajectories 187
5.5.4 Particle Diameters 192
5.5.5 Particle Velocities 197
5.5.6 Particle Residence Time 199
5.6 ETFM/DPM Conclusions 201
Chapter 6 Conclusions 204
6.1 Summary 205
6.2 Contributions to Knowledge 207
6.3 Recommendations for Future Work 208
6.3.1 Computational Investigations 208
6.3.2 Experimental Investigations 209
References 211

List of Figures

FIGURE 1.1: SCHEMATIC OF A TYPICAL THREE-SHAFT TRENT ENGINE, HIGHLIGHTING THE OIL SYSTEM AND BEARING LOCATIONS, MODIFIED FROM [7] 4

FIGURE 1.2: HP-IP HUB FOR A TYPICAL THREE-SHAFT ENGINE, MODIFIED FROM [7]. GREEN: TWO-PHASE FLOW; RED: HP SHAFT; YELLOW: IP SHAFT; BLUE: LP SHAFT; GREY: STATIC 6

FIGURE 1.3: SIMPLIFIED AEROENGINE BEARING CHAMBER FLOW PHYSICS, MODIFIED FROM [8] 7

FIGURE 1.4: BEARING CHAMBER FLOW REGIMES 8

FIGURE 2.1: CYLINDRICAL COUETTE FLOW WITH ROTATING INNER CYLINDER 15

FIGURE 2.2: DIAGRAM OF TAYLOR-COUETTE FLOW, MODIFIED FROM [12] 16

FIGURE 2.3: MEAN TAYLOR VORTEX STREAMLINES FOR EACH TURBULENCE MODEL [29] 24

FIGURE 2.4: MEAN a) RADIAL AND b) TANGENTIAL PARTICLE VELOCITIES VERSUS ROTATIONAL SPEED [45] 30

FIGURE 2.5: DROPLET DIAMETER HISTOGRAM AT 12,000 RPM [45] 31

FIGURE 2.6: CROSS-SECTIONAL VIEW OF THE BALL BEARING SHOWING AXIAL MEASUREMENT PLANES, MODIFIED FROM [55] 34

FIGURE 2.7: HIGH SPEED VISUALISATION OF DROPLET GENERATION PROCESS [55] 35

FIGURE 2.8: CONVENTION FOR ANGULAR LOCATIONS AROUND THE SHEDDING RIG [54] 36

FIGURE 2.9: FILM DIRECTION 10mm FROM FILM EDGE AT COUNTER-CURRENT REGION [54] 37

FIGURE 2.10: OIL TARGETED DIRECTLY AT THE BEARING VS BEARING UNDERRACE FEED [57] 38

FIGURE 2.11: EFFECT OF BUBBLES ON BEARING CHAMBER HEAT TRANSFER [64] 41

FIGURE 2.12: COMPARISON OF FILM AND INTERFACE REQUIREMENTS FOR VOF (LEFT) AND ETFM (RIGHT) FOR THIN FILM MODELLING [65] 42

FIGURE 2.13: SENSITIVITY OF OIL FILM DISTRIBUTION AND VELOCITY TO THE TURBULENCE DAMPING PARAMETER [68] 44

FIGURE 2.14: VOF FILM THICKNESS DISTRIBUTIONS FOR A BR275 CHAMBER [68] 45

FIGURE 2.15: CONTOURS OF ETFM FILM THICKNESS AND VOF ISO-SURFACES FOR THE VOF-ETFM RIMMING FLOW SOLUTION [65] 51

FIGURE 2.16: a) DROPLET LOADING AND b) FILM INTERFACE FOR THE INDY SUMP DPM-VOF SOLUTION [94] 53

FIGURE 3.1: THREE-DIMENSIONAL COMPUTATIONAL MESH OF EXPERIMENTAL GEOMETRY 62

FIGURE 3.2: DISCRETISATION AND CONTROL VOLUME OF A 2D CELL [108] 66

FIGURE 3.3: THE SIMPLE ALGORITHM, MODIFIED FROM [107] 68

FIGURE 3.4: NON-DIMENSIONALISED SHAFT TORQUE CONVERGENCE HISTORY FOR THE SELECTED DISCRETISATION SCHEMES 69

FIGURE 3.5: DEVELOPMENT OF TAYLOR VORTICES THROUGH THE STEADY ACCELERATION PROCEDURE WITH A MESH PARTITIONED FOR FOUR CORES 69

FIGURE 3.6: AXIAL WAVELENGTHS FOR SUDDEN START AND STEADY ACCELERATION PROCEDURES 78

FIGURE 3.7: COMPARISON OF RADIAL VELOCITY PROFILES AT r = 3.94cm AND R = 100 80

FIGURE 3.8: COMPARISON OF RADIAL VELOCITY PROFILES AT r = 3.94cm AND *R* = 220..... 82

FIGURE 3.9: COMPARISON OF NON-DIMENSIONALISED VELOCITY MAGNITUDE PROFILES ACROSS THE ANNULAR GAP AT *R* = 220..... 83

FIGURE 3.10: COMPARISON OF RADIAL VELOCITY PROFILES AT r = 3.94cm AND *R* = 220..... 86

FIGURE 3.11: COMPARISON OF NON-DIMENSIONALISED VELOCITY MAGNITUDE PROFILES ACROSS THE ANNULAR GAP AT *R* = 220..... 89

FIGURE 3.12: INNER (a) AND OUTER (b) CYLINDER WALL BOUNDARY LAYERS AT *R* = 220 91

FIGURE 3.13: ENLARGED IN-PLANE VELOCITY VECTORS OVER INNER (BOTTOM) AND OUTER (TOP) CYLINDER WALLS FOR THE k-ω TURBULENCE MODEL AT *R* = 220 92

FIGURE 3.14: COMPARISON OF RADIAL VELOCITY PROFILES AT r = 3.94cm AND *R* = 220 FOR BOTH THE STANDARD AND SST k-ω TURBULENCE MODELS 93

FIGURE 3.15: SECTION OF COMPUTATIONAL MESH FOR THE GORSE BEARING CHAMBER 96

FIGURE 3.16: GORSE PIV [33] EXPERIMENTAL MEASUREMENTS SHOWING THE RSDM (a) AND SADM (b) SECONDARY FLOW FIELDS..... 100

FIGURE 3.17: IN-PLANE VELOCITY VECTORS FOR RSDM, m_g= 0 g/s AND n = 9,700 RPM..... 101

FIGURE 3.18: RNG k-ε IN-PLANE VELOCITY VECTORS FOR RSDM, m_g= 0 g/s AND n = 9,700 RPM..... 102

FIGURE 3.19: RSM STRESS-BSL (a) AND SST k-ω (b) IN-PLANE VELOCITY VECTORS FOR RSDM, m_g= 6.2 g/s AND n = 9,700 RPM. SUPERIMPOSED WITH GORSE [33] RSDM VECTORS (BLACK) 103

FIGURE 3.20: IN-PLANE VELOCITY VECTORS FOR SADM, m_g= 12.7 g/s AND n = 9,700 RPM. SUPERIMPOSED WITH GORSE [33] SADM VECTORS (BLACK)..... 106

FIGURE 3.21: RADIAL PROFILES OF TANGENTIAL VELOCITY, m_g= 12.7 g/s AND n = 9,700 RPM..... 107

FIGURE 4.1: SCHEMATIC OF BEARING OIL SHEDDING RIG FRONT CHAMBER, ... 111

FIGURE 4.2: TWO-WAY ETFM-DPM COUPLING AND FLOW PHYSICS REQUIRED..... 115

FIGURE 4.3: IN-PLANE VELOCITY VECOTRS FOR RSDM, m_g= 6.2 g/s AND n = 9,700 RPM. SUPERIMPOSED WITH GORSE [33] RSDM VECTORS (BLACK)..... 119

FIGURE 4.4: IN-PLANE VELOCITY VECTORS FOR SADM, m_g= 12.7 g/s AND n = 9,700 RPM. SUPERIMPOSED WITH GORSE [33] SADM VECTORS (BLACK)..... 120

FIGURE 4.5: RADIAL PROFILES OF TANGENTIAL VELOCITY, m_g= 12.7 g/s AND n = 9,700 RPM 121

FIGURE 4.6: (a) 2D SCHEMATIC OF THE FILM FORMATION BY JET BREAKUP IN A CROSSFLOW AND THE PHENOMENA OBSERVED (b) FULL 3D DOMAIN..... 122

FIGURE 4.7: (a) DIAMETER HISTOGRAM EXCEEDING PARCEL LIMIT VERSUS (b) DIAMETER HISTOGRAM WITH PARCEL LIMIT REMOVED..... 129

FIGURE 4.8: ILLUSTRATION OF THE KELVIN-HELMHOLTZ AND RAYLEIGH-TAYLOR INSTABILITY MECHANISMS 130

FIGURE 4.9: PROCESS OF WAVE FORMATION, CYLINDER FORMATION/EJECTION AND DROPLET EJECTION UNDER THE SHEAR STRIPPING CRITERIA 133

FIGURE 4.10 SCHEMATIC SHOWING THE PROCESS OF EDGE SEPARATION AROUND A SHARP CORNER..... 134

FIGURE 4.11 HEX-DOMINANT MESH WITH 2,570K CELLS, DOMAIN LENGTH CLIPPED TO 0.75m FOR VIEWING PURPOSES 139

FIGURE 4.12: THREE STAGES OF THE SNAPPYHEXMESH PROCESS, MODIFIED FROM [114] 141

FIGURE 4.13 FILM THICKNESS MEASUREMENTS ALONG THE FILMER CENTRELINE FOR EACH OBJECTIVE a) SD MESH DENSITY, b) AIRFLOW TIME-STEP, c) STRIPPING CRITERION AND ED MESH DENSITY, d) STOCHASTIC DISPERSION MODEL AND SPLASHING, e) NUMBER OF INJECTION PARCELS PER SECOND, f) EDGE SEPARATION CRITERION. 146

FIGURE 4.14: MIDPLANE VELOCITY MAGNITUDE AND PARTICLE DIAMETERS 147

FIGURE 4.15: FILM THICKNESS MEASUREMENTS ALONG THE FILMER CENTRELINE FOR A MODIFIED FILM MOMENTUM TRANSPORT EQUATION 148

FIGURE 4.16: INSTANTANEOUS FILM THICKNESS MEASUREMENTS WITH PRESSURE SOURCES (TOP) AND AFTER THEY ARE REMOVED (BOTTOM) 149

FIGURE 4.17: a) AVERAGE PARTICLE DIAMETER AND b) VELOCITY 25.4mm DOWNSTREAM OF THE EXPANSION EDGE ALONG THE MIDPLANE. THE 0 LOCATION CORRESPONDS TO THE HEIGHT OF THE EXPANSION EDGE. 150

FIGURE 5.1: SCHEMATIC OF BEARING OIL SHEDDING RIG FRONT CHAMBER, ... 155

FIGURE 5.2: CROSS SECTION OF BEARING CHAMBER HEX-DOMINANT MESH EMPLOYED 156

FIGURE 5.3: CROSS SECTION OF FILM INLET SHOWING a) AXIAL FILM THICKNESS MEASUREMENT PLANES AND b) DPM MEASUREMENT PLANES, MODIFIED FROM [54] 158

FIGURE 5.4: CONVENTION FOR BEARING CHAMBER ANGULAR POSITIONS... 159

FIGURE 5.5: FILM MEAN VELOCITY VECTOR PLOT AT 7,000 RPM AND 7.3 L/MIN 163

FIGURE 5.6: INSTANTANEOUS FILM THICKNESS ON THE FRONT FACE-EDGE AT 7,000 RPM AND 7.3L/MIN (DROPLETS NOT SHOWN) 164

FIGURE 5.7: OIL WAVE FRONTS OBSERVED EXPERIMENTALLY AT P4 [55], 7,000 RPM & 7.3 L/MIN 165

FIGURE 5.8: MEAN VELOCITY MAGNITUDE VECTOR PLOTS AT EACH DIFFERENT SHAFT ROTATIONAL SPEED AND 7.3 L/MIN FOR THE P4 COUNTER-CURRENT REGIME 166

FIGURE 5.9: MEAN VELOCITY MAGNITUDE VECTOR PLOTS AT EACH DIFFERENT SHAFT ROTATIONAL SPEED AND 7.3 L/MIN FOR THE P2 CO-CURRENT REGIME 167

FIGURE 5.10: AXIAL VARIATION OF FILM THICKNESS AT CO- AND COUNTER-CURRENT REGIONS (P2 AND P4) WITH SHAFT ROTATIONAL SPEED AGAINST EXPERIMENTAL MEASUREMENTS OF HEE ET AL. [54] AT 3mm AND 10mm 170

FIGURE 5.11: VARIATION IN OIL FILM THICKNESS WITH ROTATIONAL SHAFT SPEED FOR CO- AND COUNTER-CURRENT REGIONS (P2 AND P4). TOP 5.2 L/MIN AND BOTTOM 7.3 L/MIN. 171

FIGURE 5.12: NON-DIMENSIONALISED FILM VELOCITY AT THE a) P2 SECTOR AND b) P4 SECTOR FOR EACH SHAFT SPEED AT 7.3 L/MIN 173

FIGURE 5.13: MEAN STREAMLINE PLOTS GENERATED FOR P2 (RED) AND P4 (GREEN) LOCATIONS AT EACH SHAFT SPEED (7.3 L/MIN) 174

FIGURE 5.14: AXIAL VARIATION OF FILM THICKNESS FOR THE TWO OIL INLET SPLITS AT BOTH P2 AND P4 REGIONS. COMPARISON WITH REPRESENTATIVE FILM INLET BOUNDARY CONDITION, 0/100 SPLIT 178

FIGURE 5.15: INSTANTANEOUS PARTICLE TRAJECTORIES WITHIN THE MAIN CHAMBER COLOURED BY DIAMETER FOR 7000 RPM 7.3 L/MIN (FILM NOT SHOWN) 182

FIGURE 5.16: MEAN FILM VELOCITY WITH ANGULAR COORDINATE AT THE FRONT-FACE EDGE (7.3 L/MIN) 183

FIGURE 5.17: EXPERIMENTAL OIL STRUCTURE AT P1 [55], 7,000 RPM & 7.3 L/MIN (6,000 fps) 185

FIGURE 5.18: EDGE SEPARATED PARTICLE MEAN TANGENTIAL TRAJECTORIES FOR EACH SHAFT SPEED (7.3 L/MIN) 188

FIGURE 5.19: PARTICLE TRAJECTORIES PASSING FROM P1 THROUGH P2 OBSERVED EXPERIMENTALLY AT THE P2 REGION [134], 7,000 RPM & 7.3 L/MIN 189

FIGURE 5.20: RADIAL/AXIAL EDGE SEPARATED PARTICLE TRAJECTORIES BASED ON AVERAGE PARTICLE DIAMETER 190

FIGURE 5.21: SIMPLIFIED REPRESENTATION OF WETTED AREA (BLUE) ON OUTER CASING WALLS AFTER DROPLET IMPINGEMENT 191

FIGURE 5.22: NORMALISED STRIPPED PARTICLE DIAMETERS AT 7,000 RPM AND 7.3 L/MIN 192

FIGURE 5.23: NORMALISED EDGE SEPARATED PARTICLE DIAMETERS AT EACH SHAFT SPEED 194

FIGURE 5.24: COMPARISON OF SECONDARY BREAKUP FOR THE PARTICULATE FLOW AT 12,000 RPM (7.3 L/MIN) 195

FIGURE 5.25: NORMALISED EDGE SEPARATED PARTICLE DIAMETERS AT EACH QUADRANT 196

FIGURE 5.26: CONTOUR MAP OF PARTICLE DIAMETER VERSUS VELOCITY COLOURED BY NORMALISED PROBABILITY 198

FIGURE 5.27: AVERAGE PARTICLE RESIDENCE TIME IMMEDIATELY BEFORE IMPINGEMENT ON THE OUTER CASING WALL (7.3 L/MIN) 199

List of Tables

TABLE 3.1: AXISYMMETRIC GRIDS FOR MESH INDEPENDENCE STUDY 75

TABLE 3.2: AXISYMMETRIC MESH INDEPENDENCE STUDY RESULTS FOR THE STANDARD k-ε AND STANDARD k-ω TURBULENCE MODELS ... 76

TABLE 3.3: PERCENTAGE ERROR IN BOTH AVERAGE RADIAL VELOCITY AND WAVELENGTH ACROSS TAYLOR VORTEX COMPARED TO WANG [22] AT R =100..... 80

TABLE 3.4: PERCENTAGE ERRORS IN INFLOW AND OUTFLOW TAYLOR VORTEX BOUNDARIES FOR THE TWO TURBULENCE MODELS..... 82

TABLE 3.5: NON-DIMENSIONAL VELOCITY MAGNITUDE AT NON-DIMENSIONAL DISTANCE OF 0.581 FOR THE STANDARD k-ω TURBULENCE MODEL 84

TABLE 3.6: THREE-DIMENSIONAL MESH INDEPENDENCE STUDY FOR THE STANDARD k-ω TURBULENCE MODEL..... 86

TABLE 3.7: LOG-REGION CONSTANTS FOR BOTH TURBULENCE MODELS AT THE INNER AND OUTER CYLINDER BOUNDARY LAYERS..... 90

TABLE 3.8: OPERATING CONDITIONS AND FLUID PROPERTIES..... 97

TABLE 3.9: NON-DIMENSIONAL VORTEX CENTRE LOCATIONS..... 105

TABLE 4.1: NON-DIMENSIONAL VORTEX CENTRE LOCATIONS..... 120

TABLE 4.2: PARAMETRIC STUDIES INVESTIGATED FOR: MESH DENSITY, AIRFLOW TIME-STEP, PARCEL INJECTION COUNT AND SUB-MODELS..... 138

TABLE 4.3: NOZZLE INJECTION PARAMETERS 142

TABLE 5.1: AVERAGED FILM THICKNESS MEASUREMENTS (mm) AT 7,000 RPM FOR AXIAL AND ANGULAR LOCATIONS WITHIN THE FILM SLOT 157

TABLE 5.2: COMPUTATIONAL OPERATING CONDITIONS 160

TABLE 5.3: COMPUTATIONAL AIR/OIL MATERIAL PROPERTIES..... 160

TABLE 5.4: AVERAGE CLOUD PROPERTIES AT EACH ROTATIONAL SPEED 181

TABLE 5.5: PROPORTION OF EDGE SEPARATED MASS AT EACH ROTATIONAL SPEED 181

Nomenclature

Acronyms

2D	Two-dimensional
3D	Three-dimensional
ACARE	Advisory Council for Aeronautics Research in Europe
AMR	Adaptive Mesh Refinement
ASM	Algebraic Slip Model
BSL	Baseline
CFD	Computational Fluid Dynamics
CFL	Courant-Friedrichs-Lewy
CPU	Central Processing Unit
DNS	Direct Numerical Simulation
DPM	Discrete Phase Model
DRW	Discrete Random Walk
ED	Expansion Duct
ETFM	Eulerian Thin Film Model
EWT	Enhanced Wall Treatment
FVM	Finite Volume Method
G2TRC	Gas Turbine and Transmission Research Centre
HP	High Pressure

IATA	International Air Transport Association
ICAO	International Civil Aviation Organization
IP	Intermediate Pressure
KH	Kelvin Helmholtz
LDA	Laser Doppler Anemometry
LES	Large Eddy Simulation
LP	Low Pressure
lpm	Litres per Minute
MPI	Message Passing Interface
NRMSD	Normalised Root Mean Square Deviation
PDPA	Phase Doppler Particle Analyser
PIMPLE	PISO-SIMPLE
PISO	Pressure-Implicit of Split Operations
PIV	Particle Image Velocimetry
PRESTO!	PREssure STaggering Option
RNG	Re-normalisation Group
rpm	Revolution per Minute
RSDM	Rotational Speed Driven Mode
RSM	Reynolds Stress Model
RT	Rayleigh Taylor
SADM	Sealing Air Driven Mode
SAS	Scale-Adaptive Simulation
SD	Straight Duct
SIMPLE	Semi-Implicit Method for Pressure Linked Equations

SST	Shear Stress Transport
TVF	Taylor Vortex Flow
TTVF	Turbulent Taylor Vortex Flow
QUICK	Quadratic Upstream Interpolation for Convective Kinematics
UDF	User Defined Function
URANS	Unsteady Reynolds Average Navier-Stokes
VOF	Volume of Fluid
WVF	Wavy Vortex Flow

Characteristic Numbers

F_{ratio}	Edge Separation Force Ratio
Fr	Froude Number
La	Laplace Number
Ma	Mach Number
R	Reynolds Number Ratio
Re	Reynolds Number
R_u	Shaft Speed to Sealing Air Velocity Ratio
T	Taylor Number Ratio
Ta	Taylor Number
We	Weber Number

Greek Symbols

Ω^+	Dimensionless Rotational Velocity
λ^+	Non-dimensional Wavelength

Γ	Device Aspect Ratio
Ω	Rotational Velocity $[rad.s^{-1}]$
ϕ	Transported Quantity
α	Surface Film Sheltering Parameter
β	Log-Rosin-Rammler Scaling Factor
γ	Swirl Angle [°]
δ	Film Thickness $[m]$
ε	Turbulent Dissipation Rate $[m^2.s^{-3}]$
η	Radius Ratio
κ	von Kármán Constant
λ	Wavelength $[m]$
μ	Dynamic Viscosity $[kg.m^{-1}.s^{-1}]$
ν	Kinematic viscosity $[m^2.s^{-1}]$
ρ	Density $[kg.m^{-3}]$
σ	Surface Tension $[N.m^{-1}]$
τ	Shear Stress $[Pa]$
φ	Log-Rosin-Rammler Location Parameter
ω	Specific Turbulence Dissipation Rate $[s^{-1}]$

Latin Symbols

C_A	Nozzle Geometry Coefficient
C_D	Drag Coefficient
C_H	User Defined Stripping Coefficient, Default = 1
C_f	Skin Friction Coefficient

C_l	Droplet Diameter Coefficient, Default = 3.78
L_b	Surface Film Characteristic Length
N_{TV}	Number of Taylor Vortex Pairs
N_p	Number of Particles per Parcel
$\dot{V}$	Volume Flow Rate $[m^3.s^{-1}]$
a^+	Non-dimensional Wavenumber
$\dot{m}$	Mass Flow Rate $[kg.s^{-1}]$
u^+	Dimensionless Velocity
u_τ	Friction Velocity $[m.s^{-1}]$
y^+	Dimensionless Wall Spacing
P1	Bearing Chamber: Top Dead Centre, 0°
P2	Bearing Chamber: Co-Current Side, 90°
P3	Bearing Chamber: Bottom Dead Centre, 180°
P4	Bearing Chamber: Counter-Current Side, 270°
B	Turbulence Damping Parameter
D	Chamber/Nozzle Diameter $[m]$
F	Force $[N]$
G	Non-dimensional Shaft Torque
H	Cylinder/Chamber Length $[m]$
M	Shaft Torque $[N.m]$
P	Pressure $[Pa]$
R	Non-dimensional Radial Distance
S	Stress Source Term
T	Temperature $[K]$

W	Chamber Width $[m]$
Y	Percentage of Surface Film Mass Separated
Z	Non-dimensional Axial Distance
d	Particle/Droplet Diameter $[m]$
f	Wave Frequency $[s^{-1}]$
g	Gravitational Acceleration $[m.s^{-2}]$
k	Turbulent Kinetic Energy $[m^2.s^{-2}]$
l	Axial Extent of Taylor Vortex $[m]$
m	Mass $[kg]$
n	Rotational Shaft Speed $[rpm]$
p	Surface Film Pressure Source Term
r	Radius $[m]$
s	Droplet Distortion
t	Time $[s]$
u	Velocity $[m.s^{-1}]$
y	Wall Coordinate $[m]$
z	Axial Distance $[m]$

Derivatives

Δx	Grid Spacing $[m]$
Δt	Time Step Size $[s]$
$\frac{\partial \phi}{\partial t}$	Time Evolution of Variable ϕ $[unit.s^{-1}]$
∇	Vector Differential Operator

Subscripts and Superscripts

∞	Freestream
D	Drag
Dry	Dry Film Surface
Wet	Wetted Film Surface
a	Wave Amplitude
air	Air
c	Critical
d	Droplet
f	Film
g	Gas
i	Inner
jet	Jet
l	Liquid
mag	Magnitude
o	Outer
p	Particle
r	Radial
rel	Relative
s	Surface
sh	Shaft
w	Wall
z	Axial
θ	Tangential

Chapter 1

Introduction

1.1 Background

By 2050 the aviation industry will fly 16 billion passengers and 400 million tonnes of cargo according to the International Air Transport Association (IATA) [1]. A rapid growth in passenger capacity has seen various industry leaders and institutions drive for actions to mitigate global climate change and increase environmental awareness. At a global aircraft fleet level, the IATA has published aspirational goals comprised of three major targets [2]:

1. A continuous improvement in fuel efficiency of 1.5% per annum from 2009 to 2020
2. Carbon-neutral growth, by capping net aviation CO_2 emissions from 2020
3. A reduction of 50% in net aviation CO_2 emissions by 2050, relative to 2005 levels

In order to meet the carbon targets and address aviation's climate impacts, an industry 4 pillar strategy has been established. The four pillars commit to: improving technology; increased efficiency of aircraft operations; upgrading infrastructure; and finally, to fill the remaining emissions gap, a single global market-based measure.

At an aircraft level, the European Commission has strategized its own long-term research agenda, Flightpath 2050 [3], building on the goals of Vision 2020 [4] established by the Advisory Council for Aeronautics Research in Europe (ACARE). Flightpath 2050 details a reduction in CO_2 emissions by 75% per passenger km, NO_X emissions by 90% and a decrease in the perceived noise levels of aircraft by 65%. These goals are relative to a typical aircraft entering into service in the year 2000. The targets set by the European Commission are regarded as being at an equivalent standard to those announced by the IATA and the International Civil Aviation Organization (ICAO).

With a drive to reduce the ecological footprint, as set out by the long-term research goals, aircraft manufacturers are continuously improving upon their current product portfolio with new aircraft programmes and performance increases to their existing product lines. In particular, aeroengine

manufacturers are tasked with the significant challenge of developing more efficient engines with an aim to reduce emissions. Higher propulsion and thermal efficiencies can be achieved through increasing both the turbine rotor inlet temperature and the overall bypass ratio; as such, significant progress has been achieved to date. To sustain these higher temperatures, the development of more advanced, lightweight, materials has been crucial, alongside the addition of improvements to blade or vane cooling technologies. The aim to operate at both higher temperatures and shaft speeds requires sufficient understanding of these systems for design optimisation, as components are subjected to both greater thermal and mechanical stresses. Rotating elements, such as the shafts, gears and bearings need to be appropriately supplied with oil, in order to ensure efficient lubrication and cooling. For example, due to these extreme working conditions, aeroengine oils are required to operate between -40 °C and >250 °C, [5]. However, to prevent over-heating, typically the amount of oil supplied to these rotating elements is far greater than needed. In general, the requirements of the oil can be broken down into 90% for heat transfer, 5-10% for lubrication and a remaining 2-3% for additional roles such as seals and corrosion protection [5]. Therefore, the desire for a more lightweight and robust engine design can be achieved through better understanding of the heat management process, allowing for proper dimensioning of the oil system.

Innovations and improvements to aeroengine oil systems have played a crucial role in reducing aircraft operating costs directly through oil inventory reduction, although there is still substantial progress to be made. One such example of this, is the European funded research program: Engine LUBrication SYStem technologies (ELUBSYS) [6]. The final report summaries that, through simplifications to the bearing housings, in combination with a smaller size and number of scavenge pumps, a reduction in engine mass of 18kg was possible; equivalent to a gain in the specific fuel consumption of 0.05%. Furthermore, it was suggested that improved oil system design could decrease the amount of oil consumption by 60%, leading to a reduction in the size of oil tanks by 30%, saving up to a further 6kg.

In recent years, with the development of new supercomputers and improved computing power that is more readily accessible, significant progress has been made within the field of Computational Fluid Dynamics (CFD). The capability to accurately model elements of the aeroengine is seen as key to improving efficiencies and optimising design. With a combined experimental and computational approach, CFD result can be validated against experimental measurements; whilst computationally, the results can further expand into the parameter space and provide useful insight into areas that are not feasible or too expensive to explore experimentally. The advancement of novel computational methods has allowed considerable challenges to be overcome around the modelling of aeroengine components. However, there is still a great deal of uncertainty associated with these techniques.

One such method, that has regained popularity over the last five years, is the Eulerian Thin Film Model (EFTM). Notable improvements and developments have been made to the ETFM, and with increased computational resources, more advanced aeroengine investigations have been possible. Typically, this is achieved through coupling the ETFM with additional models, such as either the Discrete Phase Model (DPM) or a Volume of Fluid (VOF) approach, allowing a greater level of complexity to be achieved. Within an aeroengine, the application of the ETFM is particularly useful for bearing chamber investigations; however, to date, prior modelling attempts have been limited by the state-of-the-art capability.

The aim of this research is to, develop and improve aeroengine bearing chamber modelling capability in an effort to better inform design optimisation and reduce parasitic losses such as windage and heat-to-oil. Through investigating new flow physics, a greater understanding of these systems can be achieved. As such, the focus of this current computational investigation considers part of the aeroengine oil system, specifically an aeroengine ball bearing and its bearing chamber.

1.2 Aeroengine Oil Systems

Within an aeroengine, the oil system is self-contained and consists of three main regions: a pressure fed oil distribution, a scavenge arrangement and a vent configuration [7]. Modern aeroengines use a full flow oil system, which benefits from the use of a series of smaller oil pumps to achieve a desired oil flow rate over a range of operational engine speeds. This is instead of the conventional pressure relief valve system, in which the feed line pressure is limited to a fixed value in order to control the oil flow rate. Typically, positive displacement pumps are employed, such as vane, gear or gerotor pumps, which supply a known oil flow rate that is proportional to the pump speed and hence overall engine operating speed. Figure 1.1 shows a typical Trent-style aeroengine and its re-circulatory oil system, which is explained below.

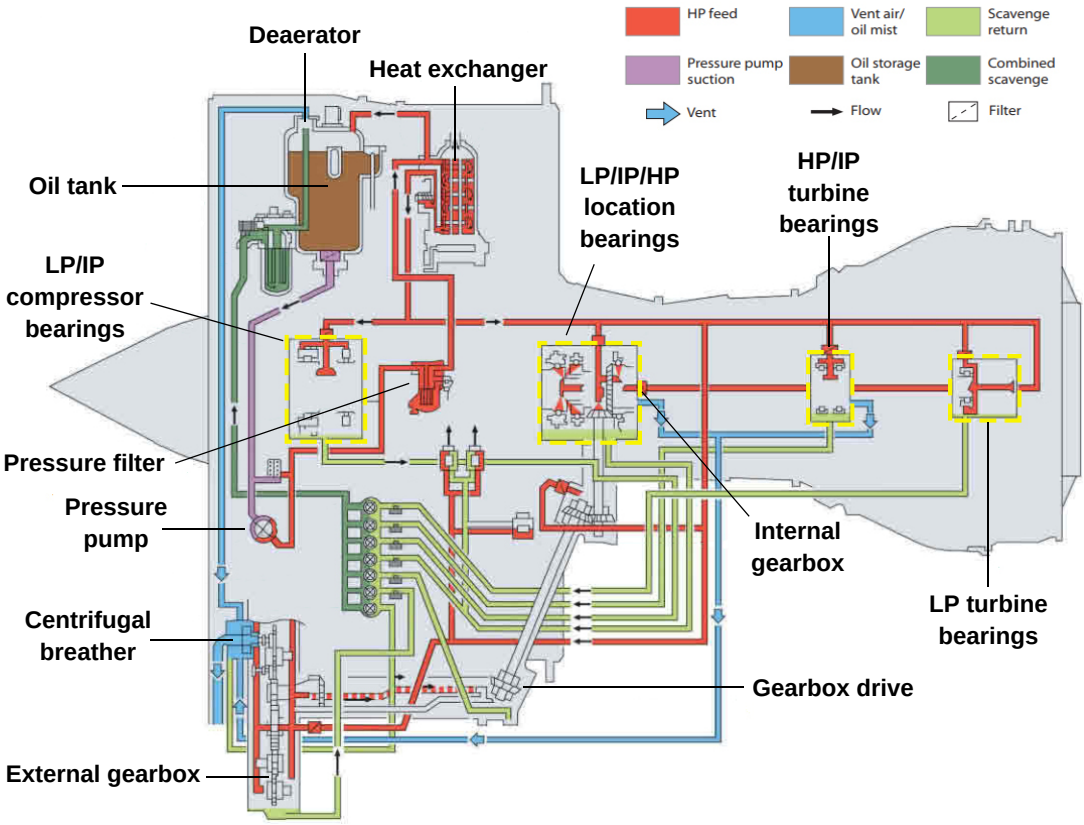


FIGURE 1.1: SCHEMATIC OF A TYPICAL THREE-SHAFT TRENT ENGINE, HIGHLIGHTING THE OIL SYSTEM AND BEARING LOCATIONS, MODIFIED FROM [7]

In general, the operation of the oil system for a Trent-style engine [7], shown in Figure 1.1, can be described as follows. The oil tank contains a reservoir of oil, this must have sufficient capacity for the maximum flight conditions and also capability to accommodate expansion of the oil as it heats up. To begin with, oil is drawn from the tank and, first, passes through a strainer to protect the system from solid contaminants. The quality of the oil is extremely important since components, such as pumps and bearings, can be significantly damaged by foreign matter; in

addition to the strainer, magnets within the scavenge system are also used to remove steel debris. Next, the oil flows through a regulator in order to avoid extreme pressures as a result of either blockages or high oil viscosities found under exceptionally cold starting conditions. Afterward, the oil passes through the heat exchangers whereby the oil transfers heat to the fuel, to maintain the oil at an appropriate temperature; usually, the fuel-oil heat exchanger is located within the high-pressure oil feed to prevent leakage by keeping the oil at a higher pressure than the fuel.

Subsequently, the oil supply is then divided into separate lines to provide oil to the gearbox and each of the bearing chambers. Oil jets can then be used to supply a precise amount of oil to the individual components, such as the ball bearings. Upstream of the jet, restrictors are used to control the pressure drop and obtain a low oil flow rate. Furthermore, these jets can be designed to either spray or target oil directly onto the part, or instead, a catching device such as a scoop can be employed. For situations in which jets are not applicable, oil distributors are used; here, oil is centrifugally dispersed through outlets located within the rotating shafts. After successful lubrication and cooling of the gearbox, and each individual bearing chamber, the oil is scavenged through the respective sumps in each component. Upon returning to the tank, the oil passes through a deaerator before being recirculated again, this ensures that any air is removed from the oil.

Within the scavenge system, it is important to return the oil fed to the bearing chambers back to the tank without delay. This is to reduce the effects of oil ‘gulp’, but also, to minimise the degradation of the oil as a result of prolonged exposure to the high temperature environments.

In general, the vent system is maintained at a lower pressure to enable a positive pressure drop across the bearing chambers. Therefore, the vent system needs to be sized appropriately to ensure that there is adequate sealing within the bearing chambers, whilst having a negligible impact on the engine performance. Furthermore, due to the complex two-phase bearing chamber environment, it is important to recognise that oil droplets will be entrained within the vented air. To make sure that this oil is not lost from the system, the vented air passes through a centrifugal breather, in which the high-speed rotation causes the oil droplets to be separated from the air. The oil is subsequently returned to the tank through the scavenge arrangement. Finally, this separated air, produced from both the vent and scavenge systems, is exhausted overboard; however, it is essential that this ejected air is sufficiently cleaned within the breather to avoid any visible oil marks on either the nacelle or the aircraft wings.

1.3 Aeroengine Rotor Support Structures

Fundamentally, the outer structure of an aeroengine acts as a pressure vessel in which hot air flows from the front of the engine to the rear. Therefore, within this arrangement, rotor support structures extend inside the domain to support the rotating elements, whilst still permitting a through flow of air [7]. At the bearings, these structures assist in transmitting the radial loads generated from the rotation of the shafts, to the outer framework and ultimately the engine mounts. Figure 1.2 highlights a typical HP-IP hub structure, which, due to the high radial loads and extreme temperatures, is a very challenging environment. Within this region, as a result of its configuration, only oil delivered through the support structure struts is available for cooling.

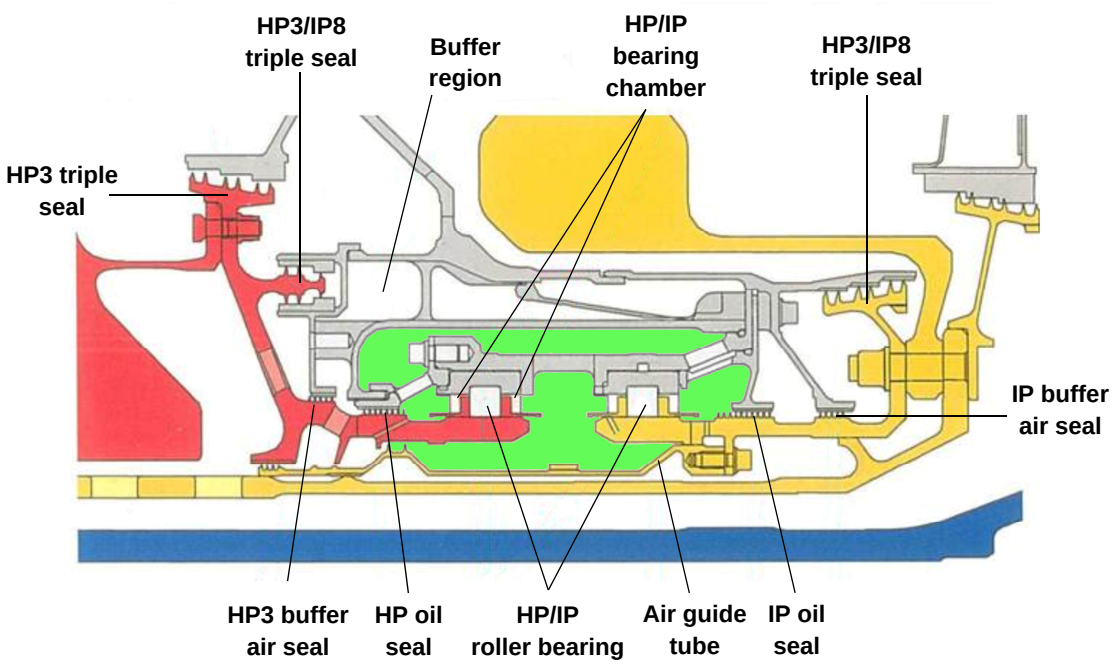


FIGURE 1.2: HP-IP HUB FOR A TYPICAL THREE-SHAFT ENGINE, MODIFIED FROM [7]. GREEN: TWO-PHASE FLOW; RED: HP SHAFT; YELLOW: IP SHAFT; BLUE: LP SHAFT; GREY: STATIC

Located at the centre of the rotor support structure, in Figure 1.2, is the HP-IP bearing chamber. Around the shafts, a combination of rotating seals are subsequently used to prevent oil leakage, but also to limit the proportion of hot air that flows into the chamber. As such, the bearing chambers are sealed using bleed air from the compressors and typically, labyrinth seals are employed [7]; however, future aeroengines will use reduced leakage, next generation seals. This sealing configuration surrounding the HP-IP bearing chamber is highlighted in Figure 1.2. Labyrinth seals drive air through a series of fins, creating an airflow resistance; as air traverses across each fin tip, the acceleration and subsequent expansion of the air causes a pressure drop. Therefore, outside of the labyrinth seals, the bearing chamber is surrounded by a buffer region of air, which is maintained at a relatively higher pressure. This causes air to flow into the chamber and consequently inhibits oil from leaking out past the labyrinth seal.

1.4 Aeroengine Bearing Chambers

In aeroengines, the shafts (high pressure, HP, intermediate pressure, IP and low pressure, LP) are supported by bearings and as shown in Figure 1.1, these bearings are supplied with oil for lubrication and cooling. The bearings are housed in bearing chambers creating a highly rotating two-phase environment. There are normally four main bearing chambers on a typical 3-shaft aeroengine [7] and as highlighted in Figure 1.1, these consist of: the LP-IP bearing at the front of the engine; the internal gearbox, containing HP, IP and LP elements, this houses the spiral bevel gear that provides the auxiliary power offtake; the HP-IP turbine bearing chamber, which is the smallest and hottest chamber; and finally the LP tail bearing at the rear of the engine. Within the scope of this thesis, only the HP-IP bearing chamber is considered. Figure 1.3 shows a simplified schematic of a typical aeroengine HP-IP bearing chamber, highlighting the relevant phenomena and key flow physics.

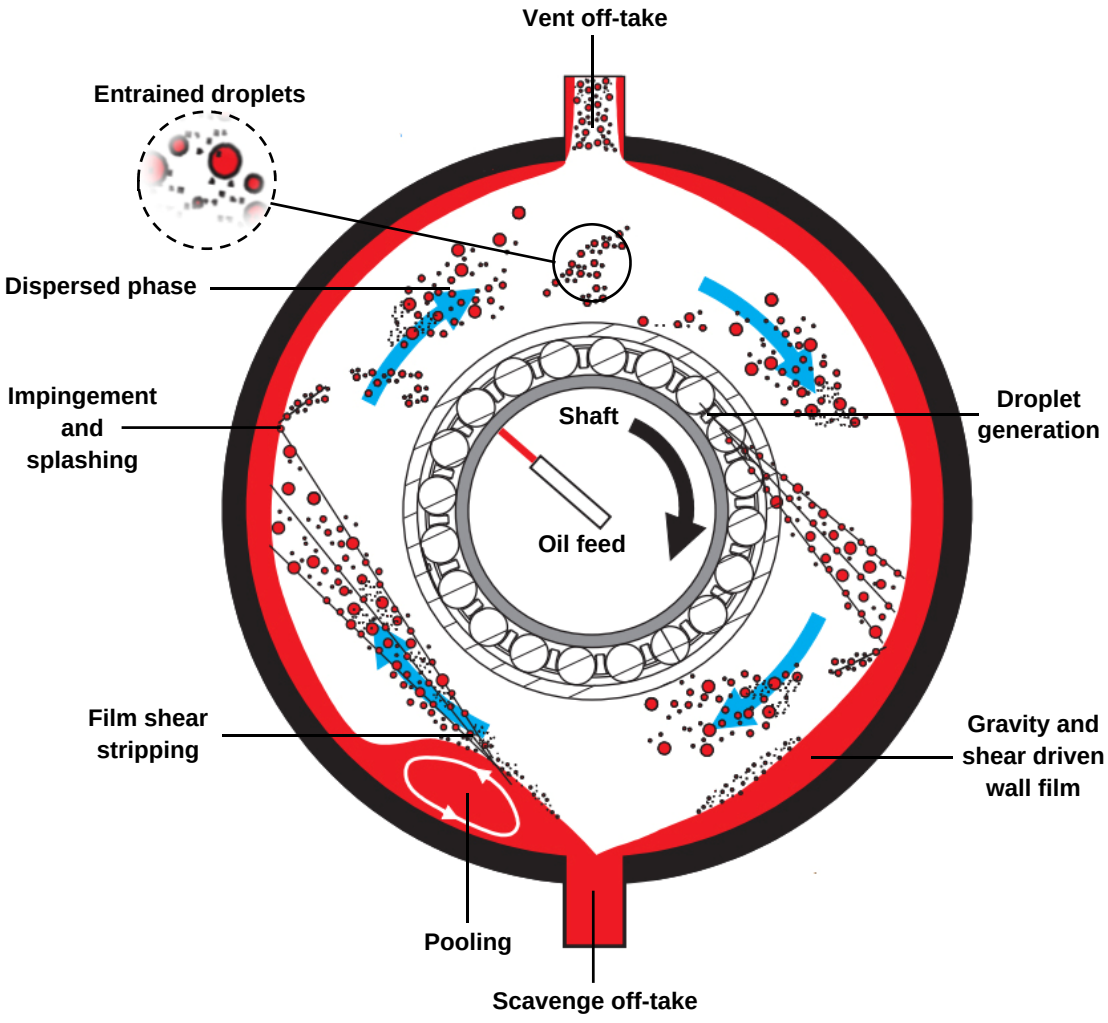


FIGURE 1.3: SIMPLIFIED AEROENGINE BEARING CHAMBER FLOW PHYSICS, MODIFIED FROM [8]

Within a bearing chamber, the detailed physics may be broken down into two distinct but interacting regions [9]. Firstly, the shear and gravitational forces drive a segregated flow regime, consisting of laminar wavy oil films ranging from thin to thick. Secondly, the turbulent gas flow transports a dispersed flow region, formed of oil droplets varying in diameter. The segregated flow regime is dependent on not only the amount of oil present, but also a balance between the gravitational, viscous and interfacial shear stresses. Depending on the operating conditions, there are three main different flow states observed within a bearing chamber and a simplified schematic of each is depicted within Figures 1.4 a) to c). At lower rotational shaft speeds, the gravitational force dominates over the shear force and a pool regime is observed; oil accumulates toward the bottom of the chamber leading to areas of dry-out on the top walls, Figure 1.4 a). As the shaft speed increases, the interfacial shear stress eventually overcomes the gravitational forces and a smooth flow regime is found; the oil begins to rotate in the same angular direction as the shaft and a thinner film is typically observed, Figure 1.4 c). When transitioning between these two states, i.e. the gravity component and shear effect are equal, a so-called shock regime is observed, as shown in Figure 1.4 b).

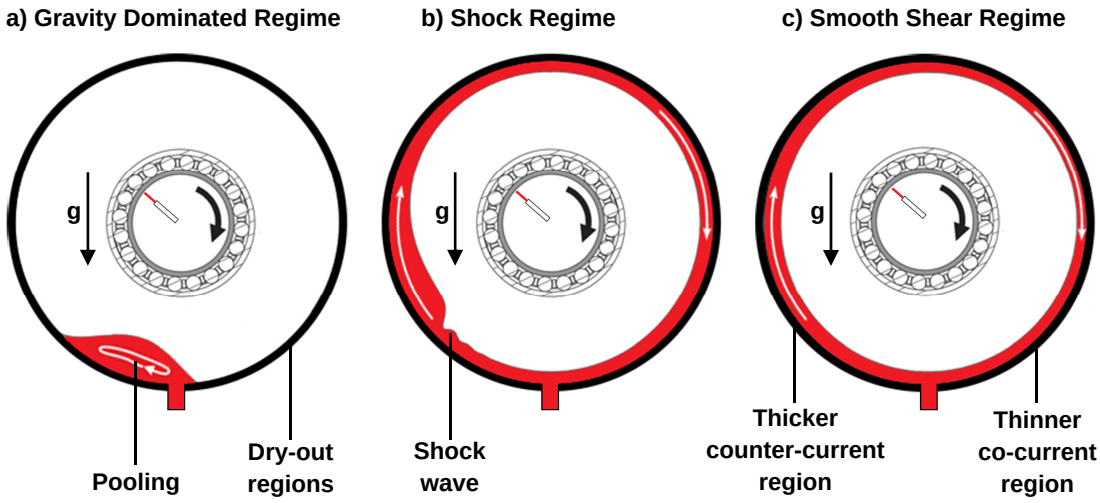


FIGURE 1.4: BEARING CHAMBER FLOW REGIMES

Around the cavity annulus of a bearing chamber, the local film thickness will influence the amount of heat transfer through the chamber housing [10]. Therefore, to prevent the formation of localised hot spots and potentially oil coking, it is desirable to have a uniform film coverage, and hence heat transfer, around the bearing chamber walls. In a perfect system, the quantity of oil supplied to the chamber would be the minimum amount required for heat transfer and cooling; ensuring that critical areas are targeted before the oil exits the system. However, due to the lack of uncertainty surrounding the oil distribution and further complexity introduced when considered

geometrical features such as struts, bolts, and spring bars, typically a far greater amount of oil than required is supplied.

Aside from the flow regime, the distribution of film thickness is determined predominantly by the impinging droplets but is also a function of the angular coordinate. The mass and momentum imparted on the film by the droplets is therefore ultimately determined by the initial conditions, namely: the shaft rotational speed, the sealing airflow and the volume flow rate of oil. Consequently, when modelling these systems, computationally, it is essential to have precise measurements surrounding the droplet initial conditions or an understanding of the solution sensitivity to the main parameters.

The capability to accurately model these bearing chambers is seen as key to reducing losses and optimising bearing chamber design. The University of Nottingham Gas Turbine and Transmission Research Centre (G2TRC) has been conducting research in this field for a number of years over which modelling capability has been significantly improved. This research has comprised of a number of key elements, including capability to model windage power losses in the internal gearbox and the ability to model aspects of the complex two-phase bearing chamber flow including film motion, oil scavenge and droplet/film impact.

One of the areas yet to be fully explored is the effect of turbulence in bearing chambers on the oil/air behaviour. In particular, there is still considerable uncertainty regarding which is the best turbulence model to use in these computational simulations; in addition to, how geometrical and operational chamber parameters influence turbulence within the chamber. Furthermore, minimal work has been carried out in order to quantify the characteristics of the droplets shed from the bearing into the bearing chamber. As such, there is a requirement to consolidate and extend the work conducted to date on two-phase modelling and develop beyond existing modelling capability to enable optimisation of bearing chamber design based on required functionality.

1.5 Aims and Objectives

The aim of the current research is to develop a modelling methodology to predict the way oil enters an aeroengine representative bearing chamber geometry following its passage through a bearing. In addition to capturing the subsequent behaviour of the oil, through exploring the complex droplet generation process and the following oil film formation. To achieve this, the bearing geometry used, models that of the Trent 1000 ball bearing. As a result of developing and improving upon existing modelling capability, the application of such techniques will aim to advance understanding and pave the way for improved design capability. Ultimately, the work carried out will assist in the design optimisation of aeroengine bearing chambers and improve knowledge surrounding the heat and oil management process. The three main objectives of the thesis, and their corresponding sub-objectives, are outlined as follows:

1. ***Exploration:*** to first provide an appropriate unsteady Reynolds-averaged Navier-Stokes (URANS) turbulence modelling methodology applicable for aeroengine bearing chamber simulations
    a. To establish a URANS best practice turbulence modelling approach, first, with respect to a Taylor-Couette system
    b. To extend this capability to a single-phase bearing chamber geometry, providing recommendations for the most appropriate turbulence model
2. ***Development:*** to establish an appropriate modelling methodology for the two-phase flow present within an aeroengine bearing chamber, utilising a fully coupled two-way Eulerian Thin Film Model (ETFM) and Discrete Phase Model (DPM) approach
    a. To consolidate the existing DPM capability, including consideration for secondary breakup of the particulate cloud
    b. To couple the ETFM with a DPM approach, establishing relevant thin film sub-models, such as either a film stripping or an edge separation criteria
    c. To validate the ETFM-DPM coupling against empirical studies, accounting for the relevant flow phenomena that may occur within a bearing chamber
3. ***Application:*** to investigate a simplified aeroengine bearing chamber using the developed ETFM-DPM methodology
    a. To analyse the film formation and subsequent dynamics on surfaces close to the aeroengine ball bearing
    b. To determine the influence of the flow regime on the film behaviour
    c. To characterise droplets shed into the bearing chamber, reporting on relevant statistics relating to size, velocity, impingement and residence time
    d. To provide knowledge of solution sensitivity to operational parameters such as the rotational shaft speed and oil flow rate

1.6 Thesis Outline

The thesis structure is categorised into five main chapters. This section provides a summary of their content and an overall outline of the methodology, described as follows.

Chapter 2 provides a review of the relevant literature surrounding both Taylor-Couette systems and aeroengine bearing chamber flows. Within computational aeroengine bearing chamber investigations, there is still considerable uncertainty regarding the selection of a turbulence modelling approach due to the complexity of the problem. In an attempt to provide closure, focus is therefore shifted to a review of more classical geometries, and specifically, Taylor-Couette flows. A Taylor-Couette apparatus can be regarded as analogous to a bearing chamber geometry, when simplified to a rotating shaft enclosed within a stationary outer cylinder. As such, a review of experimental and computational Taylor-Couette systems is conducted in an attempt to provide an appropriate URANS turbulence modelling methodology suitable for bearing chamber applications. Following this, a review of experimental bearing chamber investigations is performed, highlighting the relevant phenomena and underlying key flow physics. The literature survey concludes with an assessment of the appropriate numerical techniques available for bearing chamber modelling, these include: the VOF method, the ETFM and the DPM. The current state-of-the-art bearing chamber modelling capability utilises the coupling of these methods resulting in the following approaches: VOF-ETFM, VOF-DPM and ETFM-DPM.

Within Chapter 3, the computational modelling of turbulent Taylor-Couette flows is considered and the commercial CFD software ANSYS Fluent is utilised. To inform aeroengine bearing chamber applications, within the Taylor-Couette system, a comparison of URANS turbulence modelling approaches is performed for both axisymmetric and three-dimensional geometries. Particular attention is dedicated to the start-up procedure employed computationally, due to the dependence of the final Taylor-Couette state on both the initial conditions and acceleration of the inner cylinder; highlighting the difference between sudden starts and steady acceleration procedures. Through comparison to published experimental measurements, a recommended turbulence modelling methodology is presented for Taylor-Couette flows. This approach is extended to a single-phase bearing chamber investigation in order to confirm that the conclusions drawn from the Taylor-Couette study are transferable. Within the bearing chamber, over a combination of rotational shaft speeds and sealing airflow rates, an analysis of the secondary vortex flow field is presented and compared to available experimental data. Based on the inferences of the Taylor-Couette investigation and the conclusions of the single-phase bearing chamber study, a recommended URANS turbulence model is suggested for all future aeroengine bearing chamber investigations. The work carried out within this chapter forms the journal paper publication: “Computational Modelling of Turbulent Taylor-Couette Flow for Bearing Chamber

Applications: A Comparison of Unsteady Reynolds-Averaged Navier-Stokes (URANS) Models," *Submitted for publication, 2020*.

Chapter 4 highlights the development of the fully coupled two-way ETFM-DPM solver, *sprayParcelFilmFoam*, within the open-source CFD code OpenFOAM. A review of current literature suggests that there is a need for a more appropriate and accurate computational modelling technique that is suitable for capturing the observed oil shedding behaviour from bearings and the subsequent film formation. OpenFOAM was chosen, due to initial uncertainties surrounding modelling capability and previous attempts reported within the literature using conventional codes. Firstly, to determine the capability of OpenFOAM, a single-phase bearing chamber investigation is performed, based on the recommendations of Chapter 2. Following this, the procedure of coupling the ETFM with a DPM approach is outlined. To account for the bearing chamber flow physics, capability is included for secondary breakup of the particulate cloud. In addition, two new thin film models are implemented based on empirical studies for both a film stripping and an edge separation criteria. The newly developed *sprayParcelFilmFoam* solver is validated against an experimental study for a liquid jet injected into a high velocity crossflow. Results are compared with available film thickness measurements as well as particle diameters and velocities, demonstrating significant improvement over the existing state-of-the-art techniques. The development of *sprayParcelFilmFoam* represents an advance in bearing chamber modelling capability. This study is highlighted within the ASME conference paper: "A New OpenFOAM Solver Capable of Modelling Oil Jet-Breakup and Subsequent Film Formation for Bearing Chamber Applications," *Proceedings of the ASME Turbo Expo 2019, Phoenix, Arizona, 2019.*

Chapter 5 presents the application of *sprayParcelFilmFoam* to a simplified aeroengine bearing chamber, for which experimental data exists. This represents the first application of a fully coupled two-way ETFM-DPM approach for bearing chamber simulations, reporting on relevant statistics surround the droplet generation process. Results are presented over a combination of three different rotational shaft speeds and two oil flow rates, representative of engine operating conditions. Firstly, a qualitative and quantitative analysis of the film is presented, comparing to available high-speed imaging and film thickness measurements; overall, a good agreement is found. Subsequently, an analysis of oil shed into the chamber is performed. For these droplets, relevant statistics relating to size, velocity, impingement and residence time are presented; providing knowledge of solution sensitivity to operational parameters, such as the rotational shaft speed and oil flow rate. Overall, this work has established a firm foundation for future aeroengine bearing chamber modelling, as well as, delivering new insights into key flow elements and behaviours. This research forms a two-part investigation submitted for journal paper publication, firstly: "Simulation of A Simplified Aeroengine Bearing Chamber Using A Fully Coupled Two-

Way Eulerian Thin Film/Discrete Phase Approach: Film Behaviour Near the Bearing," *Submitted for publication, 2020*; and secondly: "Simulation of A Simplified Aeroengine Bearing Chamber Using A Fully Coupled Two-Way Eulerian Thin Film/Discrete Phase Approach: Droplet Behaviour in the Chamber," *Submitted for publication, 2020.*

Finally, the conclusions of the thesis are presented in Chapter 6. In addition, the contributions to knowledge as a result of the work carried out is presented and recommendations for future work are suggested.

Chapter 2

Literature Review

In this chapter, a detailed literature review is presented, focusing on both Taylor-Couette flows and more importantly aeroengine bearing chambers. The survey starts with an investigation into both experimental and numerical Taylor-Couette flows, to assist in the understanding of the single-phase aeroengine bearing chamber environment. Due to the uncertainty surrounding bearing chamber turbulence modelling, the turbulence modelling approaches applicable to Taylor-Couette flows are also considered. Following the review of Taylor-Couette flows, an experimental and numerical review of bearing chambers is conducted. Experimental studies surrounding both the single-phase and two-phase environment are reviewed and a summary of the different bearing chamber flow regimes is presented. An analysis into the generation of a dispersed phase is carried out, characterising the difference in droplets, ligaments and sheets. Finally, the survey concludes with a review of bearing chamber modelling approaches. The development and application of specific models is discussed and their ability to be coupled with each other. As a result, the current state-of-the-art bearing chamber modelling approaches are evaluated and presented, namely: VOF-ETFM, VOF-DPM and ETFM-DPM.

2.1 Couette Flow

A Couette flow is the laminar flow of a viscous fluid developed in a parallel-plate flow, where one plate is fixed and the other moves with a constant velocity. The viscous drag force generated by the moving boundary causes fluid motion. The simplest case arises when the applied pressure gradient is zero resulting in a linear variation of the velocity between the two plates.

Couette flow can be adapted to the flow between concentric cylinders, as shown in Figure 2.1, in which the flow is driven by rotation of either or both of these cylinders. For Figure 2.1, with the case of infinitely long cylinders and inner cylinder rotation only, the Navier-Stokes equation in cylindrical coordinates can be simplified to find an exact solution:

$$\mathrm{u}_r = 0, \quad \mathrm{u}_\theta = Ar + \frac{B}{r}, \quad \mathrm{u}_z = 0, \quad \frac{\partial P}{\partial r} = \rho \frac{{\mathrm{u}_\theta}^2}{r} \tag{2.1}$$

Where u_r, u_θ and u_z are the radial, tangential and axial components of the velocity, P is the pressure and ρ is the fluid density. The constants *A* and *B* depend on η, the radius ratio between the inner and outer cylinder, r_i/r_o, and the rotational speed of the inner cylinder, Ω_i , where:

$$A = -\Omega_i \frac{\eta^2}{1-\eta^2}, \quad B = \Omega_i \frac{r_i^2}{1-\eta^2} \tag{2.2}$$

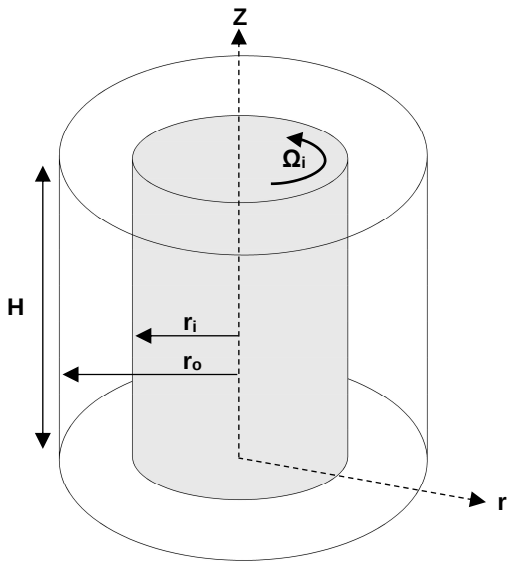


FIGURE 2.1: CYLINDRICAL COUETTE FLOW WITH ROTATING INNER CYLINDER

2.2 Taylor-Couette Flow

For the fluid flow between concentric rotating cylinders, Taylor [11] was the first to demonstrate that as the angular velocity of the inner cylinder increases, a critical condition is reached. The stable Couette flow undergoes a centrifugal-driven instability, causing the formation of counter rotating toroidal vortices, typically referred to as Taylor vortices, as shown in Figure 2.2. Further increases to the Reynolds number above the critical value causes the flow to become increasingly unsteady, displaying a sequence of time-dependent regimes, where the vortices undertake various shapes and transitions. Eventually, turbulence establishes.

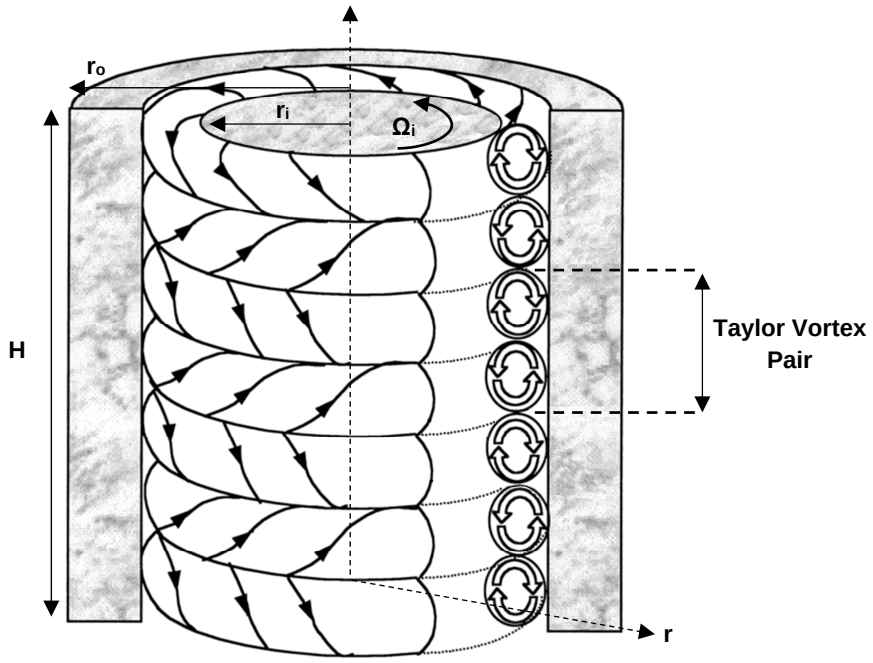


FIGURE 2.2: DIAGRAM OF TAYLOR-COUETTE FLOW, MODIFIED FROM [12]

For purely inner cylinder rotation, the Taylor-Couette system depends predominantly on three main parameters:

- Rotational Reynolds number $$Re = \frac{\Omega_i r_i (r_o - r_i)}{\nu} \quad (2.3)$$
- The device aspect ratio $$\Gamma = \frac{H}{2(r_o - r_i)} \quad (2.4)$$
- The radius ratio $$\eta = \frac{r_i}{r_o} \quad (2.5)$$

Where r_i and r_o are the inner and outer cylinder radii respectively and H is the axial extent of the chamber.

The rotational Reynolds number gives an expression for the ratio of inertial forces to viscous forces. As such the shaft speed, geometry and fluid properties are all significant parameters in defining Taylor-Couette flow. Similarly, we can define a rotational Taylor number. The Taylor number, derived directly from linear stability theory, can take various forms and the version used here is presented by Smith and Townsend [13].

$$Ta = \frac{2(1-\eta)}{1+\eta} Re^2 \tag{2.6}$$

As the rotational Reynolds number increases from zero onwards, the Taylor vortices are first observed to form at both ends of the cylinders. Increasing the angular velocity of the shaft causes additional vortices to form, spreading from the ends until reaching the critical condition for Taylor vortex flow (TVF), upon which laminar axisymmetric vortices fill the entire domain. This flow transition is defined to take place at a specific value of the Reynolds number, called the critical Reynolds number Re_c. Further increases to the Reynolds number above the critical value causes the flow to become increasingly turbulent. From the critical Reynolds number, a Reynolds number ratio, R, can be defined as $R = Re/Re_c$. Similarly, there is also an equivalent critical Taylor number, Ta_c, and as such, a resulting Taylor number ratio can be defined as $T = Ta/Ta_c$.

Taylor [11] showed theoretically, by using a linear instability analysis, that the laminar Couette flow becomes unstable leading to the formation of toroidal Taylor vortices. Taylor subsequently mapped out a series of experiments to provide detailed comparison and analysis for the conditions under which this stability boundary exists. Within this regime, Pai [14] conducted experiments using hot-wire anemometry in air between two co-axial cylinders, of which the inner cylinder rotated. Flow measurements of pressure and velocity distributions showed that ring shaped vortices persisted through the turbulent regime, for Reynolds numbers much larger than the critical value for instability. Pai was able to confirm the results of Taylor, concluding that the secondary motion is as a result of toroidal Taylor vortices. Pai demonstrated that only pairs of vortices can exist, and their size is dependent on the angular velocity of the inner cylinder; such that as the Reynolds number increases their size increases whilst the number of cells present decreases.

Roberts [15] presents calculations for the linear theory of instability for both axisymmetric and non-axisymmetric disturbances in Couette flow to describe the transition into TVF. Following the linear theory for the onset of Taylor vortices, at the critical Taylor number, there is also a corresponding non-dimensional critical axial wavenumber, a_c^+, of the toroidal vortices:

$$a_c^+ = \frac{2\pi}{\lambda^+} \tag{2.7}$$

Where λ^+ is the non-dimensional wavelength of a Taylor vortex pair, defined as the axial extent of a vortex pair, $2l$, divided by the annular gap width, $r_0 - r_i$. It is therefore possible to predict a theoretical number of vortex pairs, N_{TV}, present in a finite system using the following formula:

$$\lambda^+ = \frac{H}{N_{TV}(r_o - r_i)} \tag{2.8}$$

However, this formula does not take into account end effects and only provides an average value of the wavelength for the entire system.

It is also useful to propose a classification for Taylor-Couette flow based on the apparatus gap width, hence radius ratio η, whereby narrow gap cavities have $\eta > 0.67$ and wide gap cavities have $\eta < 0.67$.

2.2.1 Experimental Investigations

At very low Taylor number ratios, within the laminar TVF regime, Burkhalter and Koschmieder [16] investigated the wavelength of steady Taylor vortices, established through either a sudden start or a steady acceleration of the inner cylinder. For experiments using a steady acceleration of the inner cylinder, the wavelength of the Taylor cells remained fixed at that of the critical wavelength. However, for experiments carried out with rapid accelerations of the inner cylinder, regarded as a sudden start, Burkhalter and Koschmieder report that there was a wide variance in the final wavelengths. Within the work of Burkhalter and Koschmieder, a sudden start is achieved when the speed of the inner cylinder is accelerated from rest, to the desired angular velocity, in less than one second. Therefore, when considering an aeroengine under starting conditions, due to the relatively higher operating speeds, it is anticipated that a sudden start procedure analogous to that found within Taylor-Couette flows may be observed.

For purely inner cylinder rotation, the next instability to occur is when TVF transitions to wavy vortex flow (WVF). This flow has characteristic waves travelling in the azimuthal direction, superimposed on the Taylor cell structures. Coles [17] investigated experimentally the flow transition within the WVF regime. Over the speeds investigated, Coles observed many different states of both the Taylor cells and tangential waves which were not unique to the Reynolds number. As the speed of the system changes, theses states replace each other and undergo irreversible transitions; such that both the number of Taylor vortex pairs and tangential waves can either increase or decrease. This resulted in Coles mapping out more than 70 different transitions over the speed range investigated. As such, Coles demonstrated that the final state of the flow is

highly dependent on the initial conditions of the experiment, primarily the rate of acceleration of the inner cylinder.

Similar to Coles, Koschmieder [18] investigated the transition of laminar Taylor vortex flow through the WVF regime and into the turbulent Taylor vortex flow (TTVF) regime. For both a narrow and wide gap configuration, Koschmieder investigated conditions up to a maximum Taylor number of $40{,}000Ta_c$. As the Taylor number is increased, Koschmieder found that at $100Ta_c$ the transition to turbulence begins; at this Taylor number, the azimuthal waves eventually disappear until fully turbulent axisymmetric vortices forms around $700Ta_c$. Over the range of Taylor numbers investigated, Koschmieder compared the wavelength of turbulent Taylor vortices following either a slow acceleration or sudden start of the inner cylinder; confirming the observation of Coles, i.e. that the wavelength of vortices is strongly linked to both initial conditions and rotation rates. For steady acceleration procedures above $100Ta_c$, the axial wavelength remained constant and upon reaching this condition, the Taylor vortices become very stable to rapid changes in the angular velocity of the inner cylinder. Contrastingly, sudden starts above $100Ta_c$ showed a significant change in the behaviour of the flow and wavelengths produced were much shorter than that observed after a steady acceleration. The wavelengths obtained after sudden starts remained fixed regardless of subsequent changes to the Taylor number, hence rotational shaft speed.

Barcilon et al. [19] conducted experiments focused with very large Taylor numbers of up to $78{,}000Ta_c$. Their results found that two distinct length scales characterized the turbulent flow: that of the Taylor vortices, which takes the scale of the gap width, and a much smaller scale visible in the boundary layer due to ‘herring-bone’ like streaks found parallel to the walls. Hot-wire measurements showed that for their apparatus the WVF regime ends at $419Ta_c$, such that the azimuthal waves disappear giving way to fully turbulent Taylor vortex flow. Above this Taylor number, visualisation techniques showed a series of ‘herring-bone’ streaks superimposed onto the Taylor cells. Barcilon et al. suggest that this structure is evidence of Görtler vortices formed by the Taylor vortex circulation. Görtler vortices, located in the boundary layer, are the secondary flows as a result of centrifugal instabilities for high flow speeds over a concave surface. In Taylor vortex flow the mean velocity profile is redistributed near the concave walls, in which Görtler vortices form on a scale related to the boundary layer thickness, as a result of the centrifugal instabilities. Barcilon et al. report that even at the highest Taylor numbers investigated, the turbulent flow remains both steady and ordered, with motion coexisting on two different scales arising from Taylor and Görtler vortices.

Smith and Townsend [13] extended the range of Taylor numbers investigated into the region of 1×10^4 to 2.3×10^6 times the critical Taylor number, using hot-wire measurements in air. For

Taylor numbers less than $3 \times 10^5 Ta_c$ the results are in agreement of Barcilon et al. where the flow consists of uniformly spaced toroidal Taylor cells, superimposed with Görtler vortices throughout the boundary layer. Above this Taylor number, the Taylor vortices start to lose their structure as the flow becomes increasingly irregular, upon which the Taylor vortices cannot be distinguished past $5 \times 10^5 Ta_c$. This breakdown of the Taylor cells is attributed to the motion in the boundary layers changing from the characteristic Görtler vortices to more irregular motion, such as that found for plane walls. This results in the Taylor vortex cell structure breaking into varying length scales, with some scales as large as the cylinder gap width.

2.2.1.1 Velocity Distributions

Smith and Townsend [13] investigated the tangential velocity distribution across the gap, for a radius ratio of 0.667. It was reported that nearly all of the change in angular momentum occurs within the two boundary layers, each less than one-tenth the length of the gap width; subsequently as the shaft rotational speed increases their thickness decreases. Non-dimensional velocity distributions within the wall layers show that at the onset of turbulence, laminar boundary layers start to form at both the inner and outer cylinders following the Prandtl-Blasius theory; referred to as the classical regime of Taylor-Couette turbulence. As the Taylor number increases the boundary layers decrease in size and undergo a shear instability to become turbulent once sheared strongly enough. Smith and Townsend report that the turbulent boundary layer is unaffected by the flow curvature and is characterized by a logarithmic velocity profile following the Prandtl-von Kármán law of the wall.

$$u^+ = \frac{1}{\kappa} \ln y^+ + A \tag{2.9}$$

Where $u^+$is the dimensionless velocity, y^+ is the wall coordinate, κ is the von Kármán constant and A is a constant.

$$y^+ = \frac{y\, u_\tau}{\nu}, \quad u^+ = \frac{u}{u_\tau}, \quad u_\tau = \sqrt{\frac{\tau_w}{\rho}} \tag{2.10}$$

Here, u_τ is the friction velocity and τ_w is the wall shear stress.

Smith and Townsend [13] determined that the von Kármán constant, κ, is found to exhibit a dependence on the Taylor number and for large Taylor numbers, κ approaches 0.41 consistent with the universal value of 0.40. However, they report a reduced additive constant, A, of about

4.4 compared to the typical value of 5.0. Grossman et al. [20] suggest that for the log-law region the use of the angular velocity is more appropriate than the azimuthal velocity, such that:

$$\Omega^+ = \frac{1}{\kappa}(\ln y^+ + A) \tag{2.11}$$

The curvature of the apparatus results in a difference between azimuthal velocity and angular velocity profiles. For larger radius ratios the difference between the dimensionless azimuthal and angular velocity is only noticeable over large wall distances. However, for much smaller radius ratios, the smaller radius of the inner cylinder leads to a much larger difference between the velocity profiles.

The distribution of angular velocity is also highly dependent on the radius ratio η, as demonstrated in the numerical study by Ostilla-Mónico et al. [21] who looked at different ratios between 0.5 and 0.9. As the radius ratio increases, such that the gap width becomes smaller, the gradient of the angular velocity in the core of the flow decreases up to $\eta = 0.9$, where the profile is almost flat for the core flow. Contrastingly, for a large gap width, $\eta = 0.5$, the core of the flow differs from the flat profile previously observed, such that there is a considerable angular velocity gradient and velocities are on averaged reduced.

Measurements of both the axial and radial velocity profiles are also of significance in Taylor-Couette flow. Due to end effects there will be an observed variation in the axial velocity profile even if there is no imposed axial flow. Additionally, velocity vector plots in the axial and radial direction enable visualisation of the secondary flow present. Wang [22] provides Particle Image Velocimetry (PIV) measurements for the laminar TVF and WVF regimes through to the TTVF regime, comparing CFD data with experimental velocity vector fields, as well as axial and radial velocity profiles along an axial line through the domain. Wang concluded that their steady state CFD simulations were able to provide excellent predictions for both the time-independent laminar TVF and the time-dependent laminar WVF.

Similarly Wereley and Lueptow [23] used PIV in a meridional plane to measure axial and radial velocities for both wavy and turbulent Taylor-Couette flows. Within the WVF flow regime, Wereley and Lueptow investigate the time progression of the velocity vector fields through one complete azimuthal wave cycle over a range of Taylor numbers. Through tracking the vortex centres, it became clear that axial motion of the vortices exists with significant fluid transfer between adjoining vortices, suggesting that the Taylor vortex pairs are not independent of each other. There exists a cyclic transfer of fluid between Taylor cells in which a particular vortex will grow in size as a result of gaining fluid from the shrinking neighbouring vortices, after which the cycle will complete as the vortex loses fluid to the neighbouring vortices. As the Taylor number

is increased, the vortices become stronger, however with increasing the Taylor number, both the axial motion and the fluid transfer between vortices begins to diminish as the WVF regime begins to transition into the TTVF regime.

2.2.2 Numerical Investigations

To date, there are very few combined CFD and experimental studies of rotating Taylor-Couette flow. In particular, investigations into the effect of the turbulence closure model selection on the predictions of Taylor-Couette turbulence systems are scarce. In recent years, the application of direct numerical simulation (DNS) to rotating Taylor-Couette flow has been the focus of many numerical studies for Reynolds numbers as high as 300,000 [24]. DNS aims to solve the Navier-Stokes equations numerically without any turbulence model, such that the whole range of turbulence scales must be resolved. As a result, DNS is very computationally expensive and therefore is not currently viable for industrially relevant geometries, highlighting the need for a modelling approach that is industrially applicable to rotating Taylor-Couette flows. It is also important to recognise that across different CFD solvers, as well as their respective versions, the implementation of turbulence modelling approaches may vary, resulting in a wide range of solutions; demonstrating the further requirement for an up to date review of Taylor-Couette URANS turbulence modelling.

Early numerical simulations concentrated on low Taylor numbers for the laminar Taylor vortex flow (TVF) regime. However, for the turbulent Taylor vortex flow (TTVF) regime steady state RANS simulations were performed, employing a range of different turbulence models. Wild et al. [25] performed axisymmetric CFD simulations on narrow gap geometries, η = 0.941 and 0.974, using both the Reynolds Stress Model (RSM) and the k-ε turbulence model with a comparison to experimental data in the range of $1.5 \times 10^4 < Re < 4 \times 10^4$. Comparison with experimental measurements showed that the standard k-ε model over-predicted results by at least 10%; while comparison of the standard k-ε model with the re-normalisation group (RNG) k-ε model showed similar results with only a 2% difference; however, without a wall function approach the predicted torque was 40% above the measured value. The RSM with wall functions was also chosen for comparison, although was found to perform poorly, again over-predicting results by as much as 40% more than the standard k-ε model.

Batten et al. [26] extended the work of Wild et al. [25] with the use of the low Reynolds number k-ω turbulence model over the range of, $5 \times 10^3 < Re < 5 \times 10^4$, for the axisymmetric geometries, η = 0.734, 0.941 and 0.985. For the narrow gap cases η = 0.941 and 0.985, comparison to experimental measurements showed that the numerical simulations over-predicted velocities

by approximately 20%; for the wide gap case, results were unreliable due to numerical problems resulting in differences of up to 40%. In addition for the wide gap case, η = 0.734, the transition to turbulence was determined to take place at a Taylor number, $8900\,Ta_c$ which is significantly larger than that predicted experimentally by Koschmieder [18] for the case of η = 0.727 where transition takes place over, $100\,Ta_c < Ta < 700\,Ta_c$. Overall, Batten et al. [26] concluded that the k-ω turbulence model is applicable to the axisymmetric simulation of turbulent Taylor vortices associated within narrow gap geometries.

More recently Adebayo and Rona [27, 28], investigated the 3D velocity and pressure distributions for two wide gap geometries, η = 0.44 and 0.53 over the Taylor number range $600\,Ta_c < Ta < 1700\,Ta_c$. Within this weakly turbulent Taylor vortex flow regime, comparison of axial and radial velocity profiles against PIV data showed good agreement for the realizable k-ε turbulence model, with results inside the uncertainty band. Analysis of vortex wavelengths were within 5% of the wavelength for ideal coaxial cylinders determined by the analysis of Roberts [15].

Wang [22] compared CFD data obtained from axisymmetric steady state simulations with PIV experimental data over the Taylor number range, $16\,Ta_c < Ta < 48400\,Ta_c$ (TVF to TTVF). Due to the strong dependence of the Taylor cells on start-up conditions, as demonstrated by both Coles [17] and Koschmieder [18], Wang defined a start-up protocol for their geometry, η = 0.733, to ensure that a constant number of 14 Taylor vortex pairs formed over all of the rotation rates studied. Wang investigated the combination of various turbulence models with different wall functions approaches. The RSM gave the best results over the wide range of Taylor numbers investigated. Comparison of axial and radial velocity profiles showed that the RSM correctly captured the experimental trend of an axially varying radial velocity, due to the Taylor vortices, but over predicted the maximum radial velocities by as much as 40% at $R = 220$. Comparison of Reynolds stress contours also showed poor agreement.

The results of Wang are consistent with the numerical study performed by Poncet et al. [29], who considered turbulent Taylor-Couette flow for a wide gap geometry, η = 0.5. The authors investigated a range of modelling techniques, as demonstrated in Figure 2.3; such as the RSM URANS model, Large Eddy Simulation (LES) techniques, including an SST k-ω scale-adaptive simulation (SAS) approach, and DNS. Out of the models investigated, the SST k-ω SAS model performed the worst, failing to predict the mean tangential velocity with a large overestimation compared to the experimental data. The poor agreement is attributed to the Taylor vortex pair being represented by a set of four rotating structures seen in Figure 2.3 c), unlike the two counter rotating vortices typically found; the same structure is also observed for the OpenFOAM LES simulations. Surprisingly, all of the numerical approaches undertaken failed to reproduce the experimental mean tangential velocity and angular momentum profiles; both the RSM and DNS

provided the closest agreement to the experimental data, although still failed to predict the shear stress components. Since DNS remains the most computationally expensive approach, Poncet et al. recommend that for application to industrial flows, either LES or the RSM will provide adequate results. However, Poncet et al. recommended further investigation into turbulence modelling for Taylor-Couette flow, especially at even higher Reynolds numbers.

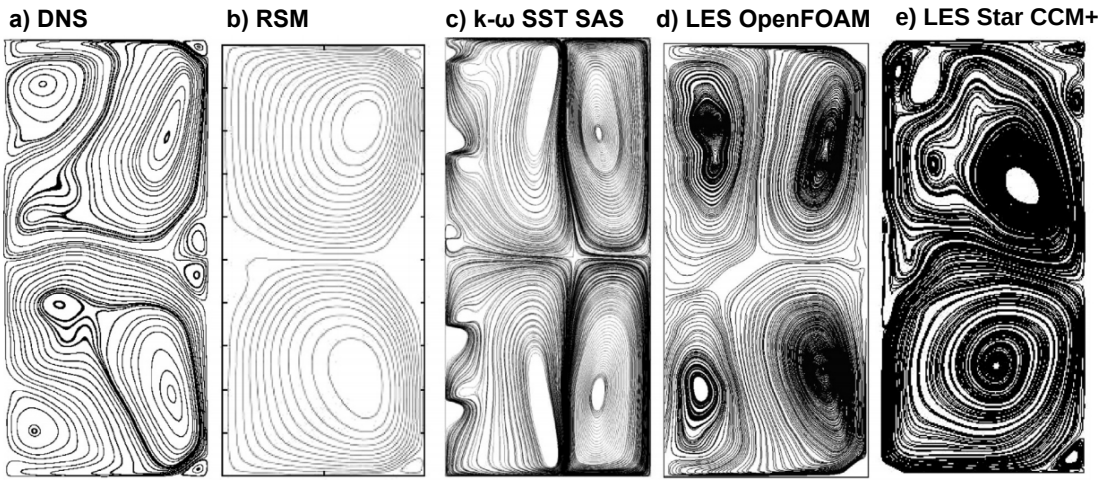


FIGURE 2.3: MEAN TAYLOR VORTEX STREAMLINES FOR EACH TURBULENCE MODEL [29]

Due to the costly memory and speed requirements of DNS, investigations had only previously considered moderate Reynolds numbers. With developments of supercomputers and parallelisation techniques for DNS, high Reynolds number simulations are now possible. Bilson and Bremhorst [30] performed one of the first DNS studies of Taylor-Couette flow at a Reynolds number of 3200, for a geometry of $\eta = 0.617$. To reduce the computational expense, the axial domain length was limited using axial periodicity. After determining the optimal aspect ratio, Bilson and Bremhorst investigated the inner cylinder start-up procedures; for shorter periodic lengths, there was no dependence on start-up conditions. Although at larger domain lengths, the sudden starts resulted in smaller vortex wavelengths, in line with the experimental results of Koschmieder [18]. Comparison of results with experimental data showed a good agreement of trends. Bilson and Bremhorst report a secondary vortex motion superimposed on the Taylor vortex pairs, characteristic of the Görtler vortices observed by Barcilon et al. [19].

Through DNS investigations into the mean velocity field, Dong [31] showed that the turbulent Taylor-Couette flow contained ordered Taylor vortex pairs superimposed with instantaneous turbulent fluctuations. In line with Bilson and Bremhorst [30], Dong reports near wall herring-bone like streaks that first form at the cylinder wall which then transition into Görtler vortices. These Görtler vortices subsequently start to transition into the characteristic structures observed for plane turbulent boundary layers, as found experimentally by Smith and Townsend [13].

Using DNS, Pirrò and Quadrio [32] performed an analysis of the wall boundary layers revealing that over both walls, a viscous sublayer forms for $y^+ \leq 5$, following the linear law $u^+ = y^+$. Above this, a limited logarithmic region is observed for $20 \leq y^+ \leq 40$ following the Prandtl-von Kármán law of the wall, with constants $\kappa = 0.39$ and $A = 4.6$, similar to that found by Smith and Townsend [13].

2.2.3 Small Aspect Ratio Chambers

Many experimental and numerical studies of Taylor-Couette flow consider very large aspect ratio devices, in order to investigate the classical Taylor-Couette system. Experimentally, aspect ratios are typically much larger than $\Gamma = 10$, with many experiments having aspect ratios of $\Gamma > 100$, such that when measurements are taken at the cylinder mid-gap, end effects become negligible and can be neglected. In theoretical studies, the assumption is made that cylinders are infinitely long and in numerical studies periodic boundary conditions are used to both simplify the domain and avoid end effects. However, very few studies have explored small aspect ratios chambers of $\Gamma < 10$, for such devices the end walls influence the secondary flow developed and therefore need to be treated carefully. The application of small aspect ratio devices is of significant importance for aeroengine bearing chamber applications, since these can be reduced to a Taylor-Couette system when simplified to just a rotating inner shaft and a stationary outer cylinder. This becomes apparent from the single-phase experimental bearing chamber investigations of Gorse et al. [33], which considered a very small device aspect ratio of $\Gamma = 0.47$. In the presence of a low sealing airflow rate and a shaft speed of 9,700 rpm, a single pair of counter rotating Taylor vortices are observed; suggesting that within the TTVF regime, end effects may become negligible. As such a review into small aspect ratio devices within the Taylor-Couette system is conducted.

In cylindrical Couette flow, far from the walls, the pressure gradient balances the centrifugal force. As such, before the critical condition for the onset of Taylor vortices there is no radial flow. However, near the end-walls, the no-slip condition disrupts the force balance resulting in a radial flow. This boundary driven flow at the end-walls is referred to as an Ekman flow, which results in the formation of a vortex, known as an Ekman vortex [34]. These end-wall effects can penetrate through the flow domain, hence the Ekman vortex can in turn drive additional vortices. For Taylor-Couette flow, past the critical Reynolds number, Taylor vortices fill the domain, however the rotation initiated by the Ekman vortices persists and the radial flow at the end-wall boundary layer drives the rotation of end-wall vortices. As such, it becomes clear that the structure of the Taylor vortex flow is influenced significantly by the end wall boundary conditions and for short aspect ratio devices this effect will by amplified. Cole [35] demonstrated that the transition from

the TVF regime to the WVF regime occurs at a much higher angular velocity for short cylinders compared to infinitely long cylinders, arising from the Ekman boundary layer flow.

Czarny et al. [34] investigated four different end-wall boundary conditions to determine the end-wall effects on Taylor vortices through the use of DNS, including: fixed end-walls, end-walls rotating with either the inner or outer cylinder and finally, end-walls without a no-slip condition. The results of Czarny et al. suggest that the influence of end-wall conditions on Taylor vortices are dependent on the Reynolds number. Once the flow reaches the WVF regime, the end-wall effects do not strongly affect the waviness of the vortices and the waviness is only suppressed very close to the end-walls. Czarny et al. show that for fixed end-walls, the DNS results show a thicker Ekman layer than theoretically predicted. The results from Czarny et al. suggest that as the Reynolds number is increased into the WVF regime, the influence from end effects as a result of the Ekman boundary layer flow, do not have a significant result on the overall Taylor vortex structure.

Whilst the study on short aspect ratio devices is limited, the application within the turbulent Taylor vortex regime is even more limited. Burin et al. [36] experimentally investigated a short aspect ratio device, $\Gamma \sim 2$, with a high wall curvature, $\eta = 0.35$, over the Reynolds number range $5 \times 10^4 < Re < 4 \times 10^5$. Burin et al. implemented two independently rotating end-rings, allowing for a significant reduction in Ekman circulation. For the range of Reynolds numbers investigated, the flow is highly turbulent, and visualisation shows a clear lack of vortex structure. Burin et al. report that due to the strongly unstable nature of the flow, the Ekman pumping has little effect on the fluid interior and therefore little influence on both the torque and velocity data.

2.3 Bearing Chamber Experimental Studies

2.3.1 Early Experimental Investigations

Wittig et al. [10] performed one of the first aeroengine bearing chamber experimental investigations, providing oil film thicknesses using an ultrasonic measurement technique. In addition, Wittig et al. performed an analysis on heat transfer coefficients, determined using a temperature gradient method. The film which develops on the chamber walls, was found to be strongly influenced by the shaft rotational speed. Wittig et al. demonstrated that, with an increase in shaft speed, the increased circumferential velocity caused a uniform distribution of the film on the chamber walls. Furthermore, the effect of the shaft rotational speed was found to strongly influence the heat transfer characteristics, as well as the oil mass flow rate entering the chamber.

Glahn and Wittig [37] extended the experimental investigations of Wittig et al. [10], using a Laser Doppler Anemometry (LDA) technique to characterise the oil film velocity profile on the bearing chamber walls. The operating conditions investigated by Glahn and Wittig, considered an oil lubrication flow rate of 2.5 l/min and a sealing airflow rate of 10 g/s over the rotational shaft speeds ranging from 3,000 rpm to 12,000 rpm. Through the experimental film velocity measurements, Glahn and Wittig were able to successfully characterise the turbulent nature of the oil film on the stationary outer walls. It was discovered, that as the rotational shaft speed increased, the film velocity also increased proportionally. Additionally, at the gas-liquid interface, the shear stress was also found to be a function of the core air velocity. As such, the authors concluded that accurate predictions and experimental validation of the air-oil interface was necessary for any future two-phase numerical modelling of bearing chamber flows.

2.3.2 Airflow Measurements

Within a bearing chamber, the capability to accurately capture and identify the key flow physics of the single-phase airflow field is essential for developing the understanding of the oil film. Early experimental investigations have shown how the oil film is driven by both the high shearing gas forces and the presence of gravity. As such, Gorse et al. [33] used 3D LDA to investigate the bearing chamber single-phase airflow over a combination of shaft speeds and sealing airflow rates. Within the experimental test rig, a bearing simulator was used to suppress the oil flow entirely, avoiding the two-phase dispersed flow typically found in bearing chambers resulting from the airflow interactions with droplets generated from the bearing. The experimental results of Gorse et al. characterised two different airflow regimes, the state of which depends on both the sealing airflow rate and the rotational shaft speed. Based on these parameters, the secondary airflow vortices can be significantly influenced. Under low sealing airflow rates, a rotational

speed driven mode (RSDM) arises, forming a pair of counter rotating Taylor vortices in the axial-radial plane, due to the strong influence of the rotational shaft speed. As the sealing airflow rate is increased, this transitions into the sealing air driven mode (SADM), where the Taylor vortex pair shifts to one large vortex with a smaller counter rotating vortex forced into the upper corner. The ratio between the speed of the shaft and sealing airflow can be used to define the transition:

$$R_u = \frac{u_{sh}}{u_{air}} \tag{2.12}$$

Gorse et al. report that when the velocity ratio drops below 4.2, the SADM is present, whereas above which, the RSDM dominates.

Using PIV, Lee et al. [38] also performed an investigation of the single-phase airflow. Within the bearing chamber, Lee at al. measured tangential velocities to a high degree of spatial resolution and accuracy, reporting an uncertainty of less than 2%. Overall, the velocity profiles and flow features were well captured, providing successful validation data for subsequent computational modelling of the geometry under investigation.

Similar to Lee et al. [38], Aidarinis et al. [39] investigated the airflow field within an aeroengine front bearing chamber using a 2D LDA system. Three different shaft speeds were investigated over the range of 4,000 rpm to 7,000 rpm, under two sealing airflow rates of 23 g/s and 33 g/s, for a fixed oil flow rate of 2.5 l/min. The main aim of the experimental investigations was to provide accurate validation data for CFD simulations in an effort to better understand the single-phase airflow field. The results of the combined experimental and CFD investigation led to the development of a pressure drop model, in order to computationally account for the effect of the bearing on the airflow through the chamber.

2.3.3 Film Thickness Measurements

In order to evaluate both heat transfer and scavenge efficiency within a bearing chamber, it is first essential to have a clear understanding of the oil film behaviour and the relevant film quantities. Gorse et al. [40] performed an investigation into the influence of operating conditions and the chamber geometrical configuration on the film thickness. Capacitive probes and an LDA technique were used to perform film thickness and velocity measurements over a range of rotational shaft speeds from 4,000 rpm to 16,000 rpm. Over these speeds investigated, Gorse et al. recorded film thickness measurements ranged between 0.5mm and 1.5mm. At low rotational shaft speeds, the interfacial shear stress was insufficient to overcome the strong influence of gravity, causing the oil to accumulate in the sump at the bottom of the chamber. As the shaft speed is increased and the effects of gravity are overcome, the oil film subsequently becomes driven by

the shaft, resulting in a uniform distribution around the chamber annulus. The results of Gorse et al. revealed how the operating conditions within the chamber strongly influenced the complex film flow, namely: the film thickness decreases as a function of increasing shaft speed. Additionally, a study on geometrical features, showed that the vent and scavenge port design heavily affected the discharge characteristics.

Using the same test rig, Kurz et al. [9] extended upon the work of Gorse et al. [40], establishing a method to predict the two-phase flow regime found within aeroengine bearing chambers. Building on the previous observations of Gorse et al., Kurz established that there are typically two distinct flow regimes that occur. For the bearing chamber geometry under investigation, the results of Kurz et al. demonstrated that the change in regime also occurred as a function of the chamber outer diameter and the flow rate of oil. The first regime, identified at lower shaft speeds, is a gravity driven oil flow, resulting in pooling of the oil and therefore a very thin oil film on the remainder of the stationary wall; within this regime the oil only exhibits minor interactions with the airflow. Furthermore, capacitive sensors also indicated possible dry-out regions within the upper section of the bearing chamber. At higher shaft speeds, the second regime occurs, in which the shearing airflow dominates, subsequently forcing the oil film on the chamber walls to rotate. These regimes relate to two very different flow states within the bearing chamber, and as such will have different consequences on the effects of heat transfer within the chamber walls. Understanding these differences becomes even more important, considering that dry-out regions can also occur within the wake of geometric features, as previously demonstrated by Eastwick et al. [41] within the shearing flow regime.

Kurz et al. [42] also investigated the influence of different offtake designs on the film thickness, using the same experimental test rig. Experimentally, Kurz et al. compared three different scavenge designs, a baseline geometry, a shallow ramp and a covered deep ramp. It was concluded that the covered ramp improved the scavenge efficiency the greatest; at 15,000 rpm the minimum scavenge efficiency recorded was 77%, compared to that of the baseline configuration achieving a scavenge efficiency of only 21%. As the scavenge efficiency is increased, the amount of oil present in the bearing chamber reduces and as a result, a relatively thinner and more uniform film develops; in contrast a poor scavenge efficiency causes a build-up of film. Similarly, Chandra et al. [43, 44] performed experimental investigations into the sump regions of a bearing chamber. Chandra et al. were one of the first to highlight the importance of a sump geometry on the oil residence volume, identifying key features that affect the efficiency of oil removal from the system.

2.3.4 Droplet Characteristics

Glahn et al. [45] were the first to present experimental data for droplet diameters and velocities shed from a roller bearing. The investigation utilised a Phase Doppler Particle Analyser (PDPA), providing novel measurements inside a bearing chamber under real engine conditions and atmospheres, for shaft speeds up to 16,000 rpm. The observations of Glahn et al., demonstrated that the cylindrical roller bearing elements generate droplets which are subsequently shed into the bearing chamber. An assessment of the rotational shaft speed on both the droplet diameters and velocity is presented, as shown in Figures 2.4 a) and b) for the particle radial and tangential velocities respectively. Across all the particle diameters observed, it was discovered that as the rotational shaft speed increases, the tangential velocity component increases rapidly, Figure 2.4 b); conversely, the radial component is seen to decrease, Figure 2.4 a). Therefore, as the shaft speed increases, the exit trajectory of the particles changes from that of a radial to a tangential direction. This effect is most notable for the smaller droplet diameters, whereas the inertia of the larger diameter particles causes them to maintain a relatively higher radial velocity component.

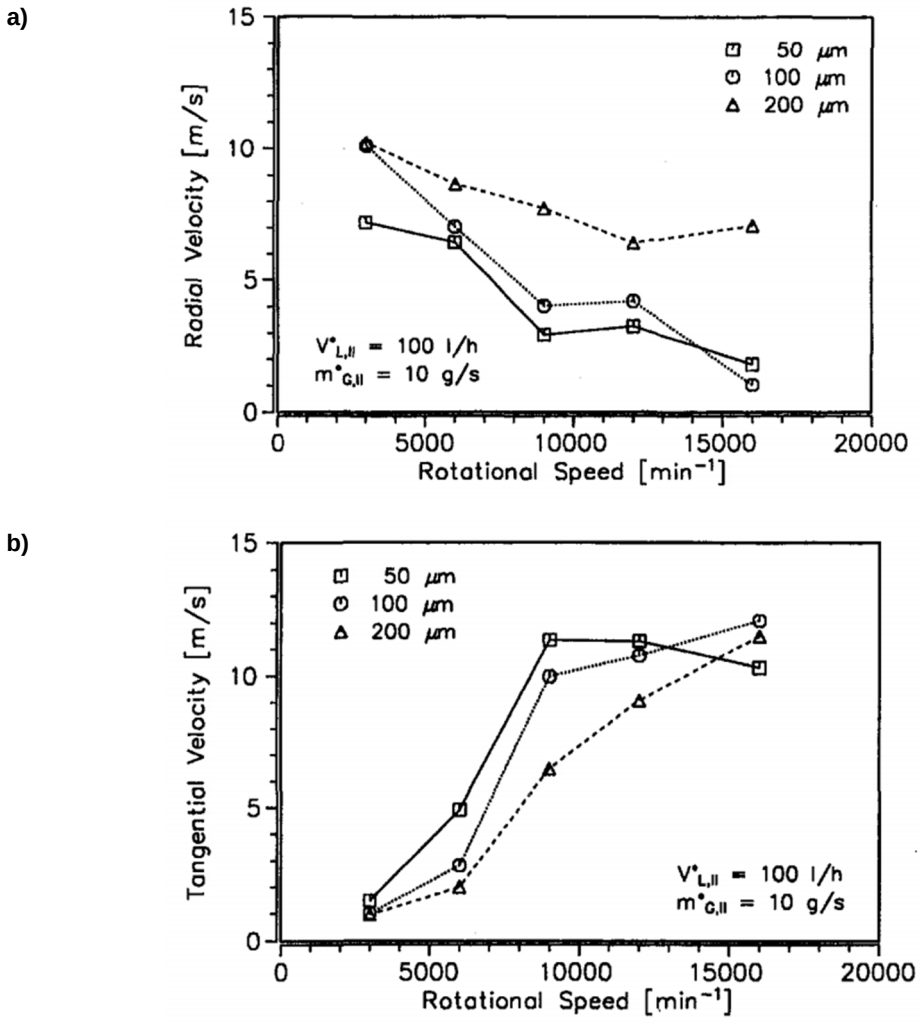


FIGURE 2.4: MEAN a) RADIAL AND b) TANGENTIAL PARTICLE VELOCITIES VERSUS ROTATIONAL SPEED [45]

Figure 2.5 highlights the droplet diameter histogram for the shaft speed of 12,000 rpm presented by Glahn et al. [45]. Here, droplets range in diameters from as small as 14μm up to a maximum of 500μm; the diameter distribution is positively skewed resulting in a mode in the range of 70μm to 80μm. Overall, the results of Glahn et al. were successful in providing a valuable first insight into droplet flows within bearing chambers.

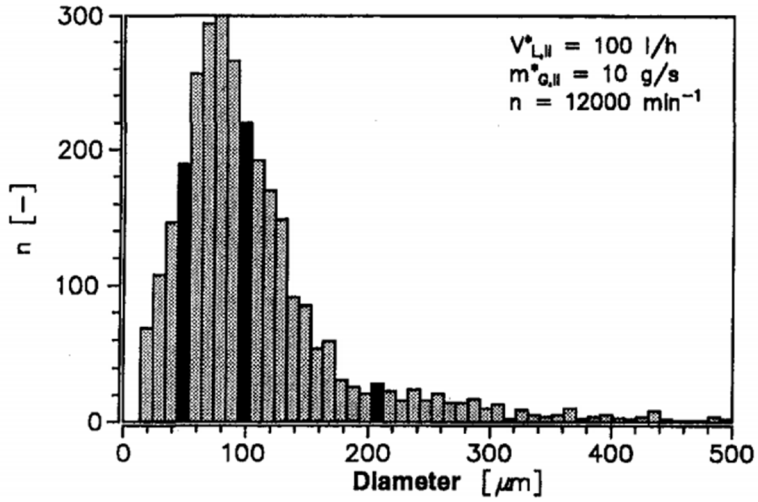


FIGURE 2.5: DROPLET DIAMETER HISTOGRAM AT 12,000 RPM [45]

Glahn et al. [46–48] extended upon their original investigation, forming a series of fundamental investigations into the atomisation process of oil systems. With respect to aeroengine bearing chamber operating conditions, the research targeted three main objectives: firstly, the identification of droplet disintegration characteristics; secondly, categorisation of droplet diameters; and finally, relevant statistics surrounding droplet velocities. These investigations demonstrated that the behaviour of oil shed from rotating elements within the bearing chamber, such as by both ball and roller bearings, could be understood from more fundamental studies of oil disintegration methods. Such methods included: oil breakup at the edge of a rotating disk; and oil jets exiting from either axial or radial holes located in a rotating cylinder. The observations concluded that three different regimes of oil disintegration exist, oil was either shed as droplets, ligaments or sheets. Glahn et al. demonstrated that these observations are dependent on both the oil flow rate and the rotational speed. For example, at the edge of a rotating disk, when both parameters are relatively low, uniform, discrete droplets are shed from the edge. With an increase to either the rotational disk speed or the oil flow rate, ligaments start to form which consequently breakup into a series of small droplets. The ligaments form intermittently around the periphery of the disk, these subsequently increase in number and size with the oil flow rate. Further increases to either the rotational disk speed or the oil flow rate causes the disintegration method to transition into a thin continuous sheet. The sheet extends radially past the rim of the disk, until it can no

longer be supported, leading to an irregular array of ligaments which ultimately breakup into a varying range of droplet diameters.

Gorse et al. [49] performed a comprehensive study on the droplet generation from a cylindrical roller bearing for a series of relevant engine operating conditions. Close to the roller bearing, flow visualisation of the oil showed the strong influence of both a pressure differential across the bearing and the impact of support structure design on the droplet generation. The change in pressure difference between each chamber resulted in an airflow across the bearing ranging from -0.5 g/s to 8.0 g/s. To assess the impact of the bearing support structure on the film instability, two configurations were investigated, namely a 90° edge versus a curved edge. Focusing at a shaft speed of 4,000 rpm, Gorse et al. noted that independent of the air crossflow, the oil successfully exited between the cage and outer-race, implying that sufficient contact for both lubrication and cooling occurred.

For the case involving the 90° edge, without a crossflow, Gorse et al. found a smooth uniform film exits the bearing which transitions to continuous wavy film upon reaching the support structure. As the crossflow was increased up to 3 g/s, the oil film became substantially more unstable and wavier. Upon reaching a crossflow of 6 g/s, the onset of droplet generation occurs, and small amounts of droplets are observed. At the maximum crossflow, the number of droplets generated increased significantly and a continuous film was still present over the bearing support. The droplet generation led to a noticeable change in the secondary flow field vortices, as previously investigated by Gorse et al. [33]. Here, due to the high amounts of droplet generation, the SADM vortical structure is no longer visible; since the axial momentum of the droplets causes a change in the secondary flow field, resulting in droplets being propelled to the front-face of the bearing chamber.

Investigations into the curved bearing support structure, revealed that the droplet generation was significantly dampened, with only a smaller number of droplets observed at the highest crossflow. Overall, the initial assessment of Gorse et al. identified that the pressure differential across the roller bearing was required for droplet generation. Furthermore, these droplets do not form within the bearing itself, instead an oil film exits the bearing which disintegrates due to the shape of the support edge and a high air crossflow rate. To develop a more complete understanding of the mechanisms behind the roller bearing droplet generation, Gorse et al. extended the experimental investigation to determine the influences of both the rotational shaft speed and oil flow rate. Somewhat contradictorily, the results of Gorse et al. suggest that through increasing either the rotational shaft speed or the oil flow rate, the number of droplets generated decreases. As either of these parameters are increased, a thicker oil film forms, which subsequently requires a higher-pressure differential across the roller bearing and therefore delays the onset of droplet generation.

Using an aeroengine ball bearing, Flouros [50, 51] performed a comprehensive experimental investigation in an effort to reduce the power losses in a bearing chamber. In the first part of his investigation, Flouros determined the influence of several operating parameters on the power consumption, namely the: oil flow rate, sealing airflow rate, oil temperature, rotational shaft speed and chamber pressure.

For the second part of his study, Flouros analysed the power losses associated with droplets generated from the ball bearing inside the bearing chamber. An investigation into reducing the power consumption was conducted by shrouding the ball bearing with porous screens which were attached to the outer ring at an axial distance of 10mm from the cage. A significant number of droplets were impeded by the porous screen. Upon impingement, this oil forms a liquid on the screen and subsequently becomes gravity scavenged. The greatest power reduction was observed for a screen with porous holes of 3mm, leading to a reduced power consumption of 11% at the highest shaft speed. In general, as the rotational shaft speed increased, the power consumption rapidly decreased. A study into moving the screen closer to the ball bearing, at a distance of 3mm away from the cage, showed no significant change in the bearing power consumption.

To determine if the use of screens promoted an overall more efficient scavenging process, the oil flow rate through the vent pipe was monitored. Across all of the cases investigated by Flouros, a much lower quantity of oil was observed within the vent pipes when the porous screens were implemented. This is of particular significance, since Willenborg et al. [52] previously demonstrated that beyond a critical limit, small droplets entrained within the vent pipes can cause an oil fire due to the very hot engine components. Overall, Flouros demonstrated that the reduction in power consumption was associated with a reduced oil residence time within the bearing chamber. The use of porous screens promotes a more efficient scavenging system, which ultimately reduces the residence time of the oil and air mixture and therefore improves the power consumption.

2.3.4.1 G2TRC Bearing Oil Shedding Rig

More recently, at the Gas Turbine and Transmissions Research Centre (G2TRC), both Santhosh et al. [53] and Hee et al. [54] used high-speed visualisation techniques to perform studies into oil shedding from an aeroengine ball bearing up to shaft speeds of 7,000 rpm. Santhosh et al. focused primarily on the oil shedding from the bearing cage, highlighting many similarities to that of rotating cups and disks. Whereas, Hee et al. characterised the subsequent film development within the slot immediately after the ball bearing. Figure 2.6 shows a cross-section of the ball bearing

investigated by both Santhosh et al. and Hee et al., highlighting the measurement planes used for image acquisition within the slot.

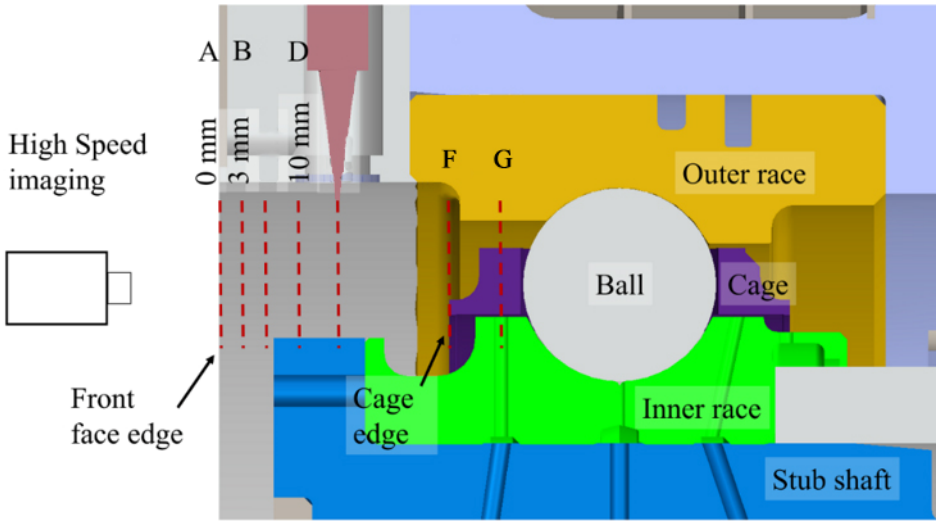


FIGURE 2.6: CROSS-SECTIONAL VIEW OF THE BALL BEARING SHOWING AXIAL MEASUREMENT PLANES, MODIFIED FROM [55]

Figures 2.7 a) to d) show the high-speed visualisation images recorded by Santhosh et al., demonstrating the droplet generation process observed at the bearing cage. These images are recorded at the cage-edge which corresponds to the measurement plane F, as shown in Figure 2.6. At the low rotational shaft speed of 1,000 rpm, Figure 2.7 a), a direct-droplet formation is seen similar to that observed for a rotating cup. With a slight increase in the rotational shaft speed to 1,700 rpm, the centrifugal forces begin to dominate. Here, two different intermittent mechanisms of shedding are observed, specifically primary ligaments and laminar sheets as demonstrated in Figure 2.7 b) and c). Both of these shedding regimes are comparable to that observed for rotating cups at relatively high rotational shaft speeds or liquid flow rates. Further increases to the rotational shaft speed increases the amount of laminar sheet formation. However, upon reaching a rotational shaft speed of 4,500 rpm, a second type of sheet breakup is observed, called ruffled sheet breakup, Figure 2.7 e). The oil sheet has a ruffled surface by nature and subsequently there are secondary ligaments that break off. These are substantially different to the primary ligaments, which are very smooth and stable, having a predictable secondary droplet distribution. Whereas, the secondary ligaments produce a more random and varied secondary droplet distribution. Finally, as the rotational shaft speed is increased to 7,000 rpm, whilst the secondary ligaments are still present, as shown in Figure 2.7 f), the radial extent of the sheet starts to diminish. Whilst the modes of droplet disintegration are similar to the classical experimental studies of rotating disks and cups, Santhosh et al. concluded that these empirical expressions were not applicable to the bearing chamber observations.

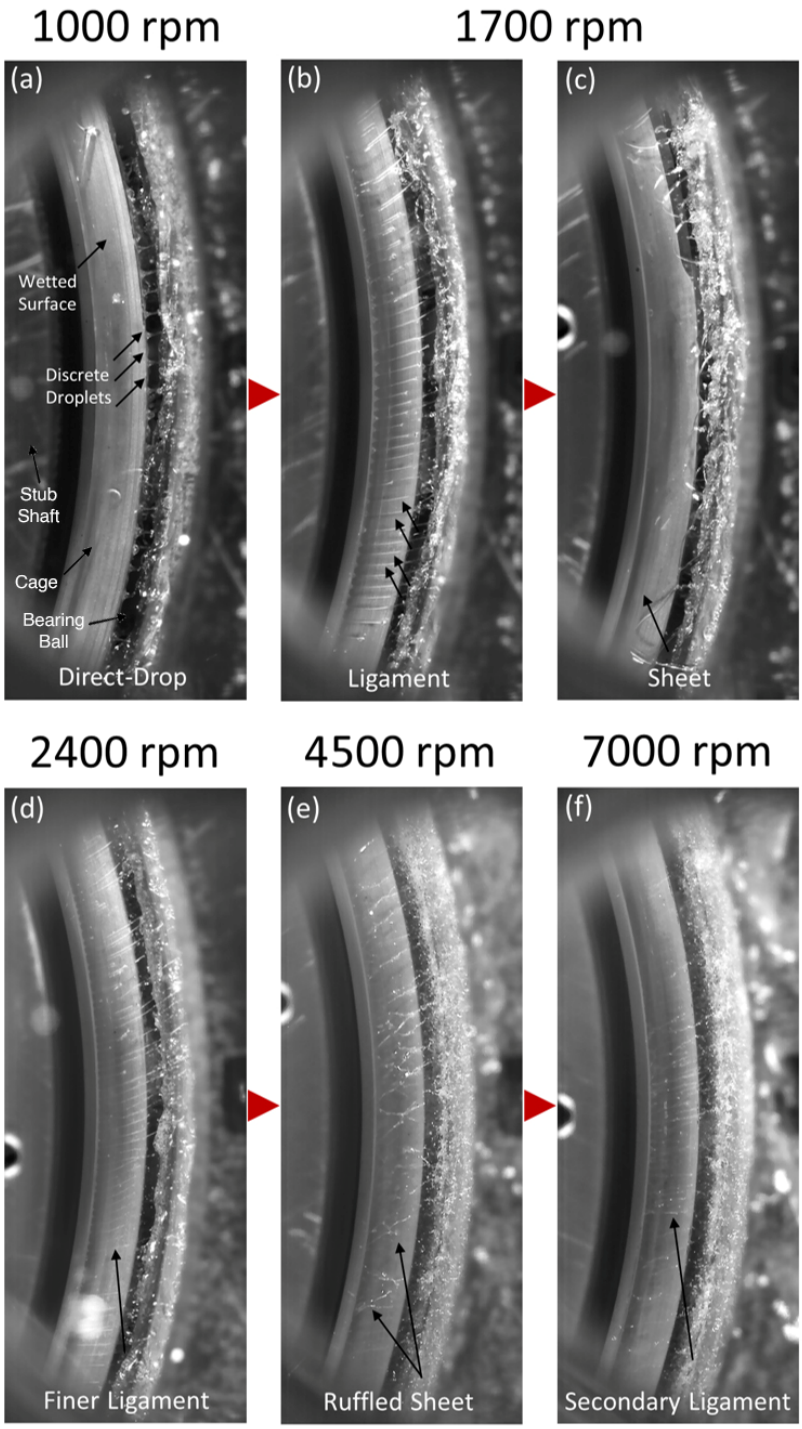


FIGURE 2.7: HIGH SPEED VISUALISATION OF DROPLET GENERATION PROCESS [55]

Beyond the bearing, Hee et al. [54] investigated the thin film formation on the static outer casing surfaces within the slot before the bearing chamber expansion. Using the same high-speed imaging technique, Hee et al. provided both a qualitative and quantitative analysis of the film at Planes B and D shown in Figure 2.6. Hee et al. identified two mechanisms for the oil film formation on the stationary outer walls. Firstly, as shown by Santhosh et al., oil is shed from the

cage-edge as either droplets, ligaments or sheets depending on the rotational shaft speed. This oil flung from the cage, subsequently impinges on the static walls, forming a thin film. Secondly, oil is axially displaced outwardly from the gap in between the outer-race and the ball bearing. The combined oil gains tangential momentum due to the circumferential shear imparted by the airflow. Upon reaching the front-face edge, Figure 2.6, the oil is shed radially outward into the main bearing chamber compartment as a combination of droplets, ligaments and/or sheets.

Around the bearing shedding rig, there are four angular locations for measurements to be taken, these are highlighted within Figure 2.8. Facing the front of the rig and moving clockwise with the direction of the shaft rotation, at the 90° viewport, the P2 co-current region, the film travels in the direction of gravity forming a smooth shear-dominated film. However, moving around the annulus to the 270° region, the P4 counter-current location, here the shaft rotation opposes that of gravity, causing an undulation effect within the film. When the shearing forces are equal to the effects of gravity, a shock regime can be found [54].

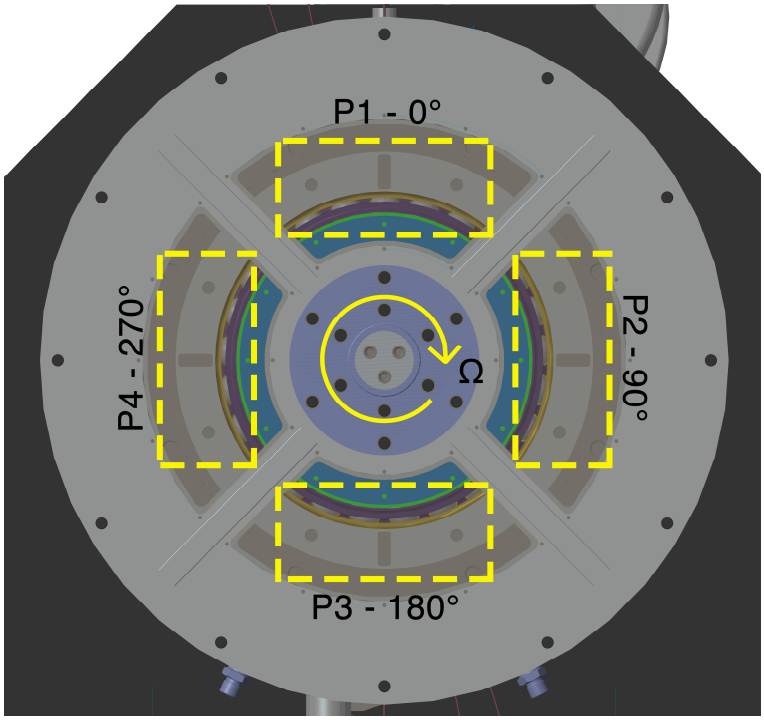


FIGURE 2.8: CONVENTION FOR ANGULAR LOCATIONS AROUND THE SHEDDING RIG [54]

At the Plane B location, in Figure 2.6, Hee et al. reports that at low rotational shaft speeds the effects of gravity dominate, and subsequently, the film is seen to be travelling downward; this can be seen within Figure 2.9 a) for the shaft speed of 3,000 rpm at a distance 10mm away from the film edge. This phenomenon causes the film to intermittently undulate resulting in a significantly more wavy and non-uniform film. In general, as the rotational shaft speed is increased, the gravity driven flow regime begins to diminish and beyond 5,000 rpm, Hee et al. report that the smooth

shear driven flow regime dominates. This is observed within Figure 2.9 b) at 5,000 rpm, whereby the film is now seen to be travelling upwards, i.e. in the same direction as the shaft rotation. In general, a quantitative analysis of film thickness measurements showed that with an increase in shaft speed, the film thickness decreased. Whereas, an increase in the oil flow rate did not produce any substantial change in the oil film thickness.

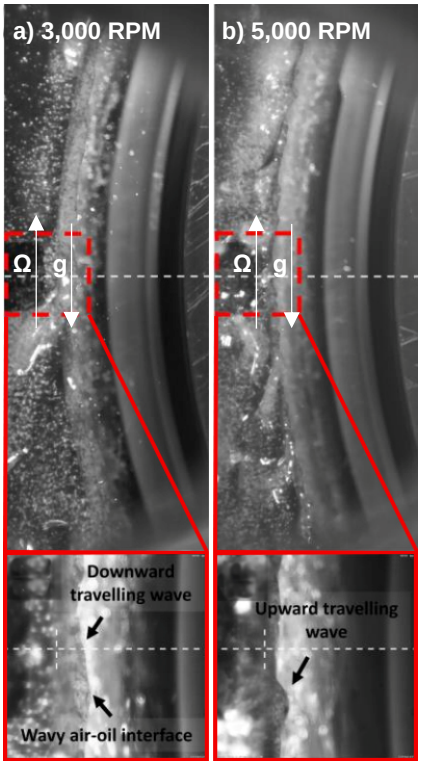


FIGURE 2.9: FILM DIRECTION 10mm FROM FILM EDGE AT COUNTER-CURRENT REGION [54]

Hee et al. [56], extended upon their work in an effort to characterise the oil film waves and also the ligaments shed from the bearing cage. The number of ligaments produced at certain test conditions was found to be in good agreement with ligament number correlations for that of rotating cups and disks. Qualitatively, it was observed that as the rotational shaft speed is increased, the ligament spacing decreases and hence the number of ligaments increases. However, at higher shaft speeds, the more transient nature of the oil film caused a greater deviation from the empirical correlations. Analysis of the surface film waves, revealed that, as the rotational shaft speed was increased, the frequency of waves also increased but their wavelength decreased. At the lower shaft speeds, gravity driven waves were observed, exhibiting low frequencies and long wavelengths. Conversely, at the higher shaft speeds and beyond 5,000 rpm, capillary waves were identified, having high frequencies but short wavelengths. The characterisation of these different wave regimes is important, since they can have a significant effect on the droplet impingement characteristics and any subsequent secondary droplets produced as a result of splashing.

2.3.5 Oil Jet Systems

Typically, the supply of oil to a bearing is delivered through a series of machined holes on the shaft, which are fed by a jet of oil targeted onto the shaft. Due to the complex two-phase interaction between the oil, airflow and the rotating shaft, only a proportion of the oil is captured and supplied to the bearing; the remainder of which is dispersed to the bearing chamber and subsequently scavenged. Figure 2.10 shows two different jet configurations for bearing lubrication, firstly oil is supplied directly to the bearing between the inner and outer race, or alternatively via an underrace feed in combination with a series of scoops to collect the oil. Typically, an underrace configuration is advantageous, although limitations can occur in a confined axial space [57].

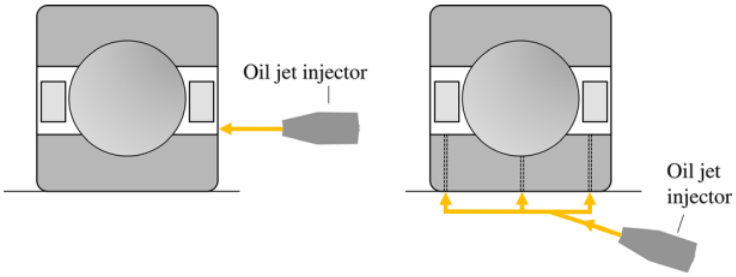


FIGURE 2.10: OIL TARGETED DIRECTLY AT THE BEARING VS BEARING UNDERRACE FEED [57]

Early investigations by Lee et al. [58] used flow visualisation techniques to assess the efficiency of oil jet delivery systems depending on the rotational shaft speed and oil flow rate. At higher jet oil flow rates, an increased amount of oil breakup was observed and an increase in rotational shaft speed led to further breakup due to the higher crossflow velocities. A greater amount of oil was supplied to the bearing with an increased oil flow rate; however, a larger proportion of oil is lost due to splashback or spillover. With an increase to either the rotational shaft speed or jet oil flow rate, Lee et al. concluded that the feed hole efficiency subsequently decreased.

Krug et al. [59], extended upon the investigations of Lee et al. [58], providing further insight into the characteristics of the oil jet, the delivery system efficiency and mechanisms for the droplet generation. Using high speed shadowgraphy, the results of Krug et al. contradict the findings of Lee et al., demonstrating an increase in efficiency of the oil jet system with the rotational shaft speed. The results of which highlighted that the design of the feed geometry and collector improved capability for these higher operation conditions. The catch efficiency of the system was defined in terms of a momentum flux ratio, based on the shaft speed and oil flow rate. At low momentum flux ratios, a low catch efficiency is observed and as the momentum flux ratio increases so does the efficiency; results suggested that an efficiency greater than 90% was not

achievable. Krug et al. also investigated three different nozzle diameters, whereby it was demonstrated that a smaller nozzle diameter provides a greater momentum flux ratio and hence an improved efficiency. The smaller nozzle diameter has a greater momentum flux due to two main reasons; firstly, a smaller nozzle results in an increased jet velocity and secondly the smaller diameter produces a relatively thinner jet, which is less susceptible to breakup. An investigation into the jet angle revealed that a shallow angle, such as 50°, resulted in a reduced amount of splashing and hence a greater efficiency. Although, for even shallower angles, such as 35°, and for high momentum fluxes, the efficiency began to decrease as a result of splashing.

More recently Cagaeo et al. [57]. investigated the catch efficiency of a scoop oil delivery system. Over a range of operating conditions Cagaeo et al. investigated several different scoop geometries and jet characteristics. In contrast to the previous studies, it was shown that as the rotational shaft speed is increased, initially the capture efficiency also increases; however, when the velocity ratio, defined as the scoop tip to jet velocity, exceeds a value of 1, a gradual decrease in capture efficiency is seen as the shaft speed is further increased. A study on the size of the scoop constriction showed minimal changes to the capture efficiency, although a marginal increase in efficiency was seen for the largest constriction. Three different configurations of jets were investigated, namely: a single jet, tandem jets and twin jets. Similar results were presented for both of the two-jet configurations, however at low shaft speeds the single jet configuration resulted in a 10% lower capture efficiency, decreasing to 3% at the highest rotational shaft speed. Similar to the work of Krug et al. [59], Cagaeo et al. identified the oil jet angle as a key parameter for scoop designs. When the jet angle was decreased by 10° from the baseline condition, an increase in capture efficiency of 11% was observed.

2.3.6 Gas-Sheared Liquid Films

The application of gas-sheared liquid films is of great significance to bearing chambers. Whilst early experimental bearing chamber studies focused on film thickness measurements and heat transfer effects, there was considerable uncertainty regarding the film dynamics. To develop the understanding of flow conditions within the bearing chamber, Hashmi et al. [60] performed investigations for a gas-sheared liquid film. The experimental conditions were used to assess the co- and counter-current regimes within a bearing chamber and identify the film dynamics arising from the shearing and gravity driven forces. Hashmi et al. report that as the high shearing gas velocity is increased beyond a critical point, the waves on the film surface transition from that of a smooth, flat structure to a three-dimensional wave; further increases to the gas velocity increases both the frequency and amplitude of the waves. To induce the effects of gravity and simulate the co-current regime, the test rig was inclined up to an angle of 25°, which resulted in a reduction of

both the wave frequency and amplitude. To recreate the conditions for the counter-current flow regime, the gas velocity was applied in the opposite direction to the film, resulting in highly turbulent waves. Overall, the work of Hashmi et al. played a fundamental role in classifying the flow regimes within a bearing chamber, which ultimately Kurz et al. [9] expanded upon as previously discussed.

Alghoul et al. [61] investigated the droplet interactions on a shear driven liquid film to better inform droplet impact correlations for bearing chambers flows; since previously, computational work had heavily relied upon correlations derived from droplet impacts on static films. Similar to the work of Hashmi et al., Alghoul et al. report that an increase to either the film or gas velocity causes the surface waves to transition from a smooth two-dimensional wave to a three-dimensional structure and finally to roll waves. Within the experimental investigations, three different types of droplet interactions were observed. Firstly, at low shearing gas velocities, the spherical droplets showed similar splashing and deposition characteristics to that on a static film. As the gas velocity is increased, the droplets become deformed leading to an increased amount of splashing. Finally, at high shearing gas velocities, the droplets become significantly distorted leading to bag breakup and coalescence upon impact. Whilst the shearing gas velocity determined both the impingement and deformation of the droplets, it was noted that the type of film waves also strongly influenced the splash characteristics and the secondary droplet sizes.

Building on the work of Alghoul et al. [61], Mitchell et al. [62] investigated the droplet interactions under the influence of gravity for supercritical films. The work of Mitchell et al. showed that the outcomes and transitions of droplet impacts derived from static film can be extended to supercritical films. Here, droplet calculations require the use of the resultant velocity magnitude as opposed to the normal velocity component. An analysis of the droplet thermal behaviours revealed that the droplet Weber number was a good indicator of heat transfer rates. The droplet Weber number provides a measure of the fluid's inertia relative to its surface tension and is defined as:

$$We = \frac{\rho u^2 d}{\sigma} \tag{2.13}$$

Where u is the droplet velocity, d is the droplet diameter and σ is the surface tension. In general, Mitchell et al. report that droplets with higher Weber numbers heated to that of the film temperature faster. Subsequent work by Mitchell et al. [63] went on to characterise the crater morphology arising from droplet impacts on a moving film.

More recently, Vasques et al. [64] studied the surface tension effects on bubbles generated within gas-sheared liquid films. The work of Santhosh et al. [53] and Hee et al. [54] identified a much higher concentration of air bubbles travelling within the oil film than expected. Figure 2.11

depicts how the presence of air bubbles within the oil film can significantly decrease the capability of the oil to transfer heat. Firstly, the air within the bubbles is typically hotter than the oil, secondly these bubbles can also act as a barrier between regions of hot and cool oil. Furthermore, the bubbles entrained within the oil will significantly change and influence the fluid parameters such as the viscosity and density of the oil.

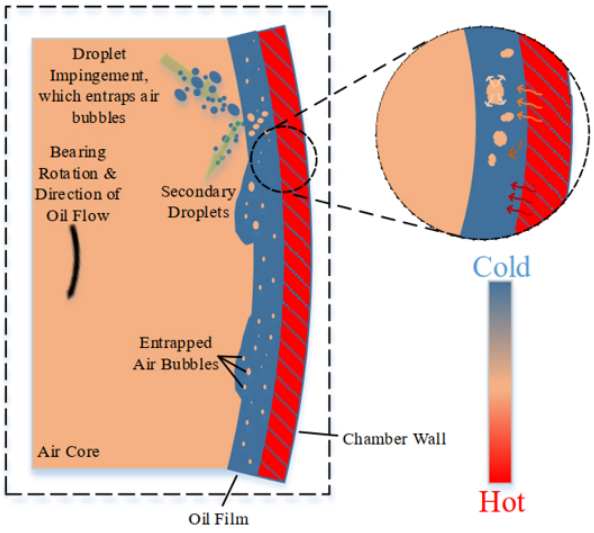


FIGURE 2.11: EFFECT OF BUBBLES ON BEARING CHAMBER HEAT TRANSFER [64]

Since these air bubbles will have a substantial impact on both the oil properties and heat transfer characteristics, Vasques et al. [64] attempted to develop an understanding of the effects that these bubbles have on the flow phenomena. The results of Vasques et al. showed that with a decrease in surface tension, the number of bubbles generated increases, but the size of these bubbles decreases. As the number of bubbles increases, so does the amount of aeration within the liquid film, a 10% reduction in the surface tension led to an increased aeration level of 100%. Finally, it was also observed that with a reduction in liquid surface tension, the overall velocity of the bubbles seemed to decrease. The work of Vasques et al. suggest that within a bearing chamber, when choosing an oil lubricant, a relatively lower surface tension oil may result in a poorer cooling performance.

2.4 Bearing Chamber Numerical Studies

In order to assist the development of CFD capability for bearing chambers, it is first necessary to highlight the relevant flow phenomena. Within a bearing chamber, the detailed physics may be broken down into two distinct but interacting regions. Firstly, a segregated flow region, characterising laminar wavy oil films with varying film thicknesses, driven by both the shear and gravitational forces. Secondly, a dispersed flow region, consisting of oil droplets with a varying degree of sizes that are transported by the turbulent gas flow.

In broader terms, a segregated flow can be regarded as a multiphase flow consisting of at least two or more immiscible fluids, with a clearly defined interface. Traditionally the Volume of Fluid (VOF) approach, has been used to model these multiphase segregated flows. Through determining the volume fraction of each of the fluid phases, the method can then track the distribution of each phase within the domain. Typically, these multiphase flow techniques, such as the VOF approach, require the use of a very fine computational domain in order to sufficiently resolve the film interface and its velocity profile, as shown in Figure 2.12 a). Such requirements can result in prohibitively high computational costs, resulting in simplifications for industrial applications and, more specifically, aeroengine bearing chambers. However, alternative methods have been developed, such as the Eulerian Thin Film Model (ETFM). Here, the three-dimensional Navier-Stokes equations are depth averaged across the film, resulting in a set of two-dimensional thin-film equations. As such, the ETFM can provide a more efficient simulation of segregated wall film flows, for which typically the length scale of the liquid film is significantly smaller than the rest of the domain, as highlighted in Figure 2.12 b). Therefore, when compared to the VOF approach, the ETFM can account for the effects of the thin film without explicitly resolving the very fine grid scales required at the interface; although, as a result, problems are faced when three-dimensional fluid effects are observed. Whilst other methods exist, these two approaches are regarded as the state-of-the-art approach for the segregated flows and thin films observed in bearing chamber modelling.

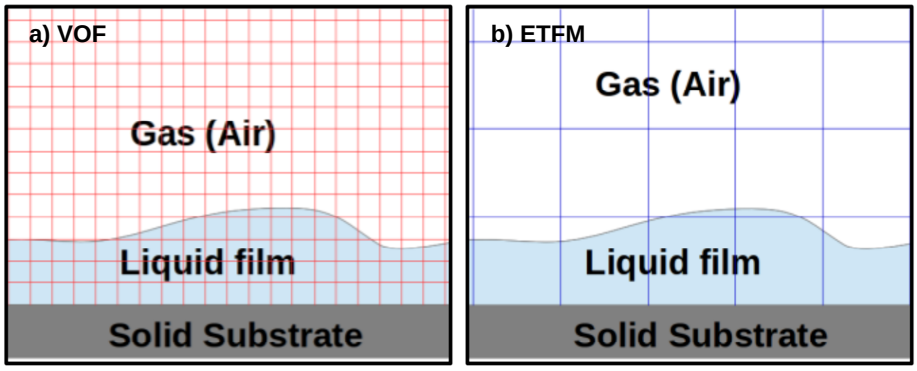


FIGURE 2.12: COMPARISON OF FILM AND INTERFACE REQUIREMENTS FOR VOF (LEFT) AND ETFM (RIGHT) FOR THIN FILM MODELLING [65]

Similarly, a dispersed flow can be identified as a multiphase flow of two or more immiscible fluid phases, whereby within the primary phase, a secondary phase is dispersed as either a range of droplets, particles or bubbles. Traditionally, within bearing chamber simulations, the Discrete Phase Modelling (DPM) approach is used, which assumes that the dispersed phase is dilute enough that particle-particle interactions can be ignored. As the number of droplets in the system increases, the Algebraic Slip Model (ASM) can provide a more efficient calculation of the dispersed phase, due to having fewer equations to solve, although it is only accurate for small particles with a low relaxation time. A multi-fluid, or Eulerian approach, becomes applicable as both the particle size and relaxation time increases, in which transport equations are solved for each phase to provide an accurate solution of the flow field. Typically, when modelling the dispersed phase for a bearing chamber simulation, out of these models, the DPM approach is most favoured.

2.4.1 The Volume of Fluid Method

The VOF method is widely used for the numerical simulation of multiphase flows with the benefit of fluid-fluid interface tracking. A significant challenge presented when using the VOF method is correctly specifying the numerical interfacial treatment. For example, first order upwinding schemes can cause numerical diffusion, whereas higher order schemes can result in unphysical or unbounded volume fractions. As such, specification of the numerical schemes is extremely important and has led to the development of many different interfacial treatments.

The VOF approach is well suited for bearing chamber CFD investigations due to the capability to capture the highly complex three-dimensional recirculating flow structures as observed experimentally. However, early VOF bearing chamber simulations were unsatisfactory leading to the development of an enhanced VOF approach, as demonstrated by Peduto et al. [66]. Peduto et al. modelled the lower half of a bearing chamber, comparing against experimental film thickness measurements, highlighting the characteristics of the flow field near the sump recirculation region. Peduto et al. demonstrated that the use of an interfacial treatment was critical for capturing the surface film instabilities, such as waves or regions of recirculation. Without the interfacial treatment, large discrepancies were seen due to the suppression of flow features.

Due to the large number of cells and computational cost associated with modelling an entire bearing chamber, initial VOF simulations, such as the one by Peduto et al. [66], were restricted to just the sump region. Krug [67] presented the first VOF investigation of a full bearing chamber, comparing against available experimental film thickness measurements and scavenge efficiencies. Using a systematic approach, Krug performed a comparative analysis of the both the

Egorov and Hashmi turbulence damping approaches. At lower shaft speeds, both models tended to under-predict the film thickness measurements and conversely, at higher shaft speeds, results were over-predicted. In general, Krug found that between the two turbulence damping methods, no significant difference was found; however, the severe computational cost and long simulation times prevented a complete comparison of the two approaches. As such, Krug suggested that further work was necessary to investigate both approaches, especially in choosing the Egorov *B* parameter.

Similar to the work of Krug, Bristot [68] also performed a comparative analysis of both the Egorov and Hashmi turbulence damping approaches. It was concluded that, for the Egorov approach to be equivalent to the Hashmi approach, a turbulence damping factor of 100 was required. However, there is no significant proof that the Hashmi approach, whilst being more rigorous, is an adequate approach to interface turbulence damping. Bristot highlighted the importance of the turbulence damping parameter on the final overall state of the bearing chamber flow regime observed. For example, Figure 2.13 a) demonstrates the result of using a turbulence damping value of $B = 100$, compared to that of Figure 2.13 b), using a default value of $B = 10$. Here, moving from Figures 2.13 a) to b), the smooth flat film regime transitions to a significantly more wavy and unstable film. However, a quantitative comparison of film thickness measurements to experimental data revealed that both cases investigated by Bristot showed poor agreement. Suggesting that over the wide range of bearing chamber flow regimes observed, there is no universally comprehensive value for the turbulence damping factor. Thus, presenting a critical problem for future bearing chamber VOF simulations, and therefore, requiring careful selection of the turbulence damping parameter.

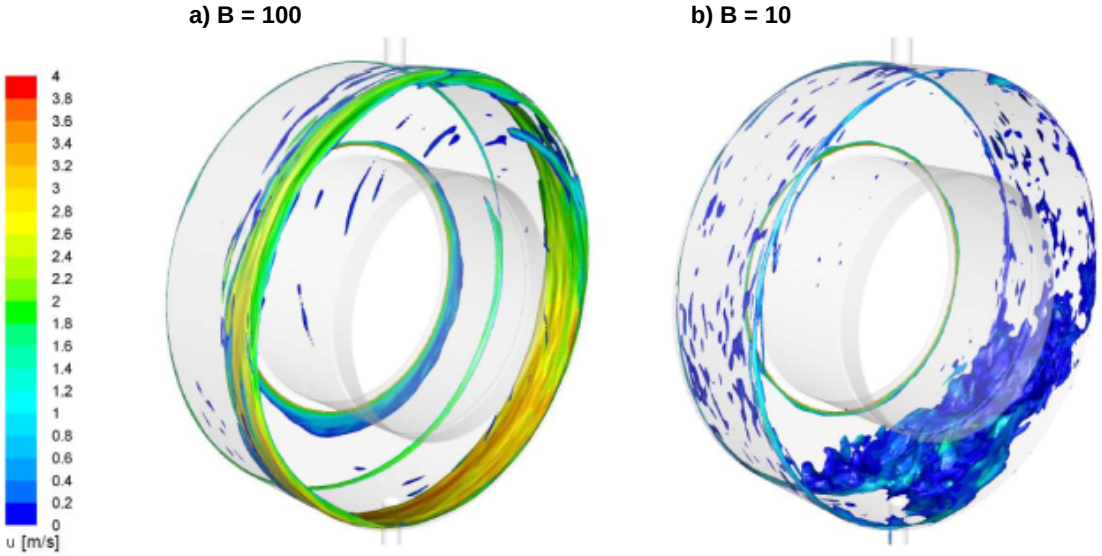


FIGURE 2.13: SENSITIVITY OF OIL FILM DISTRIBUTION AND VELOCITY TO THE TURBULENCE DAMPING PARAMETER [68]

To date, the technique implemented by Bristot using the Egorov approach and a turbulence damping factor of $B = 100$ is regarded as the best practice approach for VOF. Overall, Bristot was able to successfully demonstrate the VOF capability for bearing chamber simulations, as shown by the proficiency captured in Figure 2.14 for a full BR725 chamber geometry.

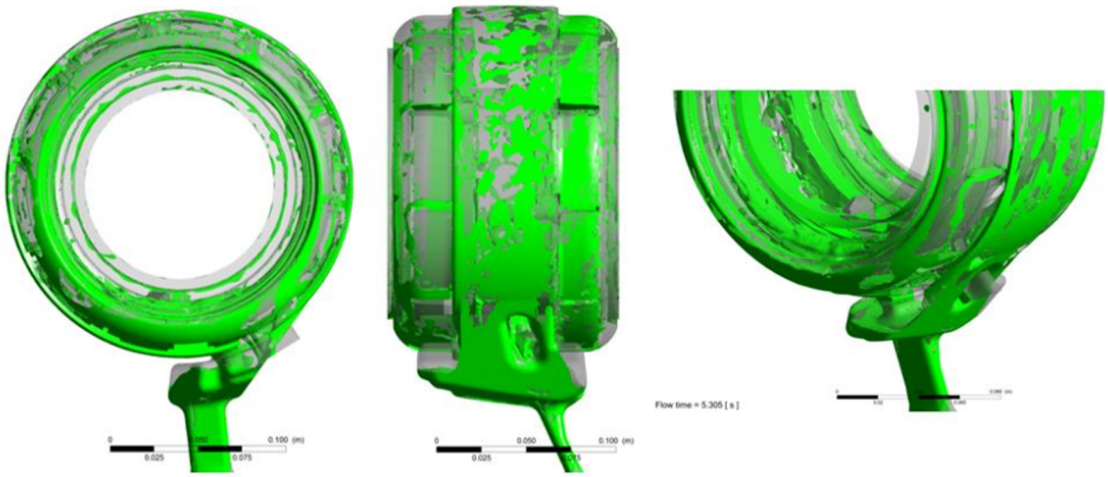


FIGURE 2.14: VOF FILM THICKNESS DISTRIBUTIONS FOR A BR275 CHAMBER [68]

Within an aeroengine bearing chamber, Jingyu et al. [69] investigated several scavenge configurations using a VOF methodology in order to improve design optimisation. Using the bearing chamber geometry of Kurz et al. [42], three different scavenge offtake designs were considered, namely: the baseline case, a shallow ramp and a deep ramp. For the baseline case, the simulation results were validated against the experimental data, although an underprediction of the scavenge efficiency across all rotational shaft speeds was observed, especially at the slower speeds. For all cases, Jingyu et al. report a decrease in scavenge efficiency with an increase in rotational shaft speed. Good scavenge efficiencies were achieved for the deep ramp configuration, maintaining a minimum efficiency of 80% even at the highest speed, compared to 45% with the baseline offtake design.

Arcila et al. [70] studied the heat and mass transfer of droplets within an aeroengine bearing chamber using a VOF approach, to gain insight into the evaporation process. Using a D^2-law evaporation model, Arcila et al. was able to model the behaviour of droplets, with an initial diameter of 200μm, subjected to a high temperature, convective, airflow. The results demonstrated that under the effects of heating, within the droplet, a convective flow field develops. Subsequently, the droplet can undergo a phase change, whereby, internally a bubble develops; this can then potentially be released, causing the ejection of liquid as a smaller, child droplet. An analysis of the droplet residence times revealed that under the effects of a very high temperature air flow, such as 550K, droplets can undergo evaporation in as little as 0.3s; although

at moderately high temperatures, for example 350K, the droplet lifetime is predicted to be 1.7s. The evaluation of droplet lifetimes is extremely important when considering that inside the bearing chamber, small droplets can become entrained in the gas flow.

2.4.1.1 VOF Mesh Requirements

Krug [67] performed a mesh independence study to determine the most optimal mesh requirements when using a VOF approach. For the case study under investigation, Krug predicted that the maximum oil film thickness needed to be modelled was approximately 1.2mm. It was therefore concluded that to sufficiently resolve the boundary layer, a y^+ wall spacing of less than one was necessary and a minimum of 6 cells was required to fully capture the oil film. However, Krug did not reach a fully mesh independent solution due to limited computational resources, and as such, a relatively coarse mesh chosen.

The subsequent investigations by Bristot [68], also documented a mesh independence study, however recommendations on mesh resolution were only made based on a single-phase grid sensitivity study. In addition to maintaining a low wall y^+ spacing, Bristot proposed a more rigorous approach for capturing the oil film; in which, Bristot suggested 4 cells should be used to resolve the minimum oil film thickness. Therefore, if the minimum oil thickness expected is 200μm, this would be covered by the first 4 cells resulting in a total of 24 cells within the first 2.3mm from the wall according to the baseline mesh of Bristot. However, since Bristot only conducted a single-phase mesh independence study, the dependence of film thickness on mesh resolution is still unclear. It is apparent that there is a need for a more systematic mesh independence study for bearing chamber simulations that takes into account the oil film.

Due to the very high computational cost associated with resolving the oil film to a fine degree of accuracy, one alternative approach is the use of an adaptive mesh refinement (AMR) algorithm. This approach has the advantage of sufficiently refining the mesh in critical regions, whilst retaining an appropriately coarse mesh in regions of less importance. For a bearing chamber geometry, Crouchez-Pillot et al. [71] was the first to successfully apply an AMR approach. Using this technique, Crouchez-Pillot demonstrated the ability to sufficiently refine the oil-gas interface; which appeared to improve the ability to resolve the oil flow field, whilst minimising the computational cost typically associated with a very fine mesh resolution. For the same case study, Krug et al. [72] extended upon the work of Crouchez-Pillot, using AMR but over longer simulation run times. Comparing scavenge efficiencies and film thickness measurements to experimental data, good agreement was found and as such an AMR approach was proposed for all further VOF bearing chamber simulations. Recommendations were also suggested to couple

the VOF approach with a droplet impingement model to better assess the complex two-phase flow phenomena typically observed within a bearing chamber. Here, the use of an AMR algorithm would be beneficial to keep a sufficiently refined gas-oil interface for the VOF, whilst maintaining a relatively coarse mesh within the core gas flow that would be suitable for a DPM approach.

2.4.1.2 Additional Aeroengine VOF Applications

Berthold et al. [73, 74] investigated, computationally, the external oil flow exiting a journal bearing within an epicyclic gearbox. Through reducing the epicyclic gearbox into a series of more simplified models, a greater understanding of the underlying key flow physics can be established. Berthold et al. used a VOF approach to model the oil exiting from the journal bearing, which, due to its momentum remains attached to the face of the rotating planet gear. At the edge of the planet gear, the oil is subsequently shed as either droplets, ligaments or a sheet much like that observed for a rotating cup. Through a series of investigations, Berthold et al. determined that a rotationally periodic sector was sufficient to simulate the non-orbiting, journal bearing case; however, the number of ligaments produced was directly influenced by the mesh resolution in the circumferential direction. A strong influence of oil viscosity on the oil flow pattern was also observed. An analysis of different interfacial reconstruction methods showed the greatest performance using the geometric phase reconstruction scheme, with the capability to capture detailed flow physics such as both droplets and ligaments.

Prabhakar et al. [75] investigated how the performance of scoop devices was influenced by the rotational shaft speed using a two-dimensional VOF approach. The results of Prabhakar et al. predicted capture efficiencies similar to that observed experimentally, showing an initial sharp increase in the capture efficiency with rotational shaft speed, however this then steadily falls as the speed is increased further. Additional investigations by Simmons et al. [76], considered the influence of the jet configurations on the capture efficiencies for scoop systems, again using a two-dimensional VOF approach. A study on the jet flow revealed that a gain in capture efficiency of approximately 10% was possible through pulsating the oil flow, when compared to the baseline case. Through pulsating the oil flow, it was possible to avoid oil losses as a result of oil deflecting from the scoop tip; however, to achieve this, an optimal timing procedure was therefore required and the volume flow rate of the pulsed jet had to be adjusted to deliver the same volume of oil. Recent studies by Jiang et al. [77] also attempted to use a VOF approach to model the liquid jets for scoops. However, when compared to the work of Prabhakar et al. or Simmons et al. who reported efficiencies of over 80% in line with the experimental measurements, Jiang et al. produced very low capture efficiencies of around 40%.

Prabhakar et al. [78] also used a VOF approach to model the two-phase flow within a Dual Drive Booster turbofan gearbox. Prabhakar et al. investigated the scavenge characteristics of the gearbox under different operating conditions and situations, such as changes in both attitude and altitude. From the baseline case, three different attitude scenarios were investigated, namely, rolling to either the left or right and a case with the gearbox pitched downward. Due to the configuration of the sump, a roll to the left saw an increase in the oil residence mass of 8.5%, since the oil had to work against gravity in order to reach the sump. Interestingly, a roll to the right, saw no change in the oil residence mass from the baseline condition. The worst performance was achieved with the downward pitch, causing an increase in oil residence mass of 18.5%; this was associated with the scavenge performance decreasing due to the change in angle and hence effect of gravity. A change in altitude to 35,000 ft was simulated through manipulating the properties of air, although no significant change was observed in the scavenge performance; Prabhakar et al. summarised that this was due to the oil trajectories being dominated by the windage effects as opposed to the airflow.

2.4.2 The Eulerian Thin Film Model

The Eulerian Thin Film Model presents an advantageous alternative to the Volume of Fluid method for resolving segregated wall-film flows. The ETFM, uses a depth-averaged approach, making it well suited to resolving thin film flows, permitting a much coarser grid spacing in the wall normal direction, and hence presenting a significant computational cost saving when compared to the VOF model. For example, the ETFM in OpenFOAM was benchmarked against a three-dimensional VOF approach by Vita [79], for the case of an impinging jet forming a thin-film over a rotating disk. Here, in terms of overall computational cost, the ETFM was over 1000 times faster than the VOF approach. More recently, Kakimpa et al. [80], performed the same benchmarking study for the ETFM in ANSYS Fluent versus a two-dimensional VOF approach, demonstrating a speed up factor of 15 using the ETFM.

Early bearing chamber thin film modelling saw the use of in-house developed models [81, 82] providing tailored CFD solutions to the bearing chamber problem using a Eulerian approach. These early models were only able to reproduce smooth flow solutions with numerical difficulties preventing an obtainable solution for shock and pool scenarios. In the Wang thin film formulation [82], within the energy and momentum equations, the advective terms were simplified and thought to cause these numerical instabilities for shock or pool solutions in which inertia plays a significant part [83]. Furthermore, in the work of Wang et al., a full two-way coupling between the gas-phase and oil film is not observed; instead, a prior simulation was used to inform the core airflow quantities between the shaft and chamber. Subsequent development of the Wang thin film

model saw its adoption into the commercial CFD code ANSYS Fluent [84]. However, whilst still demonstrating good capability for the smooth flow solutions at high shaft speeds, unphysical discontinuities were still reported at lower shaft speeds within the shock and pool regimes.

To assist the development of the ETFM, studies have focused on laminar shear-driven thin film flows called rimming flows. Here, a liquid film, in the presence of gravity, is driven around a stationary outer cylinder wall by the interfacial shear stress produced from a rotating inner cylinder. In general, a rimming flow can be regarded as an idealised bearing chamber, when simplified to a rotating inner cylinder with a stationary outer cylinder on which there is a thin film. Mathematical studies on rimming flows, [85–87], showed the capability of accurately predicting the smooth, shock and pool solutions through a more rigorous formulation and the inclusion of inertia effects. In addition, these studies highlighted a clear link between surface tension and solution stability. Within the Wang thin film formulation, the simplified inertia term arises from assuming a uniform velocity profile when calculating the depth-averaged inertia. Instead, a quadratic velocity profile is assumed to be more appropriate, due to the high shearing forces at the gas-film interface in combination with a no-slip wall condition; as demonstrated by authors such as Kay et al. [88]. This quadratic velocity profile assumption has been empirically demonstrated for falling liquid films of a laminar nature, such as in the work of Cook et al. [89]. However, due to the more complex nature of the thin films present within an aeroengine bearing chamber, it is unclear whether this approach is still applicable when considering wavy films. For example, Malamataris et al. [90] demonstrated numerically that for falling liquid films of a wavy nature, the internal velocity profile transitions away from a quadratic velocity profile. Instead, disturbances cause inflection points within the velocity profile found at locations downstream of the gravity-capillary wave front. However, for the ETFM, to date little work has been done to evaluate a higher order velocity profile and as such, the use of a quadratic velocity profile remains the best practice approach.

Kakimpa et al. [83, 91] performed a rigorous investigation of the capillary thin film waves within a rimming flow case study, using the ETFM. Kakimpa demonstrated that for high rotational shaft speeds, in which the smooth shear dominated flow regime is observed, an accurate solution is obtainable even without fully resolving the inertia effects, much like the results of Wang et al. [84]. However, for the lower shaft speeds characterised by shock and pool regimes, the representation of inertia effects was discovered to substantially affect the solution accuracy. Although, for cases with a simplified inertia term, careful selection of the numerical discretisation schemes can still produce a stable solution. For the shock and pool regimes, a simplified film inertia term resulted in a significant over-prediction of the film thickness when compared to a case study using a fully formulated inertia term. As such, subsequent developments to the ETFM source code led to the use of a corrective source term in order to modify the already existing code

which used a simplified-inertia source term [84]. Kakimpa et al. evaluated the use of different temporal numerical schemes. Previous investigations for the ETFM used a semi-implicit approach, whereby an explicit time stepping procedure is used with further sub-iterations to converge both momentum and continuity equations. However, Kakimpa et al. reported that such a procedure requires the use of a very small Courant number, as low as 0.01, to maintain stability which can led to slow converge times. In addition, for some cases using an explicit scheme, Kakimpa et al. noticed a substantial loss of mass from the domain. As an alternative, a fully implicit time stepping scheme was tested, showing an improved convergence and stability performance. As such, Kakimpa et al. recommend using a fully implicit time stepping scheme for the ETFM to ensure numerical stability. A parametric study into spatial discretisation was also considered. Kakimpa et al. suggest that in order to maintain stability for the ETFM, a minimum grid resolution can be derived; which depends on the both the gas and film properties. In conjunction with the previous ETFM recommendations, through sufficiently refining the mesh, a stable solution for the shock and pool regimes can be obtained. If the grid is not adequately refined, then certain flow characteristics associated with either gravity or capillary waves cannot be captured, leading to unstable solutions. Kakimpa et al. proposes that the capillary waves form the main source of instability for shock or pool solutions, due to their very small wavelengths. Therefore, a fine mesh is required to resolve these short wavelengths and obtain a stable solution. In order to classify the type of wave disturbance, a critical wavelength can be defined:

$$\lambda_c = 2\pi\left(\frac{\sigma}{g(\rho_l - \rho_g)}\right)^{\frac{1}{2}} \qquad (2.14)$$

$$if\begin{cases}\lambda \ll \lambda_c & Capillary\ Waves\\ \lambda \gg \lambda_c & Gravity\ Waves\end{cases}$$

Where λ_c is the critical wavelength, σ is the surface tension and ρ is the liquid and gas densities respectively. Kakimpa et al. suggest that, within the presence of capillary waves a maximum grid spacing can be defined as: $\Delta x_{max} = \frac{\lambda_c}{60}$ which should not be exceeded. Conversely, for smooth shear dominated flow regimes, the disturbances exhibit a significantly larger wavelength and therefore permit a much coarser mesh resolution. This occurs since gravity acts as the main restoring force and the effect of surface tension is less important.

2.4.3 Coupled VOF-ETFM

Whilst the ETFM is capable of accurately resolving thin films within bearing chambers, in regions of thick films such as near the sump, it becomes unacceptably inaccurate to implement due to the

three-dimensional nature of the oil film. Recently, Kakimpa et al. [65] developed a methodology to transition between the VOF and ETFM with excellent results and cost savings, demonstrating the capability on a rimming flow case study. Kakimpa et al. presents a fully coupled two-way VOF-ETFM approach, such that a thick 'VOF' film can transition to a thin 'ETFM' film and vice versa. Through a coupled VOF-ETFM model, accurate predictions of the thin film can be achieved on grid resolutions typically much coarser than a standard VOF method, away from which, in the rest of the domain, the VOF approach is retained. At the VOF/ETFM interface Kakimpa et al. defined a transition criteria in order to couple both the film mass and momentum source terms between the two models. The point at which the VOF model switches to the ETFM, is defined by a critical cut-off value for the volume fraction and is evaluated in a time stepping dynamic process, i.e. when the volume fraction drops below a certain threshold, the ETFM is used and vice-versa. Kakimpa et al. performed a qualitative comparison between a standard VOF simulation and the newly implemented coupled VOF-ETFM approach. For the rimming flow investigation, the VOF model predicted localised film dry-out regions, suspected to be a numerical error in the VOF volume fraction cut-off level, which would have required a much finer mesh in order to resolve. Conversely, the VOF-ETFM model did not produce any dry-out regions, instead a persistent thin film was observed in these previous dry-out locations, as demonstrated by Figure 2.15. Here, for the rimming flow case study, the ETFM film thickness contours are shown and, in addition, the VOF iso-surface is also included.

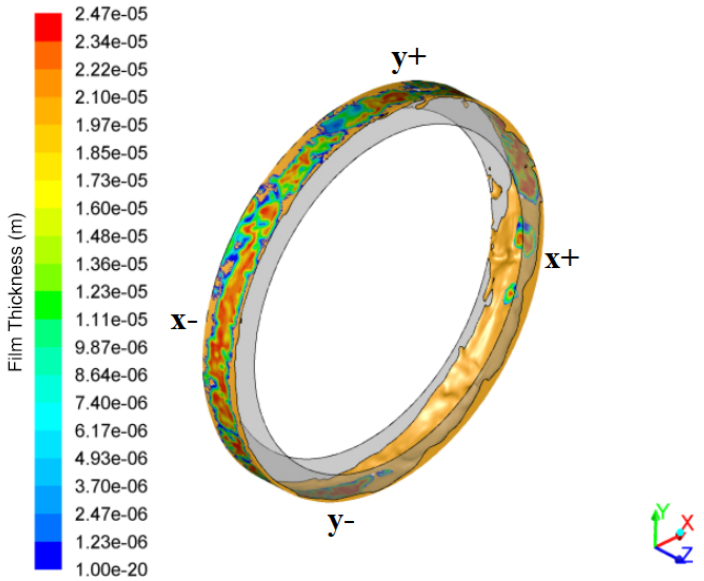


FIGURE 2.15: CONTOURS OF ETFM FILM THICKNESS AND VOF ISO-SURFACES FOR THE VOF-ETFM RIMMING FLOW SOLUTION [65]

Kakimpa et al. [65] also revealed, that through analysing cross sections of the domain, whilst both models predicted a pool solution, differences were observed in the start location and depth of the

pools captured by the VOF model. Furthermore, differences in velocity profiles were observed, although in part, Kakimpa et al. attributed this to the previously observed differences in film thickness distributions. However, this could also be associated with the difference in turbulence damping at the gas-liquid interface. Unlike the VOF model, turbulence damping is carried out within the ETFM since it is regarded as a film wall; therefore, this suggests that the coupled VOF-ETFM model may have an improved turbulence damping performance over the standard VOF approach. In general, due to the coarser grid requirements, the VOF-ETFM coupled model produced computational cost savings when compared to the VOF simulations, presenting a speed up factor of approximately 3.4.

More recently, Singh et al. [92] performed a quantitative analysis for the VOF-ETFM model within a simplified bearing chamber geometry, comparing to experimental data. The VOF-ETFM approach was able to qualitatively capture the oil film formation and distribution on the outer chamber wall, however, in general under-prediction of the film thickness was observed. A simulation was also run with a VOF approach, which in general over-predicted the film thicknesses but produced a much closer agreement to the experimental data compared to the VOF-ETFM approach. Similar to the results of Kakimpa et al., Singh et al. report a computational speed up factor of 3 when using the coupled VOF-ETFM approach. Furthermore, Singh et al. [93] also employed the coupled VOF-ETFM model to a wetting and drying bearing chamber case study. An additional source term was included within an enhanced-ETFM formulation in order to resolve the contact angle effect. However, it should be noted that the required wetting and drying parameter relies on validation from experimental results and for bearing chamber applications the value of this parameter is unclear. The performance of the model was first assessed for a flat plate geometry with excellent results, demonstrating the qualitative trend of capturing rivulets. When applied to a bearing chamber geometry, within the ETFM region, again under-prediction of the film thickness was observed, but good qualitative trends of film thickness formation and distribution were reported.

2.4.4 Coupled VOF-DPM

Experimental investigations of droplet generation from aeroengine bearings [49, 53, 54] has provided key insight into how, depending on the shaft rotational speed, oil is shed not only as droplets and ligaments into the bearing chamber, but also as sheet formation. Recent high-speed camera investigations have revealed how droplets shed from the bearing have a diameter considerably smaller than the typical CFD cell resolutions employed in a VOF approach. Here, the DPM approach becomes advantageous since these smaller diameter droplets can be tracked within a Lagrangian reference frame on a coarse computational grid, therefore presenting

considerable cost savings. On its own, when considering a bearing chamber investigation, not much can be achieved with a pure DPM approach, however it becomes considerably useful when coupled with other methodologies. A VOF approach, cannot feasibly capture these smaller droplets unless resolved on an extremely fine mesh which would present a considerable computational cost. Therefore to tackle this problem, as demonstrated by Adeniyi [94], the VOF model can be coupled with a Lagrangian DPM approach. The model developed by Adeniyi only permits a one-way coupling such that only DPM particles can be transferred into the VOF reference frame and not the other way. Within the model, Adeniyi included droplet effects such as splashing to produce secondary droplets and an inclusion for the impact of drag on particles. Testing of the DPM-VOF model was performed for the sump regions of a bearing chamber with a comparison to experimental measurements. For example, Figure 2.16 a) highlights the instantaneous droplet loading resulting from the DPM model and Figure 2.16 b) shows the subsequent film development produced by the VOF approach.

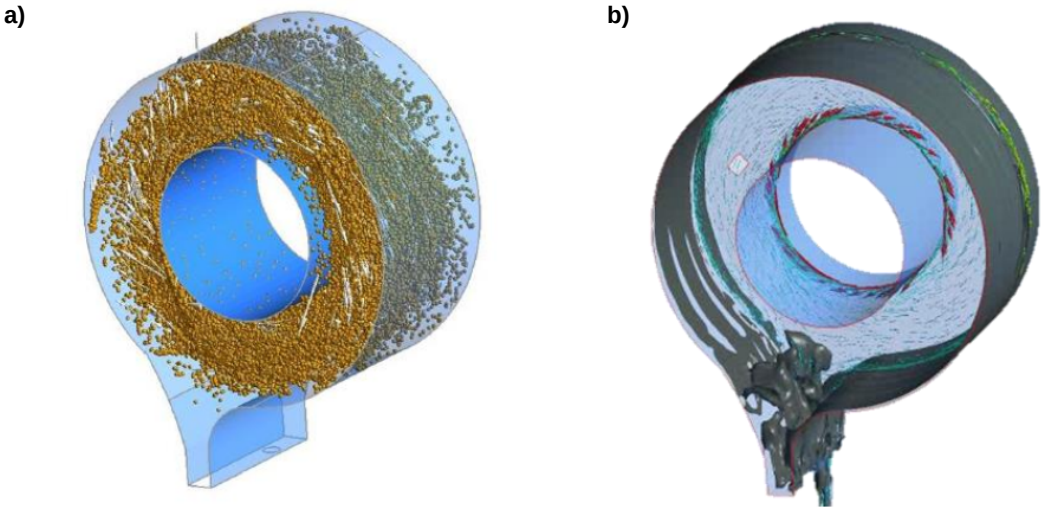


FIGURE 2.16: a) DROPLET LOADING AND b) FILM INTERFACE FOR THE INDY SUMP DPM-VOF SOLUTION [94]

Within the simulation, Adeniyi [94] used a DPM inlet boundary condition to introduce oil into the domain, subsequently, the oil is carried by the turbulent airflow and upon impingement on the static outer casing walls, the DPM particles form an oil film through transitioning to the VOF model. In general, compared to the experimental data, whilst good agreement was obtained for the film thickness distribution, the results tended to over-predict the film thickness. One of the reasons attributed to this, is that there is significant uncertainty surrounding the DPM inlet boundary condition. There is very limited experimental data quantifying the oil shed from the bearings in terms of both size and velocity distributions. To counter this, later VOF computational investigations by Adeniyi et al. [95, 96], aimed to develop a deeper understanding of the oil

exiting from a ball bearing configuration. However, there are still many significant challenges associated with quantifying the characteristics of droplets shed from a ball bearing and, in addition, there is a shear lack of experimental data to be used for validation. In general, Adeniyi et al. demonstrated that, within the bearing, the bulk of the oil is at approximately 30% of the shaft speed which is independent of the oil flow rate. Furthermore, the speed at which the oil exits the bearing, into the chamber, is directly proportional to the shaft speed. Across all shaft speeds and oil flow rates investigated, the oil exits into the chamber, at the edge of the cage, at about 10% of the shaft speed.

Outside of bearing chamber simulations the use of a VOF-DPM coupling is also of great significance for aeroengine combustion chambers as an example. For such applications, within OpenFOAM, Pringuey [97] successfully implemented a one-way VOF-DPM model, in order to achieve a more computationally efficient atomisation process. However, only recently within ANSYS Fluent, Dick et al. [98] presented a fully coupled DPM-VOF-DPM model, with an application to a simplified bearing chamber. The transition of DPM particles to the VOF regime is triggered when the size of a particle is larger than the cell volume or additionally, when the parcel reaches a certain proximity to either a wall or the gas-liquid interface. Conversely, the fluid within the VOF regime can be converted to a DPM particle when its volume drops below the volume of a cell or the asphericity of the fluid reaches a critical value. Similar to the work of Adeniyi [94], oil is introduced into the domain through a series of DPM injections. However, a very basic injection setup is used, whereby a cone injector periodically injects particles of a fixed 150μm diameter. Furthermore, within this injection, there is no consideration for either secondary breakup models or the effect of turbulence. Overall, Dick et al. report a good qualitative agreement in oil flow patterns but recommend further validation due to limited experimental data to quantitively compare to.

2.4.5 Coupled ETFM-DPM

One of the areas yet to be fully explored is the coupling of the ETFM with a DPM approach for bearing chamber applications. The previously discussed in-house thin film models developed by Farrall et al. [81] and Wang et al. [82] incorporated basic droplet impingement models to account for effects such as splashing and absorption. Improvements to the droplet impact model was made by Williams [99], who analysed the instability effects of momentum transfer to the film. For the bearing chamber applications, Farrall et al. [81] and Wang et al. [82] demonstrated that the films could be initialised using a DPM inlet boundary condition; for example, Farrall injects a Rosin-Rammler size distribution with a mean particle diameter of 480μm and a spread of 3. However, as previously discussed these early models were only successful for smooth flow solutions,

presenting significant numerical difficulties within the thin film modelling for the shock and pool regimes. Additionally, a full two-way ETFM-DPM coupling was not achieved.

Subsequent work by Farrall et al. [100] conducted a more specific DPM study into the effect of droplets on their initial injection conditions, for a simplified 2D bearing chamber. Farrall et al. report on the sensitivity of mean droplet diameters on the deposition characteristics, stating that as the mean droplet diameter reduces, less splashing is observed. As splashing increases, a greater number of secondary droplets are produced, these tend to become entrained within the gas flow leading to longer residence times and a reduced cooling efficiency. A study into varying the droplet radial velocity revealed a change in both the droplet speed and impact angle. This resulted in a greater amount of splashing as the radial velocity was increased.

Chen et al. [101] and the subsequent investigations by Sun et al. [102] also investigated the droplet interactions within an aeroengine bearing chamber environment, within ANSYS CFX. Using a droplet deformation model, the authors investigate the impingement and splash characteristics of particles at different rotational shaft speeds. The deformation of a droplet resulted in a more strongly curved trajectory and a reduced droplet velocity due to the higher drag force experienced. In addition, deformed droplets were more likely to splash. However, it should be noted that there was no validation carried out for the droplet deformation model implemented by Chen et al. To provide validation data, Sun et al. conducted experimental investigations on a simplified bearing chamber geometry. Comparison of results showed that the computational particle trajectories were able to exactly reproduce the determined experimental trajectories over a range of operating parameters. The results are surprising, since a very simplified point source DPM inlet boundary condition is used, and considerable uncertainty arises in the lack of initial conditions which are prescribed to the droplet. Overall, due to the very limited information presented, it is difficult to assess the reliability in the computational results presented by Sun et al.

Jingyu et al. [103] successfully demonstrated a fully coupled two-way ETFM-DPM model available within STAR-CD, which, included effects for both a film stripping and an edge separation criteria. Comparison was made to the available bearing chamber investigations of Gorse et al. [40], over realistic engine operating conditions ranging from 4,000 rpm to 16,000 rpm. For the computational simulations, the oil film is initialised using a DPM injection around the periphery of the rotating shaft. There is considerable uncertainty surrounding this injection mechanism implemented by Jingyu et al.; however, droplets are prescribed an initial velocity equivalent to half of the shaft speed, from which a Rosin-Rammler distribution is also derived. Comparison of film thickness measurements with the experimental results showed an excellent agreement across all of the rotational shaft speeds investigated. As the rotational shaft speed is increased, Jingyu et al. report a decrease in film thickness and, in turn, an increase in the film

velocity. As the oil flow rate is increased, the increased momentum of oil results in a reduced shearing air force, such that the oil film thickness subsequently increases. Additionally, Jingyu et al. [104] extended upon this original study and performed simulations using the ETFM-DPM approach for a representative aeroengine bearing chamber, comparing results against in-house experimental data. Experimental investigations were carried out on a rotating cylinder test rig fitted with an oil thrower, for relatively low shaft speeds of up to 3,600 rpm. Film thickness measurements were recorded experimentally at two angular locations on the outer cylinder wall. Here, across all of the rotational shaft speeds and oil flow rates, the computational results were able to accurately predict the film thicknesses, with percentage errors no greater than 10%. Similar to the previous study, an investigation into the effects of rotational shaft speed on oil film thickness was carried out, showing a trend of decreasing film thickness with an increase in shaft speed. Although, contrastingly, the results showed no significant effect on the film thickness when varying the volume flow rate of oil. Overall, these results of Jingyu et al., suggest that the ETFM present within STAR-CD is therefore able to accurately capture the shock and pool solution, which occur at these relatively low shaft speeds. Furthermore, at higher, more realistic engine operating speeds, the ETFM-DPM approach is able to accurately the capture trends of the oil film.

Within ANSYS Fluent, as the thin film model began to develop and became identified as a viable option again, the ETFM-DPM coupling was reconsidered. With an intent for bearing chamber applications, Hee et al. [105] demonstrated a two-way ETFM-DPM coupling for a liquid jet injected into a high velocity crossflow. A DPM cone nozzle injection is used to recreate the jet inlet boundary condition, these particles subsequently experience secondary breakup under the high velocity crossflow. The particles impinge on the lower surface forming a thin film, which thickens and grows toward an expansion edge, much like that of a backward facing step. Upon reaching the sharp edge, the momentum of the film causes it to separate over the surface. Additional effects are also observed, such as both splashing and stripping due to the high shearing gas forces. Hee et al. conducted a detailed parametric investigation in order to assess the effects of both DPM and ETFM configurations, in addition to changing the numerical settings. Hee et al. faced numerical difficulties in applying a stripping criteria and severe convergence stability issues were faced when an edge separation criteria was included. For the best-case scenario, Hee et al. reported an overall percentage error of 28.9% from the experimental data. For the DPM settings, a discrete random walk was determined necessary for accurate prediction of the particle trajectories, through including the effects of turbulence. Within the ETFM configuration, further numerical difficulties were faced through the inclusion of additional film source terms, such as the gas-film momentum coupling and the effects of surface tension. Overall, the results of Hee et al., suggest that further work is required in order to improve the ETFM-DPM coupling within ANSYS Fluent before moving toward an aeroengine bearing chamber simulation.

2.5 Summary of Literature Reviews

A literature review focusing on, but not limited to, bearing chambers investigations was carried out. In an effort to better understand the single-phase airflow field within an aeroengine bearing chamber, the initial focus was on Taylor-Couette flows. Whilst the typical rotational shaft speeds within a Taylor-Couette system are normally slower than that of a bearing chamber, a key understanding of the underlying flow physics can be obtained. Investigations into start-up procedures have demonstrated that the final state of the Taylor-Couette flow is highly dependent on the initial conditions. Based on these initial conditions, the total number of Taylor vortices that fill the domain can be changed. A summary of Taylor-Couette turbulence modelling approaches has revealed the possibility that the RSM may be the most adequate choice, although the results are still inconclusive. A limitation of most two-equation models is that the individual Reynolds stresses are not calculated and the three principal components ($\overline{u'u'}$, $\overline{v'v'}$ and $\overline{w'w'}$) are assumed equal: as such the turbulence is isotropic. The potential benefit of the RSM may be as a result of the ability to capture anisotropy due to resolving the individual stress components in the respective directions. Furthermore, to gain a closer insight into bearing chamber modelling, a review of short aspect ratio devices was conducted. Very limited information is available, in addition investigations into the turbulent regime are scarce. However, results suggest that there are no additional end effects that are induced within these short aspect ratio devices. This is supported by the review of single-phase experimental bearing chamber investigations, which show under a rotational speed driven mode, a singular pair of counter rotating Taylor vortices form. With the addition of a high sealing airflow rate, this Taylor vortex structure is lost.

Within a bearing chamber, when considering the highly complex two-phase environment, there are two main driving forces that determine the underlying flow physics. These forces arise from the rotation of the shaft, producing a shearing force and hence an interfacial shear stress; and secondly, from the force due to gravity. At low shaft speeds, the gravitational forces dominate over the shear forces, causing the film to accumulate as a pool toward the bottom of the chamber. Conversely, at higher shaft speeds, the shear force is able to overcome the gravitational forces resulting in a smooth, uniform distribution of the oil film around the chamber annulus. Investigations into rotating elements, such as the ball bearings, have revealed the generation of a dispersed phase consisting of either droplets, ligaments and/or sheets depending on the rotational shaft speed. This dispersed phase is transported by the turbulent airflow and subsequently impinges on the static outer casing walls, eventually forming a thin film.

Many numerical investigations have been carried out into bearing chamber flows. With the development of new techniques and improved modelling approaches, many significant challenges for bearing chamber applications have been overcome. In addition, as computational resources

have become more accessible, more complete bearing chamber simulations have been possible. These factors have given the opportunity for computational investigations to explore areas that are typically unfeasible experimentally and, therefore, provide new knowledge and understanding of the key flow physics. However, there is still considerable uncertainty surrounding some of these methodologies and further developments are required. To date, there are three main types of modelling approaches for aeroengine bearing chamber simulations; all of which have specific application within the bearing chamber, each providing unique and novel information. These are the coupling of VOF-ETFM, VOF-DPM and ETFM-DPM.

Chapter 3

Validation: Taylor-Couette Turbulence Modelling Study

This chapter considers the computational modelling of turbulent Taylor-Couette flows to better inform computational aeroengine bearing chamber applications. Within the Taylor-Couette system, a comparison of unsteady Reynolds averaged Navier-Stokes (URANS) turbulence models is made, for both axisymmetric and three-dimensional modelling within the commercial CFD code ANSYS Fluent. Additionally, due to the strong sensitivity of the Taylor-vortex structure on the start-up conditions, a study into sudden starts versus a steady acceleration procedure of the inner rotating cylinder is investigated. The developed Taylor-Couette turbulence modelling methodology is then extended to a bearing chamber geometry and evaluated for the single-phase airflow. Analysis of the secondary vortex flow field is compared both qualitatively and quantitatively to available experimental bearing chamber measurements. Based on the inferences of the Taylor-Couette study, the conclusions of the bearing chamber turbulence modelling methodology are assessed, and a recommended turbulence model is suggested for all future aeroengine bearing chamber modelling.

3.1 Introduction

The fundamental focus of the present investigation is concerned with the numerical modelling of turbulent Taylor-Couette flows. The Taylor-Couette system of interest for this paper involves the fluid flow confined between two concentric cylinders, for which the inner cylinder rotates, and the outer cylinder remains stationary. Within the field of engineering this type of Taylor-Couette flow is of great significance for industrial applications, especially within turbomachinery such as for bearing chambers [9, 33, 38, 40] and journal bearings [45].

Under single-phase conditions, an aeroengine bearing chamber, can be reduced to a Taylor-Couette system when simplified to a rotating inner shaft and a stationary outer cylinder. The single-phase experimental bearing chamber investigations of Gorse et al. [33] have revealed the significance of the shaft rotational speed on the secondary airflow field. Under low sealing airflow rates, the strong influence of the rotational shaft speed causes the secondary airflow structure, in the axial-radial plane, to form a pair of counter rotating Taylor vortices. This flow behaviour is referred to as the rotational speed driven mode (RSDM) and eventually transitions to a sealing air driven mode (SADM), when the bearing chamber sealing airflow rate is increased.

Inside a bearing chamber, the flow is characterised as turbulent with the high-speed shafts transferring momentum to the core airflow, as demonstrated by Gorse et al. [33]. The current best practice is to model turbulence quantities and account for turbulence effects using URANS based turbulence models. Considered as the state-of-the-art approach, the shear stress transport (SST) k-ω turbulence model has been widely used within bearing chambers [59, 60, 62–65, 67, 74, 84, 85, 90], demonstrating the ability to capture the large vortical and swirling structures which dominate the flow. However, previous bearing chamber computational investigations have also explored the capability of the k-ε model [66, 77, 78, 84, 100] and for either the re-normalisation group (RNG) variant [72, 75] or the alternative Realizable model [104]. In addition, several studies have been performed using the Reynolds stress model (RSM) [38, 39, 106]. In the literature, whilst there have been a wide range of URANS turbulence modelling applications, currently there is no systematic data available which benchmarks the performance of these different turbulence modelling approaches.

3.2 Objectives

The aim of the current chapter is to first perform a numerical comparison of both axisymmetric and three-dimensional URANS turbulence modelling approaches for the simulation of Taylor-Couette systems. An objective of the work is to therefore validate CFD results against experimental measurements and to provide best practice guidance for using conventional URANS schemes; including how geometrical and operational parameters influence turbulence within Taylor-Couette flows. The Taylor-Couette apparatus under investigation corresponds to the configuration employed by Wang [22]. Experimental measurements from the PIV data of Wang [22] and the hot-wire results of Smith and Townsend [13] are used for comparison.

Following the Taylor-Couette study, this modelling capability will be extended to a bearing chamber geometry, in order to improve understanding and establish a solid foundation for future aeroengine bearing chamber modelling. The bearing chamber geometry of Gorse et al. [33] is investigated and results are compared to the corresponding 3D LDA measurements.

3.3 Taylor-Couette Geometrical and Flow Field Parameters

The geometry, shown in Figure 3.1, represents the experimental apparatus used by Wang [22] which consists of two concentric cylinders with inner and outer radii of 0.0349m and 0.0476m respectively. This gives a radius ratio η of 0.718 resulting in a critical Reynolds number of Re_c = 83.6, for the onset of instability for Taylor-Couette flow; found through numerical calculation of the linear theory presented by Roberts [15]. The length of the cylinders is 0.432m, such that the aspect ratio of the apparatus is 34 based on the gap size of 0.0127m.

Wang focuses on only inner cylinder rotation, controlled through a precision motor. Through a specific start-up procedure, Wang ensures a fixed number of 14 Taylor vortex pairs formed at each rotation rate investigated. This was achieved through accelerating the inner cylinder from rest to a speed of 17.27 rad/s, at a constant angular acceleration of 0.0314 rad/s^2, then maintaining this speed until 14 stable Taylor vortex pairs form, excluding the end cells. Subsequently, the inner cylinder is then either accelerated or decelerated at a constant rate of 0.314 rad/s^2 and 0.126 rad/s^2 respectively, until the final desired state is reached. Wang maintained this final angular velocity for a short period of time before collecting PIV data. The measurements described were made for flow Reynolds numbers ranging from 335 to 18,392, corresponding to Reynolds number ratios, $R = Re/Re_c$, of 4 to 220; this covers the laminar TVF regime up to the weakly TTVF regime.

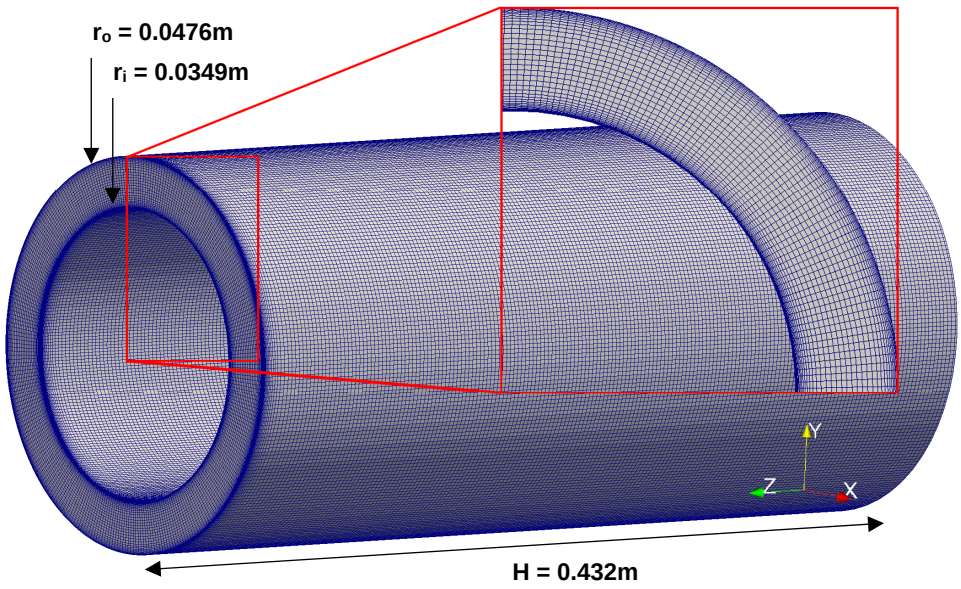


FIGURE 3.1: THREE-DIMENSIONAL COMPUTATIONAL MESH OF EXPERIMENTAL GEOMETRY

As demonstrated both by Coles [17] and Koschmieder [18], the final state of Taylor-Couette flow exhibits a strong dependence on starting conditions. In order to reproduce the experimental data

of Wang, it proved necessary to compile a user defined function (UDF) to exhibit the same start-up procedures used experimentally. A typical acceleration procedure obtained through the UDF is described below, the process can be split into four stages:

- Stage 1 – Acceleration at 3.14 rad/s^2 to $\Omega_i = 17.27$ rad/s
- Stage 2 – Maintain angular velocity till 14 Taylor vortex pairs form and stabilize
- Stage 3 – Accelerate at 3.14 rad/s^2 or decelerate at 0.126 rad/s^2 to the final desired speed
- Stage 4 – Maintain angular velocity till solution stabilizes

The time taken to ramp up to a shaft speed of 17.72 rad/s, as in stage 1, is the same for every simulation carried out, taking a flow time of 56.5s under a constant acceleration of 3.14 rad/s^2. However during stage 2, the time taken for the simulations to stabilize varies depending on a combination of the mesh density, turbulence model and parallel configurations; for example, some simulations required a flow time of greater than 600s to converge to the expected 14 Taylor vortex pairs.

3.4 Numerical Modelling

The finite volume incompressible solver, ANSYS Fluent 17.1, was used for all calculations presented within this chapter. There are several justifications for choosing ANSYS Fluent, predominantly due to the previous experience with the program and the prior knowledge within the Gas Turbine and Transmission Research Centre (G2TRC). However, from reviewing the literature it is also clear that significant developments to ANSYS Fluent have been made as a result of bearing chamber modelling. It is therefore unsurprising that within the literature reviewed, amongst authors, ANSYS Fluent has become the solver of choice for almost all of the numerical bearing chamber simulations undertaken. Therefore, a brief review of the main aspects of numerical modelling is presented, including an overview of the flow equations, as well as the discretisation and solution techniques available within ANSYS Fluent. Following this, the numerical settings implemented for the Taylor-Couette study is discussed, as well as the URANS turbulence modelling approach. A more detailed analysis of both the governing equations and numerical methods can be found in the work of Versteeg and Malalasekera [107], as well as the ANSYS theory guide [108].

3.4.1 Governing Equations

The governing equations that describe the flow of fluids can be summarised as follows:

- The fluid mass is conserved
- The rate of change of momentum of the fluid equals the total force acting on the fluid, i.e. the Navier-Stokes equations
- The change in energy of a fluid equals the sum of the heat flux and work done on it

These expression are known as the continuity, momentum, and energy equations. The following sub-sections provides a brief description of the continuity and momentum terms and their corresponding equations for a continuum fluid.

3.4.1.1 Continuity Equation

For a given control volume, the continuity equation defines that the rate of change of mass within the volume is equal to the overall mass flow.

$$\frac{\partial \rho}{\partial t} + \nabla \cdot (\rho \boldsymbol{u}) = 0 \tag{3.1}$$

Where, ρ is the fluid density and $\boldsymbol{u}$ is the flow velocity vector. The first term in Equation (3.1) represents the rate of change of density with time, whilst the second term describes the net mass flow rate across the fluid volume. Assuming incompressibility, Equation (3.1) becomes:

$$\nabla \cdot \mathbf{u} = 0 \tag{3.2}$$

3.4.1.2 Momentum Equation

Assuming incompressible flow, the conservation of momentum can be described by the following form of the Navier-Stokes equations:

$$\frac{\partial}{\partial t}(\rho \boldsymbol{u}) + \nabla \cdot (\rho \boldsymbol{u}\boldsymbol{u}) = -\nabla p + \nabla \cdot \mu[\nabla \boldsymbol{u} + (\nabla \boldsymbol{u})^{\mathrm{T}}] + \rho \boldsymbol{g} - \boldsymbol{F_s} + \boldsymbol{S_m} \tag{3.3}$$

The inertial terms on the left-hand side of Equation (3.3) represents the unsteady and convective acceleration per unit volume, respectively. This is balanced by the pressure term, $-\nabla p$; the viscous stress term $\nabla \cdot \mu[\nabla \boldsymbol{u} + (\nabla \boldsymbol{u})^{\mathrm{T}}]$; the gravitational, $p\boldsymbol{g}$, and surface tension, $-\boldsymbol{F_s}$, body forces; and finally any additional source terms which are represented by $\boldsymbol{S_m}$.

3.4.2 Discretisation and Solution Method

The governing equations represent a set on non-linear, second order partial differential equations and as such a discretisation procedure is required for their numerical solution. Consequently, within ANSYS Fluent, the Finite Volume Method (FVM) is used to divide the domain into multiple control volumes over which the Navier-Stokes equations are solved.

3.4.2.1 Spatial Discretisation

For each control volume, the information is stored within the cell centroid, for example, within Figure 3.2 this is situated the C_0 and C_1 positions. For a generic quantity, $\boldsymbol{\phi}$, the unsteady conservation equations are integrated over the volume, V, as follows:

$$\int_V \frac{\partial \rho \phi}{\partial t} dV + \oint_S \rho \phi \boldsymbol{u} \cdot \boldsymbol{dA} = \oint_S \Gamma_\phi \nabla \phi \cdot \boldsymbol{dA} + \int_V S_\phi dV \tag{3.4}$$

Here, S represents the control volume surface, Γ_ϕ is a diffusion coefficient, and $\boldsymbol{A}$ is the vector area. When discretised into a given control volume, of N faces, the transport equation becomes:

$$\frac{\partial \rho \phi}{\partial t} V + \sum_{f=1}^{N} \rho_f \phi_f \boldsymbol{u_f} \cdot \boldsymbol{A_f} = \sum_{f=1}^{N} \Gamma_\phi \nabla \phi_f \cdot \boldsymbol{A_f} + S_\phi V \tag{3.5}$$

Where ϕ_f is the value of ϕ convected across the face, f, and respectively $\nabla \phi_f$ is the gradient at the face. The mass flux through the face is captured by the $\rho_f \boldsymbol{u_f} \cdot \boldsymbol{A_f}$ expression. For a transient simulation, due to the time dependency of the first term within Equation (3.5), temporal discretisation is required. In general, there are a range of spatial discretisation schemes available, such as the central differencing scheme, first and second order upwinding schemes and other higher order schemes; a more comprehensive overview and the advantages of these schemes is covered by Versteeg and Malalasekera [107].

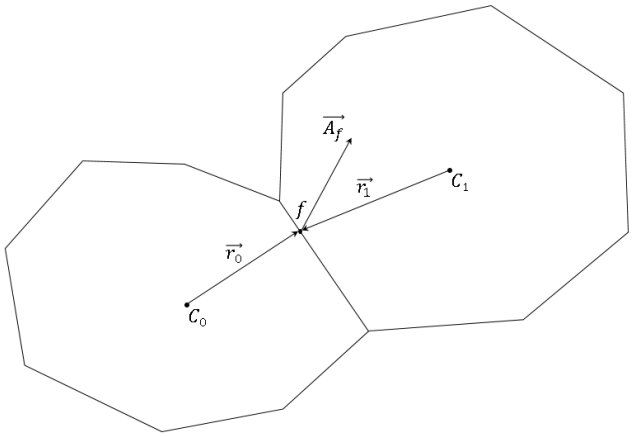


FIGURE 3.2: DISCRETISATION AND CONTROL VOLUME OF A 2D CELL [108]

3.4.2.2 Temporal Discretisation

For an unsteady, transient, simulation the time evolution of a transported quantity, ϕ, must be evaluated, therefore the partial differential equations must be temporally discretised. Considering the generic expression for the time evolution of the quantity, ϕ:

$$\frac{\partial \phi}{\partial t} = F(\phi) \tag{3.6}$$

Here, F, represents any spatial discretisation. As such, using a backwards-differencing scheme, the first order time discretisation becomes:

$$\frac{\phi^{n+1} - \phi^n}{\Delta t} = F(\phi) \tag{3.7}$$

Whereas the second order becomes:

$$\frac{3\phi^{n+1} - 4\phi^{n} + \phi^{n-1}}{2\Delta t} = F(\phi) \tag{3.8}$$

For Equations (3.7) and (3.8), $n+1$ represents the solution at the next timestep, whilst n is the current timestep and consequently, $n-1$, is the value at the previous timestep. To maintain stability, for all of the work carried out, only an implicit time stepping scheme is considered, as opposed to an explicit formulation.

To further ensure solution stability, for all cases, it is important that the chosen time-step satisfies the Courant-Friedrichs-Levy (CFL) condition, where:

$$CFL = \left|\frac{u.\Delta t}{\Delta x}\right| \tag{3.9}$$

The CFL condition is determined by mesh structure and fluid characteristics, giving the maximum permissible time-step for accurate results. As such for all simulations, the time-step was chosen to maintain a maximum Courant number of 1, as recommended by Fluent [108].

3.4.2.3 Solution Algorithms

In general, the numerical methods implemented in ANSYS Fluent can be separated into two categories. These consist of, a pressure-based approach, which is suited for incompressible flows and secondly, a density-based solver, to account for compressibility effects, typically found within high-speed flows. In both methods, the momentum equation is used to calculate the velocity field, however, between the two approaches, the pressure and density formulation differs. Within the density-based approach, the continuity equation is used to determine the density and subsequently, the equation of state provides the pressure field. However, within the pressure-based solver, since a constant density is assumed, a pressure correction equation is derived using the continuity and momentum equations. Overall, for both techniques, the solution procedure can be summarised as follows:

1. Discretise the fluid domain into a series of control volumes;
2. For each control volume, integrate the governing equations to generate a series of algebraic equations for the unknown variables (e.g. pressure, velocity…);
3. Solve iteratively and update variables until convergence.

In order to reach a solution, an iterative process is required due to the intricate coupling and non-linearity of the governing equations. As such, several different solution algorithms are available to solve the pressure-velocity coupling in either a segregated or a coupled manner. The segregated approaches include the SIMPLE, SIMPLEC and PISO algorithms, whereas the Coupled approach

links both the pressure and momentum equations. Typically, this often results in an increased computational effort and memory requirement but can lead to improved convergence rates compared to the segregated approaches. For all of the approaches, the iteration process requires under-relaxation to stabilise the calculation process. Figure 3.3 demonstrates an example of the SIMPLE pressure-velocity coupling method.

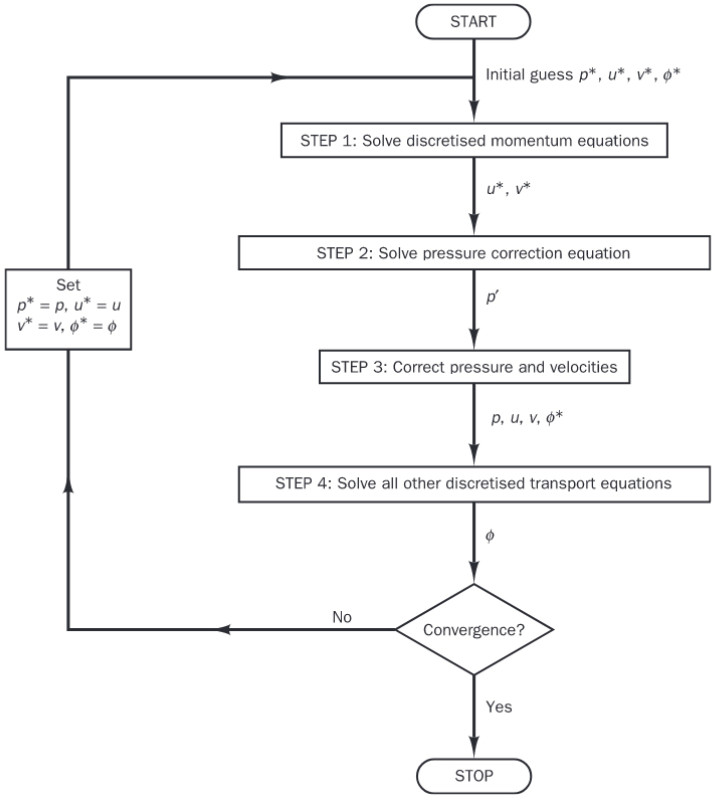


FIGURE 3.3: THE SIMPLE ALGORITHM, MODIFIED FROM [107]

3.4.2.4 Numerical Approach

Within the scope of the Taylor-Couette study, for the pressure-velocity coupling method, the Semi-Implicit Method for Pressure Linked Equations (SIMPLE) was chosen within the pressure-based solver. Within the SIMPLE algorithm, to ensure mass conservation, the velocity correction is explicitly solved whilst the pressure and momentum equations are implicitly solved. As such, to discretise the pressure equation, the PREssure STaggering Option (PRESTO!) discretisation scheme was chosen due to the nature of the problem and based on the Fluent recommendations for high speed rotating flows [108]. A second order upwinding scheme was chosen for both the turbulent quantities and momentum terms in order to provide a more accurate solution. Higher order schemes are available within Fluent, such as the QUICK or power law schemes [108], however, as shown in Figure 3.4, their application did not lead to any appreciable change in the

predicted shaft torque. Here, Figure 3.4 presents the convergence history of the non-dimensionalised torque, $G = M/(2\pi\rho\nu^2 H)$, for the PRESTO! pressure scheme, when varying the remaining turbulent and momentum discretisation schemes between 2nd order, power law and QUICK.

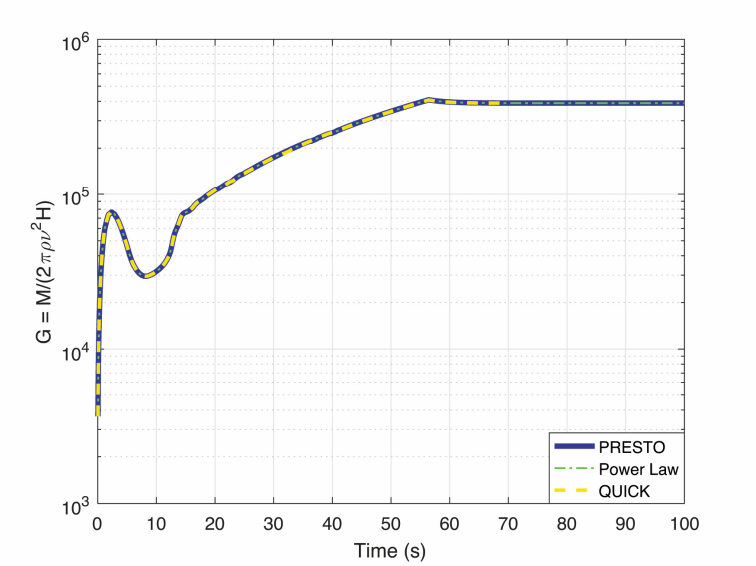


FIGURE 3.4: NON-DIMENSIONALISED SHAFT TORQUE CONVERGENCE HISTORY FOR THE SELECTED DISCRETISATION SCHEMES

For time discretisation, a bounded second order implicit temporal discretisation scheme [108] was chosen to improve the accuracy and stability of the solution. In general, the solver was implemented with double precision and Message Passing Interface (MPI) libraries were used for domain decomposition; most calculations used between 4 and 32 cores.

It should be noted that whilst the parallel configuration, such as partition method and number of CPU cores, affected the approach to the solution, after a sufficient period of time the long term solution was unaffected, resulting in the formation of 14 Taylor vortex pairs. This is shown in Figure 3.5, which shows the critical point for the formation of the Taylor vortex pairs, under the steady acceleration procedure, for a mesh partitioned with four cores. The vertical solid black lines represent the mesh partition lines.

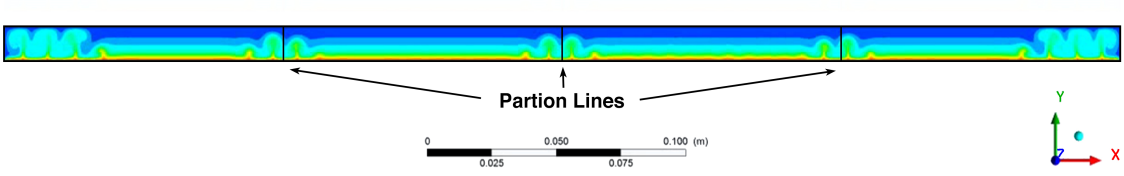


FIGURE 3.5: DEVELOPMENT OF TAYLOR VORTICES THROUGH THE STEADY ACCELERATION PROCEDURE WITH A MESH PARTITIONED FOR FOUR CORES

Within Figure 3.5, the first instabilities develop at the column ends and start to spread out towards the centre of the domain, forming the Taylor vortex pairs. However, the partition lines also act as a location for the instabilities to occur, causing the Taylor vortex development to spread throughout the domain. As such this affects the total number of Taylor vortex pairs that form throughout the domain, since as the number of partitions increases, the number of Taylor vortex pairs also artificially increases. Once the Taylor vortex pairs stabilize and are held at the desired rotational Reynolds number ratio, then gradually the solution converges to the correct number of Taylor vortex pairs and therefore the long-term solution is unaffected. As a result, there can be a significant increase in computational time to reach the desired number of Taylor vortex pairs, which therefore does not necessarily justify the use of a higher number of CPU cores.

3.4.3 URANS Turbulence Modelling

The focus of this current work is to evaluate the turbulence models available for the problem in consideration. Wang [22] concluded that the RSM with standard wall functions was the most suited to model the flow field. Whilst it was found that for low rotation rates, the RSM predicted the mean velocity field with a reasonable degree of accuracy, at higher shaft speeds, there were large discrepancies. For example, at $R = 220$, the maximum radial velocities were over predicted by as much as 40%. As such, various URANS models available within Fluent are investigated for modelling to assess the suitability for Taylor-Couette flow, these include: the standard, Realizable and RNG k-ε turbulence models; the standard, baseline (BSL) and SST k-ω turbulence models and either the linear or quadratic and stress-Omega or stress-BSL Reynolds stress models.

In general, within a fluid, as the Reynolds number is increased the flow undergoes a transition, after which turbulent flow exists. Typically, the turbulent flow is composed of time dependent, random fluctuating components superimposed on the mean flow; such that when the Navier-Stokes equations are time-averaged, extra terms appear called the Reynolds stresses. In total there are six independent Reynolds stress terms. These terms cannot be directly be solved, which results in a closure problem. Therefore, in order to close the set of governing equations, a turbulence modelling approach is subsequently implemented. Turbulence modelling aims to provide closure to these RANS equations through providing the remaining number of equations required and approximations for the unknown Reynolds stress terms. Experimental data within the turbulent regime is therefore essential for validating these turbulence modelling strategies due to the lack of a current exact solution. It is therefore important to evaluate the turbulence models available for the problem under consideration, since there is no single model that performs the best for all

applications. The following presents a review of the relevant turbulence models available within ANSYS Fluent.

The k-ε model is regarded as the simplest of the two-equation models, it is a semi-empirical model based on the equations for the transport of turbulence kinetic energy (k) and its dissipation rate (ε). The k-ε model has been implemented and validated for a wide range of turbulent flows showing good accuracy, robustness and computational cost, although for complex flows, including those with rotating flows, strong streamline curvature and severe adverse pressure gradients, the k-ε model can perform poorly. The RNG k-ε and the Realizable k-ε model have been shown to have improved accuracy over the standard k-ε model, without a significant increase in computational cost [108]. The RNG model includes the effect of swirl on turbulence and the accuracy for rapidly strained flows is improved through the addition of an extra term in the ε equation. The Realizable k-ε turbulence model includes a new transport equation for the dissipation rate (ε) and the turbulent viscosity has a new formulation that varies the C_μ coefficient. For the Realizable model, studies show an improved performance for rotating flows through including the mean rotation in the turbulent viscosity definition. One disadvantage of the all k-ε models is that the individual Reynolds stresses are not calculated and the three principal components ($\overline{u'u'}$, $\overline{v'v'}$ and $\overline{w'w'}$) are assumed equal: as such the turbulence is isotropic.

The next two-equation model is the k-ω model, which is an empirical model that incorporates low-Reynolds number effects and shear flow spreading; it is based on transport equations for the turbulence kinetic energy (k) and the specific dissipation rate (ω). In general, the k-ω model has been shown to have an improved performance for wall-bounded flows, in particular those with an adverse pressure gradient, when compared to more conventional models such as the k-ε model. Two additional variants of the k-ω model exist, the BSL k-ω model and the SST k-ω model. The standard k-ω model can exhibit a strong sensitivity to freestream conditions and, as such, the BSL k-ω model was developed, which blends the k-ω model in the near-wall region with the k-ε model in the free-stream. The SST k-ω model includes the improvements of the BSL k-ω model, however it also accounts for the transport of the turbulent shear stress. This results in a more robust formulation than the standard and BSL k-ω models, that is accurate and reliable for a wider class of problems compared to the standard k-ω model, especially for adverse pressure gradients and separating flow [108]. However, as a result, there is an increase in the computational cost associated with using either the BSL or SST k-ω models.

The Reynolds stress model solves a transport equation for each of the Reynolds stresses, in addition to an equation for the dissipation rate. Solving for each Reynolds stress has the advantage of being inherently anisotropic and therefore is more complex and computationally expensive compared to the k-ε and k-ω models. However, by relying on scale equations and underlying

assumptions associated with ε or ω equation modelling, the RSM can perform just as poorly as the k-ε or k-ω models [108]. Within Fluent, the default RSM is based on the ε-equation and uses either a linear or quadratic model for the pressure-strain term. The ω variants of the RSM both use a linear model for the pressure-strain term however, they solve the scale equation differently. The stress-Omega model is derived from the ω-equation, whereas the stress-BSL model solves the BSL k-ω scale equation, consequently removing the free-stream sensitivity found with the stress-Omega model. It is reported that both the ω-equation based RSM variants are advantageous for modelling flows over curved surfaces and those involving swirling flows [108].

3.4.4 Wall Function Approach

The presence of walls greatly influences turbulent flows. The no-slip condition imposed at the wall affects both the mean velocity field and the turbulence. As such, the fidelity of numerical solutions is greatly affected by the near-wall modelling approach and must be considered carefully. Within a fluid flow, the no-slip condition assumes that at a stationary wall, for a viscous fluid, the velocity will be zero normal to the boundary.

Experimentally, it has been shown that the near-wall region consists namely of three sublayers. At the wall, there exists a narrow laminar boundary layer due the flow satisfying the no-slip condition, this region is known as the viscous sub-layer. This layer is very thin with a non-dimensional wall distance spacing of y^+ less than 5, here the viscous effects greatly outweigh the turbulent effects. Newton's Law of Viscosity can be applied within the viscous sub-layer and when integrated a linear relationship is obtained between the velocity and the non-dimensional distance from the wall. In the outermost layer, there exists a turbulent boundary layer, known as the log-law layer where inertia effects begin to dominate, typically between $30 < y^+ < 500$. Within this layer, it can be assumed that the shear stress is equal to the shear stress at the wall. Between the viscous sub-layer and the log-law layer there is an interim region where the effects of turbulence and viscosity are equally important, this layer is referred to as the buffer layer.

A very fine mesh is required to resolve both the viscous sub-layer and log-law layer, which is not always feasible due to the large computational cost associated with such fine meshes. Instead, wall functions can be implemented, typically there are two main methods, either: a standard wall function approach or a two-layer enhanced wall treatment.

3.4.4.1 Standard Wall Functions

The standard wall function approach uses the logarithmic velocity profiles of the turbulent boundary layer. The viscosity affected near wall region is not resolved by the standard wall function approach, as such the first boundary cell must be well outside of the viscous sublayer. This means that the turbulence model requires no modification as a linear profile is assumed within the viscous sublayer, as such the computational cost is greatly reduced whilst still providing a robust and reasonably accurate solution. However, where low-Reynolds number effects are observed, the standard wall function approach is no longer valid.

In Fluent the log-law approach is implemented when the flow is turbulent, this is considered when the non-dimensional wall distance, y^+, is greater than 11.225, as such the turbulence model can be applied. When the non-dimensional wall distance is less than 11.225, a laminar stress-strain relationship is applied. Therefore, to implement the standard wall function approach suitably, the wall adjacent cell must have a y^+ larger than 11.225. In general, it is recommended to have a wall spacing of $30 < y^+ < 60$, with a few cells placed inside the boundary layer for the log-law to be valid. Where possible a large wall spacing, $y^+ > 100$, should be prevented to avoid limiting the number of nodes placed within the boundary layer.

3.4.4.2 Enhanced Wall Treatment

The Enhanced Wall Treatment (EWT) is an alternative near-wall modelling method that combines a two-layer approach suitable for finer meshes, $y^+ < 1$, with an enhanced wall function approach that is typical of coarser meshes. The domain is divided into either a viscosity affected region or a fully turbulent region. Within the fully turbulent region, the corresponding RSM or k-ε turbulence models are used. However, within the near-wall viscosity-affected region, a low Reynolds number one-equation k-ε model [108] is employed. To achieve this, the enhanced wall treatment subsequently uses a blending function, modified depending on the wall distance between these two layers. Within Fluent, for the EWT approach, it is recommended that the first wall cell to be placed at $y^+ = 1$, with at least 10 cells located in the near-wall region to produce accurate velocity and turbulent quantities. When a relatively large wall y^+ spacing is used with the EWT, the model acts like a standard wall function approach due to the nature of the blending function. Overall, for all ε-equation based turbulence modelling in this current chapter, the enhanced wall treatment approach is used.

3.4.4.3 Insensitive Near-Wall Treatment

In contrast to the standard ε-equation, it is possible to integrate the ω-equation through the viscous sub-layer without the necessity for a two-layer approach. Within Fluent this feature is the default for all ω-equation based models and is applied through blending the viscous sublayer with the logarithmic layer as a function of the y^+ spacing. Similar to the EWT approach, whilst not always necessary, it is still recommended that the first wall adjacent cell should be placed at $y^+ = 1$, with a minimum of at least 10 cells spanning the boundary layer.

3.5 Axisymmetric Configuration

The experimental apparatus of Wang [22], was modelled initially as an axisymmetric case within Fluent using a structured grid, based on the suggestions of the literature reviewed. The computational domain is enclosed within the stationary outer cylinder and end walls while the inner cylinder rotates; at the walls, a no-slip condition is applied. The CFD domain represents a 2D slice of the Taylor-Couette experimental geometry, which greatly reduces the computational cost. It is possible to reduce the axisymmetric computational expense even further by simulating only one Taylor vortex pair through applying either periodic or symmetry boundary conditions at either end of the domain. However, such an approach dictates the size of the Taylor vortex pair based on the domain length. Instead, Wang adopted a different method whereby one quarter of the domain was modelled, incorporating one end wall and a symmetry boundary, resulting in the formation of only 3.5 Taylor vortex pairs. Despite this, as the Reynolds number was increased further, the number of vortex pairs varied such that Wang had to optimise the axial length for each rotational speed investigated. In this study, initial simulations showed that, whilst the domain maintains central symmetry, i.e. at a point along half the length of the cylinder, a $H/2$ domain with a symmetric condition cannot be used. Imposing a symmetric boundary at $H/2$ is not valid if the symmetry condition cuts a single Taylor vortex in half. With the steady acceleration procedure, the shaft is accelerated to 17.27 rad/s, after which the speed is maintained until 14 stable Taylor vortex pairs form. Typically, more than 14 Taylor vortex pairs first form and, after maintaining this speed, this number converges down to a fixed state of 14 Taylor vortex pairs. The use of a symmetry condition fixes the position of Taylor vortices and therefore does not allow the vortices to reduce in number, to converge down to 14 pairs. It is clear that to eliminate these uncertainties it is necessary to model the full length of the computational domain, in order to incorporate end effects and achieve the final desired state of 14 Taylor vortex pairs.

Ansys ICEM software was used to generate all of the grids in the present study. For simplicity, initial computational modelling is two-dimensional where an axisymmetric grid is used. Table 3.1 summarises the grid configurations explored in the subsequent mesh sensitivity study.

TABLE 3.1: AXISYMMETRIC GRIDS FOR MESH INDEPENDENCE STUDY

Mesh	*Grid (Radial × Axial)*	*Number of cells*	y^+ *values*
A	20 × 680	13,600	$5 < y^+ < 15$
B	40 × 1050	42,000	$1 < y^+ < 10$
C	40 × 1050	42,000	$y^+ \leq 1$
D	75 × 2100	157,500	$y^+ \leq 1$
E	110 × 3150	346,500	$y^+ \leq 1$

CFD predictions are compared to the mean axial and radial velocities from the experimental data of Wang [22], initially at a rotational Reynolds number ratio of $R = 100$. It is also essential to ensure that the number of vortex pairs obtained computationally is the same as found experimentally by Wang, which excluding end cells is observed to be 14. This means that the same experimental conditions must be reproduced, specifically the start-up procedure outlined by Wang. This is achieved through the UDF introduced in Section 3.3.

The mesh dependency tests showed that with the k-ω turbulence model, it was significantly more difficult to reach a mesh independent solution when compared to the k-ε turbulence model. The k-ω model not only required a finer mesh than the k-ε model, but also required a computational runtime of approximately four times longer to reach a converged state of 14 stable Taylor vortex pairs. This suggests that the formation of Taylor vortex pairs may exhibit a strong dependence on the core flow, to which the k-ω model has been shown to be more sensitive [108].

Whilst a fully mesh independent solution was not reached for all simulations, it was judged that sufficiently low mesh dependence was achieved for the purpose of this study. Table 3.2 presents the computed non-dimensionalised shaft torque, $G = M/(2\pi\rho\nu^2 H)$, and gauge static pressure at $H/2$ on the outer cylinder wall, which are used to assess mesh independence for both the standard k-ε and k-ω turbulence models. For all further investigations using ε-equation based turbulence models, Mesh C was selected since there was a negligible difference of $< 1\%$ between the respective torque and pressure values for Meshes C and D. Similarly, for the ω-equation based turbulence models, there was a difference of $< 1\%$ between Meshes D and E, suggesting that Mesh D provided an adequate solution and was therefore chosen for all further investigations using ω-equation based turbulence modelling strategies.

TABLE 3.2: AXISYMMETRIC MESH INDEPENDENCE STUDY RESULTS FOR THE STANDARD k-ε AND STANDARD k-ω TURBULENCE MODELS

Mesh	*Standard k-ε*		*Standard k-ω*	
	G $(\times 10^5)$	*Static Pressure (Pa)*	G $(\times 10^5)$	*Static Pressure (Pa)*
A	4.930	29.19	6.219	38.19
B	4.065	27.24	4.997	38.21
C	3.892	26.88	4.926	40.26
D	3.893	26.95	4.901	40.70
E	3.893	26.96	4.861	41.64

3.5.1 Axisymmetric Results

Axisymmetric CFD results are compared to the axial and radial velocity profiles of Wang [22] in addition to the velocity magnitude profiles of Smith and Townsend [13]. These experimental studies are discussed within Section 2.2.1.1 of the literature review, and in Section 2.2.2, the corresponding computational results of Wang are assessed. For all simulations, results were time-averaged over a duration of at least six inner cylinder rotations.

3.5.1.1 Start-up Procedure

To begin with, the sensitivity of the solution to start-up conditions was investigated computationally through comparing Taylor vortex axial wavelengths with that observed experimentally by Wang [22]. The developed start-up UDF was compiled and linked within Fluent for both the k-ε and k-ω models over the range of rotational Reynolds number ratios considered experimentally by Wang [22]. This was to assess the influence of sudden start accelerations of the inner cylinder compared to the steady acceleration procedure outlined by Wang, as described in Section 3.3.

Figure 3.6 shows a comparison of the different non-dimensional wavelengths obtained for the rotational Reynolds number ratios ranging from 4 to 220. The wavelength is defined as the axial extent of one Taylor vortex pair and this is non-dimensionalised by the gap width. The black dashed line shows the wavelength extrapolated from the experimental data of Wang, for which the non-dimensional wavelength varied from 2.268 to 2.284 resulting in a total number of 14 Taylor vortex pairs.

The average wavelength recorded for sudden start cases is displayed, with the red circles representing the standard k-ε turbulence model and the k-ω turbulence model shown with blue squares. For each data set, the error bars represent the standard deviation in the axial wavelength. Immediately, it is clear that there is a significant difference in wavelength obtained based on the turbulence model used. In general, the k-ω turbulence model produced Taylor vortices with a larger average wavelength than the PIV data, meaning that the number of vortex pairs was less than the desired value of 14. For example, at $R = 55$, there were in total 12 Taylor vortex pairs and this decreased to 7 pairs at $R = 220$. In contrast, the k-ε turbulence model produced a uniform but shorter wavelength over all of the rotational Reynolds number ratios, resulting in 15 Taylor vortex pairs.

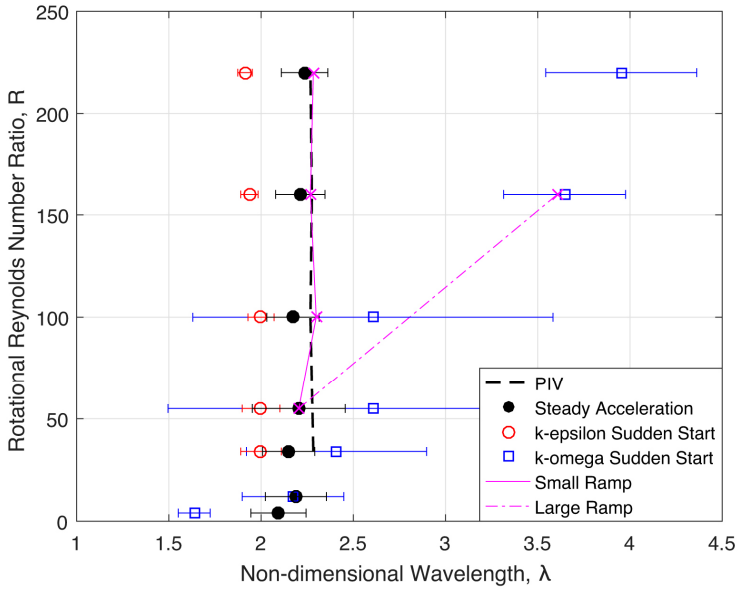


FIGURE 3.6: AXIAL WAVELENGTHS FOR SUDDEN START AND STEADY ACCELERATION PROCEDURES

The simulations carried out under the steady acceleration procedure, depicted by the solid black circles, were carried out for both the k-ε and k-ω models. Between the two models there was a negligible difference in results, hence only the results from the k-ω model are shown in Figure 3.6. At all of the rotation rates investigated, 14 Taylor vortex pairs were formed following the steady acceleration period. Furthermore, the PIV data of Wang falls within the standard deviations for all cases, resulting in a percentage error in average wavelengths of 1.4% - 5.9%; with the greatest difference occurring at the slowest speed for $R = 34$. Interestingly, as the rotational Reynolds number ratio is increased, the difference in average wavelengths between the PIV and steady acceleration data decreases and at $R = 220$, the percentage error is only 1.4%. The results of the steady acceleration procedure are in agreement with the experimental data of Koschmieder [18] produced for the wide-gap apparatus.

Figure 3.6 also shows a comparison of the non-dimensional axial wavelength following either a small or large step in the rotation rate of the inner cylinder once the 14 Taylor vortex pairs have first formed and stabilised at $R = 55$. For the small step in rotation rate (solid line), the rotational Reynolds number was increased in steps from $R = 55 \rightarrow 100 \rightarrow 160 \rightarrow 220$; whereas the large step in rotation rate (dashed-dot line) was increased in a step from $R = 55 \rightarrow 160$. For a large step in the inner cylinder speed, the average wavelength obtained was 3.606, which is much larger than that experimentally, resulting in the formation of only 10 Taylor vortex pairs and therefore closely resembling the result obtained after a sudden start to $R = 160$. In contrast, for a small step in the inner cylinder speed, there is much less variation in the wavelength obtained

compared to the steady acceleration procedure. Furthermore, following a small step, the axial wavelength approaches the experimental results of Wang resulting in a percentage error of wavelengths ranging from 0.5% - 1.4%. These results support the findings of Koschmieder [18], showing that once the Taylor vortex pairs are established, they are very stable to small steps in the rotational Reynolds number ratio, as opposed to a large step.

Overall, these results show that by using an appropriate start-up approach, it is possible to obtain good agreement with the number of Taylor cells, compared to the experimental data of both Wang and Koschmieder for wide-gap geometries. This gives confidence in the steady acceleration procedure employed computationally, showing that it is possible to achieve the same time-averaged number of Taylor vortices reported in the experiment within the TTVF regime.

3.5.1.2 URANS Turbulence Modelling

The turbulence models described in Section 3.4.3 are evaluated against the PIV velocity profiles of Wang, including comparison of both maximum and minimum radial velocities. The aim of this study is to determine the most appropriate turbulence modelling strategy applicable to a rotating Taylor-Couette geometry.

The computational results of Wang suggest that depending on the rotation rate, a number of different turbulence models are satisfactory to model the flow field, with the RSM giving the best agreement. However, within the turbulent Taylor vortex flow regime, the RSM over-predicted results by as much as 40%. Furthermore, Wang's results were not mesh independent and a new mesh was generated at each different rotational Reynolds number investigated. In addition to this, Wang provides very limited details of the numerical investigation and based on the literature surveyed, there is inconclusive evidence as to which turbulence model yields the most satisfactory results. Hence within this section, a more systematic study into turbulence modelling is conducted.

Firstly, the results from the turbulence models at $R = 100$ are compared to radial PIV velocity profiles of Wang; measurements are taken along an axial line placed at one third of the gap width, when positioned from the inner cylinder. Out of all of the turbulence models investigated, it was found that both the standard k-ω and RSM stress-BSL models gave the closest agreement to the experimental data. A sample of the results obtained is provided in Figure 3.7, showing a comparison of the radial velocity profile predicted by these two turbulence models. Additionally, the predictions of the standard k-ε turbulence model are also included for reference within Figure 3.7.

Furthermore, Table 3.3 highlights the corresponding percentage error at $R = 100$, compared to the experimental results of Wang, in the average Taylor vortex inflow (negative u_r) and outflow (positive u_r) boundaries across all of the turbulence models investigated. A Taylor vortex inflow boundary occurs where fluid is convected radially inward between a pair of Taylor vortices, the opposite is true for the outflow Taylor vortex boundary. Additionally, within Table 3.3, the percentage error between the average Taylor-vortex wavelengths predicted computationally versus that measured experimentally is also shown.

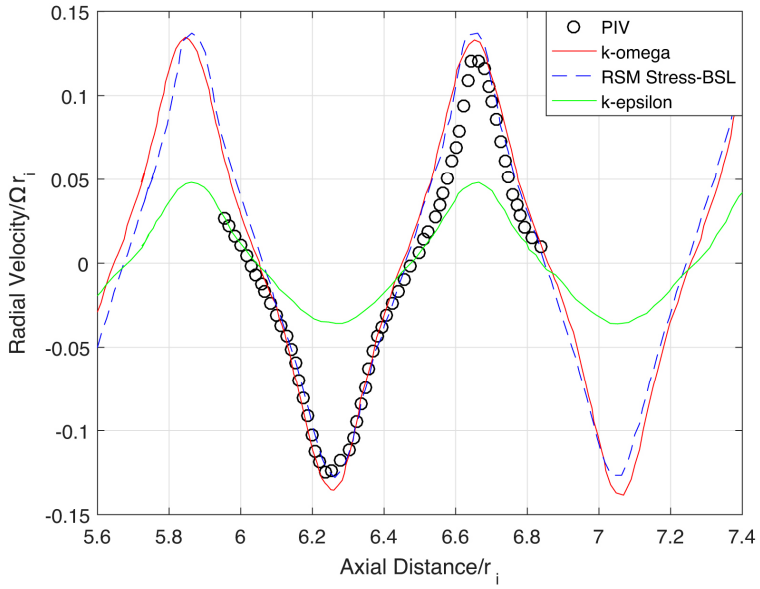


FIGURE 3.7: COMPARISON OF RADIAL VELOCITY PROFILES AT r = 3.94cm AND R = 100

TABLE 3.3: PERCENTAGE ERROR IN BOTH AVERAGE RADIAL VELOCITY AND WAVELENGTH ACROSS TAYLOR VORTEX COMPARED TO WANG [22] AT R =100

Turbulence Model	*Inflow v_r*	*Outflow v_r*	*Wavelength*
Standard k-ϵ	59.1	36.6	3.6
RNG k-ϵ	55.0	28.6	3.6
Realizable k-ϵ	61.9	40.1	3.6
Standard k-ω	8.4	10.8	2.4
BSL k-ω	10.4	12.2	5.1
SST k-ω	9.5	11.6	4.8
RSM	69.9	57.8	4.8
RSM Stress-Omega	6.0	14.5	6.9
RSM Stress-BSL	2.3	13.9	3.3

Results obtained for the standard, RNG and Realizable k-ε turbulence models showed a significant deviation from the PIV measurements of Wang in terms of radial velocities. There was very little deviation in results across the ε-based turbulence models, however whilst these models all predicted a similar radial velocity profile, the peak values differed by as much as 60% from the experimental measurements, as shown in Table 3.3, and by the standard k-ε turbulence model in Figure 3.7. Overall, from the investigation into ε-equation based turbulence modelling, it was clear that the none of the models investigated produced satisfactory results.

In contrast, the standard, BSL and SST k-ω turbulence models all produced a much closer agreement with the experimental data, however the standard k-ω turbulence model provided the most accurate results for the radial velocity profile, evident from Table 3.3. The BSL and SST k-ω models produced reasonable agreements compared to the standard k-ω model, although as highlighted in Table 3.3, the axial wavelength of the Taylor vortex pairs was slightly worse, here, over-predicting by approximately 5%, resulting in smaller end cells for these two models.

An investigation into the RSM variants was also carried out. The standard RSM, which relies on the underlying assumptions associated with ε-equation modelling, was found to be inappropriate in predicting the flow field for the radial velocity profile, with results similar to those produced by the standard k-ε model, shown in Table 3.3. Interestingly, the quadratic-pressure strain model failed to produce any Taylor vortex structure over the whole range of rotational Reynolds number ratios investigated. However, the ω-based variants of the RSM showed significant improvements, with the best results obtained using the RSM stress-BSL model, as opposed to the RSM stress-Omega variant, which in relative comparison, over-predicted the average Taylor vortex axial wavelength, Table 3.3.

From the turbulence modelling study carried out, based on the results achieved, the subsequent investigations used both the standard k-ω and RSM stress-BSL turbulence models. To assess their suitability, further comparison is made to the experimental data of Wang over the full range of rotational Reynolds numbers investigated, from $R = 34$ to $R = 220$.

As the rotational Reynolds number is increased, the differences between the computational and experimental results start to become apparent. This is evident from Figure 3.8 which shows the radial velocity profile comparison at $R = 220$. Here, both the standard k-ω and the RSM stress-BSL turbulence models over predict the inflow (negative u_r) and outflow (positive u_r) Taylor vortex boundaries, resulting in differences as large as 70%. From Figure 3.8, it can be seen that the standard k-ω model provides a slightly closer fit to the experimental data, with the RSM stress-BSL predicting a similar transition across the inflow to outflow Taylor vortex boundary.

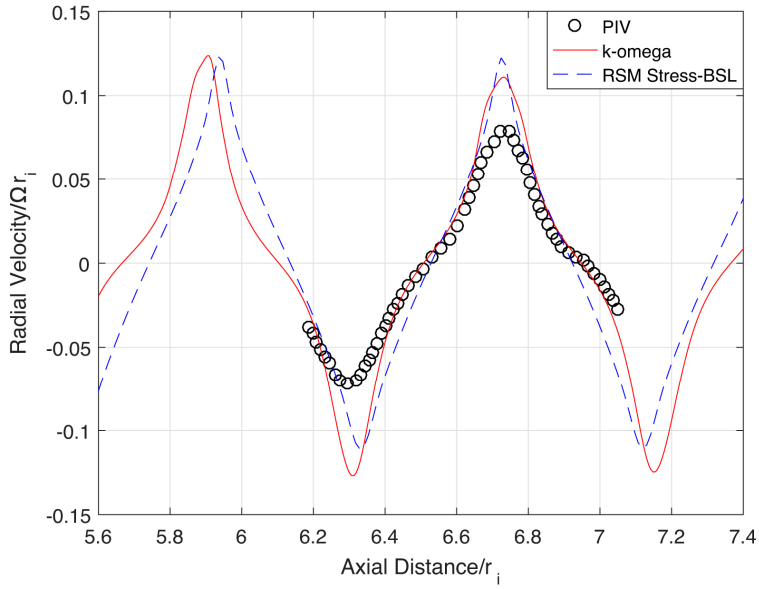


FIGURE 3.8: COMPARISON OF RADIAL VELOCITY PROFILES AT r = 3.94cm AND *R* = 220

Table 3.4 summarises the percentage error in the maximum inflow and outflow velocities, averaged over all of the 14 Taylor vortex pairs, for each rotational Reynolds number ratio investigated. As the rotational Reynolds number ratio is increased, it is clear that the percentage error from the experimental data rapidly increases for both turbulence models, becoming very large at $R = 220$.

TABLE 3.4: PERCENTAGE ERRORS IN INFLOW AND OUTFLOW TAYLOR VORTEX BOUNDARIES FOR THE TWO TURBULENCE MODELS

	Standard k-ω		***RSM Stress-BSL***	
R	***Inflow u_r***	***Outflow u_r***	***Inflow u_r***	***Outflow u_r***
34	2.9	32.2	2.0	28.7
100	8.4	10.8	2.3	13.9
160	22.2	13.3	31.0	31.4
220	70.1	54.3	55.0	71.1

Further comparison can be made using the experimental hot-wire data of Smith and Townsend [13] who investigated a radius ratio $\eta = 0.667$ over the rotational Reynolds number ratios of $R = 95$ to $R = 1350$. This is similar to the experimental investigations of Wang who considered a device radius ratio of $\eta = 0.718$ for $R = 4$ to $R = 220$. Figure 3.9 shows the velocity magnitude profile radially across the annular gap, non-dimensionalised by the inner cylinder

velocity, for the both k-ω and RSM stress-BSL turbulence models at $R = 220$. This is compared to the available data presented by Smith and Townsend at the equivalent Reynolds number ratio of $R = 225$. The velocity magnitude profiles are averaged over the central Taylor vortex pair, since within the experiments of Smith and Townsend, a slow axial flow was induced to traverse the stationary Taylor vortices over the stationary hot-wire anemometers.

From Figure 3.9, it is clear that there is a significant difference between the two turbulence models. The standard k-ω model provides a closer agreement to the experimental data compared with the RSM stress-BSL, which predicts a lower core velocity across the gap. Smith and Townsend report that at the non-dimensional distance of 0.581 the non-dimensional velocity was nearly independent of the rotation rate with a value of 0.390 ± 0.001, across the whole data range. This location corresponds to the Taylor vortex centre, which within the TTVF regime has a fixed location. At the Taylor vortex centres, both radial and axial velocity contributions become zero resulting in only an azimuthal velocity contribution. For the k-ω turbulence model, Table 3.5 summarises the computed non-dimensional velocity magnitude at this location proposed by Smith and Townsend. The results show that the non-dimensional velocity was nearly independent of the shaft speed over the range of rotation rates investigated. For $R = 220$ and within Figure 3.9, at this non-dimensional distance, the standard k-ω model predicts a value of 0.401 compared to the RSM stress-BSL prediction of 0.332, which is significantly lower than expected. Overall, this give a percentage error from the value reported by Smith and Townsend of 2.8% and 14.9% respectively.

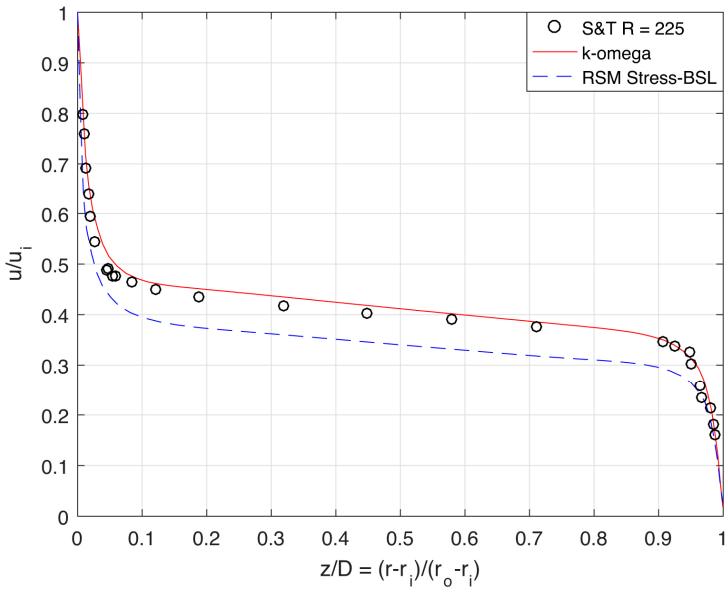


FIGURE 3.9: COMPARISON OF NON-DIMENSIONALISED VELOCITY MAGNITUDE PROFILES ACROSS THE ANNULAR GAP AT *R* = 220

TABLE 3.5: NON-DIMENSIONAL VELOCITY MAGNITUDE AT NON-DIMENSIONAL DISTANCE OF 0.581 FOR THE STANDARD k-ω TURBULENCE MODEL

R	***55***	***100***	***160***	***220***
u_{mag}/u_i	0.389	0.393	0.395	0.401

In conclusion, the axisymmetric URANS turbulence modelling study has shown the standard k-ω model provides satisfactory results and is able to capture the key characteristics of the flow; although at large Reynolds number ratios, this agreement is poor in terms of both maximum and minimum radial velocities. The RSM stress-BSL model provides comparable results to the standard k-ω turbulence model, although at a significant increase in computational cost. However, again, as the rotational Reynolds number is increased poor agreement is found, suggesting that an axisymmetric approach is unsuitable. It is suspected that the axisymmetric modelling methodology starts to break-down, as a result of not being able to predict the three-dimensional structures typically found within turbulent Taylor-Couette flows, such as Görtler vortices [13, 19, 30, 31] present within the boundary layers; as opposed to the lack of capability within the turbulence models. As such, subsequent modelling will apply the axisymmetric methodology developed to a three-dimensional domain for both the standard k-ω and RSM stress-BSL turbulence models.

3.6 Three-Dimensional Configuration

Following the results of the axisymmetric URANS study, the start-up procedures and turbulence models used are applied to a three-dimensional geometry. From the axisymmetric simulations, it has been observed that there are a number of three-dimensional effects that may be suppressed by axisymmetric modelling. As such, it is still unclear whether the axisymmetric turbulence modelling approach is still applicable when applied to three-dimensional modelling.

For 3D Taylor-Couette simulations, Brauckmann and Eckhardt [109] showed simulation complexity could be heavily reduced through applying both axial and rotational periodicity. Brauckmann and Eckhardt demonstrated that in general, the modelled geometry could be heavily simplified through, firstly, using axial periodicity to simulate only one Taylor vortex pair and secondly, by applying rotational periodicity. However, more recently, the DNS study carried out by Ostilla-Mónico et al. [110] suggest that both axial and rotational periodicity imposes constraints on the flow field, which despite generating accurate velocity data, can affect the overall bulk statistics. The results from Ostilla-Mónico et al. did not reach an independent solution and recommendations were made to determine the extent to which the domain can be limited in order to produce accurate velocity and pressure fluctuation statistics, as well as higher order moments. The results from the 2D axisymmetric case study suggest that to achieve accurate velocity and turbulence data, the whole domain may need to be modelled. This will be investigated by carrying out a study into applying both rotational periodicity, as well as modelling the whole three-dimensional domain; comparing results to the available experimental data.

Similar to the axisymmetric URANS study, a three-dimensional mesh independence study was first carried out. Whilst Mesh D was chosen to be appropriate for the axisymmetric modelling, the coarser mesh, Mesh C was chosen as a guideline for the three-dimensional modelling. To start with, the radial and axial grid spacing of Mesh C was transformed through 360° about the axis of rotation, resulting in a mesh of 1.7 million cells. Through removing the axisymmetric assumption, it is deemed appropriate to start the three-dimensional meshing from a coarser grid and subsequently refine the mesh until a mesh independent solution is achieved. Although a fully mesh independent solution was not obtained, through monitoring torque values and static pressure on the outer cylinder wall, a relatively low mesh dependence was observed. A final mesh containing 4.8 million cells with a wall spacing of $y^+ \leq 1$ and a growth ratio of 1.2 was deemed adequate; resulting in a difference of less than 2% in computed torque values. This mesh is depicted in Figure 3.10, for which Table 3.6 presents the computed non-dimensionalised shaft torque, G, and static pressure at H/2 on the outer cylinder wall at $R = 220$, which was used to assess mesh independence.

TABLE 3.6: THREE-DIMENSIONAL MESH INDEPENDENCE STUDY FOR THE STANDARD k-ω TURBULENCE MODEL

Mesh	*Number of Cells (million)*	*G* $(\times 10^6)$	*Static Pressure (Pa)*
F	1.7	3.538	310.21
G	2.9	3.452	372.76
H	4.8	3.386	374.12

3.6.1 Three-Dimensional Results

Within a fully developed turbulent flow, the turbulent structures and generating processes are inherently three-dimensional. Therefore, it is important to re-assess if the conclusions drawn from the URANS axisymmetric turbulence modelling study still remain valid. As such, a turbulence modelling study was performed for the three-dimensional configuration.

Within the three-dimensional domain, unlike the axisymmetric case study, all of the ε-equation based turbulence models severely over-predicted the radial velocity profiles, with maximum radial velocities over-predicted by as much as 85%. Figure 3.10 shows an example of the k-ε turbulence model compared against the PIV data of Wang [22] at $R = 220$. In contrast, good agreement was still found for the ω-equation turbulence models, suggesting that the inferences on model effectiveness from the axisymmetric simulations remained valid. As such, for the three-dimensional simulations, the numerical modelling strategy outlined previously was carried forwards for both the standard k-ω and RSM stress-BSL turbulence models. Similarly, for both turbulence models, results were time-averaged over a minimum of six inner cylinder rotations.

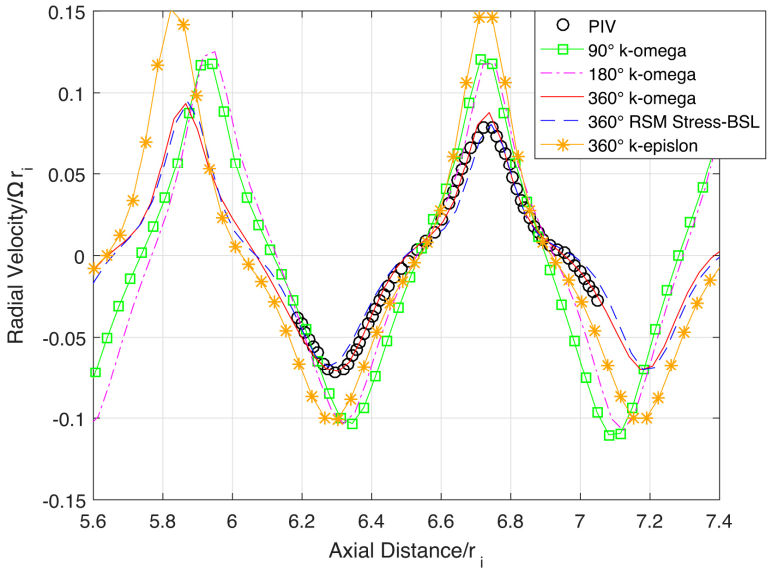


FIGURE 3.10: COMPARISON OF RADIAL VELOCITY PROFILES AT r = 3.94cm AND *R* = 220

3.6.1.1 Start-up Procedure

The results obtained from the axisymmetric investigation into the start-up procedure were also investigated for the three-dimensional configuration. The start-up procedure remained accurate for three-dimensional simulations and as such a new custom UDF was developed and linked within Fluent. This new UDF included the previous steady acceleration to $R = 55$, which is the point at which 14 Taylor vortex pairs form and stabilise, after which the UDF was optimised to incorporate small steps in the inner cylinder speed. These varied the inner cylinder speed in steps from $R = 55 \rightarrow 110 \rightarrow 165 \rightarrow 220$. At each step of the inner cylinder speed, in addition to verifying the 14 Taylor vortex pairs, several parameters were monitored for convergence including: the residuals, each velocity component, and the turbulent kinetic energy. Typically, after six revolutions of the inner cylinder the monitors had converged.

The purpose of modifying the UDF was to remove the substantial computational cost associated with slowly accelerating from $R = 55$ to $R = 220$, and therefore, significantly reducing the computational runtime required for three-dimensional simulations. This resulted in reducing the computational cost of simulations by as much as 20% and 25% for the standard k-ω and RSM stress-BSL turbulence models respectively.

3.6.1.2 Rotational-Periodicity Study

In order to see if the computational cost associated with the three-dimensional simulations could be reduced further, a study into applying rotational periodicity was carried out. Brauckmann and Eckhardt [109] suggest that for a DNS approach, a rotational periodicity of 60° provides accurate results; however, with a geometry of η = 0.714, Brauckmann and Eckhardt were also successful in applying a rotational periodicity as small as 40°. However, it should be noted that in their DNS study, Brauckmann and Eckhardt simulate only one Taylor vortex pair through the use of axial periodicity. As a result, for the current computational investigation, three new geometries were generated from the full three-dimensional mesh, resulting in the periodic segments of: 45°, 90° and 180°. However, the use of either axial periodicity or a symmetry boundary condition in the axial direction is not investigated, based on the conclusions drawn from the axisymmetric study; therefore, whilst rotational periodicity is applied, the whole length of the domain is still modelled. The new optimised UDF was used for all of the periodic meshes in order to reach a rotational Reynolds number ratio of $R = 220$, for both the standard k-ω and RSM stress-BSL turbulence models. Subsequently, the results are compared to the radial velocity profiles presented by Wang, in addition to the experimental velocity measurements of Smith and Townsend [13].

A sample of the results is shown in Figure 3.10; only the results obtained with the standard k-ω turbulence model for the 90° and 180° meshes are shown, since there was a negligible difference compared to the RSM stress-BSL predications. Results are not shown for the simulations carried out using the 45° mesh. At 45°, once the rotational Reynolds number ratio of $R = 55$ was reached, the simulation converged to a fixed state of 17 Taylor vortex pairs for both turbulence models, even after maintaining this velocity for a prolonged period of time; i.e. the required final state of 14 Taylor vortex pairs was never reached. As such, further investigations into the 45° mesh were not carried out.

In addition to this, similar problems were also experienced with the 90° mesh, the simulations converged to and remained fixed at 15 Taylor vortex pairs over all of the rotational Reynolds numbers investigated. The same outcome was still reached even without the optimised start-up procedure. Here, whilst both turbulence models did not reach the desired 14 Taylor vortex pairs, a comparison was still made to the radial PIV velocity data of Wang. It should be noted that the results from the 180° mesh did indeed result in the formation of 14 Taylor vortex pairs. From Figure 3.10, it is clear that both periodic segments over predict the inflow and outflow Taylor vortex boundaries significantly, similar to the results obtained from the two-dimensional axisymmetric modelling approach. Furthermore, a linear transition across the inflow to outflow vortex boundary is observed for both of the 90° and 180° periodic cases.

Analysis of the velocity magnitude profile across the annular gap with the hot-wire data of Smith and Townsend is presented in Figure 3.11. The results of both the 90° and 180° sectors with the standard k-ω turbulence model reveal that, between the two cases whilst there is a negligible difference, when compared to the experimental results, the core velocity is significantly reduced. At the non-dimensional distance of 0.581, the non-dimensional velocity magnitude for the standard k-ω turbulence model is approximately 0.277, compared to that reported by Smith and Townsend of 0.390, giving a percentage error of almost 29%. A slight improvement in this core velocity is seen when switching to the RSM stress-BSL turbulence model, however, a poor agreement is still found; here, only the results of the 90° sector are shown due to the negligible difference observed for the 180° segment. Furthermore, in Figure 3.11 for the RSM stress-BSL turbulence model, at the non-dimensional distance of 0.581, the non-dimensional velocity was 0.306 giving a percentage error of 21.5%.

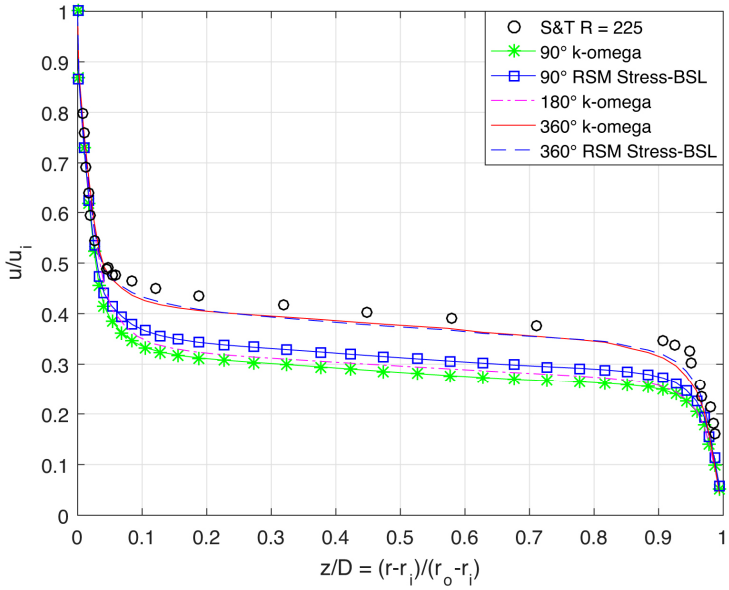


FIGURE 3.11: COMPARISON OF NON-DIMENSIONALISED VELOCITY MAGNITUDE PROFILES ACROSS THE ANNULAR GAP AT *R* = 220

These results contrast with the findings from the DNS study of Brauckmann and Eckhardt [109] relating to the use of rotational periodicity. For the current geometry, with a URANS turbulence modelling approach, it has been demonstrated that applying rotational periodicity is not feasible and results in a significantly reduced core velocity. This suggests that the use of rotational periodicity may only be feasible when combined with axial periodicity and therefore through constraining the domain to only one Taylor vortex pair. This implies that for three-dimensional URANS turbulence modelling, the full 360° geometry must be implemented in order to not impose any constraints on either the domain or the Taylor-vortex wavelength, and thus, accurately resolve the flow field.

3.6.1.3 Full 360° Domain

For the 360° geometry, the results of the standard k-ω and RSM stress-BSL turbulence models were compared to the radial velocity profiles of Wang, then subsequently to the velocity magnitude profiles of Smith and Townsend.

The radial velocity profiles shown in Figure 3.10 illustrate that both turbulence models provide excellent agreement with the PIV data of Wang at $R = 220$, significantly improving on the two-dimensional axisymmetric results and the periodicity study. The radial velocity distributions across Taylor vortex boundaries are accurately represented, with the percentage error for both

turbulence models much less than 1%. Upon closer inspection, the RSM stress-BSL turbulence model predicts the overall PIV radial profile to a slightly greater degree of accuracy.

Comparison of velocity magnitude profiles across the annular gap with the hot-wire data of Smith and Townsend shown in Figure 3.11, reveal that there is negligible difference between the two turbulence models. Both turbulence models predict a slightly reduced core velocity of 0.371 at the non-dimensional distance of 0.581 which results in a percentage error of less than 5% when compared to that of 0.390 reported by Smith and Townsend; most likely, as a result of the slight differences in flow conditions and geometry between the two experimental studies.

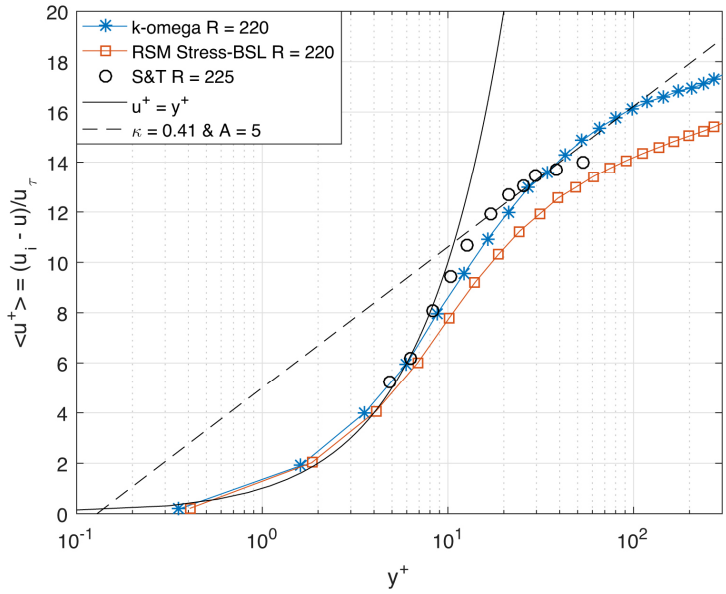
Almost all of the variation in the azimuthal velocity component occurs within the two wall layers and at $R = 220$, the thickness of each boundary layer covers less than one-tenth of the flow width. As the Reynolds number is increased, curvature effects within the wall layers start to diminish and eventually become negligible, this is caused by the breakdown of the Görtler vortices. To determine the influence of curvature on the flow, the wall boundary layers can be compared to the Prandtl-von Kármán logarithmic law of the wall. Figures 3.12 a) and b) show the inner and outer cylinder boundary layers respectively. Profiles are plotted in wall units, calculated using the friction velocity $u_\tau = \sqrt{(\tau_w/\rho)}$, where τ_w is the wall shear stress. Table 3.7 summarises the straight-line fits for the logarithmic region of each boundary layer.

Comparison of the cylinder boundary layers with the data of Smith and Townsend shows that both turbulence models predict similar trends, with the k-ω turbulence model providing the closest agreement to the experimental measurements. For both the boundary layers, the two URANS turbulence models predict a viscous sublayer in the region of $y^+ < 10$, closely following the expected linear-law profile of $u^+ = y^+$. Above this region, the mixing layer can be observed over the range of $20 \leq y^+ \leq 90$. For the outer cylinder wall, Figure 3.12 b), comparison with the classical log-law values of $\kappa = 0.41$ and $A = 5$ shows that there is no significant log-law region. This can be associated with the formation of Görtler vortices in the boundary layer and, hence, a fully turbulent logarithmic region is not identifiable. These results support the boundary layer analysis and conclusions of both Pirrò and Quadrio [32] and that of Ostilla-Mónico et al. [111]

TABLE 3.7: LOG-REGION CONSTANTS FOR BOTH TURBULENCE MODELS AT THE INNER AND OUTER CYLINDER BOUNDARY LAYERS

	Standard k-ω		***RSM Stress-BSL***	
	κ	***A***	***κ***	***A***
Inner	0.42	4.5	0.40	2.9
Outer	0.40	5.0	0.43	4.6

a) Inner Cylinder



b) Outer Cylinder

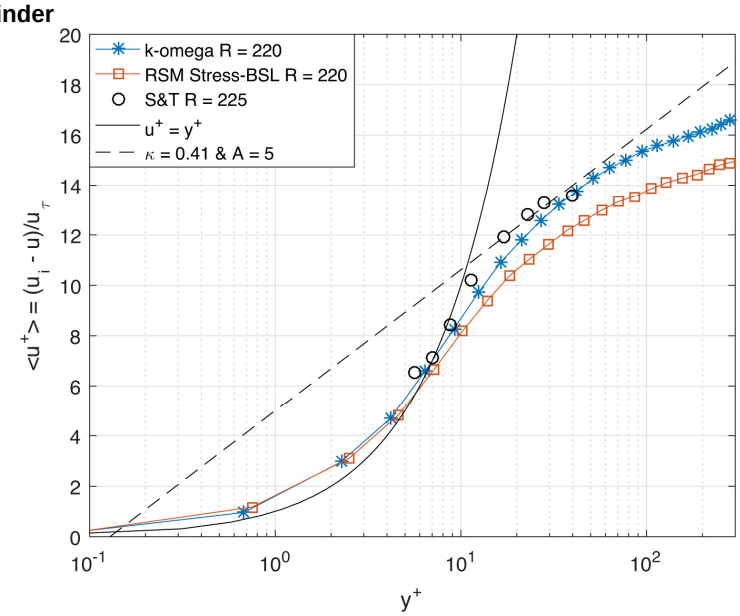


FIGURE 3.12: INNER (a) AND OUTER (b) CYLINDER WALL BOUNDARY LAYERS AT *R* = 220

Görtler vortices, located in the boundary layer, are the secondary flows as a result of centrifugal instabilities for high flow speeds over a concave surface. In a Taylor vortex flow, the mean velocity profile is redistributed near the concave walls, in which Görtler vortices form on a scale related to the boundary layer thickness, as a result of the centrifugal instabilities. Evidence of Görtler vortices can be seen over the concave outer cylinder wall from the enlarged instantaneous velocity vectors shown in Figure 3.13, here only the results of the standard k-ω turbulence model are shown. Conversely, these Görtler vortices do not form over the inner cylinder which is convex. At $R = 220$, the flow exhibits two different scales of motion arising from uniformly spaced Taylor vortices, superimposed with Görtler vortices throughout the boundary layer. On the outer

cylinder wall, Figure 3.13 depicts a Görtler vortex pair which forms at the Taylor vortex radial inflow boundary. These Görtler vortices redirect fluid from the neighbouring Taylor vortex pair towards the outer cylinder wall, resulting in a stagnation point and a reduction in wall shear stress. As such, the Görtler vortices play a defining role in the outer cylinder boundary layer and therefore no significant log-law region is observed.

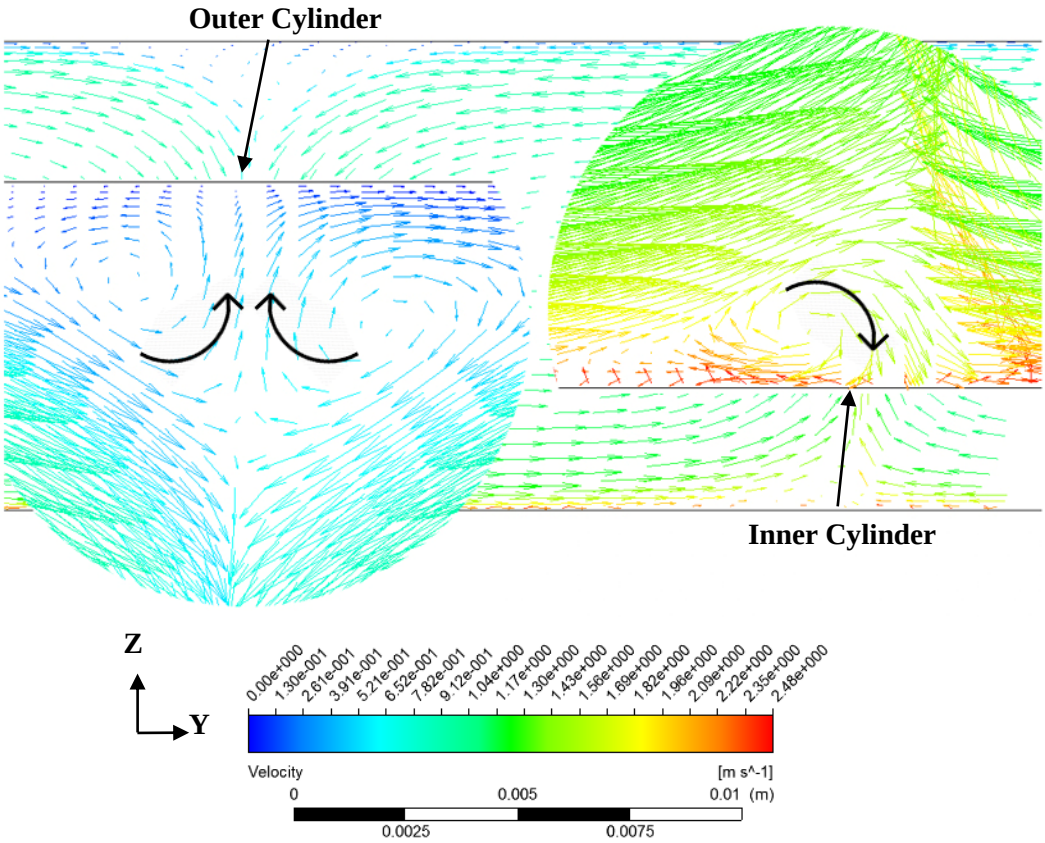


FIGURE 3.13: ENLARGED IN-PLANE VELOCITY VECTORS OVER INNER (BOTTOM) AND OUTER (TOP) CYLINDER WALLS FOR THE k-ω TURBULENCE MODEL AT R = 220

3.6.1.4 SST k-ω Turbulence Model

For industrially relevant flows, such as bearing chamber applications, the current state-of the art approach is to use the SST k-ω turbulence model, as demonstrated by the sheer number of numerical investigations presented in Section 3.1. One advantage of all the k-ω turbulence models reviewed, is the ability to automatically blend the near-wall formulation for solving the viscous sublayer to a wall function approach based on the cell y^+ value. Within Fluent, this blending function has been optimised using Couette flow conditions [108], and therefore, should be well suited to Taylor-Couette flows. The benefit of the SST k-ω turbulence model arises from combining the robust formulation of the k-ω model in the near-wall region, with the free-stream independence of the k-ε model, making it more accurate and reliable for a larger range of problems [108]. As such, within the three-dimensional study, a comparison between the standard

k-ω and SST k-ω turbulence models is made in Figure 3.14, in order to assess any significant differences between the two models. It is found that, much like the 2D axisymmetric results, a closer agreement to the experimental data is found with the standard k-ω turbulence model. With the SST k-ω turbulence model, the maximum and minimum radial velocities are overpredicted by less than 10%. However, the SST k-ω model still accurately captures the axially varying radial velocity. It can also be observed that the SST k-ω model, overpredicts the axial wavelength of the Taylor vortex pairs, on average by 4%, resulting in reduced Taylor vortex end cells. Whilst the standard k-ω turbulence model is more suited to Taylor-Couette flows, a reasonable agreement is also found with the SST k-ω model, and therefore, may present an alternative for a wider classer of industrially relevant flows that the standard k-ω model may fail to capture.

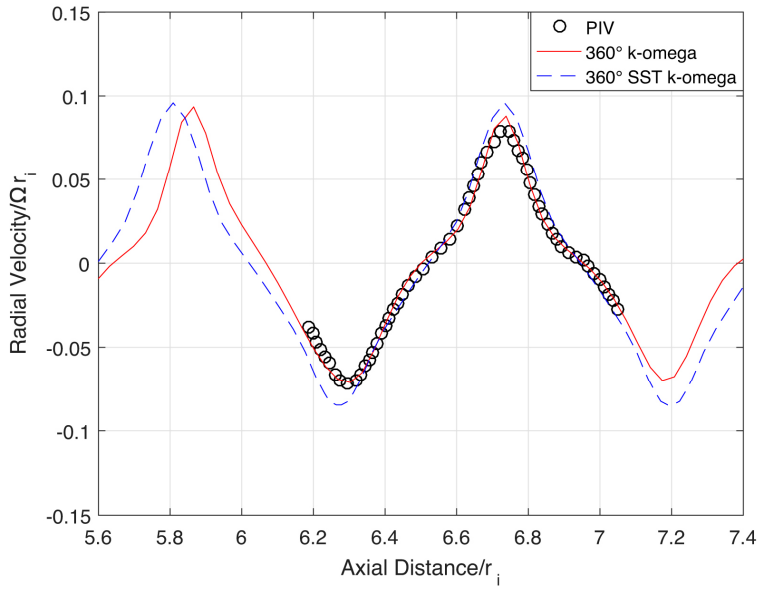


FIGURE 3.14: COMPARISON OF RADIAL VELOCITY PROFILES AT r = 3.94cm AND *R* = 220 FOR BOTH THE STANDARD AND SST k-ω TURBULENCE MODELS

3.7 Taylor-Couette Recommendations

Axisymmetric and three-dimensional CFD modelling of Taylor-Couette flow within the turbulent Taylor vortex flow regime was analysed and compared to available experimental data, with a view of establishing a methodology applicable to future bearing chamber modelling. As such, the following recommendations are presented.

Start-up. *An optimised steady acceleration start-up procedure is indicated for bearing chamber modelling.* An investigation was performed into the start-up procedure. Sudden starts of the inner cylinder were compared to results obtained following a steady acceleration procedure. Through sudden starts, a large variation in the wavelength of Taylor vortices was obtained, resulting in different configurations in the number of Taylor vortex pairs. However, through a steady acceleration procedure it was possible to achieve a final desired state over the whole range of rotational Reynolds number ratios investigated. Once the Taylor vortices form and stabilise, after a steady acceleration procedure, it is then possible to increase the speed of the inner cylinder in small steps whilst still preserving the same number of Taylor vortex pairs. This optimisation allows the computational cost of simulations to be reduced over accelerations to large rotational Reynolds numbers.

Axisymmetric modelling. *Axisymmetric modelling is likely inadequate for bearing chamber modelling.* An URANS turbulence modelling study was performed on an axisymmetric grid. Good agreement was obtained for both the standard k-ω and RSM stress-BSL turbulence models at low rotational Reynolds number ratios. However, it was observed that as the speed of the inner cylinder is increased, the agreement between CFD and experimental results became poor. This is suspected to be as a result of not capturing the three-dimensional structures present within turbulent Taylor-Couette flow, such as boundary layer Görtler vortices.

Three-dimensional modelling with rotational periodicity. *Rotational periodicity is unlikely to be adequate for bearing chamber modelling.* The axisymmetric CFD methodology was extended to modelling in three-dimensions, building on the previous knowledge acquired. A study into applying rotational periodicity was carried out in order to reduce the computational cost. Poor agreement was achieved over all of the rotational periodicities investigated. The radial velocity profiles were overestimated, and a much-reduced core velocity was observed across the gap.

Recommended methodology. *A full 360° model with either the standard k-ω or RSM stress-BSL turbulence model is recommended for the bearing chamber study.* Finally, the full 360° geometry was modelled. The results showed negligible difference between the standard k-ω and RSM stress-BSL turbulence models. Good agreement was achieved with the experimental PIV data of Wang [22] and the hot-wire measurements presented by Smith and Townsend [13]. These results

show that it is possible to accurately capture the velocity flow field within 5% using an URANS turbulence modelling approach. This is achieved through simulating the full 360° geometrical domain, using either the standard k-ω or RSM stress-BSL turbulence models. For industrially relevant flows, this work suggests that either turbulence model will be suitable. However, it should be noted that whilst the RSM is more computationally expensive it has the advantage of being anisotropic, hence turbulence statistics are readily available.

3.8 Aeroengine Bearing Chamber Investigations

Following the previous work, the Taylor-Couette URANS turbulence investigation is extended to an aeroengine bearing chamber application. A study into the single-phase airflow is conducted with comparison to the experimental 3D LDA measurements performed by Gorse et al. [33] on a high speed bearing chamber test rig. The experimental configuration of Gorse et al. focuses purely on the influence of airflow within the chamber, highlighting the dependence of secondary airflow structures on both the rotational shaft speed and sealing airflow rates in the absence of oil. A cross-section of the front bearing chamber under investigation is shown in Figure 3.15. The chamber consists of a shaft throughout the length of the domain, with a diameter D = 128mm. The resulting outer diameter and axial length of the bearing chamber are 1.73D and 0.34D respectively. In relation to the Taylor-Couette analogy, this results in a radius ratio, $\eta = 0.577$, and a device aspect ratio, $\Gamma = 0.47$; therefore, a small aspect ratio, wide-gap system.

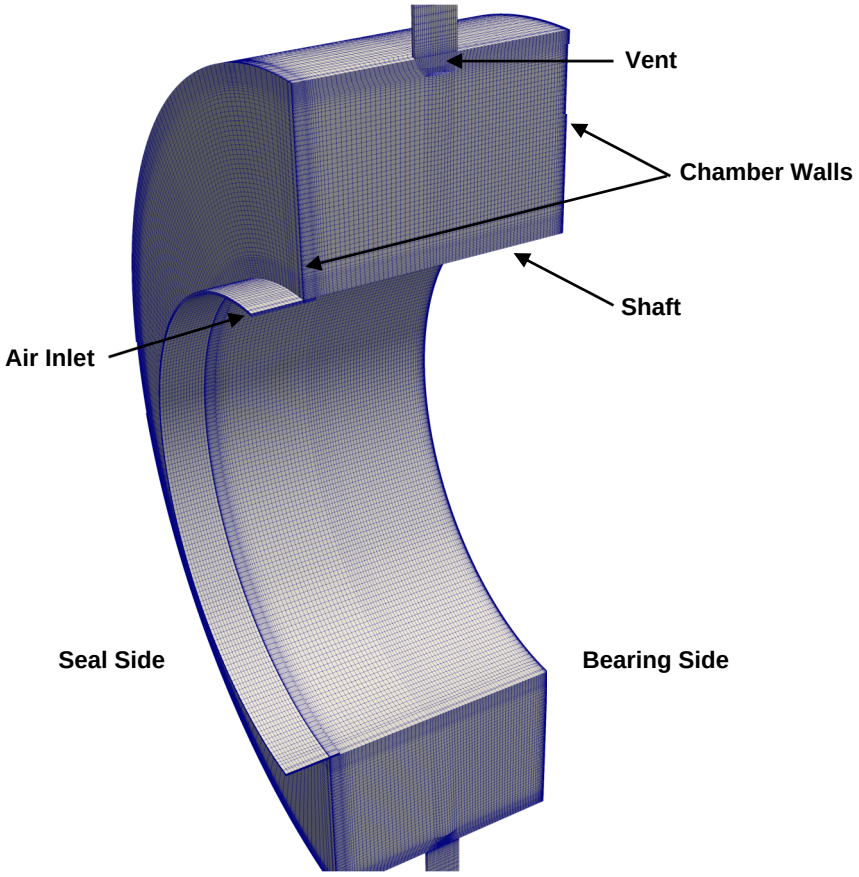


FIGURE 3.15: SECTION OF COMPUTATIONAL MESH FOR THE GORSE BEARING CHAMBER

Within the experimental test rig, the shaft is supported by a roller bearing simulator. A bearing simulator was used to suppress the oil flow entirely, avoiding the two-phase dispersed flow typically found in bearing chambers; this occurs from the resultant airflow interactions with droplets generated from the bearing. Compared with a roller bearing, the simulator forms one

single non-rotating part. Gorse et al. reported that these simplifications resulted in a negligible difference due to the relatively small size of the cage compared to the bearing chamber. At the opposite end of the chamber, air enters via a pressurized labyrinth seal, with a tip clearance of 0.7mm. Two vent pipes, located at the top and bottom angular locations, discharge the airflow, both with a diameter of 10mm.

3.8.1 Computational Set-up

Within the bearing chamber investigation, the operating conditions and fluid properties are derived from the experimental work of Gorse et al. and listed in Table 3.8. Experimentally, the shaft speed is operated between 3,000 rpm and 13,000 rpm with sealing airflow rates adjusted from 4.2 g/s to 17.0 g/s. However, Gorse et al. only present experimental measurements at a shaft speed of 9,700 rpm. For all cases investigated, the chamber was maintained at a constant pressure of 2.5 bar and an air temperature of 298 K.

TABLE 3.8: OPERATING CONDITIONS AND FLUID PROPERTIES

Operating Conditions		***Fluid Properties***	
Rotational Shaft Speed	9,700 rpm	***Air Density***	2.92 kg/m^3
Air Mass Flow Rate	0 - 12.7 g/s	***Air Viscosity***	1.85×10^{-5} kg/ms
Inlet Swirl Angle	50°	***Air Temperature***	298 K
Chamber Pressure	2.5 bar		

3.8.1.1 Boundary Conditions and Mesh

The boundary conditions implemented within the computational domain are depicted in Figure 3.15. Air enters from the left-hand side of the domain, though a small 12mm long channel, ensuring a fully developed airflow profile upon reaching the main chamber. The gap has a clearance of 0.7mm, representative of the labyrinth seal found experimentally. This computational representation of the labyrinth seal has successfully been demonstrated in the previously investigations of Peduto et al. [66], Bristot [68] and Singh et al. [92]. Based on their investigations, a mass flow inlet boundary condition is chosen, with a recommended swirl angle of $\gamma = 50°$. The shaft is specified as a rotating wall, such that when viewed from the front of the bearing, the shaft is rotating in a clockwise direction. At both the top and bottom vent pipes, a pressure outlet boundary condition is applied. On all the other surfaces, a no-slip wall boundary condition is imposed.

In the present study, a non-uniform structured grid based on the previous work of Singh et al. [92] is used. For the Gorse bearing chamber investigation, the mesh independence study of Singh et al. resulted in a final grid of 2,205,854 cells, which is used in this present study and shown in Figure 3.15.

3.8.1.2 Numerical Methods and Solution Procedure

In accordance with the Taylor-Couette investigation the finite volume incompressible solver, ANSYS Fluent 17.1, was used for all calculations presented. For the present investigation, the use of an incompressible solver is deemed adequate since Gorse et al. report that, within the chamber, the pressure and temperate are kept at a constant 2.5 *bar* and 298 *K* respectively; such that across all operating conditions, the highest Mach number is 0.19. Within this study, a similar numerical modelling methodology as outlined in Section 3.4 was used. Initial simulations applied the SIMPLE algorithm for the pressure-velocity coupling method, however due to convergence issues, instead, the Coupled algorithm was implemented based on the recommendations of Singh et al. [92]. The PRESTO! discretisation scheme was chosen for the pressure equation and a second order upwinding scheme was used to discretize the remaining equations. For time discretisation, again, a bounded second order implicit temporal discretisation scheme was chosen.

3.8.1.3 URANS Turbulence Modelling

Within bearing chamber applications, the airflow is highly turbulent due to the presence of a rotating shaft throughout the domain, much like a Taylor-Couette flow, however, typically the operational shaft speeds are significantly greater. As such, the previous Taylor-Couette URANS turbulence modelling is extended to the bearing chamber under investigation. The Taylor-Couette study demonstrated that for a full 360^0 domain, either the standard k-ω or RSM stress-BSL turbulence models were most suited; although it is important to assess whether the conclusions drawn still remain valid, and therefore, a more extensive turbulence modelling study is presented.

As such, for the bearing chamber investigation, in addition to the standard k-ω and RSM stress-BSL turbulence models, simulations are also performed for the RNG k-ε and SST k-ω turbulence models. For the Taylor-Couette study, all of the investigated ε-based turbulence models severely over-predicted the radial velocity profiles, although, as shown in Section 3.1 for a bearing chamber application, the RNG k-ε model has previously been successfully implemented within VOF investigations, such as that demonstrated by Krug [72]. Krug reported good prediction of scavenge quantities, although the results for oil distribution were less successful. In addition, as previously discussed, the SST k-ω turbulence model has dominated bearing chamber simulations

and is said to represent the state-of-the-art modelling approach, although to date there has been no attempt to justify this statement. Surprisingly, within the Taylor-Couette study, it was demonstrated that for three-dimensional modelling, the SST k-ω turbulence model performed worse than the default standard k-ω model. The main source of difference was an over-prediction, by approximately 4%, in the Taylor-vortex axial wavelengths, resulting in smaller end cells. However, it is suspected that for bearing chamber modelling, due to the short chamber axial length permitting only one Taylor-vortex pair, this will be inconsequential; hence, for clarity the SST k-ω turbulence model is also included within the current investigation.

3.8.2 Bearing Chamber Results

Within a bearing chamber configuration, Gorse et al. [33] report that the secondary airflow vortices can either be categorised into a rotational speed driven mode (RSDM) or a sealing air driven mode (SADM), with a transitional mode occurring between the two. When the sealing airflow rate is small, the RSDM is present and as the sealing airflow rate is linearly increased, the flow transitions to a SADM. As shown in Equation (2.12), the ratio between the speed of the shaft and sealing airflow can be used to define this transition, whereby:

$$R_u = \frac{u_{sh}}{u_{air}}$$

Gorse et al. [33] report that when the velocity ratio drops below 4.2, the SADM is present, whereas above which the RSDM dominates. Figures 3.16 a) and b) show the secondary flow velocity vectors observed experimentally by Gorse et al., for a shaft speed of 9,700 rpm. Figure 3.16 a) highlights the RSDM, with two counter rotating vortices analogous to a Taylor vortex pair; closest to the seal, a slightly larger vortex is observed due to the weak sealing airflow rate. As the sealing airflow rate is increased beyond the critical value, the secondary flow pattern transition to a SADM, shown in Figure 3.16 b). Here, the left vortex becomes much smaller and is forced to the upper left-hand corner, such that the vortex separation line no longer resides on the shaft. Within the bearing chamber, Gorse et al. define non-dimensional axial (Z) and radial (R) positions as:

$$Z = \frac{z}{W} \; and \; R = \frac{r}{H} \tag{3.10}$$

Here, the chamber width, W = 47mm and the chamber height, H = 44mm.

In order to benchmark simulations, calculations are therefore first performed without a sealing airflow, to achieve a pure RSDM. After which, the sealing airflow rate is gradually introduced until the flow transitions into a SADM.

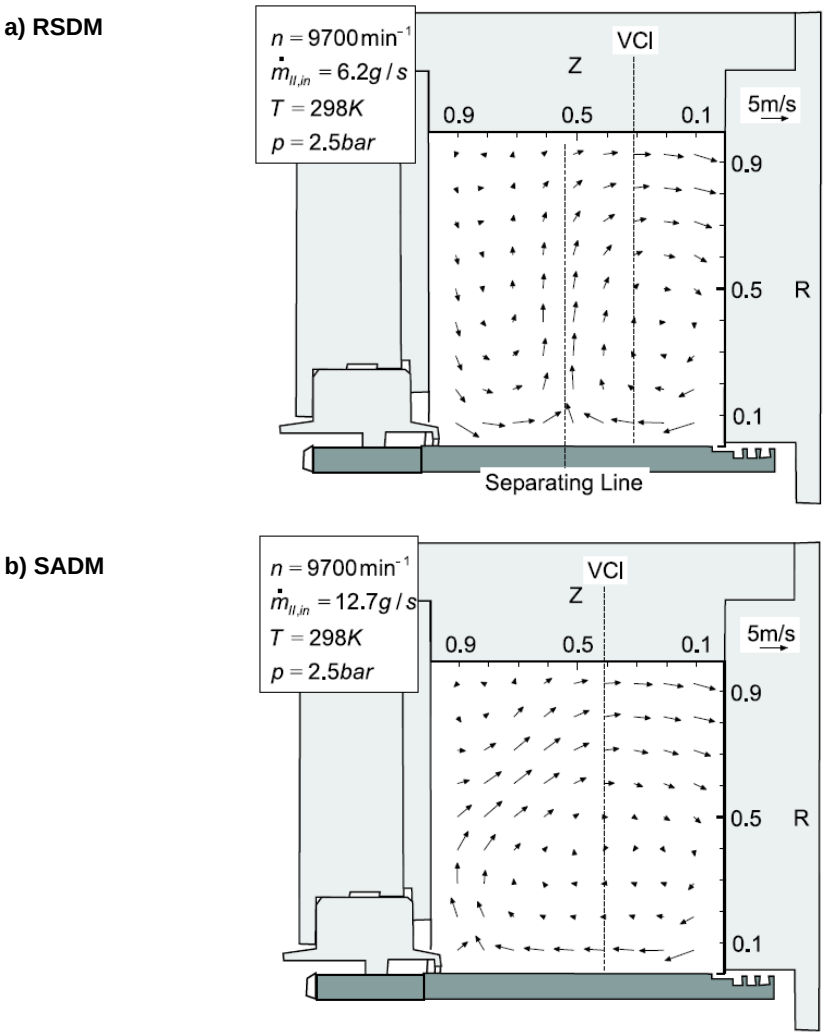


FIGURE 3.16: GORSE PIV [33] EXPERIMENTAL MEASUREMENTS SHOWING THE RSDM (a) AND SADM (b) SECONDARY FLOW FIELDS

3.8.2.1 Rotational Speed Driven Mode

Computationally, within the bearing chamber, much like the Taylor-Couette flow, it was observed that the vortical structure is extremely dependent on the initial conditions; even in the absence of a sealing airflow. Initial simulations at moderate shaft speeds, i.e. below 9,000 rpm failed to reproduce the Taylor vortex-like structure observed experimentally. Instead, depending on the turbulence model employed, either only one large rotating vortex was present, or for some cases, a vortical structure resembling the SADM, shown in Figure 3.16 b), was observed. Gorse et al. [33] provide no information regarding the start-up conditions exhibited experimentally, which therefore computationally, becomes extremely difficult in providing a start-up procedure as recommended in the Taylor-Couette study. Therefore, in order to accurately reproduce the flow structure, several different start-up conditions were tested computationally. As a result, across all

turbulence models, the only case in which a flow structure resembling the RSDM was achieved, was when the simulations were first initialised to the highest shaft speed of 13,000 rpm. Subsequently, it was observed, that after the Taylor vortex structure formed and stabilised, it was possible to preserve the structure by reducing the shaft speed in small steps down to 9,700 rpm following the optimised start-up procedure methodology outlined within the Taylor-Couette study, Section 3.6.1.1; here a small step of 1,000 rpm was deemed suitable. Following this technique, the RSDM was preserved and two counter rotating vortices were identified, as shown by the averaged secondary velocity vectors in Figure 3.17. Here, as expected, due to the lack of a sealing airflow, two equally sized, counter-rotating vortices were observed.

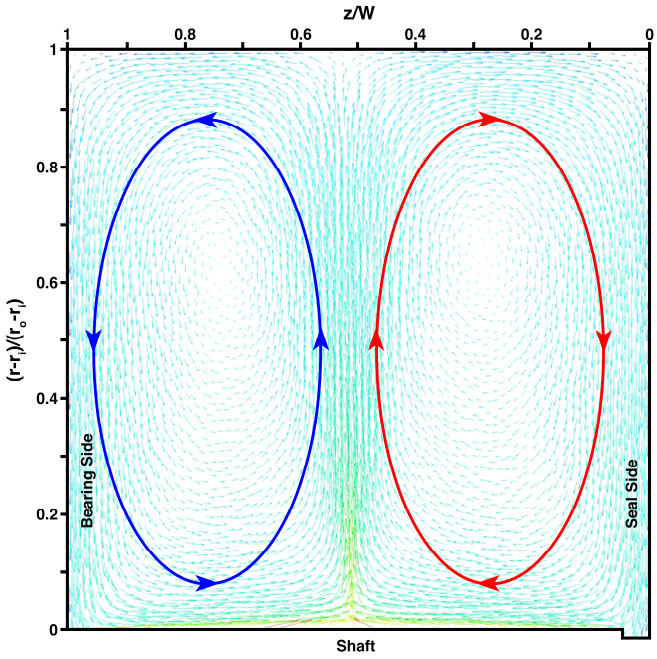


FIGURE 3.17: IN-PLANE VELOCITY VECTORS FOR RSDM, m_g= 0 g/s AND n = 9,700 RPM

Interestingly, over all of the turbulence models investigated, the only case to not reproduce the RSDM, was the RNG k-ε turbulence model, even at 13,000 rpm. Instead, one large rotating vortex is observed, with two very small corner vortices as shown in Figure 3.18. It was previously determined that the ε-based turbulence models were unsuited to the model the Taylor-Couette flow investigated earlier, due to over-predicting the radial velocities. However, it becomes surprising that the model fails to even reproduce the Taylor vortex structure within the bearing chamber geometry; especially since the RNG variant is reported to have improved accuracy for flows with rotation and vortices [108]. Even more so, due to the number of previous bearing chamber investigations that have utilised the k-ε turbulence model, shown in Section 3.1.

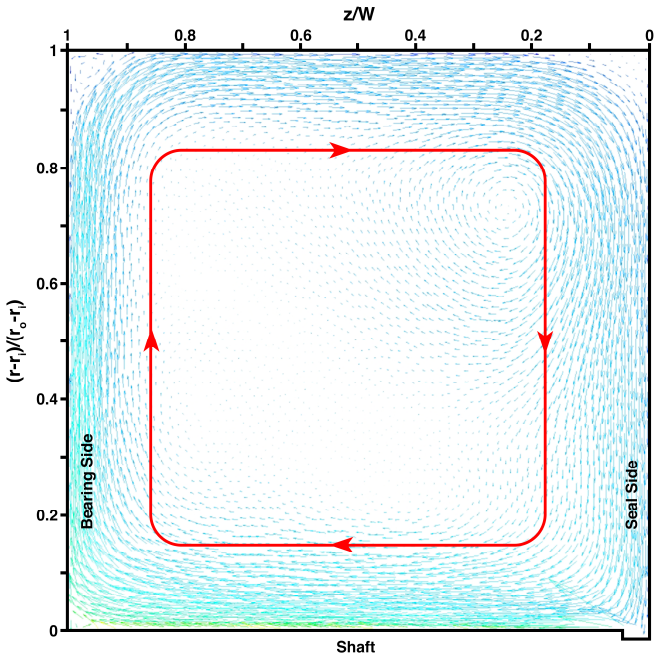


FIGURE 3.18: RNG k-ε IN-PLANE VELOCITY VECTORS FOR RSDM, m_g= 0 g/s AND n = 9,700 RPM

Computationally, once the stable counter rotating vortex pair had formed, at the shaft speed of 9,700 rpm, a sealing airflow was subsequently introduced. As the sealing airflow rate is gradually increased, computationally the right-hand vortex, closest to the seal, gradually increases in size causing the left-hand vortex to diminish in size. The first available experimental measurement point to compare to is at a shaft speed of 9,700 rpm and an airflow rate of 6.2 g/s. At this operating condition, all of the turbulence models investigated struggled to fully reproduce the RSDM presented by Gorse et al. [33], as shown in Figure 3.16 a). Both the standard k-ω and RSM-BSL turbulence models predicted very similar secondary flow patterns, whereby a large, dominating, right-hand vortex forms, with substantially smaller counter rotating vortices forming at both the top and bottom on the left-hand side of the chamber. This can be seen in Figure 3.19 a), which shows the secondary flow field pattern for the RSM stress-BSL turbulence model at 9,700 rpm and an airflow rate of 6.2 g/s. Whilst not shown, an almost identical pattern is seen for the standard k-ω turbulence model. However, this flow field pattern, although similar, is still noticeably different to that of the SADM presented by Gorse et al. [33] in Figure 3.16 b). This is because in Figure 3.19 a), it can be seen that the vortex separation line still remains attached to the shaft, unlike the experimental SADM results. For reference, within Figures 3.19 a) and b), the RSDM vectors of Gorse et al. are superimposed in black to highlight the difference in results.

The closest agreement found to the RSDM presented by Gorse et al. was with the SST k-ω turbulence model, for which the averaged secondary flow field vectors are presented in Figure 3.19 b). Here, the turbulence model is able to capture the counter rotating Taylor vortex-like

structure, however compared to the results of Gorse et al., a greater right-hand vortex is observed. Experimentally the vortex separation line occurs at a non-dimensional distance of Z = 0.55, measured from the sealing side of the chamber; whereas computationally this occurs at the non-dimensional distance of $Z = 0.70$.

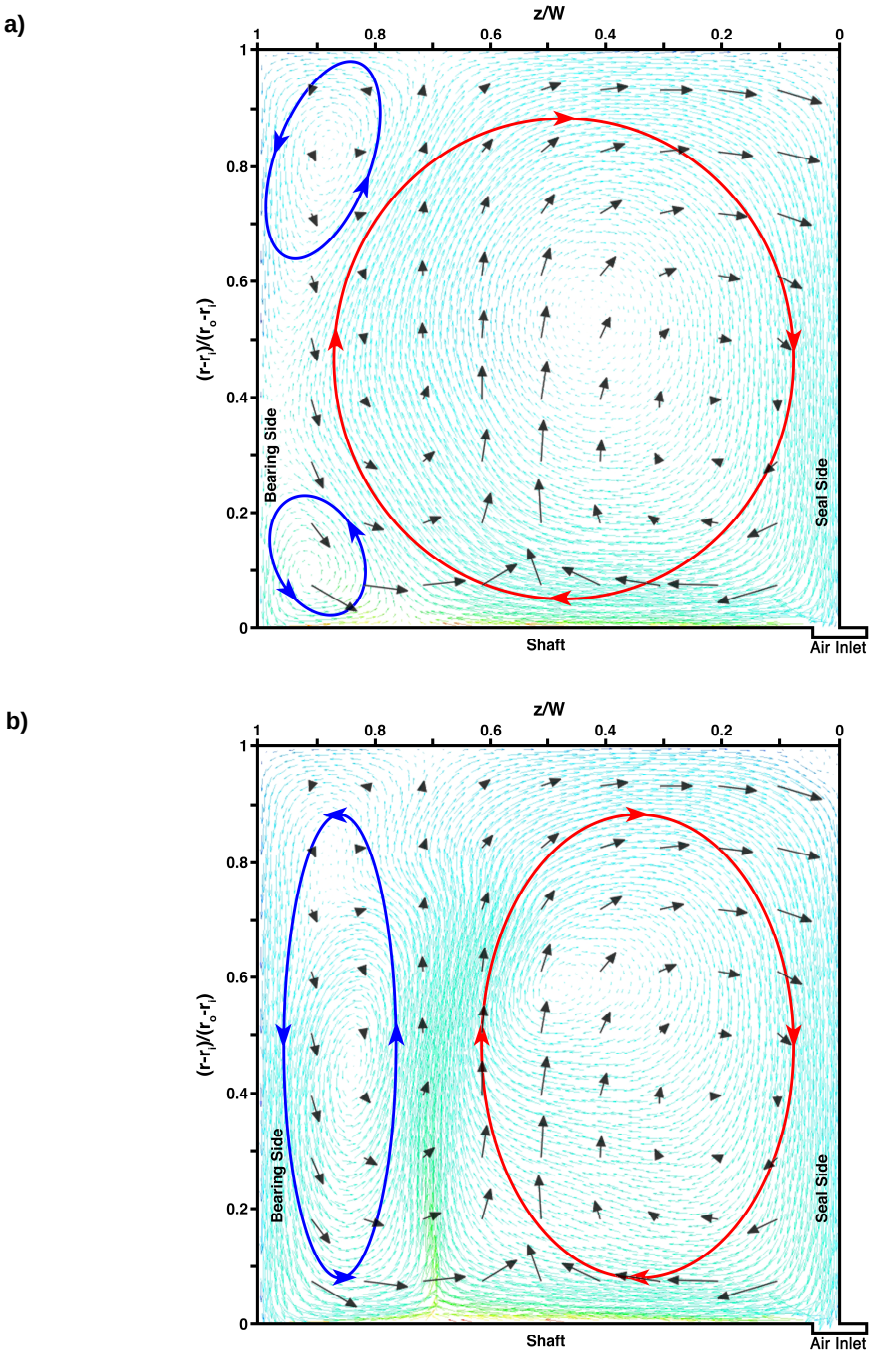


FIGURE 3.19: RSM STRESS-BSL (a) AND SST k-ω (b) IN-PLANE VELOCITY VECTORS FOR RSDM, m_g= 6.2 g/s AND n = 9,700 RPM. SUPERIMPOSED WITH GORSE [33] RSDM VECTORS (BLACK)

These results are surprising since both Bristot [68] and Singh et al. [92] successfully demonstrated the capability to capture the RSDM using the SST k-ω turbulence model on the bearing chamber geometry of Kurz et al. [9]. The bearing chamber employed by Kurz is almost identical to the test rig presented by Gorse et al. [33], except that the axial extent of the chamber is 1.4 times longer. Both Bristot and Singh et al. used the same sealing airflow boundary condition presented in this current computational investigation, using a swirl angle of 50°. For the shaft speed and sealing airflow rate investigated by Bristot, the velocity ratio was R_u = 7.09 and conversely, Singh et al. investigated a velocity ratio of R_u = 5.50; for reference the velocity ratio for the current Gorse operating condition is R_u = 8.59. Therefore, the operating spaces investigated by both Bristot and Singh are significantly closer to the transitional state of the flow field, whereby Gorse et al. report that below a value of R_u = 4.2 the SADM is present. For the current computational investigation, the numerical methods employed are equivalent to those used by Singh et al. and it is therefore unexpected as to why, computationally, the SST k-ω turbulence model fails to accurately capture the RSDM, suggesting that the difference in chamber axial length is responsible.

It is apparent that at low sealing airflow rates, the secondary flow field pattern observed is very sensitive to both the initial conditions and choice of turbulence model. As such, a parametric investigation into the effect of the inlet boundary condition was also performed, in which the swirl angle was varied from 30° up to 70°. This investigation showed that this parameter had very little impact on the final state of the secondary flow structure, since the swirl angle of flow naturally develops within the 12mm long channel, representative of the labyrinth seal, at the inlet boundary condition.

3.8.2.2 Sealing Air Driven Mode

As the sealing airflow rate is increased, the flow state transitions from a RSDM to that of a SADM. Gorse et al. [33] show that this first starts to take place at an airflow rate of 12.7 g/s, as shown in Figure 3.16 b). Experimentally, at this flow rate, the vortex separating line becomes detached from the shaft surface and moves along the bearing chamber left-hand wall. At a shaft speed of 9,700 rpm and an airflow rate of 12.7 g/s, this separation line occurs at the non-dimensional radial distance of R = 0.60, measured from the shaft. As a result, the left-hand vortex reduces in size significantly and is forced into the top left corner of the bearing chamber, with the vortex centre, experimentally, located at the non-dimensional location R = 0.90 and Z = 0.88.

Figures 3.20 a) to c) show the averaged secondary flow field vectors for each of the turbulence models investigated at a shaft speed of 9,700 rpm and a sealing airflow rate of 12.7 g/s. The results for the RNG k-ε turbulence model, are not shown, since under these operating conditions there

was no change in the secondary flow field and an identical vortex structure as previously shown in Figure 3.18 was observed. Additionally, within Figures 3.20 a) to c), the SADM vectors of Gorse et al. are superimposed in black to show the similarity between results.

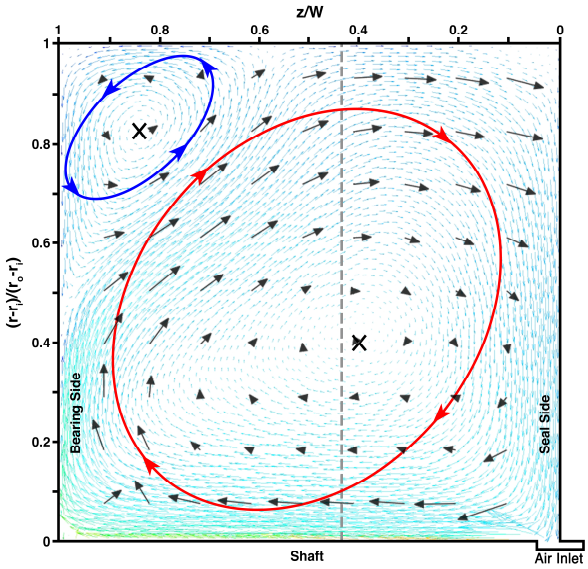
Overall, within the bearing chamber geometry the RNG k-ε turbulence model completely failed to capture the flow field patterns reported by Gorse et al. for all of the shaft speeds and airflow rates investigated. Figure 3.20 a) shows the results of the standard k-ω turbulence model, here the SADM mode is fully captured with the vortex separating line occurring at the non-dimensional location $R = 0.47$. As a result, a slightly larger corner vortex is observed when compared to the experimental results of Gorse et al., in which the vortex separation line occurs at the distance of $R = 0.60$. Similarly, the results of the SST k-ω turbulence model are shown in Figure 3.20 b). With the SST k-ω turbulence model, a closer agreement to the experimental data is observed, with the vortex separation line located at $R = 0.61$ and therefore a similar sized vortex is found at the top left corner of the chamber. Finally, the results of the RSM stress-BSL turbulence model are shown within Figure 3.20 c). Here, whilst a comparable SADM vortex structure is observed, visually, the most noticeable difference is the presence of two vortex separation lines, one located at $R = 0.44$ and the second attached to the shaft at $Z = 0.9$.

Table 3.9 summarises the centre location of the each of two main vortices highlighted in Figures 3.20 a) to c), these are compared to the results of Gorse et al. [33]. The axial location of the left-hand vortex remains fairly consistent over all of the turbulence models investigated. However, the greatest difference lies within the radial co-ordinate, resulting from the difference in separation lines and hence the vortex size as previously discussed. The closest agreement to the experimental data is found with the SST k-ω turbulence model; although, when considering the larger, right-hand, vortex all of the turbulence models showed a much greater deviation from the experiment, with percentage errors in the region of 20%.

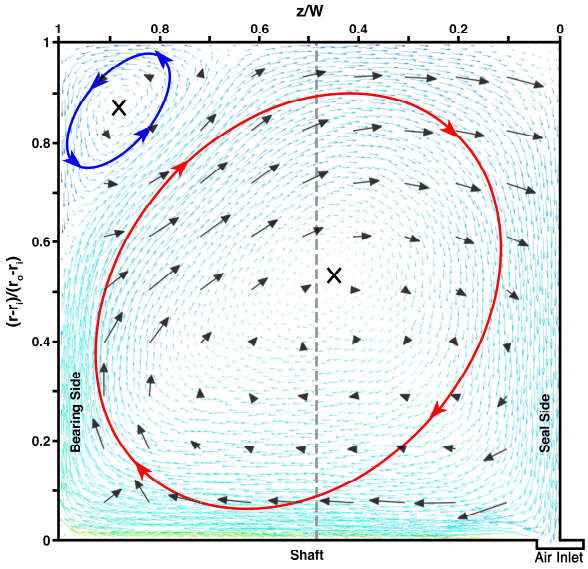
TABLE 3.9: NON-DIMENSIONAL VORTEX CENTRE LOCATIONS

	Left Vortex		***Right Vortex***	
Case	***Z***	***R***	***Z***	***R***
Gorse et al.	0.88	0.90	0.35	0.45
Standard k-w	0.84	0.81	0.40	0.40
SST k-w	0.88	0.87	0.46	0.53
RSM-BSL	0.88	0.81	0.32	0.32

a) Standard k-ω



b) SST k-ω



c) RSM Stress-BSL

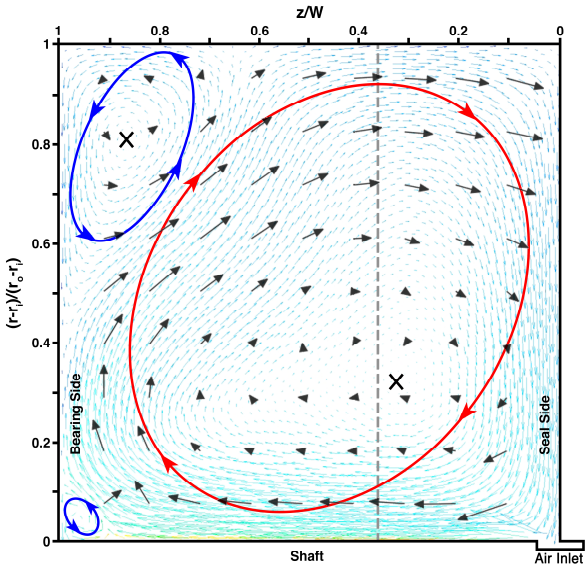


FIGURE 3.20: IN-PLANE VELOCITY VECTORS FOR SADM, m_g= 12.7 g/s AND n = 9,700 RPM. SUPERIMPOSED WITH GORSE [33] SADM VECTORS (BLACK)

Under the SADM operating conditions, Figure 3.21 shows the non-dimensional radial profiles of the mean tangential velocity at the axial positions defined by the dashed lines within Figures 3.20 a) to c). The axial lines are placed immediately left of the right-hand vortex centre location, which is defined in Table 3.9 and marked by the crosses in Figures 3.20 a) to c), this is in line with the experimental method presented by Gorse et al. [33]. Across all cases, the mean tangential velocity is non-dimensionalised by the shaft speed. Whilst a SADM was not achieved using the RNG k-ε turbulence model, a comparison is also made. Within Figure 3.21, it is clear that across all of the turbulence models investigated, the SST k-ω turbulence model provides the closest agreement to the experimental data. This can be associated with the ability of the model to accurately capture the secondary flow field as evident in the comparison to the visualisation measurements. For the SST k-ω turbulence model, the greatest discrepancy occurs over the non-dimensional radial distance of R = 0.4 to R = 0.8, however over this range the maximum percentage error in the tangential velocity was less than 5%. In contrast, the RSM stress-BSL model produced the greatest deviations from the experimental measurements, with a maximum percentage error of 12%, at R = 0.18.

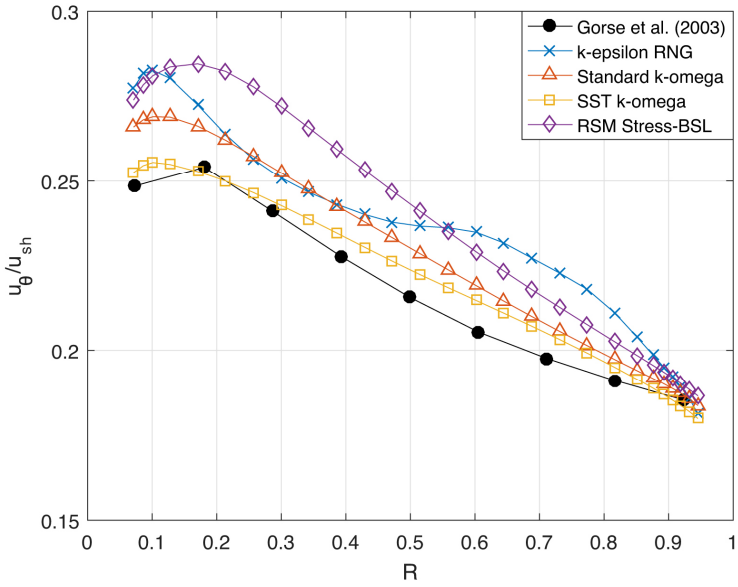


FIGURE 3.21: RADIAL PROFILES OF TANGENTIAL VELOCITY, m_g= 12.7 g/s AND n = 9,700 RPM

The recommended turbulence modelling methodology presented in the Taylor-Couette study suggested that the most appropriate models were either the standard k-ω or RSM stress-BSL. However, it was noted that whilst the SST k-ω model predicted very similar velocity profiles to the standard k-ω model, the biggest difference occurred within the axial wavelength of the Taylor vortex pairs. For the SST k-ω model, the size of the Taylor vortices was approximately 4% larger, therefore resulting in smaller end cells. It is noted that, within a bearing chamber, due to the

constrained axial length of the geometry, this phenomenon does not present a problem, since the space only permits a single vortex pair to form. Surprisingly, the RSM stress-BSL model, unlike in the Taylor-Couette study, performed quite poorly especially when comparing velocity profiles. In addition, due to the more complex nature of the RSM formulation, as expected, simulations were considerably more expensive; numerically taking up to 5 times as long to reach the same flow time, when compared to the two-equation models. Overall, for the bearing chamber geometry under investigation, it is clear that both quantitatively and qualitatively the SST k-ω model is the most suitable choice of URANS turbulence model.

3.9 Single-Phase Bearing Chamber Modelling Conclusions

The three-dimensional Taylor-Couette turbulence modelling methodology has been expanded and applied to a bearing chamber geometry. Numerical studies are conducted over a range of shaft speeds and sealing airflow rates. A qualitative and quantitative analysis of the secondary airflow structure is carried out and compared to the experimental measurements of Gorse et al. [33]. Initial calculations determined that it was necessary to include a start-up procedure, as highlighted by the Taylor-Couette study. As such, simulations were first initialised to 13,000 rpm after which the rotational shaft speed was reduced in small steps to the final desired state.

Qualitatively, without a sealing airflow, all of the turbulence models investigated were able to fully capture the RSDM, except for the RNG k-ε model. Over the range of the experimental operating conditions investigated, the RNG k-ε turbulence model performed poorly, producing only one large rotating vortex structure. At low sealing airflow rates, all of the turbulence models struggled to capture the RSDM presented by Gorse et al. [33]. The closest agreement was found with the SST k-ω turbulence model, although compared to the experimental measurements, a larger than expected right-hand vortex was observed. At high sealing airflow rates, the SADM was predicted well by both the standard/SST k-ω models and also by the RSM stress-BSL turbulence model, all reasonably capturing the vortical structure presented by experimentally.

Quantitatively, for the SADM, a comparison of vortex central locations revealed good agreement across all of the turbulence models. For the left-hand vortex location, the closest agreement was achieved using the SST k-ω turbulence model, as a result of accurately capturing the vortex separation line. However, for all of the cases investigated, the central location of the right-hand vortex was not captured well. A comparison of non-dimensionalised tangential velocity profiles radially across the gap were compared to the available measurements of Gorse et al. [33]. Out of all of the turbulence models investigated, the closest agreement was observed for the SST k-ω turbulence model, with local percentage errors no greater than 5%. Surprisingly, the poorest agreement was found with the RSM stress-BSL model, with percentage errors as large as 12%.

The results of the bearing chamber investigation differ slightly to that of the Taylor-Couette study. Within the Taylor-Couette methodology, the standard k-ω and RSM stress-BSL turbulence models were recommended as the most suitable choices; but, for the bearing chamber investigations, the best results were achieved using the SST k-ω turbulence model. Even under single-phase conditions, as a result of the more complex bearing chamber environment, the flow conditions cannot be as easily simplified as originally anticipated, and therefore, the Taylor-Couette turbulence modelling approach is not entirely transferable. Overall, a good agreement is presented with the SST k-ω model and is therefore recommend for the future bearing chamber modelling.

Chapter 4

Development: sprayParcelFilmFoam

A Fully Coupled Two-Way ETFM-DPM Solver

In this chapter the use of the open-source CFD code OpenFOAM is used to create and develop the fully coupled two-way ETFM-DPM solver: *sprayParcelFilmFoam*. To establish an adequate computational model of oil behaviour in an aeroengine bearing chamber, a review of current literature suggests that it is necessary to be able to model oil shedding from bearings; this oil breaks up into droplets/ligaments which subsequently forms both thin and thick films driven by either gravity or shear forces. As such, a transient solver for spray particle modelling and thin liquid film transport has been developed and incorporated within OpenFOAM. A fully coupled ETFM-DPM solution is presented, capable of modelling both primary atomisation and secondary breakup of the particulate phase. In addition, two new thin film sub-models have been implemented, both a film stripping and an edge separation criteria. Furthermore, in order to achieve accurate statistical representation of the droplets, modifications to the DPM particle injector code were implemented. The newly developed solver is validated against previously published experimental measurements, involving a liquid jet which is injected into a high-velocity crossflow, undergoing breakup and the formation of a wall film. In addition, comparison is made to available computational results also reported for the same case study, obtained by authors within ANSYS Fluent. The development of *sprayParcelFilmFoam* illustrates an advance in bearing chamber modelling capability and has established a necessary foundation for future aeroengine bearing chamber film modelling.

4.1 Introduction

Recent high-speed camera investigations into oil behaviour exiting an aeroengine-representative ball bearing have been conducted by Santhosh et al. [53] and Hee et al. [54]. A detailed overview of the G2TRC bearing oil shedding rig is found in Section 2.3.4.1 and a more complete description is presented by Hee [55]; Figure 4.1 presents a diagram of the experimental test rig. Optical image visualisation identified that depending on the rotation speed, oil is shed as both droplets and ligaments into the bearing chamber, as well as oil sheet formation. Droplet impingement results in the formation of a continuous thin film on the stationary outer walls, which is subsequently driven by the high-speed rotating airflow. These experimental studies have highlighted that the droplets shed from the bearing, have diameters considerably smaller than the typical cell resolutions employed in a VOF simulation. This suggests that, instead, the use of a DPM approach may be a more appropriate alternative in order to feasibly capture these very small droplets without incurring a significant computational cost. Furthermore, this can be coupled with the ETFM to resolve the film formation to achieve a more computationally efficient approach to the problem.

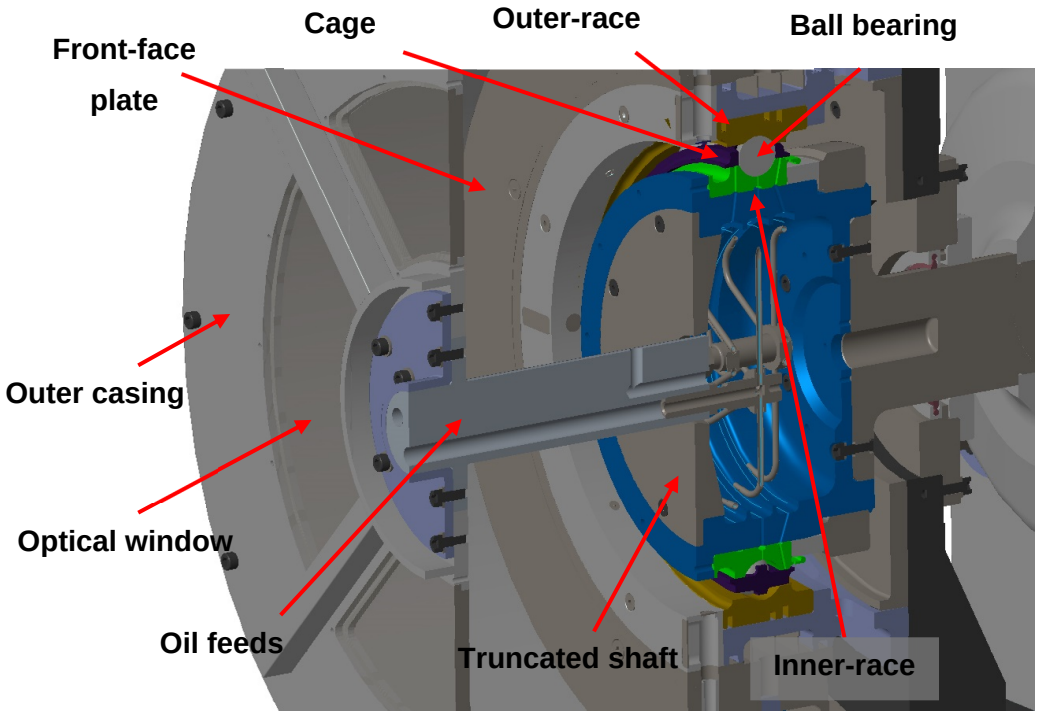


FIGURE 4.1: SCHEMATIC OF BEARING OIL SHEDDING RIG FRONT CHAMBER, MODIFIED FROM [54]

It is clear that there is a need for a methodology to capture the relevant phenomena observed experimentally [53, 54]. Within the bearing chamber, these key flow physics can be broken down into four main areas:

- Oil exiting from the bearing forms a thin film on the stationary outer casing wall through impingement of liquid on the surface. At the cage-edge, oil is observed as a combination of either droplets, ligaments and/or sheets. Further interactions of these droplets can result in splashing.
- The film develops along the outer casing wall, moving toward the bearing chamber expansion region. Film shear stripping takes place as the relative velocity between the airflow and thin film increases, resulting in the ejection of droplets.
- At the front-face edge, before the bearing chamber expansion, the oil breaks down and separates from the surface, resulting in a combination of droplets and ligaments entering the main chamber compartment. These droplets can potentially undergo secondary breakup resulting in smaller secondary droplets.
- Finally, these droplets impinge on the outermost chamber walls forming a thin film. Additionally, oil accumulates on these surfaces from the proportion of liquid that remains attached and flows over the front-face edge. The oil subsequently pools downward toward the sump, where it is gravity scavenged and returned to the tank.

One of the areas yet to be fully explored is the capability of a coupled ETFM-DPM approach, which, in theory, is able to capture the oil shedding behaviour observed within the bearing chamber, as described above. From the literature review carried out in Section 2.4, within ANSYS Fluent, whilst early thin film modelling approaches incorporated droplet interactions, such as impingement and splashing, many numerical difficulties were faced and solutions for the shock or pool regimes were unobtainable [81, 82]. Subsequent developments to the ETFM, as explored by Kakimpa et al. [91], led to a more accurate representation of the film inertia source term. In addition, a more rigorous numerical approach for the thin film modelling methodology, saw that solutions were indeed possible for these shock and pool regimes. With these improvements to the ETFM, the coupling of a two-way ETFM-DPM approach was reconsidered as a viable option for bearing chamber modelling. To assess the suitability of a coupled ETFM-DPM approach for bearing chamber simulations, Hee et al. [105] investigated the case study of a liquid jet injected into a high velocity crossflow. This validation study was based on the experimental investigations of Shedd [112] and the combined computational and experimental work of Arienti et al. [113]. Hee et al. proposed that this was a necessary step in improving bearing chamber modelling capability, through first assessing the ability of the coupled ETFM-DPM approach in capturing the more fundamental key flow physics observed within a bearing chamber. In the experiments of Shedd, droplet interactions such as: impingement, splashing and secondary breakup were observed; and furthermore, film mechanisms are identified including shear stripping and edge separation.

Hee et al. [105] investigated the ETFM-DPM coupling within ANSYS Fluent. For the computational investigation, Hee et al. performed a parametric study to systematically assess the effects of mesh density, DPM settings and film sub-models on the fidelity of the film solution; comparing results of computed film thickness against the experimental measurements of Arienti et al. [113]. Significant improvements were observed with the addition of a discrete random walk model to account for turbulence within the particle trajectories. However, with the inclusion of a film stripping criteria, in order to account for Kelvin-Helmholtz instabilities, Hee et al. reported a computed film thickness with a normalised root mean squared deviation of 28.9% from the experimental measurements. In addition, further simulations failed to achieve a solution when including the effects of either gas-film momentum coupling, edge separation or surface tension, resulting in severe convergence stability issues. Whilst the work of Hee et al. represents a necessary first step in the ETFM-DPM coupling for bearing chamber modelling capability, it is clear that further work is essential.

The results of Hee et al. [105] are somewhat surprising, since outside of ANSYS Fluent, Jingyu et al. [103, 104] successfully demonstrated the capability for a two-way coupled ETFM-DPM approach within STAR-CD. Initially, Jingyu et al. [103] investigated the experimental bearing chamber of Gorse et al. [40], demonstrating good agreement for a wide range of realistic engine operating speeds between 4,000 rpm and 16,000 rpm. Subsequently, Jingyu et al. [104] performed a combined computational and experimental study on a representative aeroengine bearing chamber. The simplified experimental test rig consisted of a rotating cylinder fitted with an oil thrower, capable of speeds up to 3,000 rpm. Whilst the experimental operating conditions are considered as relatively low rotational shaft speeds, compared to a typical aeroengine bearing chamber, again the computational results showed excellent agreement. The methodology implemented by Jingyu et al. included a droplet interaction model for both impingement and splashing characteristics; in addition, thin film sub-models accounted for both film shear stripping and edge separation. Although, it should be noted that within the droplet impingement model, there was no inclusion for secondary breakup of the droplets. Furthermore, no information is provided on how the scavenge arrangement is represented using the ETFM approach. Additionally, the ETFM-DPM methodology used by Jingyu et al. is also capable of modelling heat transfer effects. It is clear that within STAR-CD, the two-way coupled ETFM-DPM methodology used by Jingyu et al., is capable of modelling a wide range of bearing chamber thin film flow regimes, covering the smooth, shock and pool solutions. Furthermore, the results of Jingyu et al. suggest that these results are numerically stable when including additional thin film capability, such as either a stripping or edge separation criteria, but also for both gas-film momentum coupling and surface tension effects.

Overall, the work of both Hee et al. [105] and Jingyu et al. [103, 104] suggest that there is a clear need to provide a more appropriate and accurate ETFM-DPM coupled approach for aeroengine bearing chamber applications. This approach must be capable of capturing the key flow physics as observed experimentally [53, 54]. However, within ANSYS Fluent, there are many convergence and numerical instabilities issues faced, especially when incorporating both film stripping and edge separation sub-models [105]. Furthermore, whilst such an approach may be viable in STAR-CD, or the newer variant STAR-CCM+, uncertainties surrounding modelling techniques and the large cost associated with license fees does not make this a viable option. As such a proposed solution is to explore the feasibility of the ETFM-DPM coupling within the open source CFD software, OpenFOAM. OpenFOAM is a highly competitive toolbox that is technologically equivalent to commercial solutions, such as ANSYS Fluent or STAR-CCM+, with the advantage of having a fully documented source code [114]. One benefit of OpenFOAM comes from the fact that there are no initial costs or licensing fees. However, the greatest advantage comes from the open source philosophy and large user base, which creates a platform for users to develop its code and implement custom libraries within the already wide range of applications and models ready to use.

4.2 Objectives

The objective of this current chapter is to explore the capability of fully coupling the effects of jet-breakup and subsequent film formation within OpenFOAM, using a Lagrangian DPM approach with the ETFM. This work, whilst different, will advance upon the computational study of Hee et al. [105]. A two-way coupling is investigated such that Lagrangian droplets impinge on the surface, forming a thin film, but can also be removed through either splashing, film stripping or edge separation. As such, Figure 4.2 highlights a flow diagram of the two-way ETFM-DPM coupling with the required flow physics that need to be captured. However, within OpenFOAM, currently there is no thin film sub-model to account for the film stripping phenomenon, and whilst an edge separation model exists, it is heavily simplified and too inaccurate to use. In addition, within the ETFM-DPM methodology, there is no capability for secondary breakup of the particulate phase. Therefore, a major objective of the work carried out in this chapter, is the implementation of these models into OpenFOAM. For validation purposes, the ETFM-DPM approach will first be applied to the experimental geometry of both Shedd et al. [112] and Arienti et al. [113]. The experimental film thickness measurements and phase Doppler particle statistics of Arienti et al. are used for comparison. This work will develop and improve upon the existing bearing chamber modelling capability such that, in the future, a fully coupled two-way ETFM-DPM approach is feasible.

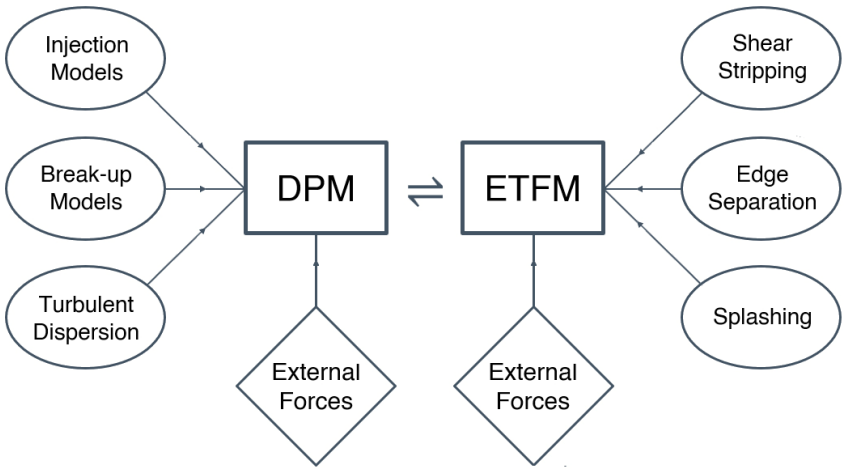


FIGURE 4.2: TWO-WAY ETFM-DPM COUPLING AND FLOW PHYSICS REQUIRED

4.3 OpenFOAM

The thin film model implemented in OpenFOAM differs from that available within ANSYS Fluent and, instead, more closely resembles that present within STAR-CCM+. In all of the codes, the momentum sources are comprised of both pressure and stress-based forces. However, in OpenFOAM, much like STAR-CCM+, all of the forces acting on the thin film are resolved, whereas in ANSYS Fluent, these forces are presented as optional settings. Hee et al. [105] experienced severe numerical instability issues when including the source terms for gas-phase momentum coupling, hydrostatic pressure head and surface tension forces. Therefore, it is unclear whether the same issues will be faced within OpenFOAM, or due to the completeness of the thin film model, these will be overcome as demonstrated by Jingyu et al. [103, 104] within STAR-CD.

To date, good results have been achieved for thin film modelling within OpenFOAM. The ETFM, first implemented by Meredith et al. [115], demonstrated capability for thin liquid film transport and was able to reproduce the partially wetted behaviour observed experimentally, for the thin film flow over a vertical plate. Through the implementation of a contact angle force, Meredith et al. were able to capture the experimental trends of falling rivulets over this vertical plate. Meredith et al. [116], developed the thin film model further, providing a more robust formulation including coupling with a spray model for impingement and splashing. A basic film separation sub-model was included to account for film transport through dripping, however this model has since been improved upon through incorporating the Rayleigh-Taylor stability analysis derived experimentally by Brun et al. [117]. Meredith et al. [116] also identify the need to account for film separation at the corners and sharp edges of a solid surface. A simplistic approach is taken and a force balance based on the description of Owen and Ryley [118] is included. This film separation sub-model assesses film curvature and once the sum of forces reaches a critical value, the film completely separates. This binary approach results in the film either completely separating at a corner, or remaining fully attached, with no range in-between.

Meredith et al. [119, 120] subsequently combined the surface film model with a sprinkler injection model, achieving a coupled DPM-ETFM approach, for validation of the fire growth and suppression within a rack storage fire. Within OpenFOAM, these implementations led to the development of the solver called *fireFoam*. Simulations were compared against experimental data, successfully allowing the determination of whether a fire will propagate or be suppressed within a rack storage. More recently, this work has been extended upon [121, 122], and understanding of the thin film modelling has revealed key aspects of fire-suppression behaviour.

The thin film methodology implemented by Meredith et al. [115, 116] was initially developed for fire growth and suppression concerned with corrugated cardboard boxes and significant progress

has been made within this field. However, whilst the thin film model is extendable to liquid flow over any surface, the authors recommend that improvements to the various sub-models are first made, before simulating other surface film flows and their associated phenomena. This becomes apparent when considering the edge separation criteria implemented by Meredith et al. [116]. For a bearing chamber simulation, it is clear that the simplified, binary approach to separation will be inadequate. The experimental visualisation results of both Gorse et al. [49] and Hee et al. [54] have revealed that, at the point of edge separation, whilst liquid separates from the surface, a proportion of fluid still remains attached. Therefore, it is likely that a more rigorous approach will need to be implemented for bearing chamber modelling. Furthermore, within OpenFOAM, there is no thin film sub-model that accounts for film shear stripping effects, due to being unnecessary within the previous investigations surrounding fire suppression systems. Finally, whilst Meredith et al. [119, 120] demonstrated capability for a DPM injection, representative of a fire sprinkler system, the boundary condition is only capable of injecting a particle diameter distribution. This is achieved using a DPM injection model, such as the *nozzle injector*, however as a result, there is no inclusion of primary atomisation or secondary breakup for the particulate cloud. Secondary breakup arises from the high shearing gas forces forming droplet Kelvin-Helmholtz and Rayleigh-Taylor instabilities, leading to the generation of smaller secondary droplets. As demonstrated in the investigation of Arienti et al. [113], it is necessary to capture such phenomena and, additionally, whilst not substantiated, it is also required for a bearing chamber simulation, especially at high rotational shaft speeds.

4.3.1 Single-Phase Validation

In order to assess the suitability of OpenFOAM, for bearing chamber applications, firstly a single-phase validation case study is performed. As such, OpenFOAM is benchmarked against both the single-phase experimental LDA measurements of Gorse et al. [33] and the previous numerical simulations for the same geometry obtained within ANSYS Fluent, as outlined in Section 3.8. To maintain compatibility, the same computational mesh is used, consisting of 2.2 million cells as shown in Figure 3.15.

In an effort to preserve consistency, an almost identical numerical methodology is outlined. For all pressure, momentum and turbulence terms, a second order upwind-biased discretisation scheme was chosen. Unlike ANSYS Fluent, there is no PRESTO! pressure scheme available within OpenFOAM, although the use of a second order discretisation scheme is suitable. For time discretisation, the Crank-Nicolson time scheme is chosen to achieve a similar bounded second order approach. However, the main difference in numerical settings arises from the pressure-velocity coupling method. Within the ANSYS Fluent bearing chamber investigation, the SIMPLE

algorithm was found to be inappropriate, leading to convergence stability issues and instead, based on the recommendations of Singh et al. [92], a Coupled algorithm was implemented. It is clear that the pressure-velocity coupling method changes the initial solution, for which as demonstrated in Section 3.8.2.1, can heavily influence the state of the RSDM, and hence, the final Taylor vortex structure. Therefore, it is important to maintain a similar pressure-velocity coupling method across the two solvers. However, within OpenFOAM the methods for the pressure-velocity coupling differ slightly; instead three main option are presented: SIMPLE, PISO (Pressure-Implicit of Split Operations) and PIMPLE (merged PISO-SIMPLE). In OpenFOAM, the SIMPLE algorithm is only available for steady state calculations, and therefore, for transient calculations the PISO algorithm must be used. The PISO approach includes a time derivation term and a more consistent equation for the pressure-velocity coupling. As a result, there is no need for under-relaxation, however, in order to satisfy the stability criteria, the Courant number must be maintained at a value less than one. In general, the OpenFOAM PISO algorithm can be regarded as equivalent to the ANSYS Fluent PISO algorithm. The PIMPLE approach offers a more advantageous alternative, permitting Courant numbers larger than one. Here, for a single time-step, first a steady state solution is obtained, using an under-relaxation approach. Once converged, the explicit parts of the equation, such as the pressure field, are solved using a number of 'outer' correction loops. Upon reaching the user-defined residual convergence criteria, the simulation then proceeds to the next time-step. Therefore, the PIMPLE algorithm available within OpenFOAM, closely resembles that of the Coupled approach found within ANSYS Fluent. As such, within this investigation, the PIMPLE algorithm is chosen through using the *pimpleFoam* solver. For the URANS turbulence modelling approach, due to the previously demonstrated success and recommendations made in Section 3.9, the SST k-ω turbulence model is selected.

4.3.1.1 Rotational Speed Driven Mode

Similar to the simulations performed within ANSYS Fluent, calculations were first initialised to a rotational shaft speed of 13,000 rpm. Following the steady deceleration procedure, outlined in Section 3.8.2.1, the shaft speed was reduced in small steps to 9,700 rpm. Once the stable Taylor vortex-like structure formed and stabilised, a sealing airflow rate was gradually introduced to the first operating condition at 6.2 g/s, allowing for comparison to both the experimental and numerical results. Figure 4.3 shows the averaged computational secondary velocity vector fields obtained within OpenFOAM, using the SST k-ω turbulence model; which has an identical formulation to that found in ANSYS Fluent. Here, within OpenFOAM, a much closer agreement to the experimental measurements of Gorse et al. [33] is found. Two similarly sized counter rotating vortices are observed, with a slightly larger right-hand, sealing side vortex; strengthened

as a result of the weak sealing airflow. Within ANSYS Fluent, for the SST k-ω turbulence model, the vortex separation line occurred at the non-dimensional axial distance of $Z = 0.70$. This resulted in a significantly larger and more dominant right-hand vortex than that observed experimentally. Gorse et al. report that within this RSDM, the vortex separation line occurs at the non-dimensional distance of $Z = 0.55$. Computationally, the OpenFOAM results predict that this separation line occurs at the distance $Z = 0.59$, therefore achieving a much closer representation of the secondary flow field structure than within ANSYS Fluent.

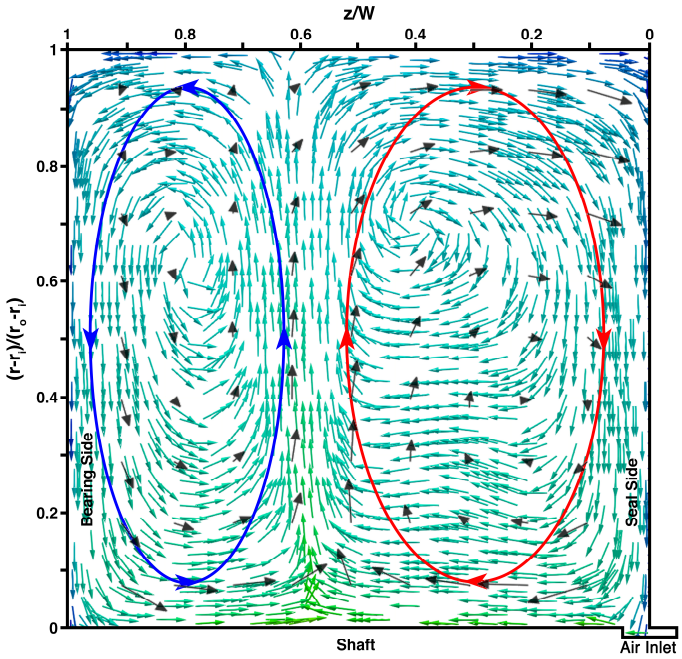


FIGURE 4.3: IN-PLANE VELOCITY VECOTRS FOR RSDM, m_g= 6.2 g/s AND n = 9,700 RPM. SUPERIMPOSED WITH GORSE [33] RSDM VECTORS (BLACK)

4.3.1.2 Sealing Air Driven Mode

As the sealing airflow rate is increased, the flow state transitions from the RSDM to a SADM. Gorse et al. [33] demonstrated that this is first observed at a sealing airflow rate of 12.7 g/s. Figure 4.4 shows the secondary flow field obtained within OpenFOAM for the SST k-ω turbulence model upon reaching this operating condition.

Similar to the results obtained within ANSYS Fluent, the vortex separation line detaches from the shaft surface and moves up the wall closest to the bearing. OpenFOAM predicts that this separation line occurs at the radial non-dimensional distance of $R = 0.63$, compared to the radial distance of $R = 0.61$ within ANSYS Fluent. For reference, the experimental results of Gorse et al. depict the vortex separating line at a distance of $R = 0.60$. Therefore, within OpenFOAM, an almost negligible difference is found, resulting in a slightly smaller than expected corner vortex

than that observed experimentally. This is also apparent from Table 4.1, which highlights the vortex central locations for both OpenFOAM and ANSYS Fluent. Both solvers, whilst predicting a similar centre for the right-hand vortex, still show large deviations from the experimental results, again with percentage errors in the region of 20%.

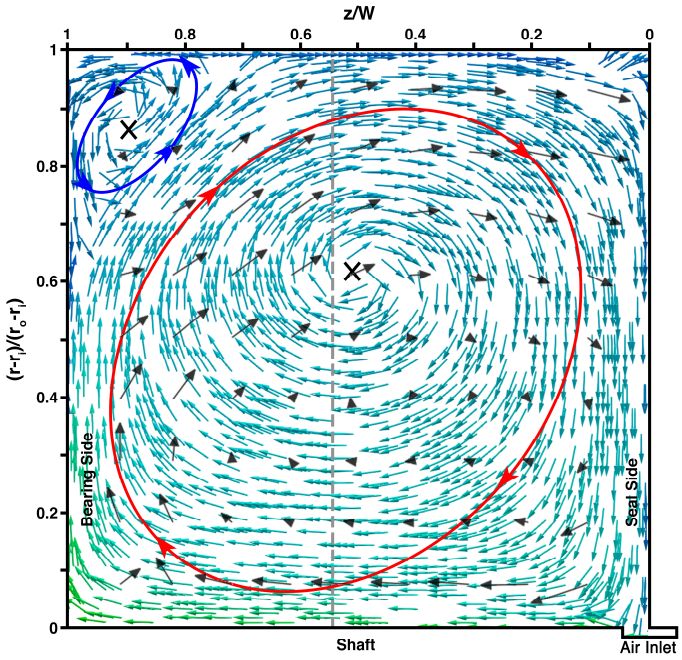


FIGURE 4.4: IN-PLANE VELOCITY VECTORS FOR SADM, m_g= 12.7 g/s AND n = 9,700 RPM. SUPERIMPOSED WITH GORSE [33] SADM VECTORS (BLACK)

TABLE 4.1: NON-DIMENSIONAL VORTEX CENTRE LOCATIONS

	Left Vortex		*Right Vortex*	
Case	***Z***	***R***	***Z***	***R***
Gorse et al.	0.88	0.90	0.35	0.45
ANSYS Fluent	0.88	0.87	0.46	0.53
OpenFOAM	0.90	0.88	0.48	0.55

Figure 4.5, shows a comparison of the non-dimensional mean tangential velocity profiles taken radially across the gap. Measurements are taken at the axial position defined by the dashed line in Figure 4.4, following the experimental procedure of Gorse et al. [33]. This axial lines is placed immediately left of the right-hand vortex centre location, which is defined in Table 4.1 and marked by the cross in Figure 4.4. Between the two CFD solvers, there is an almost negligible difference, with the discrepancies most likely occurring as a result of the prediction in vortex separation lines.

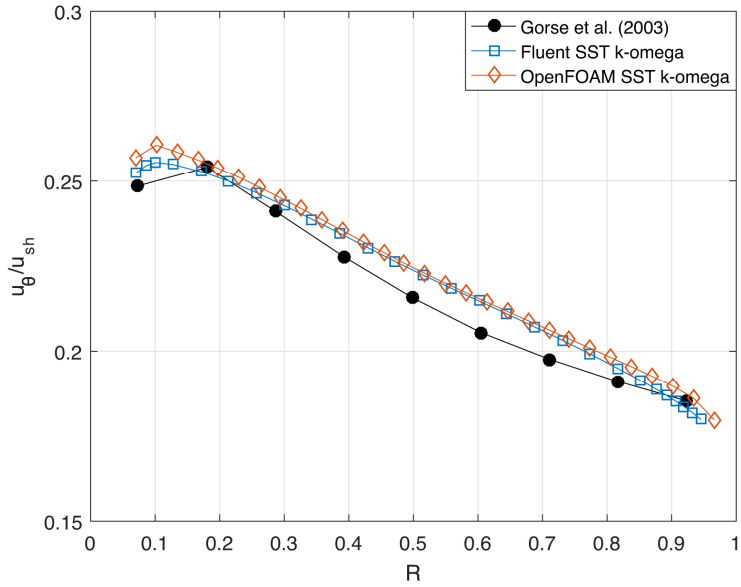


FIGURE 4.5: RADIAL PROFILES OF TANGENTIAL VELOCITY, m_g= 12.7 g/s AND n = 9,700 RPM

4.3.1.3 Single-Phase Study Conclusions

Overall, the single-phase bearing chamber study has more than demonstrated the capability of OpenFOAM when compared to the commercial solver ANSYS Fluent. Whilst a negligible difference was observed within the SADM, a much closer agreement was found to the experimental measurements within the OpenFOAM RSDM. The results of this validation study have demonstrated the single-phase capability within OpenFOAM, such that the investigation can now shift focus toward a two-phase bearing chamber simulation. However, highlighted as a necessary first step, the following section explores the capability the two-way ETFM-DPM approach within OpenFOAM, validating the findings against the case study for jet-breakup and subsequent film formation.

4.4 Validation Case Study: Jet-Breakup and Film Formation

For the aim of this current section, the geometry presented here is based on the experimental investigations of Shedd [112] and the combined computational and experimental work of Arienti et al. [113]. Figures 4.6 a) and b) illustrate the geometry and the various phenomena that result in the atomisation process of the liquid jet and thin film subjected to a high velocity crossflow.

A liquid jet is injected into a high velocity crossflow of 82 m/s, with u_{jet} = 12.7 m/s. This undergoes breakup, whereby droplets subsequently impact and become absorbed on the bottom surface causing the initial stages of film formation. The film begins to develop, growing in thickness in the direction of the crossflow; further collision of droplets with the film surface result in splashing, creating a crown and satellite drops. In addition to the droplets generated from splashing, droplets shear from the film surface due to the high velocity crossflow. Finally, at the edge of the expansion, the aerodynamic shear of the free film causes droplets to be separated from the film surface.

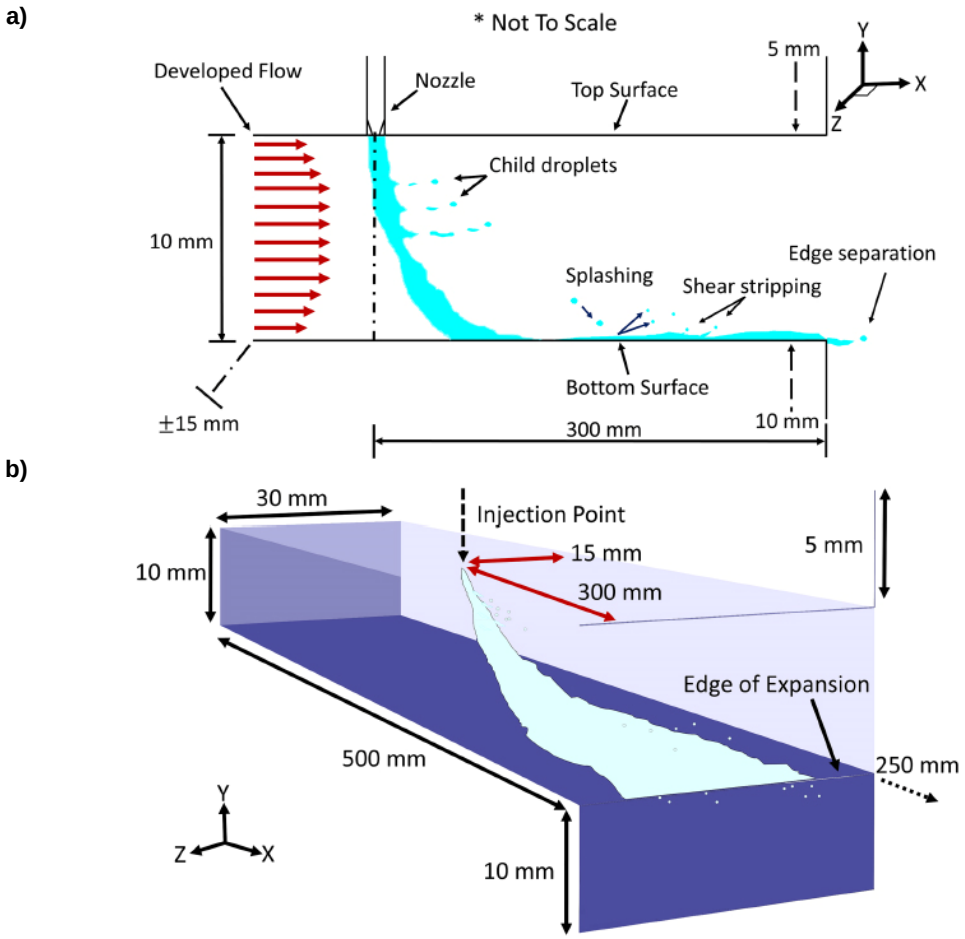


FIGURE 4.6: (a) 2D SCHEMATIC OF THE FILM FORMATION BY JET BREAKUP IN A CROSSFLOW AND THE PHENOMENA OBSERVED (b) FULL 3D DOMAIN

The computational approach undertaken by Arienti et al. [113] used their in-house code, AtoMIST. AtoMIST is a fully coupled VOF-DPM model based on empirical prescriptions for transforming liquid elements of the jet or film surface into Lagrangian parcels by atomisation and conversely through impingement directly at the film surface. AtoMIST is comprised of user-defined functions implemented within ANSYS Fluent version 6.3. When solved with a large eddy simulation (LES) approach, Arienti et al. reported that to reduce the computational cost, the VOF fluid interface was sufficiently coarsened and only first order discretisation schemes were used. Although, as demonstrated by Hee et al. [105], a more computationally efficient approach to capture the jet-breakup and thin film formation can be achieved using a coupled ETFM-DPM methodology. However, there is still considerable uncertainty regarding this approach.

4.5 Coupled Euler-Lagrange and Eulerian Thin Film Method (ETFM-DPM)

Within OpenFOAM there is not a standard solver that can be applied to every simulation. Instead the user must choose from a range of solvers with careful consideration to the problem under investigation. For the case study under consideration, the following highlights the possible choices that are applicable to solving the current flow field.

One such solver, *reactingParcelFilmFoam* is a compressible, transient solver for turbulent flows with the capability to track reacting, multiphase particle clouds in addition to surface film modelling; therefore, a fully coupled ETFM-DPM solver. The *reactingParcelFilmFoam* solver is derived from the original *fireFoam* solver, developed by Meredith et al. [119, 120], intended for a more generic application of the two-way ETFM-DPM coupling. For the geometry and flow conditions under consideration, the highest Mach number is 0.27 and whilst the flow can be assumed to be incompressible, the use of a compressible solver is the only option for ETFM-DPM coupling within OpenFOAM. Another major limitation of *reactingParcelFilmFoam* is the inability for both primary atomisation of a liquid jet and the secondary breakup of droplets.

Within the OpenFOAM Lagrangian solver library, there exists the solver *sprayFoam*, this is a similar compressible solver to reactingParcelFilmFoam, although its purpose is to model spray characteristics. The main advantage is that the spray particle cloud includes models for both primary and secondary atomization, however the biggest drawback is that there is no capability for surface film modelling. Clearly, both *reactingParcelFilmFoam* and *sprayFoam* have the capability to model certain characteristics of the phenomena observed during the experiments of Arienti et al. [113], however, individually, neither solver is suitable at capturing the full features and flow physics required.

4.5.1 The Newly Developed Solver: sprayParcelFilmFoam

Out of the necessities of the current experimental case study, highlighted in Section 4.4, and ultimately for bearing chamber investigations discussed in Section 4.1, the new in-house OpenFOAM solver *sprayParcelFilmFoam*, has been developed and its application is demonstrated within scope of this work. This new solver takes the foundation of the *reactingParcelFilmFoam* solver and replaces the reacting multiphase particle cloud libraries with the spray particle cloud libraries of *sprayFoam*, hence the name *sprayParcelFilmFoam*. Thus, generating a compressible transient solver capable of a full two-way ETFM-DPM coupling with models for both primary atomisation and secondary breakup of the particulate cloud. Two new thin film sub-models have been developed and implemented, these are based on the empirical

studies for both a film stripping and edge separation criterion. Furthermore, in order to achieve a more accurate statistical representation of droplets, modifications to the DPM particle injector code are established. In addition, for the DPM particles, the need for specifying transport and thermodynamic models has been modified within the scope of this work, such that, constant particle properties (ρ, μ, σ) can now also be applied, meaning that any liquid can be implemented. Without full knowledge of the liquid thermophysical property data, this approach is more than suitable for both the Arienti case study and the G2TRC bearing oil shedding rig which are operated under atmospheric conditions.

The following sub-sections describe in detail the development of *sprayParcelFilmFoam*. This includes the DPM and surface film configurations implemented within this new in-house solver intended for simulating the two-phase flow, and specifically for aeroengine bearing chamber applications.

4.5.1.1 Discrete-Phase Modelling

Within the Euler-Lagrange approach, for the fluid phase, Eulerian continuum equations are solved using a conservation of momentum approach, whilst the particle trajectories are determined through evaluating Newton's equations for the particulate phase. For the present work, a two-way turbulence coupling is enabled to account for the force exerted by the particles on the fluid and vice-versa. This is instead of the default one-way coupling, where particles have a negligible effect on the flow. As such, the following equation is solved to obtain the particle trajectories:

$$m_p \frac{d\boldsymbol{u}_p}{dt} = \boldsymbol{F}_p \tag{4.1}$$

Once the particle force has been calculated, through integrating the particle velocity, the trajectories are determined. $\boldsymbol{F}_p$ represents the sum of forces acting on the particle. For a standard spherical particle:

$$\boldsymbol{F}_p = \boldsymbol{F}_D + \boldsymbol{F}_g + \vec{\boldsymbol{F}} \tag{4.2}$$

Where $\boldsymbol{F}_D$ represents the drag force, this is the dominant force that determines the particle trajectory. $\boldsymbol{F}_g$ is the gravity and buoyancy force and $\vec{\boldsymbol{F}}$ represents the external forces acting on the particle that can be specified by the user. Some examples include the pressure gradient force $\boldsymbol{F}_p$, the Saffman lift force $\boldsymbol{F}_S$, the Basset acceleration force $\boldsymbol{F}_B$, the Magnus force $\boldsymbol{F}_M$ and finally the virtual mass force $\boldsymbol{F}_m$. For the Arienti validation case study, and additionally bearing chamber simulations, these additional user-defined particle forces are not always necessary. The following provides a brief description of each force and a justification as to why they are not implemented:

- The pressure gradient force, $\boldsymbol{F}_p$, alters the droplet trajectory based on the pressure differential in the gas flow, incorporating the effects of either shock or expansion waves. *A pressure gradient is not observed in the Arienti case study. However, this may be required for bearing chamber investigations which utilise a pressure differential across the bearing.*
- The Saffman force, $\boldsymbol{F}_S$, is the lift force due to shear intended for small particles on the submicron scale. *This is not applicable for either case study: Arienti et al.* [113] *report a minimum particle diameter of 20μm; and within bearing chambers, Glahn et al.* [45] *observed a minimum of 14μm.*
- The Basset acceleration force, $\boldsymbol{F}_B$, accounts for the past acceleration of droplets due to viscous effects. *This can effectively be ignored for both cases, since the gas-fluid density ratio is very small, due to the proportionally larger droplet densities.*
- The Magnus force, $\boldsymbol{F}_M$, occurs due to the rotation of a droplet moving through the gas-phase. *For either case, whilst droplet rotation may occur due to the high gas flow velocities, the resultant effect on particle trajectories will be negligible, hence it is ignored.*
- The virtual mass force, $\boldsymbol{F}_m$, arises from the acceleration of droplets within the gas-phase, it is the force needed to accelerate the gas surrounding the droplet. *The virtual mass effect is only applicable when the fluid density is significantly smaller than that of the gas-phase; hence for both cases it is not included.*

The viscous drag force, $\boldsymbol{F}_D$, provides the force acting on the particle as a result of the difference in velocity between the gas-phase and the liquid droplet. For a spherical droplet, the drag force is therefore assumed proportional to this velocity differential, $(u_g - u_p)$, and determined by:

$$\boldsymbol{F}_D = \frac{18\mu_g}{\rho_p d_p^2}\frac{C_D Re_{rel}}{24}(u_g - u_p) \tag{4.3}$$

Here, the particle density and diameter are defined by ρ_p and d_p, μ_g is the gas viscosity and C_D is the drag coefficient. Re_{rel} is the relative Reynolds number, which is defined as:

$$Re_{rel} = \frac{\rho_g d_p |u_p - u_g|}{\mu_g} \tag{4.4}$$

For the default droplet drag model, it is assumed that the droplet exists as a sphere throughout the domain, as such the drag coefficient, C_D, for a spherical droplet can be predicted as:

$$C_{D,sphere} = \begin{cases} \dfrac{24}{Re_{rel}}\left(1 + \dfrac{1}{6}Re_{rel}^{2/3}\right) & Re \leq 1000 \\ 0.424 & Re > 1000 \end{cases} \tag{4.5}$$

However, an initially spherical droplet moving through a gas-phase may become significantly distorted if the gas Weber number becomes sufficiently large. To account for this droplet distortion, as a result of the high shearing gas forces, a dynamic drag model can be used [123]. The dynamic drag model linearly varies the drag force from a sphere to a disc based on the particle spherical deviation, which is calculated from the oscillation equations present in the secondary breakup models. The use of a blending function makes the dynamic drag model applicable to almost any type of flow. Furthermore, within a bearing chamber application, the use of a dynamic drag model will also help to better account for the drag on ligaments shed from the front-face edge into the bearing chamber. Whilst these ligaments are not strictly discs, this approach is a necessary approximate to account for their complex and non-spherical shape, as observed experimentally [54]. In general, for the dynamic drag model, the drag coefficient, C_D, is determined as:

$$C_D = C_{D,sphere}(1 + 2.632s) \tag{4.6}$$

Where s is the droplet distortion, calculated when using a secondary breakup model. When there is no distortion, $s = 0$, such that the drag coefficient is equal to the spherical drag coefficient and at the maximum distortion, $s = 1$, the drag coefficient subsequently resembles that of a disk.

Finally, the gravity and buoyancy force, $\boldsymbol{F}_g$, is automatically enabled and required for all simulations, this occurs through including the gravity sub-dictionary file; here, specifying both the magnitude and direction of the gravity vector. To determine the importance of the gravity source term, the dimensionless Froude number, Fr, can be evaluated.

$$Fr = \frac{|u_{p,\infty}|}{\sqrt{d_p g}} \tag{4.7}$$

The velocity of the droplet, $u_{p,\infty}$, is that found in the freestream. The Froude number gives a ratio of the droplet inertial forces to the gravitational forces, therefore at high Froude numbers, the inertia effects will dominate, and a negligible effect of gravity will be observed. Within the experimental results of Arienti et al. [112], downstream of the expansion edge, droplet diameters are in the range of 20μm to 60μm, with axial velocities ranging from 20 m/s up to 80 m/s. Therefore, over this range, the Froude number is approximately 2.5×10^3, suggesting that inertial effects will dominate over the gravitational forces. However, at the injection location of the liquid jet, based on the experimental conditions, a smaller Froude number in the order of 10^2 is observed. For bearing chamber applications, based on experimental observations, at high rotational shaft

speeds, the effects of gravity are almost negligible within the smooth shear dominated flow regime. Although, at low rotational shaft speeds, the effects of gravity are more noticeable and therefore will likely have an impact on the trajectories of large diameter particles and ligaments. Overall, in certain cases whilst the effects of gravity might be negligible, there is uncertainty at which point this occurs, as such for all of the simulations carried out, the effects of gravity are included. Additionally, for both the Arienti validation case study and bearing chamber applications, whilst the buoyancy force is calculated by default, it can be effectively ignored since the gas-fluid density ratio is very small, as a result of the large droplet densities.

Primary Atomization

For the experiments of Arienti et al. [113], when exiting the nozzle, the liquid jet accelerates through the orifice and subsequently causes the ligaments to break up to due instabilities on the gas-liquid interface. To simulate this primary atomisation of the liquid jet, the *coneNozzleInjector* injection model is employed in combination with a droplet diameter distribution.

A major limitation of all OpenFOAM injection models is that, the number of particles injected per parcel, N_p, cannot be less than one. As with most spray injections, not every single droplet injected is tracked. To reduce the computational expense, the concept of a parcel is introduced, in which several droplets all of which have identical properties (e.g. position, velocity and diameter) can be represented and tracked under a single parcel. For unsteady tracking, each parcel represents a fraction of the total mass flow released in a given time-step. The user specifies a fixed number of parcels or injection streams to produce a statistical representation of the particulate distribution. For a mass-based injection, such as one where a mass flow rate is provided, it is required that the same amount of liquid mass must be carried by all parcels. To account for the momentum exchange with the gas, the sum of the parcel mass flow rate and the number of particles per parcel is equal to the actual mass flow rate multiplied by the real sum of particles. This means that the number of particles and the mass flow rate is fixed, but the number of parcels can vary.

For a given size distribution and mass flow rate, it is therefore possible that a single parcel can carry a fraction of a particle, i.e. the number of particles carried per parcel is less than one, $N_p < 1$. Within OpenFOAM, if this happens, then the parcel will not be injected into the domain and a reduced amount of mass will reported. The historical documented solution to this, was to reduce the number of parcels injected per time-step. This phenomenon is highlighted in Figures 4.7 a) and b) for a generic injection condition, using a normal distribution. Figure 4.7 a) shows the resulting diameter histogram when the parcel limit is exceeded. However, under the same injection conditions, but with this limit removed, Figure 4.7 b) displays the correct normal

diameter distribution. It is clear that from Figure 4.7 a), overall there are a reduced number particles, and hence particulate mass, resulting from the lack of larger diameter particles injected into the domain.

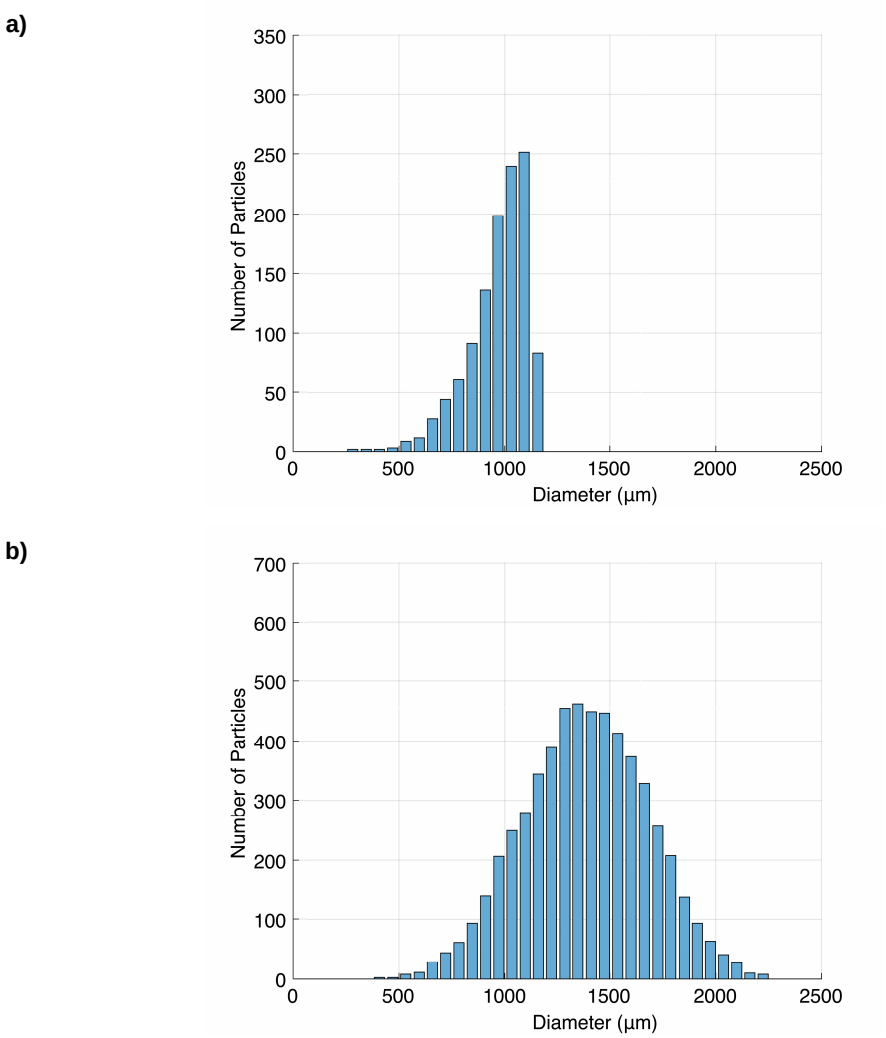


FIGURE 4.7: (a) DIAMETER HISTOGRAM EXCEEDING PARCEL LIMIT VERSUS (b) DIAMETER HISTOGRAM WITH PARCEL LIMIT REMOVED

Under the nozzle operating parameters found in the experiment of Arienti et al. [113], to achieve a full injection of the size distribution, $N_p \geq 1$, the number of parcels injected per second must be reduced to less than 100,000. Initial simulations showed that the constraint of 100,000 parcels per second limited the statistical approximation of the particulate flow and led to inaccurate results. For reference, Hee et al. [105] investigated 500 to 2000 injections streams, which corresponds as 10 to 40 million parcels per second. Therefore, this lower limit of one particle per parcel was removed, in order to achieve mass conservation of the particulate flow when exceeding the previous injection limit of 100,000 parcels per second, i.e. $N_p < 1$. Furthermore, the use of a high number of parcels injected per second is also advantageous in other aspects of the DPM

injection. For example, the effects of incorporating a particulate size distribution with additional DPM sub-models, such as the particle turbulent dispersion model, are multiplicative. This subsequently means that a larger number of parcels may be required to accurately capture the particle distribution and its trajectory. Therefore, if we consider the number of parcels to be a statistical approximation of the particulate flow field, then it is also reasonable to want to simulate more elements or trajectories than there are physical particles. As a result of this work, this change has now been fully implemented in all OpenFOAM builds for versions 6.0 and above.

Secondary Breakup

Droplets can experience high shear-forces imparted by the gas flow, leading to Kelvin-Helmholtz (KH) and Rayleigh-Taylor (RT) instabilities at the fluid interfaces. This subsequently leads to breakup of the particulate phase. There are many breakup models available within OpenFOAM, although the KHRT model is the most popular and successfully validated hybrid breakup model available [124, 125]. The KHRT breakup model is chosen for the scope of this work, with model constants being set to the default values as recommended, these are based on the original formulation by Reitz [126].

Small child droplets are sheared off the parent droplet due to droplet slip velocities which result in Kelvin-Helmholtz instabilities. In addition, the droplet acceleration forms Rayleigh-Taylor instabilities, which eventually, act to completely shatter the droplet. Both KH and RT instabilities grow simultaneously and therefore compete with each other; such that breakup will occur due to RT instabilities given sufficient time, meanwhile KH breakup occurs continuously. Figure 4.8 shows the two types of breakup. Both mechanisms model droplet breakup through tracking the wave growth on the droplet surface, breakup occurs due to the fastest growing instability.

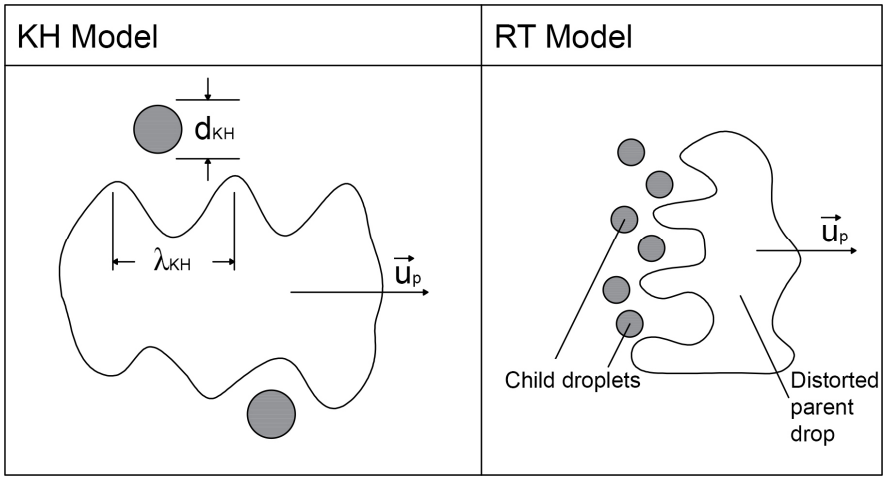


FIGURE 4.8: ILLUSTRATION OF THE KELVIN-HELMHOLTZ AND RAYLEIGH-TAYLOR INSTABILITY MECHANISMS

Particle Turbulent Dispersion

Hee et al. [105] demonstrated the importance of including the effects of turbulence on the particle motion, as opposed to the default method which calculates particle trajectories from the mean velocity. Using a stochastic discrete random walk (DRW) approach, the interaction of a fluid particle with a gas-phase turbulent eddy is modelled. As such, the velocity is perturbed in a random direction following a Gaussian random number distribution. A characteristic time scale is also defined based on either the lifetime of the turbulent eddy or the time taken for the particle to cross the eddy. Upon exceeding either of these time scales, a new velocity fluctuation is calculated.

4.5.1.2 Surface Film Modelling

Within OpenFOAM, Meredith et al. [115] were the first to implement a thin film model. Due to the thin nature of the film, 2D continuity and momentum equations can be solved to obtain the film thickness and wall-tangential velocity components. For mass conservation, the integrated equation is defined as:

$$\frac{\partial \rho_l \delta}{\partial t} + \nabla_s . \left[\rho_l \delta \boldsymbol{u}_f\right] = S_{\rho_l \delta} \tag{4.8}$$

$\boldsymbol{u}_f$ is the mean film velocity, ∇_s is the surface tangential vector differential operator and $S_{\rho_l \delta}$ is the mass source per unit wall area due to the various film phenomena such as impingement, splashing, separation and stripping. Integrating over the film height, the momentum transport equation becomes:

$$\frac{\partial \rho_l \delta \boldsymbol{u}_f}{\partial t} + \nabla_s \left[\rho_l \delta \boldsymbol{u}_f \boldsymbol{u}_f\right] = -\delta \nabla_s p + \boldsymbol{S}_{\rho_l \delta \boldsymbol{u}_f} \tag{4.9}$$

The momentum source terms are comprised of both pressure-based and stress-based forces. The capillary effects, p_σ, due to surface tension, hydrostatic pressure head, p_δ, due to gravity and the local gas-phase pressure, p_g, comprise of the forces within the pressure term, p. Whereas, the gravity body force, $\rho g_\theta \delta$, the contact-angle force, τ_θ, and the viscous shear stresses at both the film-gas interface, τ_g, and the film-wall interface, τ_w, make up the stress term, $\boldsymbol{S}_{\rho_l \delta \boldsymbol{v}_f}$. Similar to the STAR-CCM+ solver, within OpenFOAM these sources are inherent to the thin film formulation, unlike the optional settings within ANSYS Fluent. The following provides a brief description of each force.

- The capillary effects, p_σ, arises from the surface tension forces, typically this works as a restoring force acting to dampen surface waves.
- The hydrostatic pressure head, p_δ, results from the normal force due to gravity acting on the film. This is responsible for the effect of film spreading, causing the film to accelerate and move toward regions of lower thickness.
- The gas-phase pressure momentum coupling, p_g, accelerates the film in the direction of the pressure gradient, i.e. the film will move from a region of high pressure to low pressure.
- The gravity body force, $\rho g_\theta \delta$, is the gravity component in the tangential direction of the wall, typically accelerating the film in a direction parallel to the wall.
- The contact-angle force, τ_θ, is used to simulate the partially wetting behaviour of the film, resulting in wet and dry regions separated by the contact line.
- Together, the shear stress terms at the gas interface, τ_g, and the film-wall interface, τ_w represent the net viscous shear force, this is derived from the assumption of a quadratic film velocity profile at the wall.

To date, within OpenFOAM, there exists no surface film sub-model for a film stripping criterion. Whilst an edge separation criteria exists, it is heavily simplified and too inaccurate to use within this scope. As an objective of the work carried out, new film stripping and separation sub-models were developed and incorporated into OpenFOAM for the very first time, this is highlighted in the following sub-sections.

Shear Stripping

Under a shear stripping criterion, it is possible to model wave-induced instabilities on the film surface which result in the ejection of droplets. The model assumes, a flat film surface is disturbed by sinusoidal perturbations for which there is one linearly growing most unstable wavelength. A three stage process governs the wave stripping phenomena and the model implemented here is based on the work of Mayer [127]. Figure 4.9 highlights this three-stage process.

At a sufficiently high shearing rate and a minimum film thickness, the critical conditions for droplet ejection are satisfied. For the first stage, at the liquid-gas interface, waves develop on the film surface as a result of the shearing forces between the high velocity gas flow and the fluid film. These waves grow, rolling up to form cylinders of fluid on the film surface due to the Kelvin-Helmholtz instability; eventually the cylinders become unstable and are ejected into the neighbouring gas-phase. For the final stage, spherical droplets form as the cylinders further break up, as a result of Rayleigh-Taylor instabilities. The most unstable wavelength which defines the

surface instability determines the diameter of these child droplets. It is accepted that ejection can occur once the minimum height for surface stripping is exceeded.

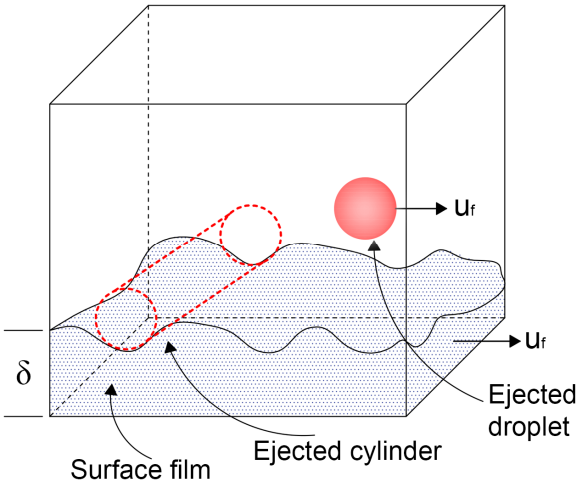


FIGURE 4.9: PROCESS OF WAVE FORMATION, CYLINDER FORMATION/EJECTION AND DROPLET EJECTION UNDER THE SHEAR STRIPPING CRITERIA

As waves form on the fluid surface, the film viscous forces damp them. Through balancing the wave growth and damping characterizes a wave frequency, f. Mayer states that, for wave growth and eventual break off, f must be greater than zero, such that there must be a minimum wavelength for growing waves, λ_{min}:

$$\lambda_{min} = 2\pi\sqrt[3]{16}\left(\frac{\mu_l\sqrt{\sigma/\rho_l}}{\alpha\rho_g u_g^2}\right)^{2/3} \tag{4.10}$$

Here, α is a sheltering parameter with a default value of 0.3, which defines the proportion of the wave crest exposed to the shearing airflow. Based on the minimum wavelength, the minimum film height required for droplet ejection is:

$$\delta_{min} = C_H\frac{\lambda_{min}}{2\pi} \tag{4.11}$$

Where C_H is a user defined coefficient to initiate film stripping. Within the scope of this thesis, the default value is one used, however lowering this limit reduces the film thickness threshold for wave stripping to occur. The surface wave amplitude then determines the film height to strip:

$$\delta_a = \left[\frac{3}{4}\left(\frac{2}{3.78}\right)^3\right]^2\pi\lambda_{min} \tag{4.12}$$

This results in a droplet diameter of:

$$d_d = C_l \sqrt{\frac{\lambda_{min}\delta_a}{\pi}} \tag{4.13}$$

C_l is the droplet diameter coefficient which arises from Rayleigh theory and has a default value of 3.78. The coefficient determines the ratio of the droplet diameter generated to that of the parent cylinder diameter. Stripped droplets injected into the gas-phase have an initial velocity and trajectory equivalent to that of the film prior to stripping, surface tension effects are assumed constant. No consideration of a time scale is included in the original stripping model and therefore a sufficiently small time-step is required for simulations.

Edge Separation

The curvature separation model within OpenFOAM is based on the force balance of Owen and Ryley [118]. This model does not include surface tension forces and separation occurs on a binary level: either all the mass becomes separated or the film remains fully attached. For the scope of this work, the curvature separation model is too inaccurate and oversimplified, therefore an edge separation criterion is implemented based on the work of Friedrich et al. [128]. Friedrich et al. provide an experimentally validated force balance model which includes surface tension forces and a wall angle dependence, therefore improving on the analysis of Owen and Ryley.

Depending on both the gas and liquid flow conditions, when a liquid film reaches a sharp edge, a proportion of the film may separate from the surface and undergo breakup, or conversely, it may turn the corner and remain fully attached to the wall. This phenomenon is shown in Figure 4.10. Friedrich et al. propose an edge separation model based on two criteria: a critical wall angle and a critical force ratio. As the film approaches the corner, the film separation is driven by its momentum, which is balanced by the surface tension and gravitational forces.

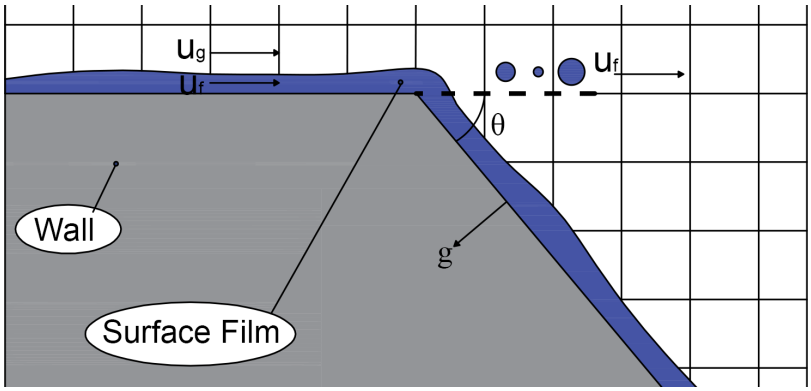


FIGURE 4.10 SCHEMATIC SHOWING THE PROCESS OF EDGE SEPARATION AROUND A SHARP CORNER

Friedrich et al. present a force balance between the film inertia, surface tension and body forces acting on the film. Thus, giving a non-dimensionalised force ratio:

$$F_{ratio} = \frac{We_f}{1 + \frac{1}{sin\theta} + Fr_f We_f \left(\frac{L_b}{\delta}\right)\left(\frac{1}{tan\theta}\right)} \tag{4.14}$$

Where We_f, is the film Weber number, Fr_f is the film Froude number and L_b is the characteristic length of the film after the corner and is based on the experimental correlations of Arai and Hashimoto [129]. Edge separation begins when the force ratio becomes greater than one, which implies that the inertial force becomes large enough for the film to separate from the wall. At a given force ratio, an experimentally derived percentage of mass is separated from the film. Which is calculated as a function of:

$$Y = 1 - e^{0.411544\left(\frac{1-F_{ratio}^2}{F_{ratio}}\right)} \tag{4.15}$$

This is obtained through a curve fit to the experimental data of Friedrich et al. Overall, the mass separated from the film is injected back into the Lagrangian frame of reference as droplets, which by Friedrich's separation model are assumed to have a diameter equal to the separated proportion of the film thickness at the edge. Separated droplets injected into the gas-phase have an initial velocity equivalent to that of the film prior to separation. More complex methods exist for determining the droplet diameter, although these are not included in the work presented.

Splashing

Finally, within OpenFOAM, a splashing criterion is available for the parcel interaction with the surface film, this is based on the work of Bai et al. [130]. Both wet and dry surface roughness coefficients need to be supplied, for which the recommended values presented by Bai et al. are $A_{Dry} = 2630$ and $A_{Wet} = 1320$ respectively. Bai et al. report that the surface roughness coefficient is conducive to a splashing event and is a decreasing function of surface roughness, which is derived from experimental measurements:

$$A = \frac{3.8578 - \log(r_s)}{0.0013} \tag{4.16}$$

Where r_s is the surface roughness and typical values of A range from a smooth surface of 5,200 to a rough surface of 1,300. Bai et al. propose that for a wet surface, the continuous impingement of droplets will sufficiently disturb the surface of the film, causing the splashing dynamics to behave similar to that of a rough wall, hence the recommended value of 1320 for A_{Wet}.

Subsequently, these surface roughness coefficients are used to determine the critical splashing Weber number for either a wet or dry surface, this is calculated as a function of the Laplace number using the following formula:

$$We_c = A_{Dry/Wet} La^{-0.183} \tag{4.17}$$

Whereby, the Laplace number represents the ratio of the droplet surface tension to its momentum transport. If the droplet Weber number exceeds the critical Weber number then splashing occurs, otherwise the droplet adheres to the surface/film. Furthermore, to resolve the magnitude and direction of splashed droplets, the skin friction coefficient, C_f, also needs to be provided for which typical values are in the range of $0.6 < C_f < 0.8$, here the default value of 0.6 is chosen [114].

4.6 Parametric Study: Jet-Breakup and Film Formation

The follow section describes in detail the process of modelling of the experimental domain explored by both Shedd [112] and Arienti et al. [113] involving the jet-breakup and subsequent film formation due to a high velocity crossflow.

A series of parametric studies were performed in order to isolate certain parts of the problem, systematically develop the *sprayParcelFilmFoam* solver and test both the newly created film stripping and separation sub-models. Preliminary studies considered numerical settings for a case involving only a straight duct mesh (i.e. no expansion), exploring the effects of mesh density and time-step size. This baseline provided the necessary steps to investigate the film stripping sub-model in isolation. The results of the straight duct mesh study were extended to evaluate the full expansion duct domain, representative of the experimental geometry shown in Figure 4.6. The straight duct mesh and expansion duct domain are abbreviated to SD and ED respectively. Subsequent investigations focused on the number of parcels injected per second, additional DPM configurations and finally the problem as a whole through including the edge separation criterion. A further case study into the removing certain film momentum source terms was also conducted, to better understand their individual effects on the overall film thickness.

Table 4.2 summarizes these parametric studies, for which the outcomes and results are discussed in Section 4.6.3. Within Table 4.2, for cases 1 to 6, a straight duct mesh (SD) is considered, such that the film stripping criteria could be isolated from the effects of the edge separation and their respective sub-models could be tested independently. Cases 7 to 14 employed the extended expansion duct domain (ED). The following highlights the objectives of the parametric studies conducted.

a) A mesh independence study is performed for cases 1, 2 and 3, to establish a suitable mesh that minimises cost. Mesh densities range from 380 thousand to 2.2 million cells, all satisfying a y^+ criteria of less than one.

b) Cases 2, 4 and 5 evaluate the impact of the airflow time-step on the particle trajectories and surface film formation. A time-step of 5×10^{-6} corresponds to a maximum cell Courant number of 1, whereas this becomes 20 at a time-step of 1×10^{-4}.

c) Case 6 includes the addition of the film stripping sub-model and is compared to case 2. This is used to assess the fidelity of the film stripping sub-model implemented here within OpenFOAM.

d) Once the film stripping sub-model was established within the straight duct geometry, the extended expansion duct geometry was investigated. Mesh densities were extrapolated from the straight duct geometries, resulting in two hex-dominant meshes. Case 7 uses 2.57 million cells (2.54 million hexahedral and 30 thousand polyhedral cells) with case 8 resulting in 3.74 million cells (3.72 million hexahedral and 20 thousand polyhedral cells).

e) Cases 7, 9 and 10 are used to examine the effect on the film solution by including particle turbulent dispersion (DRW) and then subsequently a splashing criterion.

f) The optimum number of parcels injected per second is assessed between cases 10, 11 and 12. To obtain an accurate statistical representation of the particulate flow this is necessary, due to the multiplicative effect of including the various DPM sub-models.

g) Case 13 incorporates all the previously investigated DPM and film sub-models with the inclusion of the novel edge separation model.

Case 14 investigates removing both pressure-based and stress-based source terms from the film momentum transport equations to assess the differences between both OpenFOAM and ANSYS Fluent. Within OpenFOAM, the film momentum equation solves for both pressure and stress-based source terms; whereas within Fluent, these are presented as additional options controlled by the user. Hee et al. [105] experienced significant numerical instability and convergence issues when including either of the pressure forces: p_g, p_δ or p_σ. Further issues with the edge separation criteria resulted in Hee et al. performing the majority of simulations on a straight duct case; meaning the gravity body force term: $\rho g_\theta \delta$, where g_θ is the gravity component parallel to the wall, will have no effect. As such a simulation is run with these source terms removed, to better understand their effects. The case is run with all previous sub-models included within Case 13.

TABLE 4.2: PARAMETRIC STUDIES INVESTIGATED FOR: MESH DENSITY, AIRFLOW TIME-STEP, PARCEL INJECTION COUNT AND SUB-MODELS

Case No.	*Time-step (s)*	*No. of Parcels Injected (s^{-1})*	*Sub-models*	*Mesh & Cell Count (k)*
1	5×10^{-6}	10×10^{6}	-	380 (SD)
2	5×10^{-6}	10×10^{6}	-	920 (SD)
3	5×10^{-6}	10×10^{6}	-	2200 (SD)
4	1×10^{-5}	10×10^{6}	-	920 (SD)
5	1×10^{-4}	10×10^{6}	-	920 (SD)
6	5×10^{-6}	10×10^{6}	Stripping	920 (SD)
7	5×10^{-6}	10×10^{6}	Stripping	2570 (ED)
8	5×10^{-6}	10×10^{6}	Stripping	3740 (ED)
9	5×10^{-6}	10×10^{6}	Stripping DRW	2570 (ED)
10	5×10^{-6}	10×10^{6}	Stripping DRW Splashing	2570 (ED)
11	5×10^{-6}	20×10^{6}	Stripping DRW Splashing	2570 (ED)
12	5×10^{-6}	40×10^{6}	Stripping DRW Splashing	2570 (ED)
13	5×10^{-6}	20×10^{6}	Stripping DRW Splashing Separation	2570 (ED)
14	5×10^{-6}	20×10^{6}	$-(p_g, p_\delta, p_\sigma)$ $-(\rho g_t \delta)$	2570 (ED)

4.6.1 Mesh

Figure 4.11 shows the computational domain modelled for the expansion duct geometry under investigation. A hex-dominant mesh was generated within the OpenFOAM meshing tool snappyHexMesh. In order to fully capture the recirculation region, the whole domain length was parametrically tested and extended to 2.5m. Prior to simulating the full expansion duct case, the expansion section was removed, creating a straight ‘filmer’ duct domain. This filmer duct allowed the stripping phenomena to be isolated and investigated individually.

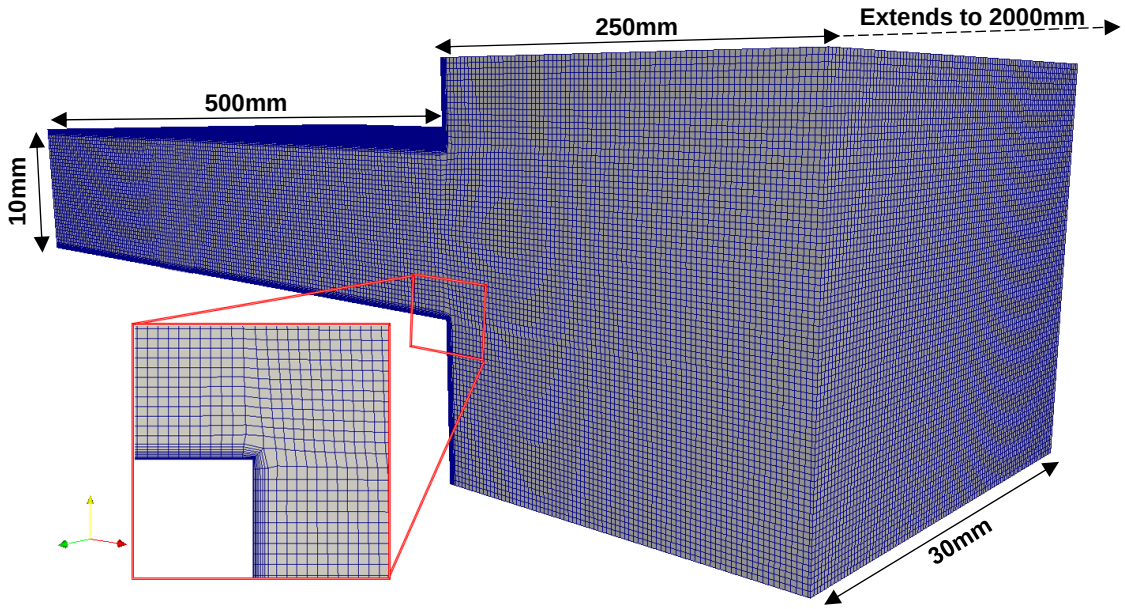


FIGURE 4.11 HEX-DOMINANT MESH WITH 2,570K CELLS, DOMAIN LENGTH CLIPPED TO 0.75m FOR VIEWING PURPOSES

4.6.1.1 Hex-Dominant Meshing

Within OpenFOAM, in order to solve for the thin film region, an additional 'dummy' mesh is generated to store the fluid properties and computed variables. This secondary mesh is extruded from the film surface of the primary mesh region by a uniform cell thickness specified by the user. This cell thickness has no implication on the final film solution; however, it needs to be carefully selected in order to generate a suitable mesh, such that there are no overlapping, highly skewed or non-orthogonal cells. Within the context of this study it has also been observed, that in some certain special cases, such as the current expansion duct geometry, a uniform cell aspect ratio within the dummy mesh is required to avoid numerical instabilities within the film velocity. This type of extruded film mesh can easily be achieved using a hex-dominant meshing approach, as a result of the method in which boundary layers are developed.

Instead, these numerical instabilities arise from the extruded film mesh region when using a structured hexahedral grid. Within the Arienti case study, when using a pure hexahedral mesh, the y^+ grading around the expansion edge causes difficulties in the extruded film mesh region. In order to prevent overlapping cells, a very thin extrusion height has to be specified. However, more importantly, the difference in wall spacing around the corner causes very high aspect ratio cells in the extruded film mesh, resulting in the film velocity diverging. One such solution would be to ensure an equal mesh spacing around the corner, however due to the strict meshing constraints of structured hexahedral meshes, this results in a very fine mesh and hence a significant computational cost. This is in part due to having a very fine mesh region in the critical part of the

flow field and therefore, in order to satisfy the Courant number, a very small time-step needs to be specified. Overall, whilst a solution can be obtained using this methodology for a structured hexahedral mesh, it is not feasible due to the computational cost associated. Instead a much more readily available solution can be achieved using a hex-dominate polyhedral mesh.

Historically within CFD studies, hexahedral elements have been favoured over tetrahedral elements due to having greater numerical accuracy and being able to maintain orthogonal grids for wall-bounded flows. Whilst tetrahedral elements are easy to generate and can map complex geometries; numerical diffusions are high and large densities of elements are required for near-wall treatments. Hexahedral and tetrahedral elements have been well studied and it is generally agreed that due to numerical instabilities and convergence issues, tetrahedral elements are not ideal. However, more recently the use of polyhedral elements has been investigated, showing that the limitations linked with tetrahedral elements can be surpassed, whilst producing fewer elements and maintaining the same levels of automatic mesh generation [131]. In addition, it is proposed that to the greater number of connected elements within a polyhedral, there is an improvement in accuracy over tetrahedral cells [131, 132]; however, this can also lead to a greater computational expense as a result of increased complexity. Typically for polyhedral meshes, there is an increase in computational time required during mesh generation, however this increased pre-processing effort is far outweighed by the faster and more accurate solutions produced when compared to tetrahedral meshes and in some cases hexahedral meshes [131]. Previously, polyhedral meshes have received less popularity due to the inaccessibility of both generating and solving for within commercial CFD codes. Although more recently, Bristot [68] successfully demonstrated a polyhedral meshing approach within a bearing chamber application.

A hex-dominant mesh is one that consists predominantly of hexahedral elements whilst incorporating a small number of irregular polyhedral elements, allowing meshes to be generated with an extremely high level of isotropy. Thus, preserving the accuracy of using hexahedral elements whilst being able to map the complex parts of a geometry using polyhedral elements. Within OpenFOAM, the mesh generation tool snappyHexMesh allows the user to automatically generate a robust hex-dominant mesh controlled by a large range of user specified controls provided as an input file. The 3 stages of the snappyHexMesh process involves castellation, snapping and boundary layer refinement, as shown in the example presented in Figure 4.12. The first stage, castellation, involves splitting cells at feature edges and surfaces, after which, the cells that lie outside the domain are removed. The next stage focuses on removing the jagged castellated surface by snapping cell vertex points onto the surface geometry. The final, although optional stage, introduces layers of hexahedral cells aligned to the boundary surface for boundary layer refinement. This last stage allows boundary layers to be ‘grown’ around surfaces without having an impact on the rest of the domain, unlike traditional structured hexahedral meshes, thus

heavily reducing the mesh density whilst achieving an equivalent wall normal cell spacing. Within the hex-dominant meshing procedure, this placement of the boundary layer is the main reason for avoiding any numerical errors that are associated with the extruded film mesh, i.e. over the sharp expansion corner in the Arienti case study.

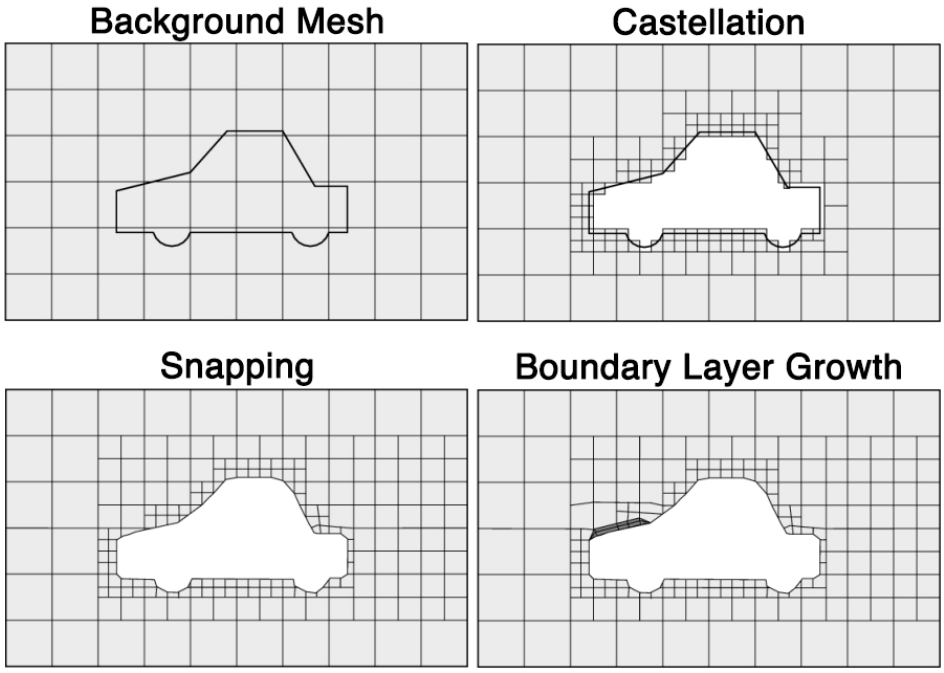


FIGURE 4.12: THREE STAGES OF THE SNAPPYHEXMESH PROCESS, MODIFIED FROM [114]

4.6.2 Numerical Settings

A single-phase steady state solution was first obtained using *simpleFoam*, and then imported into *pimpleFoam* to achieve a transient single-phase solution. A development duct section was run in isolation to get a fully developed flow profile, which was used to prescribe flow inlet boundary conditions for all cases investigated; this duct was initialized using a constant inlet velocity of 82 m/s, based on the experimental operating conditions. The single-phase solution was used as the initial condition for all of the following simulations within the *sprayParcelFilmFoam* solver.

All chemistry and combustion elements of the solver are switched off and air properties are set to a temperature of 288.15 K resulting in a density of 1.225 kg/m^3 to match that of air at sea level. The secondary phase consists of mineral spirits, with constant fluid properties, which are defined in the following Section 4.6.2.1, DPM injection configuration.

The pressure velocity coupling is solved using the PIMPLE algorithm, with *nCorrectors* and *nOuterCorrectors* set to 3 and 50 respectively, such that convergence at each time-step is instead controlled using a residual convergence criterion of 1×10^{-6} for the pressure, velocity and turbulent quantities. Overall, simulation convergence is assessed primarily through monitoring

the sum of mass on the film wall surface and once a steady state solution is achieved, results are analysed; this typically required a flow time of 0.5s, after which a further 0.5s was simulated for temporal averaging. A second order upwind-biased discretisation scheme was chosen for all pressure, momentum and turbulence terms. For solving the surface film, due to initial poor convergence stability, the film was first converged using a first-order bounded scheme and then switched to a second order upwind-biased scheme. The time discretisation scheme used the Euler transient, first order implicit, bounded scheme.

The solver was implemented with parallel capabilities; most calculations used 4 to 32 CPU compute threads, with an average runtime of 24 to 48 hours. Initial simulations demonstrated that the number of parcels injected per second was heavily reduced when the injection location was split over more than one CPU core. To avoid this, mesh decomposition was carried out using the scotch method and care was taken to ensure that the injection location was preserved.

4.6.2.1 DPM Injection Configuration

To simulate the primary atomisation process of the liquid jet, the *coneNozzleInjector* injection model is employed. The experiments of Shedd et al. [112] were used to determine the nozzle parameters, which are shown in Table 4.3.

TABLE 4.3: NOZZLE INJECTION PARAMETERS

coneNozzleInjector Settings	
Nozzle diameter, D	0.5 mm
Nozzle length	1 mm
$\boldsymbol{C_A = 3 + \frac{l}{3.6D}}$	3.556
Spray angle	0.0081 radians
Jet velocity, $\boldsymbol{u_{jet}}$	12.7 m/s
Mass flow rate, $\boldsymbol{\dot{m}}$	0.001945 kg/s

Inert particles are injected with constant properties matching that of mineral spirits, such that the density ρ_l = 780 kg/m^3, dynamic viscosity μ_l = 0.0085 kg/ms and surface tension σ = 0.0024 N/m. The particles are injected following a Rosin-Rammler diameter distribution, by specifying a Rosin-Rammler diameter of 0.15mm and a size distribution parameter of 3.76, with no maximum or minimum diameters, which was derived from the experiments.

4.6.3 Results

Results of mean film thickness are compared against the experimental data of Arienti et al. [113] to assess the effects of both the numerical settings and *sprayParcelFilmFoam* sub-models as outlined by objectives a) to g) in the parametric studies section. These results are shown in Figures 4.13 a) to f). Film thickness measurements are taken along the centreline of the film, starting from the injection location at 0mm to 30mm downstream, corresponding to the expansion edge.

Figure 4.13 a) presents the mesh independency study for the straight duct geometry investigated, objective a). Other variables, such as the airflow velocities and turbulent quantities were also assessed for mesh independence, however since the film formation and thickness is also dependent on these aspects of the flow field, it is a good quantity to inspect. Whilst a mesh independent solution is not achieved, there is a negligible difference between the results for mesh densities of 920k and 2200k. As such, further simulations for the straight duct geometry were carried out using the mesh of 920k cells and this was used as the baseline for generating the extended expansion duct hex-dominant meshes.

Objective b) considers the effects of changing the time-step on the film formation and thickness. The three time-steps considered correspond to maximum airflow Courant numbers of 1, 2 and 20. For Figure 4.13 b) the results are in agreement for the film thickness up until 5mm away from the expansion edge, where percentage errors of around 6% can be seen. Whilst only a small percentage error is observed, it was decided to run further simulations using the smallest time-step of 5×10^{-6}s to maintain a maximum Courant number of 1 and achieve an accurate coupling between the particles and the air-flow.

Figure 4.13 c) contains objective c), the comparison of the straight duct (SD) hexahedral mesh with and without the newly created stripping sub-model. An additional comparison is also made to the results of objective d), which investigates the mesh independency of the hex-dominant expansion duct (ED) meshes. For the results of the mesh independence study, again whilst a mesh independent solution is not obtained, the results between mesh densities of 2570k and 3740k cells are negligible. As such, all further simulations for the extended expansion domain used the mesh of 2570k cells and for clarity in Figures 4.13 c) only the results from this mesh are shown. For the straight duct, objective c), the inclusion of the film stripping model results in significant amounts of liquid being removed from the film, especially towards the expansion edge at 30mm. From Figures 4.13 c), it is clear that as the film gets closer to the edge, greater amounts of fluid are removed from the surface. Overall, these results show the successful implementation of a film stripping model within OpenFOAM, however further systematic analysis is still required to demonstrate validity.

Figure 4.13 c) shows that for the straight duct geometry, excellent agreement with the experimental data of Arienti et al. [113] is achieved towards the edge location, predicting a film thickness of 90.7μm, giving a percentage error of 1.6%. In general, good agreement is seen and although a thicker film is predicted computationally, all results are within error bounds. The largest discrepancy occurs over the distance ranging from 20mm to 25mm, with a maximum percentage error of 29.3% at the distance of 22.5mm. Comparing the results of the straight duct with the extended expansion duct, a slightly thicker film is produced for the expansion geometry. When compared with the experimental data, the final film thickness is again in excellent agreement with a percentage error of only 2.7%. However, large differences occur over the same distance of 20mm to 25mm, with some points greater than the error bounds. The difference between the straight duct and expansion geometry can be accounted for by the slight changes in velocity field and particle trajectories in the immediate region around the expansion edge.

For objective e), the effect of turbulence on particle trajectories and film thickness is considered in Figure 4.13 d). A much closer agreement to the experimental data is observed with the inclusion of the DRW model. At the distance of 22.5mm, the maximum percentage error reduces from 29.3% to 15.9%, without and with the model respectively. In addition, the film thickness predicted falls within the error bounds for all of the experimental data points. The reduction in film thickness, with the DRW model is not as prevalent as reported by Hee et al. [105], however the results are in agreement. Furthermore, for objective e), the inclusion of a splashing criterion is investigated alongside the DRW model. The splashing model is proposed by Bai and default model constants are used. Whilst there is no change in the final average film thickness, splashing does occur, which may contribute to the fine mist of droplets reported by Arienti et al. [113] over the height ranging from 4mm to 10mm above the film surface. As such, the effects of splashing may also be a necessary addition for accurately representing the particulate flow that is observed beyond the expansion edge.

The effects of including stochastic dispersion with a particulate size distribution are multiplicative. Therefore, in order to achieve an accurate statistical representation of the flow, careful consideration for the number of parcels injected per second is required. Figure 4.13 e), shows the results of this parametric study, described by objective f). Results show that the impingement location of the jet is not affected by altering the number of parcels injected per second, however a change in the film thickness is observed beyond the axial distance of 20mm. Increasing the number of parcels, results in a thicker film by approximately 5%. This can be attributed to a more accurate statistical representation of the smaller diameter droplets, which can ultimately exit the domain instead of impinging on the surface.

After concluding the parametric studies into the DPM configuration and relevant sub-models, objective g) evaluated the edge stripping criterion. Figure 4.13 f) compares the newly implemented edge separation sub-model with the experimental film thickness measurements of Arienti et al. [113] and the computational results of Hee et al. [105]. Excellent agreement with the experimental data is observed through including the edge separation model. Particles separated from the edge create an aerodynamic blocking effect, resulting in a slightly higher upstream airflow velocity just before the expansion, which results in more stripping over the last 10mm of the filmer surface. For reference, at a distance of 5mm before the expansion edge, the gas phase velocity at the film surface is 15.8 m/s compared to 11.2 m/s for a case with and without edge separation respectively; a difference of almost 30%. A normalised root mean square deviation (NRMSD) can be calculated through interpolating the predicted film thickness results and then evaluating the standard deviation from the experimental data; data is normalised using the experimental film thickness range. Final film thickness measurements, with the edge separation model, result in a NRMSD of 5.1%, which is a significant improvement over the results of Hee et al. [105], who achieved a NRMSD of 28.9% with just a film stripping sub-model.

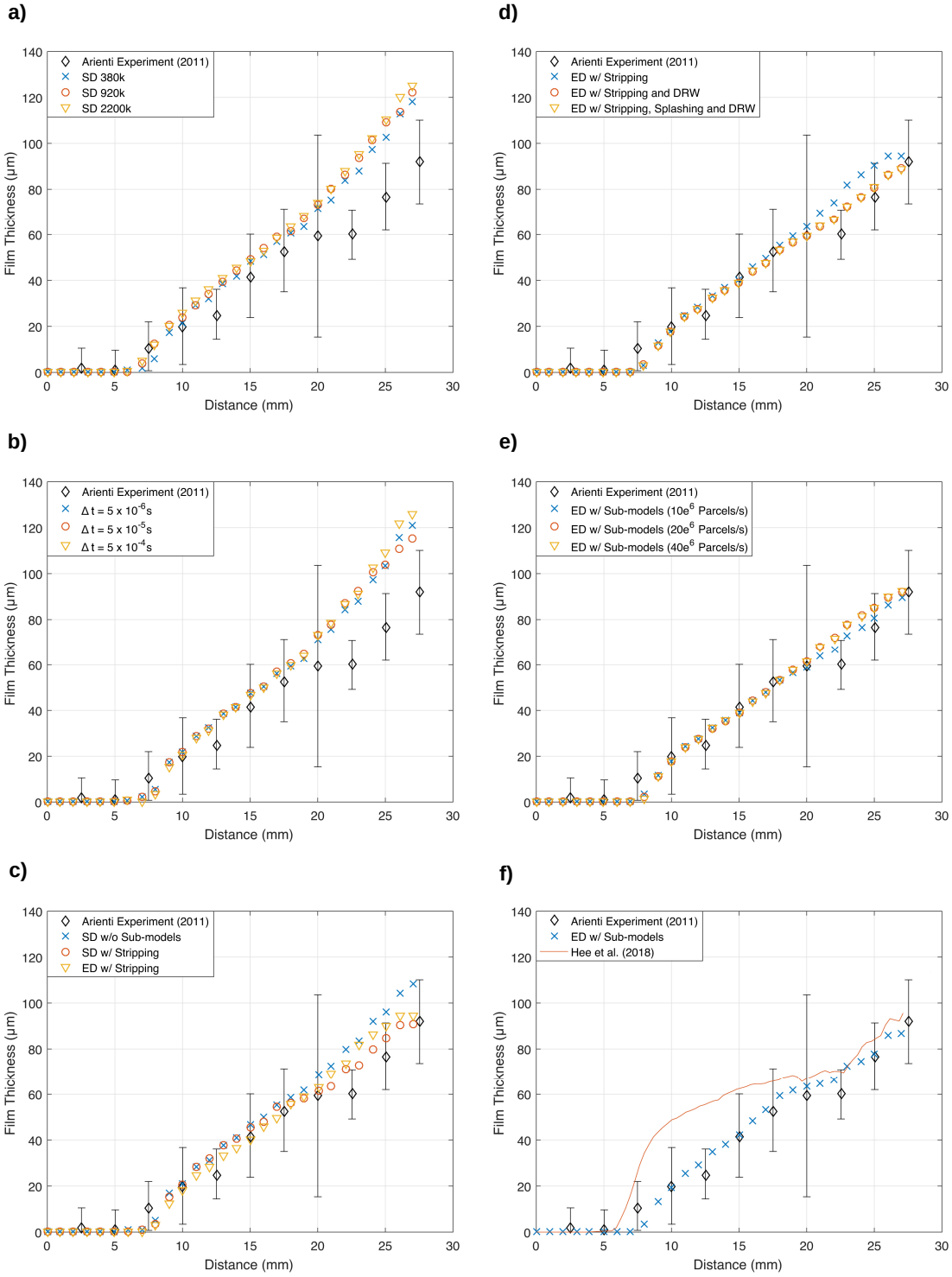


FIGURE 4.13 FILM THICKNESS MEASUREMENTS ALONG THE FILMER CENTRELINE FOR EACH OBJECTIVE a) SD MESH DENSITY, b) AIRFLOW TIME-STEP, c) STRIPPING CRITERION AND ED MESH DENSITY, d) STOCHASTIC DISPERSION MODEL AND SPLASHING, e) NUMBER OF INJECTION PARCELS PER SECOND, f) EDGE SEPARATION CRITERION. FOR ALL CASES: INJECTION LOCATION AT 0 mm, EXPANSION EDGE AT 30mm.

For case 13, Figure 4.14 shows the velocity magnitude contour plot, along the mid-plane, with Lagrangian particles coloured by their diameter. The domain length has been limited to show only the first 0.75m of the domain. Particles injected 30mm upstream of the expansion edge, are deflected by the shearing crossflow and immediately undergo secondary breakup. As the instabilities in the droplets grow, breakup occurs through both Kelvin-Helmholtz and Rayleigh-Taylor instabilities resulting in an average particle diameter of ≈ 70µm. The injected particles create a low-pressure region behind the jet through obstructing the crossflow, which leads to a decrease in core velocity from 92 m/s to roughly 50 m/s. With the KHRT breakup model, a small number of droplets with a diameter between 25µm and 50µm are produced; these droplets do not impinge on the film surface and exit the domain, corresponding to the fine mist of droplets reported by Arienti et al. that occur at a height of 4mm to 10mm above the film surface which can be seen in Figure 4.14.

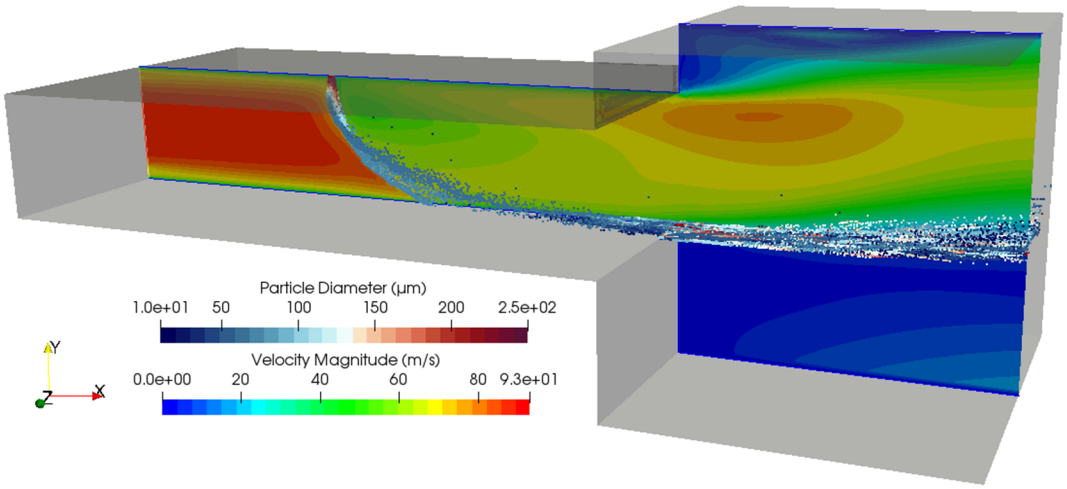


FIGURE 4.14: MIDPLANE VELOCITY MAGNITUDE AND PARTICLE DIAMETERS

4.6.3.1 Momentum Source Terms

Figure 4.15 presents the results of case 14, using a modified film momentum transport equation and comparison is made to original formulation in case 13. Here for case 14, and as outlined in Table 4.2, the various pressure and stress-based sources are removed from the transport equation. From Figure 4.15, a clear difference in film thickness measurements is observed when removing these pressure and stress source terms. For case 14, beyond the axial distance of 20mm, a thicker film builds up, which decreases slightly before increasing again, reaching a final film thickness of approximately 120µm. This final film thickness is approximately 40% greater than that for case 13 with source terms, which predicted a thickness of 85µm at the edge. Overall, towards the expansion edge at 30mm, the results of the modified transport equation are in somewhat of an agreement with the results of Hee et al. [105].

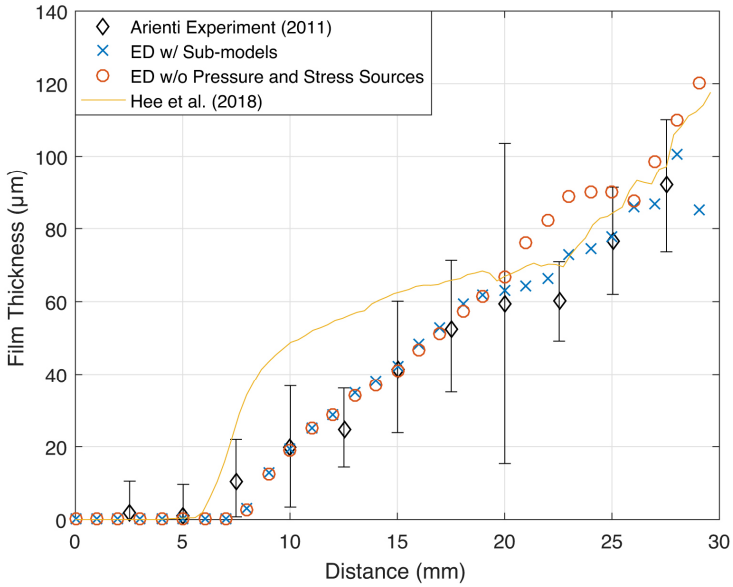


FIGURE 4.15: FILM THICKNESS MEASUREMENTS ALONG THE FILMER CENTRELINE FOR A MODIFIED FILM MOMENTUM TRANSPORT EQUATION

In addition to the phenomena already observed, it is also expected that as the film approaches the expansion edge, the film will increase in velocity and thin, much like the fluid flow over a weir [133]. As the film travels around the expansion corner, the gravity body force, $\rho g_\theta \delta$, which acts in the direction tangential to the wall, accelerates the film downwards along the vertical wall, since the gravity component g_θ becomes that of gravity. This gravity body force is the main driving force for flows over vertical and inclined surfaces [116]. The acceleration of the fluid film results in the film upstream of the expansion edge increasing in velocity and thinning. When combined with an edge separation criteria, this effect is reduced as not all of the liquid travels around the corner but, instead, is separated. With the pressure and stress momentum source terms included, case 13, before the expansion edge, the film thickness reduces to 85µm in part due to this body force. The next most dominant term is the normal force due to gravity, p_δ, this source results in the spreading of the film. Without this effect the width of the film is reduced by approximately 10%, as shown in Figure 4.16. Interestingly, whilst removing the source terms from the film momentum equation has a significant effect on the final film thickness over the last 10mm, no variation in film thickness is observed over the initial film distance of 5mm to 20mm.

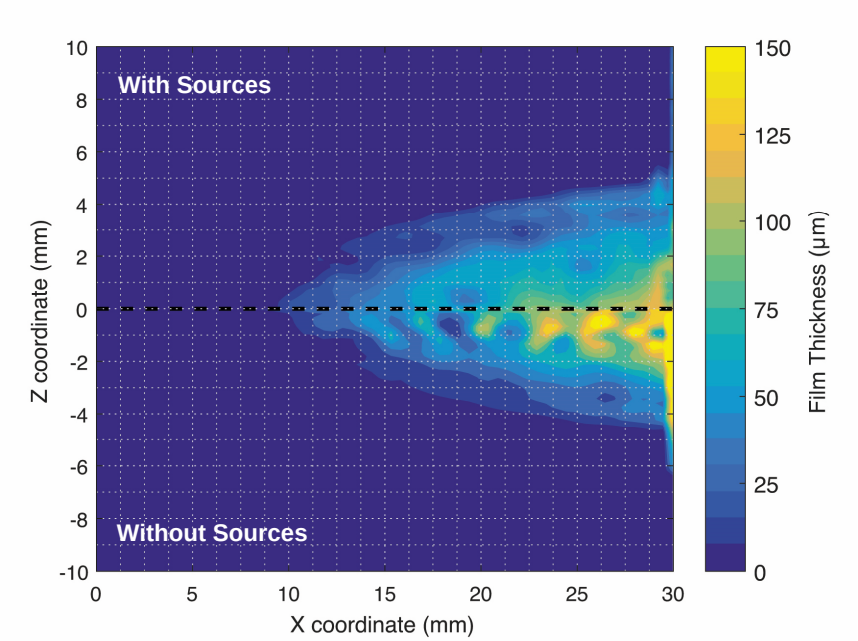


FIGURE 4.16: INSTANTANEOUS FILM THICKNESS MEASUREMENTS WITH PRESSURE SOURCES (TOP) AND AFTER THEY ARE REMOVED (BOTTOM)

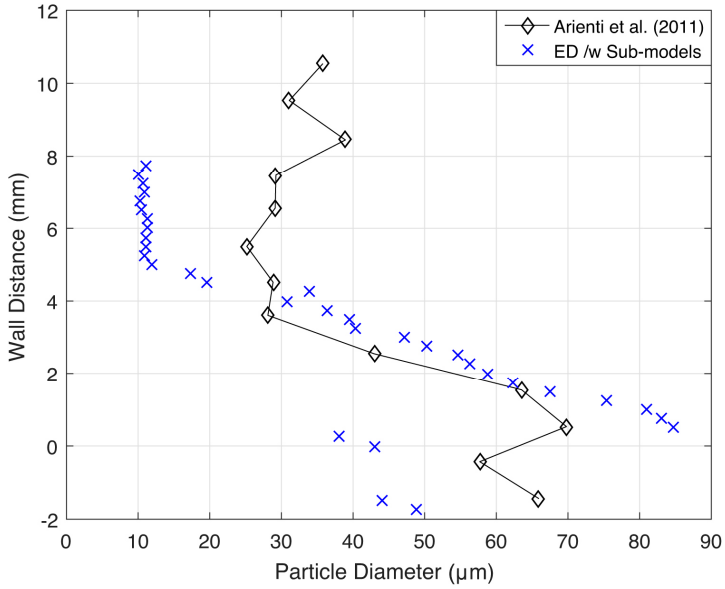
4.6.3.2 Particle Diameters and Velocities

Particle velocity and mean diameter distributions are compared with the phase Doppler particle analysis carried out by Arienti et al. [113]. Results are taken along the midplane, 25.4mm downstream of the expansion edge. The wall distance is recorded along the *y*-axis, where the location of 0mm corresponds to the height of the edge. The computational results of case 13 are presented within Figures 4.17 a) and b) for the particle diameter and velocity distributions respectively.

For Figures 4.17 a) and b), comparing average particle diameters and velocities with Arienti et al. [113], the same overall trend is observed. Above the expansion edge, Arienti et al. report a fine mist of particles over the height of 4mm to 11mm, with a uniform diameter of approximately 30µm. Within the computational results, this fine mist of particles is captured, however smaller diameters of 10µm to 20µm are recorded, suggesting that excessive breakup occurs due to the KHRT model. No particles are observed at the height of 8mm to 12mm, however within the experimental data of Arienti et al., there is no mention of the frequency of particles passing at each measurement location. In the range of 0mm to 2mm, the largest particle diameters are observed, corresponding to the liquid separated from the expansion edge. At the expansion edge, these particles are shed with a droplet diameter corresponding to the film height, which in Figure 4.15 is approximately 85µm. In this region diameters range from 75µm to 85µm due to the transient nature of the film. These edge separated particles are carried by the airflow, deflecting upwards and due to the lower gas-phase velocities in this region, no further secondary breakup is

observed. Since these particles have a larger diameter than that observed experimentally, it is also expected that these particles will have a slower velocity than predicted by Arienti et al. [113], as shown in Figure 4.17 b). Below the edge region, particle diameters decrease to 40µm and 50µm, these particles originate from the film stripping and secondary breakup of the jet, upstream of the expansion edge. Here, particles increase in velocity due to momentum exchange with the crossflow, penetrate downwards, and are eventually captured by the recirculation region below the expansion edge.

a)



b)

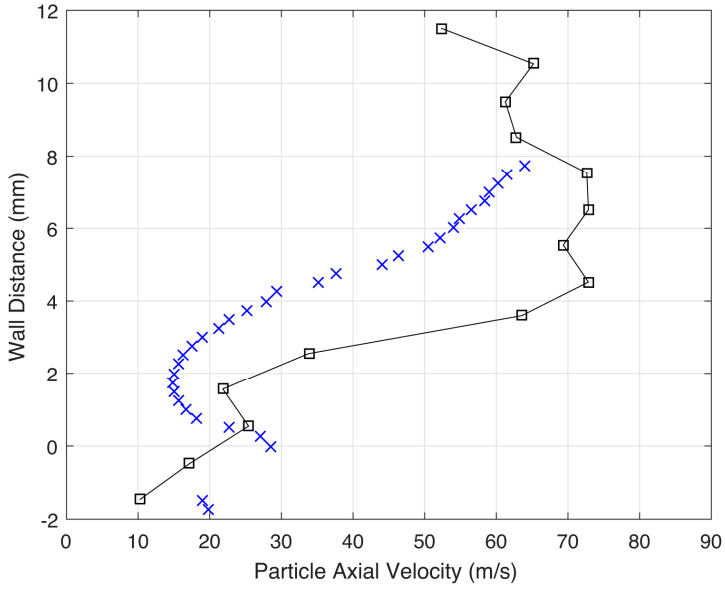


FIGURE 4.17: a) AVERAGE PARTICLE DIAMETER AND b) VELOCITY 25.4mm DOWNSTREAM OF THE EXPANSION EDGE ALONG THE MIDPLANE. THE 0 LOCATION CORRESPONDS TO THE HEIGHT OF THE EXPANSION EDGE.

An analysis of the particle characteristics, shows that a good overall agreement is found between the computational data presented and the experimental results of Arienti et al. [113]. However, it is difficult to assess the reliability of the experimental results reported, limited information is provided surrounding the phase Doppler particle analysis carried out. No insight into the frequency of particles passing at each location point is given and furthermore, data is presented without error bars; as such, only a qualitative analysis is carried out.

4.7 Conclusions

A two-way coupled ETFM-DPM solver has been successfully developed called *sprayParcelFilmFoam*, including the effects of both primary atomisation and secondary breakup. Computational modelling of jet breakup and subsequent film formation in a high velocity crossflow is studied using the *sprayParcelFilmFoam* solver and validated against the experimental film thickness measurements of Arienti et al. [113]. To achieve an accurate representation of the flow field, two new film sub-models were implemented and validated: a film stripping model and an edge separation model.

sprayParcelFilmFoam is a new transient solver, capable of compressible, turbulent flow with Lagrangian particle tracking, fully coupled with surface film modelling including optional reacting and multiphase physics. The spray particle cloud incorporates primary atomisation and secondary breakup models; in addition, the numerical lower limit of one particle per injection parcel is removed, to achieve a more accurate statistical representation of the particulate flow and a correct mass flow rate. As a result of this work, this change has now been fully implemented in all OpenFOAM builds for versions 6.0 and above.

With the inclusion of both novel film stripping and separation sub-models, an accurate ETFM-DPM coupling is achieved; these are the parameters are required to produce close agreement with the experimental results. The film stripping sub-model is based on the work of Mayer [127] has been developed, accounting for surface Kelvin-Helmholtz instabilities. With this inclusion, final film thicknesses are within 3% of the experimental data. In addition, an edge separation sub-model is established from the separation criterion presented by Friedrich et al. [128] and predicts the onset of shear-driven film separation over a corner. The average film thickness predicted is compared to the experimental measurements of Arienti et al. [113], resulting in a NRMSD of 5.1%, significantly improving on the work of Hee et al. [105] who achieved a NRMSD of 28.9%. Good agreement is also achieved for particle velocities and diameters downstream of the expansion edge.

An analysis into modifying the film momentum transport equations revealed the effect of the gravity body force. This force, $\rho g_\theta \delta$, is responsible for the film thinning by as much as 40% and increasing in velocity as it approaches the expansion edge. The normal force due to gravity, p_δ, provides a spreading effect resulting in a wider film by approximately 10%.

A fully coupled ETFM-DPM solver has been established within OpenFOAM, that can now facilitate future modelling of aeroengine bearing chamber film flow. A significant advance in ETFM-DPM modelling capability has been achieved within OpenFOAM and the work can now progress in applying the *sprayParcelFilmFoam* solver to a bearing chamber geometry.

Chapter 5

Application: Aeroengine Bearing Chamber Modelling

In this chapter, the previously developed ETFM-DPM solver *sprayParcelFilmFoam* is, for the first time, extended to an aeroengine representative bearing chamber. The configuration matches that of the G2TRC simplified aeroengine bearing chamber presented in Section 2.3.4.1, this rig has been previously investigated by researchers, resulting in the publication of high-speed camera images and film thickness/wave behaviour. The experimental measurements provide vital validation data for this current study. In the experimental test rig, oil is supplied to a ball bearing via underrace feed. Oil sheds from both the bearing and cage elements onto the nearby static surfaces, where it is subsequently transported by the shearing airflow generated from the shaft rotation. The film travels along the static surfaces towards an edge, where a proportion of oil separates into the chamber forming droplets and ligaments. Numerical investigations are conducted for three different shaft speeds namely 5,000, 7,000 and 12,000 rpm, at two different oil flow rates: 5.2 and 7.3 l/min. The bearing itself is not modelled, however, two different, but representative, boundary conditions are investigated in order to simulate oil exiting from the bearing and the cage-edge. Computationally, results are validated against existing experimental film thickness measurements for the two lower shaft speeds. Evaluation of the film dependence on the rotational shaft speed, is used to develop understanding of the transition from a gravity driven flow state to that of a smooth shear dominated flow regime. An analysis of the oil shed into the chamber is performed. For these droplets, relevant statistics relating to size, velocity, impingement and residence time are presented; providing knowledge of solution sensitivity to operational parameters such as the rotational shaft speed and oil flow rate. This work represents the first successful fully coupled two-way ETFM-DPM investigation, quantifying droplets shed into the bearing chamber. Overall, this work has established a firm foundation for future aeroengine bearing chamber modelling, as well as, delivering new insights into key flow physics.

5.1 Objectives

The aim of this chapter is to investigate the detailed flow physics of an aeroengine representative bearing chamber using a two-way ETFM-DPM coupling. The bearing chamber under investigation corresponds to the bearing oil shedding test rig facility investigated by both Santhosh et al. [53] and Hee et al. [54]. In general, within a bearing chamber, whilst there are some experimental studies surrounding the rotational shaft speed and the influence of air on the oil film, to date the air-oil interaction itself is not well understood. Furthermore, minimal work has been carried out in order to quantify the droplets and their characteristics that are shed from the bearing into the bearing chamber. As such, the first objective of the work is to validate *sprayParcelFilmFoam* and the ETFM-DPM coupling methodology through comparing film thickness results against the available experimental measurements of Hee et al. [54]. A two-way coupling is implemented and investigated such that Lagrangian droplets can be transferred to a thin film through impingement, but can also be removed from the surface of the film due to either, splashing, stripping or edge separation. The second main objective will focus on providing accurate droplet statistics and knowledge of solution sensitivity to important operational parameters. This work builds upon the existing modelling capability developed in Chapter 3, in order to improve understanding and investigate new flow physics for aeroengine bearing chamber modelling.

5.2 Bearing Oil Shedding Rig

For the purpose of this chapter, the computational investigation focuses on the aeroengine representative ball bearing described by both Santhosh et al. [53] and Hee et al. [54], and more specifically, modelling of the front bearing chamber. Figure 5.1 presents a diagram of the experimental test rig. The front chamber of the bearing oil shedding rig has a static annular outer casing enclosing a rotating, truncated, shaft, which is capable of shaft speeds up to 7,000 rpm. The rig is designed in a way, such that, this front chamber is used to analyse the oil shedding behaviour exiting from, what would be, the rear of the actual aeroengine bearing. Experimentally, two oil flow rates are investigated, whereby at the test bearing, oil is fed from three under-race locations based on an aeroengine representative oil split. A more detailed overview is found in Section 2.3.4.1 and a more complete description is presented by Hee [55].

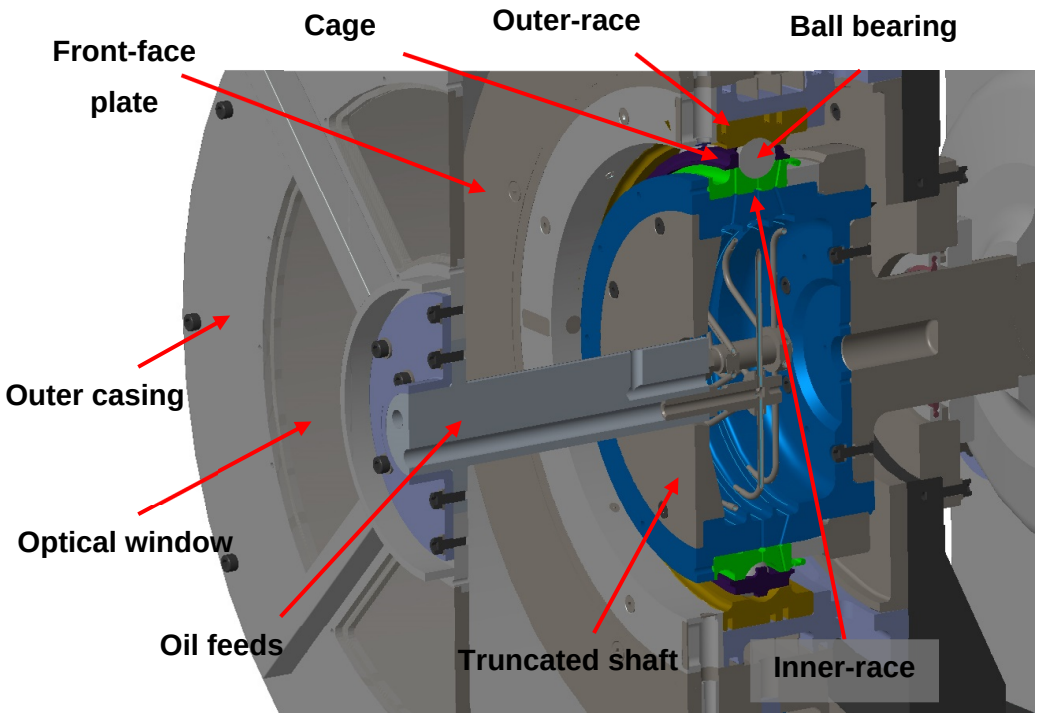


FIGURE 5.1: SCHEMATIC OF BEARING OIL SHEDDING RIG FRONT CHAMBER, MODIFIED FROM [54]

Figure 5.2 shows a cross-section of the front bearing chamber geometry modelled for the aeroengine ball bearing under investigation. The computational domain consists of a hex-dominant mesh created using a cut-cell approach within snappyHexMesh. To ensure sufficient resolution of the oil film, the boundary layer was refined over the static outer casing walls where the film develops. Initially, based on the knowledge acquired in Chapters 3 and 4, a single-phase, air-only, mesh independence study was conducted with 4 grids generated using baseline cell sizes of 4mm, 3mm, 2mm and 1mm. Bodies of influence were used to refine the mesh by up to 2 levels

in regions where there are high gradients of flow variables, such as the initial slot between the shaft and stationary outer casing, where the film first develops. Equally, the mesh was coarsened in locations far away from the oil phase, such as the static central tube, which experimentally houses the oil delivery system. Inflation layers were also applied over the walls towards the shaft edge and near the stationary outer casing, achieving a wall spacing of $y^+ < 1$ and a growth ratio of 1.2. Overall, analysis of the single-phase averaged velocity vectors demonstrated a negligible difference in the secondary flow field produced, between the grids of baseline cells sizes 2mm and 1mm. Subsequently, a two-phase investigation was performed, comparing film thickness measurements at several different angular and axial locations from the front-face edge. In general, a relatively low mesh dependence was found, with only small differences between the two finest meshes at 7,000 rpm, as shown in Table 5.1. However, at a shaft speed of 12,000 rpm, severe convergence stability issues were faced for the mesh with a core cell sizing of 2mm and a stable solution was not achieved. Consequently, the finest mesh at a core cell sizing of 1mm and a total count of 35 million cells was chosen for all two-phase simulations, in order to maintain consistency across all shaft speeds. Further mesh refinements beyond this level were not feasible, due to a significant increase in the number of cells, and hence, the computational cost associated with the simulations.

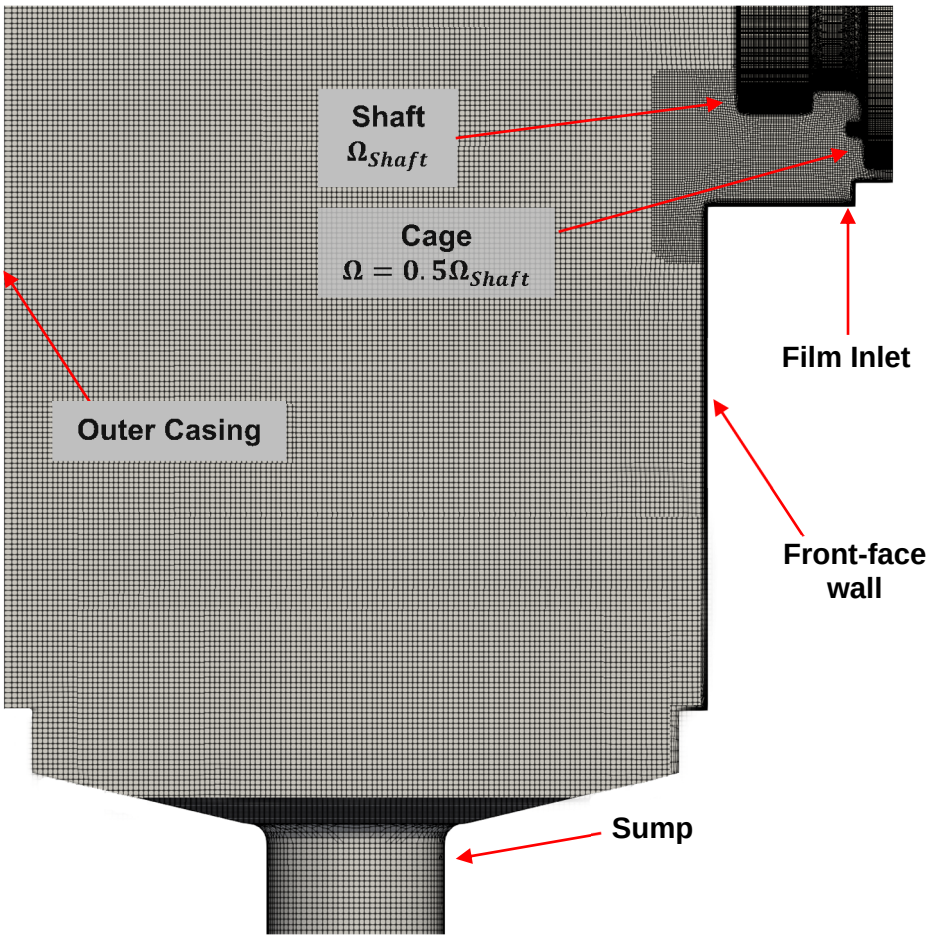


FIGURE 5.2: CROSS SECTION OF BEARING CHAMBER HEX-DOMINANT MESH EMPLOYED

TABLE 5.1: AVERAGED FILM THICKNESS MEASUREMENTS (mm) AT 7,000 RPM FOR AXIAL AND ANGULAR LOCATIONS WITHIN THE FILM SLOT

	z = 3mm		***z = 10mm***	
Cell Sizing	***90°***	***270°***	***90°***	***270°***
3mm	0.55	0.88	0.96	1.10
2mm	0.51	0.81	0.91	1.02
1mm	0.50	0.77	0.91	1.04

For the two-phase flow, an investigation into applying rotational periodicity was unsuccessful, resulting in a wave-like structure imposed on the surface of the thin film depending on the degree of periodicity. In a periodic annulus, with the inclusion of a gravity body force, the gravity component transforms into a 'rotational' force acting to accelerate the film in the direction of the shaft rotation; as such the film exiting one periodic boundary is not a true representation of the film entering the opposing periodic boundary. Furthermore, it is also not possible to represent the sump outlet boundary condition in a periodic mesh. Without the sump, the thin film builds up on the stationary outer casing walls leading to pooling and a thick, more three-dimensional, film, for which the ETFM is insufficiently accurate. At higher rotational speeds, where the shear driven airflow dominates the force due to gravity, it may be possible to use rotational periodicity, however for the present study the full 360° domain is modelled.

Due to its highly complicated nature, the test bearing itself is not modelled, as such the computational domain starts immediately after the ball bearing, at the cage. To further reduce the simulation complexity, a representative film inlet boundary condition is proposed, which starts beyond the sharp corner of the outer race as shown in Figure 5.3. This is described as follows:

Representative Film Inlet Boundary Condition. Hee et al. [54] demonstrated that there are two mechanisms for film formation; firstly, oil is shed from the cage-edge, and secondly, oil is axially displaced from the bearing at the outer-race. It is therefore assumed that all of the oil exiting from the cage-edge impinges on the film surface, similar to the flow past the edge of a rotating cup as discovered experimentally by Santhosh et al. [53]. As such, to simplify the film inlet boundary condition, all of the oil is therefore introduced axially into the domain beyond the sharp corner of the outer-race, as depicted in Figure 5.3. At this inlet location, oil is supplied into the domain based on the experimental measurements of Hee et al. [54] and given a rotational velocity derived from the VOF investigations performed by Adeniyi et al. [96], who investigated the same aeroengine ball bearing representative configuration.

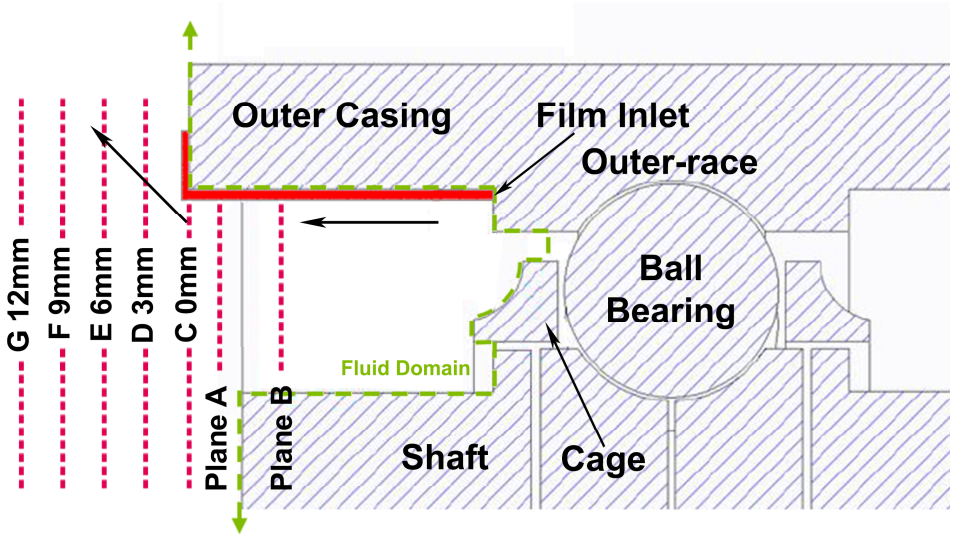


FIGURE 5.3: CROSS SECTION OF FILM INLET SHOWING a) AXIAL FILM THICKNESS MEASUREMENT PLANES AND b) DPM MEASUREMENT PLANES, MODIFIED FROM [54]

Experimentally, and within Figure 5.3, Hee et al. derived film thickness data from image analysis at planes A and B. Upstream of the front-face edge, these measurement planes are located at an axial distance of 3mm and 10mm respectively; the 0 location corresponds to the front-face edge. To analyse particle statistics, computationally and within Figure 5.3, measurement planes are placed in series of 3mm spacings away from the front-face edge up to a distance of 12mm.

Using high speed imaging, Santhosh et al. [53] and Hee et al. [54] investigated two angular positions around the bearing chamber annulus. Measurements were taken at both 90° and 270° locations, which in Figure 5.4, when moving clockwise with the rig shaft rotation (yellow) are denoted as P2 and P4. At the P2 location, gravity acts parallel to the air-oil interfacial shear and is therefore regarded as the co-current side. Conversely, at the P4 location, the counter-current side, gravity acts against the circumferential shear. Furthermore, with reference to Figure 5.4, location P1 refers to the top of the chamber at 0° and the P3 location corresponds to the bottom of the chamber at 180°. However, computationally, due to a misinterpretation, the shaft rotation is applied in the anti-clockwise direction (red), as shown Figure 5.4. This therefore means, that when facing the front of the rig, the P2 region is now located on the left-hand side of the chamber, and conversely, the P4 section on the right-hand side. Overall, this implication has no effect on the results, however, to ensure consistency the P2 computational region is always compared with the P2 experimental region and vice versa; the same is true for the P4 sector.

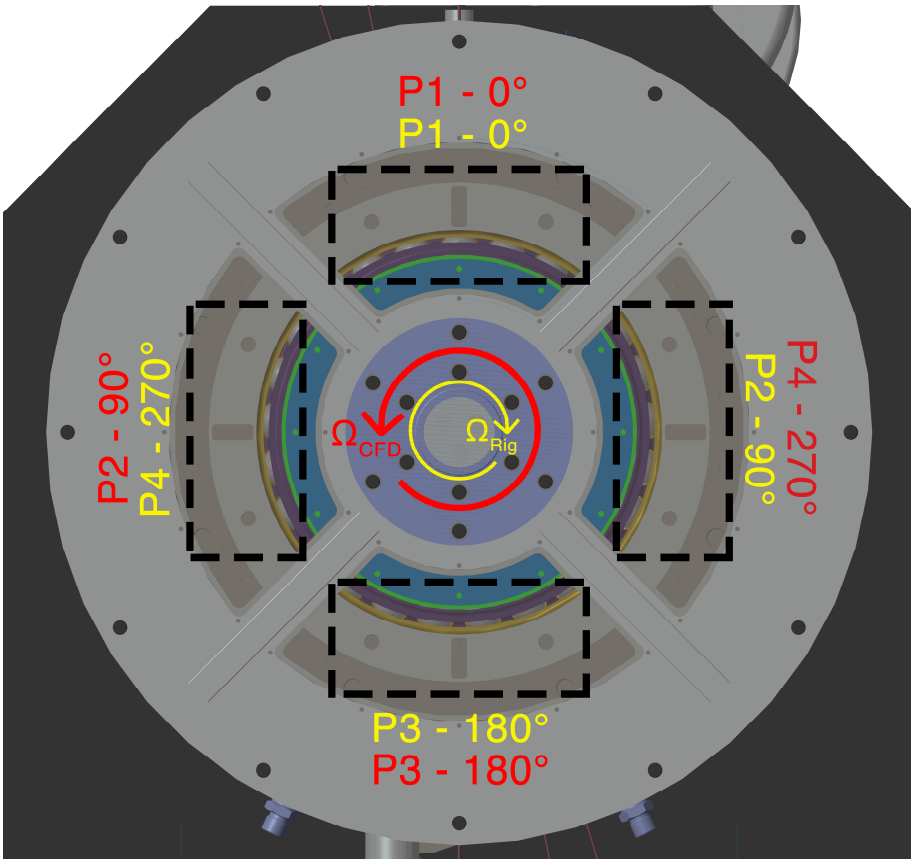


FIGURE 5.4: CONVENTION FOR BEARING CHAMBER ANGULAR POSITIONS

5.2.1 Computational Setup

The operating conditions were chosen to represent the experimental conditions employed by Hee et al. [54]. Three different rotational shaft speeds were investigated, for which at each speed, two different oil flow rates were studied. Experimentally, the lubrication oil chosen was Aeroshell Turbine Oil 390, fed at a fixed temperature of 35 °C. This subsequently heated up to an average recorded temperature of 60 °C as it passed through the bearing. Table 5.2 summarises the operating conditions and Table 5.3 highlights the material properties employed computationally.

Experimentally, Santhosh et al. [53] and Hee et al. [54], investigated rotational shaft speeds up to 7,000 rpm. However, for the present computational study, in order to investigate more realistic engine speeds, this range has been extended to 12,000 rpm for both of the oil flow rates. Image analysis conducted by Santhosh et al. [53], determined the cage speed to be approximately 50% of the shaft rotational speed. Computationally, both the shaft and bearing cage, shown in Figure 5.3, are represented as rotating walls whilst the other walls remain stationary.

TABLE 5.2: COMPUTATIONAL OPERATING CONDITIONS

Operating Conditions			
Shaft rotational speeds	Ω	5,000 7,000 12,000	rpm
Air temperature	T_g	333.15	K
Oil inlet temperature	T_l	333.15	K
Oil inlet volume flow rates	$\dot{V}_l$	5.2 7.3	l/min
Chamber absolute pressure	P	1.01	bar

TABLE 5.3: COMPUTATIONAL AIR/OIL MATERIAL PROPERTIES

Material Properties			
Air density	ρ_g	1.059	kg/m^3
Air viscosity	μ_g	2.008×10^{-5}	kg/(m.s)
Oil density	ρ_l	890.8	kg/m^3
Oil viscosity	μ_l	0.00681	kg/(m.s)
Oil-air surface tension	σ	0.0302	N/m

For the three shaft speeds under investigation, two different oil flow rates to the ball bearing are considered, specifically: 5.2 l/min and 7.3 l/min. Not all of the oil supplied to the bearing exits into the front chamber. On the experimental test rig, oil is supplied to three underrace locations, at the front, middle and rear of the bearing. The flow rate through each of these locations is independently controlled, such that the proportion of oil supplied is 1:1.33:0.67 respectively, chosen as an engine-representative split. Over each of the rotational speeds investigated experimentally, approximately 89% of the oil exits through the front chamber sump [54], meaning that computationally, the flow rates of oil supplied to the front chamber are 4.6 l/min and 6.5 l/min respectively.

As shown in Figure 5.3, the film inlet boundary condition starts beyond the sharp corner of the outer race. Within OpenFOAM, at the film inlet, quantities for both the film thickness and film velocity were specified. Film thickness quantities are determined through linear interpolation of the experimental film thickness measurements of Hee et al. [54], for each combination of rotational shaft speed and oil flow rate investigated. For the 12,000 rpm cases, this is determined from the experimental data based on the observations of Hee et al. [54]. Film inlet velocities are predicted using the work of Adeniyi et al. [96], who presented a VOF computational study of the

oil-air flow within the same aeroengine ball bearing. The authors provide oil speed measurements towards the front bearing chamber over a combination of two shaft speeds and two oil flow rates: 5,000 and 13,000 rpm for 4 and 8 l/min respectively. Adeniyi et al. report that, over all of the cases investigated, the oil slows down, exiting past the bearing cage into the chamber at roughly 10% of the shaft speed. Knowing the film thickness around the chamber annulus and the oil mass flow rate, hence volume flow rate, the axial velocity of oil entering the domain can be determined. Finally, the tangential velocity component is calculated to make up the remaining 10% of the shaft speed.

For the bearing chamber investigations, Santhosh et al. [53] and Hee et al. [54], maintained a rig operating pressure close to ambient in order to minimise the pressure difference across the bearing. This was to reduce the impact on the oil shedding behaviour, which can be influenced by a differential pressure drop across a bearing, as previously reported by Gorse et al. [49]. This also means that numerically, the DPM particle pressure gradient force, $\boldsymbol{F}_p$, can effectively be ignored. Overall, the test rig operates on a gravity scavenged system, such that computationally, the scavenge pipe is represented as a pressure outlet at ambient conditions, also acting as a film outlet for the ETFM.

5.2.1.1 Numerical Settings

For the three shaft speeds under consideration, initially a single-phase steady-state solution was first obtained using *simpleFoam*, after which a transient single-phase solution was achieved using *pimpleFoam*. This transient single-phase solution was used as the initial condition for all of the following two-phase simulations within the *sprayParcelFilmFoam* solver.

For this current chapter, the numerical settings and solution procedures implemented follow the same methodology as previously discussed in Section 4.6.2 for the *sprayParcelFilmFoam* solver. This includes the DPM sub-models for secondary breakup of the particulate cloud; and furthermore, the two newly developed and validated thin film sub-models for both a film stripping and an edge separation criteria. As such, the work carried out in this section demonstrates the first application of *sprayParcelFilmFoam* to an aeroengine representative bearing chamber.

In general, the PIMPLE algorithm is used to solve the pressure-velocity coupling, with *nCorrectors* and *nOuterCorrectors* set to 3 and 50 respectively, such that convergence of the pressure, velocity and turbulence quantities are instead controlled using a residual convergence criteria of 1×10^{-6} for the maximum average. Overall, aside from measuring global quantities such as the shaft torque coefficient, convergence is primarily assessed through monitoring both the oil film residence volume on the stationary outer casing wall and the DPM oil residence

volume. A steady state solution of the oil can be assumed once the oil residence volume fluctuates periodically around a constant average value. Typically, a steady solution was achieved after a flow time of 1.0s, after which data was temporally averaged over a further 1.5s; approximately 5 film cycles from inlet to edge. A second order upwind-biased discretisation scheme was chosen for all pressure, momentum, turbulence and surface film terms. The time discretisation scheme used the Euler transient, first order implicit, bounded scheme.

Finally, the SST k-ω turbulence model was chosen for all simulations due to its robust formulation and previously demonstrated capability within both the Gorse bearing chamber and Arienti validation case studies in Chapter 3 and Chapter 4 respectively.

5.3 ETFM Results

5.3.1 Qualitative Oil Distribution

Figure 5.5 shows mean velocity vectors of the oil film within the slot after the bearing, as such, the mechanism for oil formation on the stationary outer cylinder wall, highlighted in Figure 5.3, can be observed. Within Figure 5.5, observation of the co-current side shows that the direction of the oil film is significantly more uniform compared to the counter-current side. This can be accounted for, since within the P4 counter-current side, the interfacial rotational shear acts in the opposing direction to the downward force due to gravity. As a result, there is a reduction in the tangential velocity component in the counter-current oil film, causing a flow reversal. The incoming upstream oil mass, which is flowing axially outward, causes the oil film to intermittently undulate resulting in a non-uniform wavy film compared with the P2 co-current side.

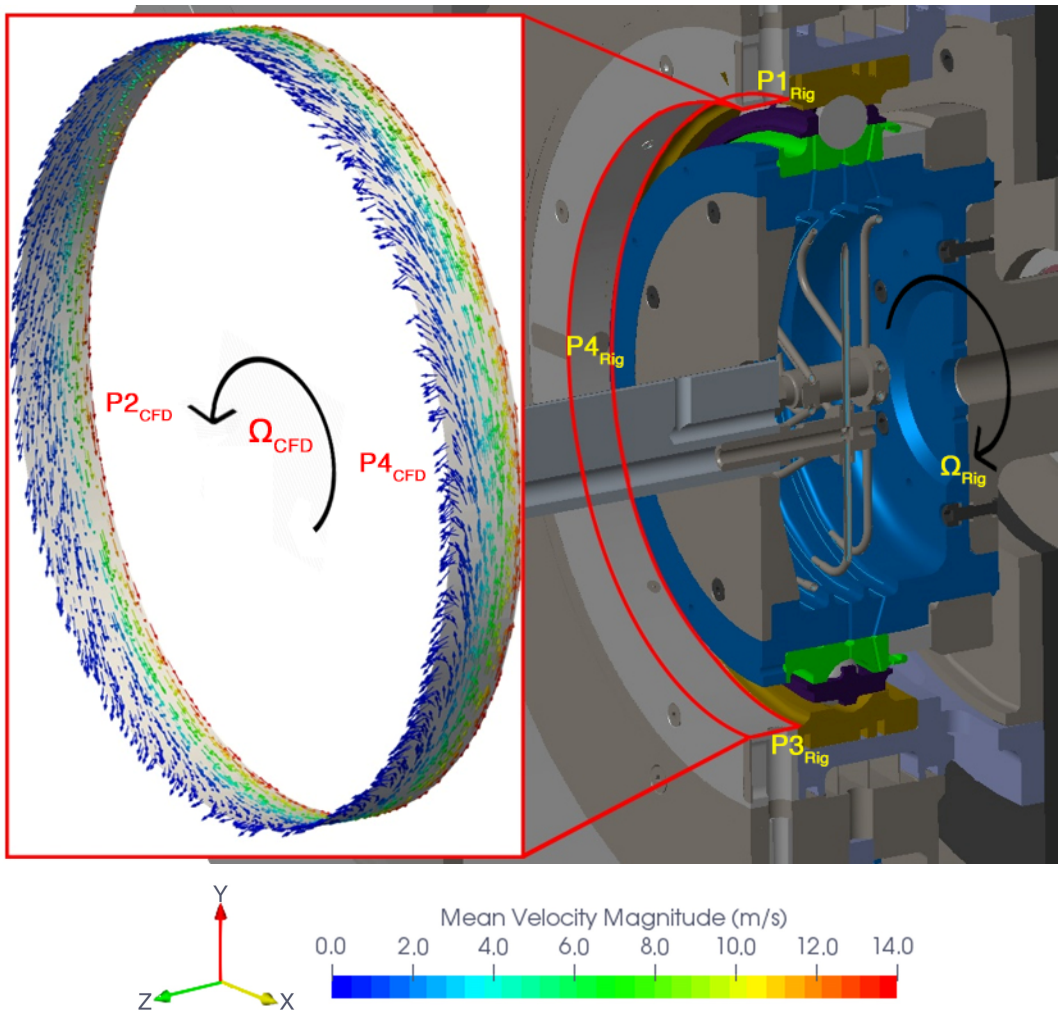


FIGURE 5.5: FILM MEAN VELOCITY VECTOR PLOT AT 7,000 RPM AND 7.3 L/MIN

Figure 5.6 shows a view of the front face-edge and the instantaneous film thickness measurement due to the attached film as it flows over the corner, in part due to this undulation effect. For clarity, in Figure 5.6, the droplets are not shown.

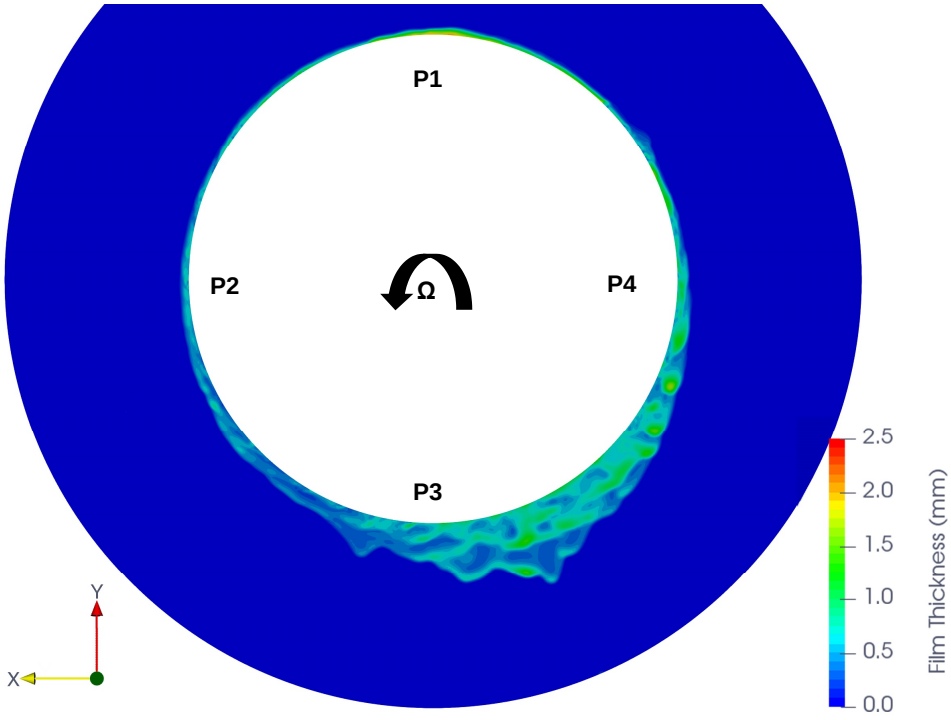


FIGURE 5.6: INSTANTANEOUS FILM THICKNESS ON THE FRONT FACE-EDGE AT 7,000 RPM AND 7.3L/MIN (DROPLETS NOT SHOWN)

Over a sharp edge, liquid may separate from the surface, whilst a proportion may turn the corner and still remain attached. The amount of mass to be separated is dependent on the critical force ratio, derived from a force balance between the film inertia, surface tension and body forces. From Figure 5.6, it is apparent that at P2, the co-current region, very little mass remains attached, suggesting that that the critical force ratio is satisfied and the liquid becomes separated as droplets. Conversely, as we move around the chamber from the P3 to the P4 sector, a larger proportion of mass remains attached and flows over the edge. Upstream of the edge, the film velocity slows as it is pulled downwards due to the effect of gravity, and therefore, does not have sufficient inertia to fully separate from the edge. Instead, waves of film fall over the edge due to the undulating effect of the upstream flow reversal, shown by the velocity vectors in Figure 5.5.

At the P4 region, a very similar wave-like structure is observed experimentally, as shown in Figure 5.7, taken from the P4 visualisation results of Hee [55], at a shaft speed of 7,000 rpm and an oil flow rate of 7.3 l/min. Here, the oil film travels down the front-face plate in an anti-clockwise direction, i.e. against the shaft rotation, with a series of wave fronts forming. At the top of Figure 5.7, the radial extent of the film is much smaller than that observed towards the bottom.

Overall, the film development predicted computationally over the front-face plate, in Figure 5.6 is in excellent agreement with the visualisation results produced experimentally in Figure 5.7.

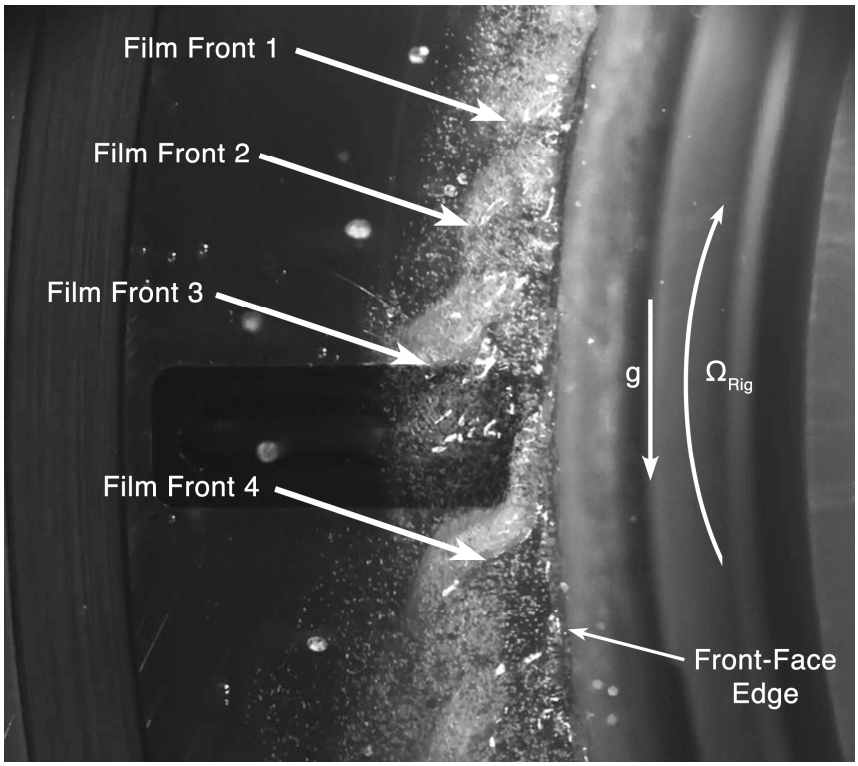


FIGURE 5.7: OIL WAVE FRONTS OBSERVED EXPERIMENTALLY AT P4 [55], 7,000 RPM & 7.3 L/MIN

Computationally, these effects of undulation and film slowing can be observed in Figures 5.8 a) to c). For all of the shaft speeds investigated, Figures 5.8 a) to c) show the mean film velocity magnitude vector plots for the P4 counter-current regime. Similarly, the P2 co-current regime is shown within Figures 5.9 a) to c), whereby, over all cases a smooth shear driven flow regime was observed. For clarity, only the last section of the film is shown and a reference location for Plane B is highlighted for comparison to the experimental measurement plane which is located at an axial distance of 10mm from the front-face edge.

Within Figures 5.8 a) to c), only the higher oil flow rate at 7.3 l/min is shown for simplicity, although comparable results and trends were observed for the cases at a flow rate of 5.2 l/min. For the counter-current regime, it is observed that the oil velocity changes direction as it is pulled downward due to the gravitational force. Within bearing chambers, a shock regime refers to the transitional period when the gravity dominated pool regime moves toward a smooth shear dominated flow. When the gravity component is equal to the shear effect, the observed undulation effect reaches a maximum. Beyond this critical point, when the shear force dominates the gravitational force, a further flow reversal within the counter-current region is observed and the waves begin to travel upwards with the direction of the shaft rotation.

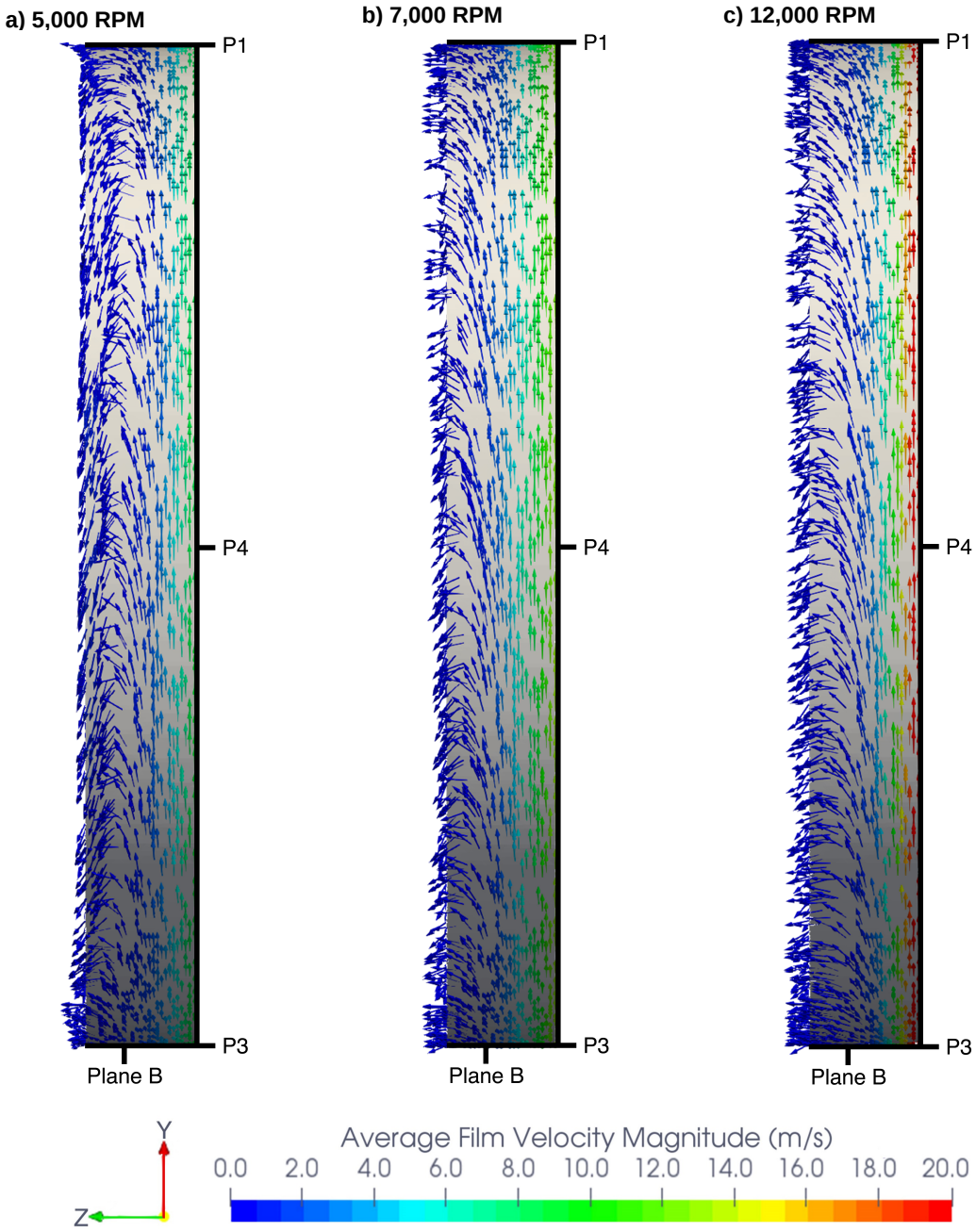


FIGURE 5.8: MEAN VELOCITY MAGNITUDE VECTOR PLOTS AT EACH DIFFERENT SHAFT ROTATIONAL SPEED AND 7.3 L/MIN FOR THE P4 COUNTER-CURRENT REGIME

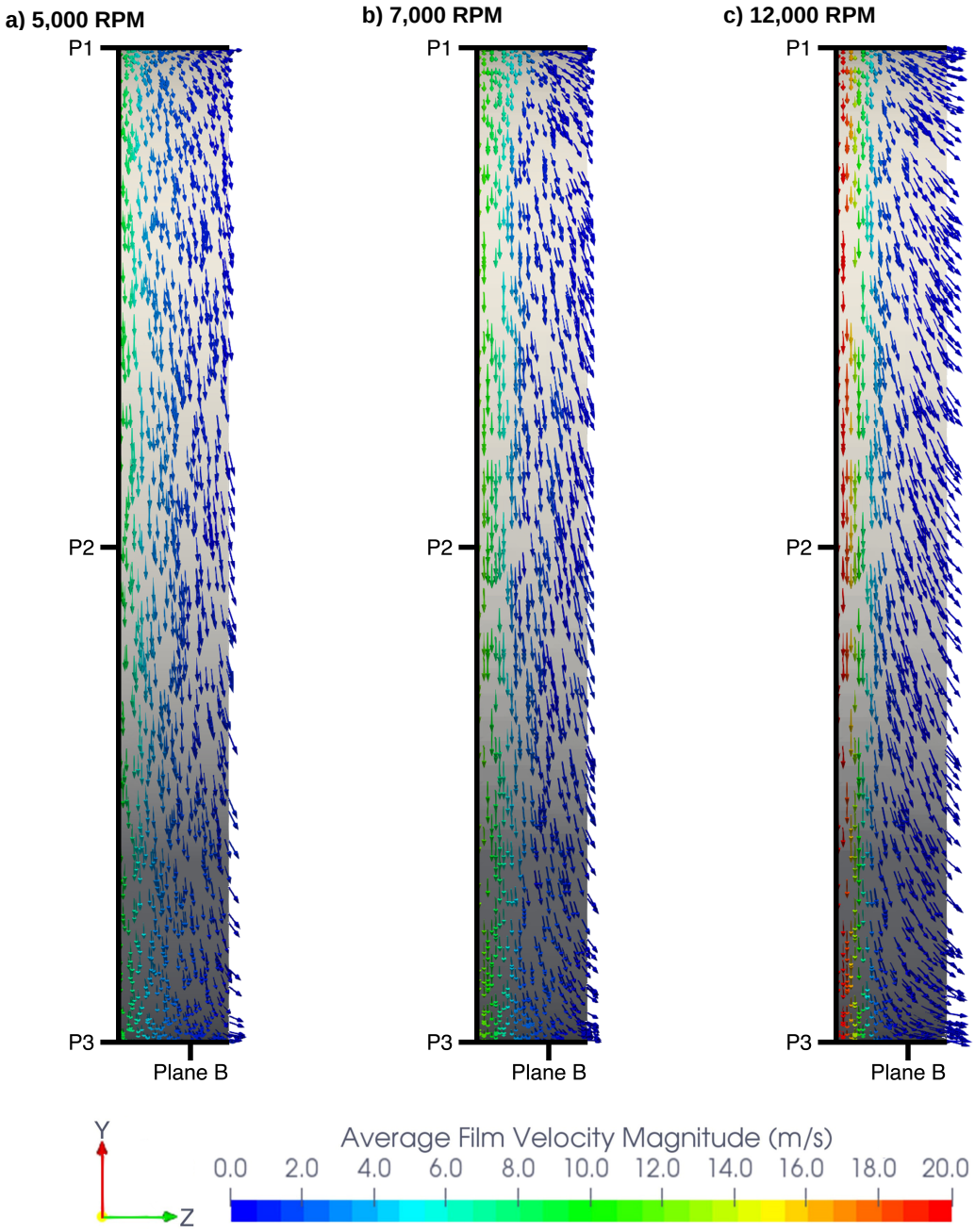


FIGURE 5.9: MEAN VELOCITY MAGNITUDE VECTOR PLOTS AT EACH DIFFERENT SHAFT ROTATIONAL SPEED AND 7.3 L/MIN FOR THE P2 CO-CURRENT REGIME

The experimental investigations of Hee et al. [54] revealed that, at the observational measurement plane B, the critical speed at which this second flow reversal takes place is observed between 3,000 and 5,000 rpm, beyond which the shear-dominated smooth flow regime is witnessed. From the experiments of Hee et al., it is not reported whether this observation is also apparent at Plane A, 3mm before the front face-edge. However computationally, for all cases from Figures 5.8 a) to c), at the Plane B location, the film is travelling upwards suggesting a smooth shear dominated flow regime, much like the experimental observations of Hee et al. [54]. Immediately afterward, we can see the effect of gravity pulling the film downward, suggesting that this shear dominated smooth flow regime has not been fully reached at the counter-current side. Even at 12,000 rpm, Figure 5.8 c), a transitional period within the shock regime is observed, with oil waves towards the top of the chamber traveling upwards, and waves seen to be pulled slightly downward at the bottom of the chamber. Since the bearing chamber runs with a truncated shaft, as depicted in Figure 5.10, it may be possible that this smooth shear dominated flow regime is not achievable even at 12,000 rpm. As the airflow moves towards the bearing chamber expansion, the shearing velocity decreases and hence the shearing force is reduced, potentially to the point where gravity still dominates. In addition, this effect of the truncated shaft is compounded by the absence of a sealing airflow within the bearing shedding rig. As previously demonstrated by Gorse et al. [33, 49], under single-phase conditions, a sealing airflow can have a significant effect on the secondary flow field structure and, similarly, within the two-phase flow, the droplet generation process.

However, the reason why, computationally, a fully shear driven smooth flow regime is never reached, may also be attributed to the formulation of the thin film representative inlet boundary condition. Experimentally, the mechanism for oil film formation on the outer stationary cylinder walls can be broken down into two components: oil shed from the cage-edge and the axial displacement of oil at the outer-race location. Without directly modelling the oil breakup from the cage-edge, a significant proportion of the tangential momentum imparted on the oil film could be lost, due to not capturing the momentum exchange of the droplets or ligaments impinging on the surface film. Therefore, this gain in tangential momentum could, in turn, transition the film into a fully shear driven flow regime within the counter-current region. As such, a more comprehensive film inlet boundary condition is proposed and explored later in Section 5.4.

5.3.2 Quantitative Oil Distribution

The axial variation in the average film thickness at the P2 and P4 locations are shown in Figures 5.10 a) to f). For all of Figures 5.10 a) to f), the axial extent of the film is presented, whereby 0 corresponds to the front-face edge and, for clarity, only the distance over the last 20mm of the film is shown. Experimental film thickness data, derived from image analysis, are presented by Hee et al. [54] for both P2 and P4 regions at Planes A and B, these correspond to the axial location of 3mm and 10mm upstream of the front-face edge respectively. For all of the shaft speeds and flow conditions presented in Figures 5.10 a) to f), the average film thickness of the oil film ranges between a minimum of 0.4mm up to a maximum 1.4mm. This is in excellent agreement with the results of Hee et al., who report that for a shaft speed of 5,000 rpm and above, under the same operating conditions, the film thickness varied between a value of 0.5mm to 1.4mm.

With an increase in flow rate from 5.2 l/min to 7.3 l/min, i.e. comparing Figures 5.10 d) to f) with Figures 5.10 a) to c), at each shaft speed, the same overall trend is captured with only minor deviations. The most notable difference occurs at 7,000 rpm where at the lower volume flow rate, Figure 5.10 e), a thicker film initially builds up in both P2 and P4 regions, which then thins equally; whereas at 7.3 l/min, Figure 5.10 b), a relatively stable film is formed. In general, whilst there may be some variations between the P2 or P4 regions, at the two volume flow rates, the differences are small but not consistent.

The main trend observed from the film thickness measurements plots is the decreasing film thickness with an increase in rotational shaft speed, again in agreement with the experimental measurements of Hee et al. [54]. This result is expected due to the dependence of the film thickness on the rotational shaft speed; since an increase in speed, will increase the circumferential air velocity and hence increase the interfacial shear force. Subsequently, the film velocity increases and as a result, the oil film thickness is reduced to satisfy mass continuity. It is important to note that the film thickness is also a local function of both the angular coordinate and axial location on the stationary outer wall. Within the co-current region, for both Planes A and B, Hee et al. report a decrease in film thickness of approximately 50% between shaft speeds of 3,000 and 5,000 rpm; with a further reduction of 25% seen as the speed is increased to 7,000 rpm. Conversely at the counter-current side, the film thickness drops by 60% with an increase in shaft speed from 3,000 rpm to 5,000 rpm; and a further increase in shaft speed to 7,000 rpm subsequently sees a drop in film thickness of approximately 30%.

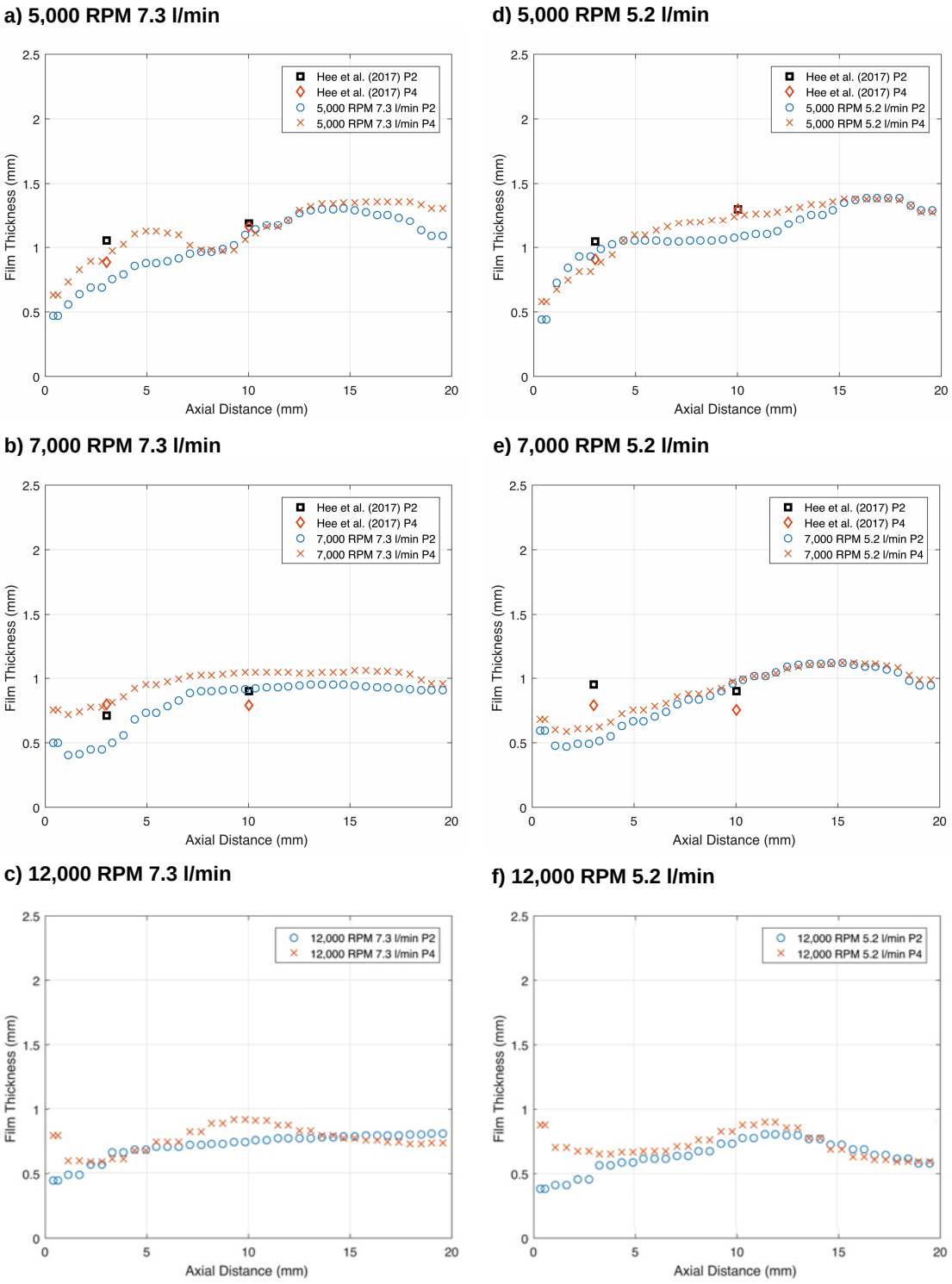


FIGURE 5.10: AXIAL VARIATION OF FILM THICKNESS AT CO- AND COUNTER-CURRENT REGIONS (P2 AND P4) WITH SHAFT ROTATIONAL SPEED AGAINST EXPERIMENTAL MEASUREMENTS OF HEE ET AL. [54] AT 3mm AND 10mm

Over the experimental data range investigated, Hee et al. report that for both P2 and P4 regions, with every step in shaft speed of 2000 rpm, the fraction that the film thickness reduces by each time is halved. For example, within the P2 region, as the rotational shaft speed increases from 3,000 rpm to 5,000 rpm and then subsequently to 7,000 rpm, the film thickness reduces first by 50% and then by a further 25% respectively. Therefore, it is not unreasonable to assume that this trend carries forward, reducing by a further 12.5% up to 9,000 rpm and, for arguments sake, reducing by a final 6.25% moving to 12,000 rpm. Similarly, for the P4 region, this would lead to the series of reductions: 60%, 30%, 15% and finally 7.5%. Figures 5.11 a) to d) show the experimental variation in film thickness measurements with rotational shaft speed presented by Hee et al. [54]; data is shown for planes A and B. For the purpose of the work carried out here, the results of Hee et al. are extrapolated (dot-dashed lines), to shaft speeds of 9,000 rpm and 12,000 rpm for both P2 and P4 region following the previous diminishing returns theory. It should be noted that for both the computational and experimental results, whilst the plot markers represent the discrete shaft speeds investigated, these are connected by lines to show the overall trend.

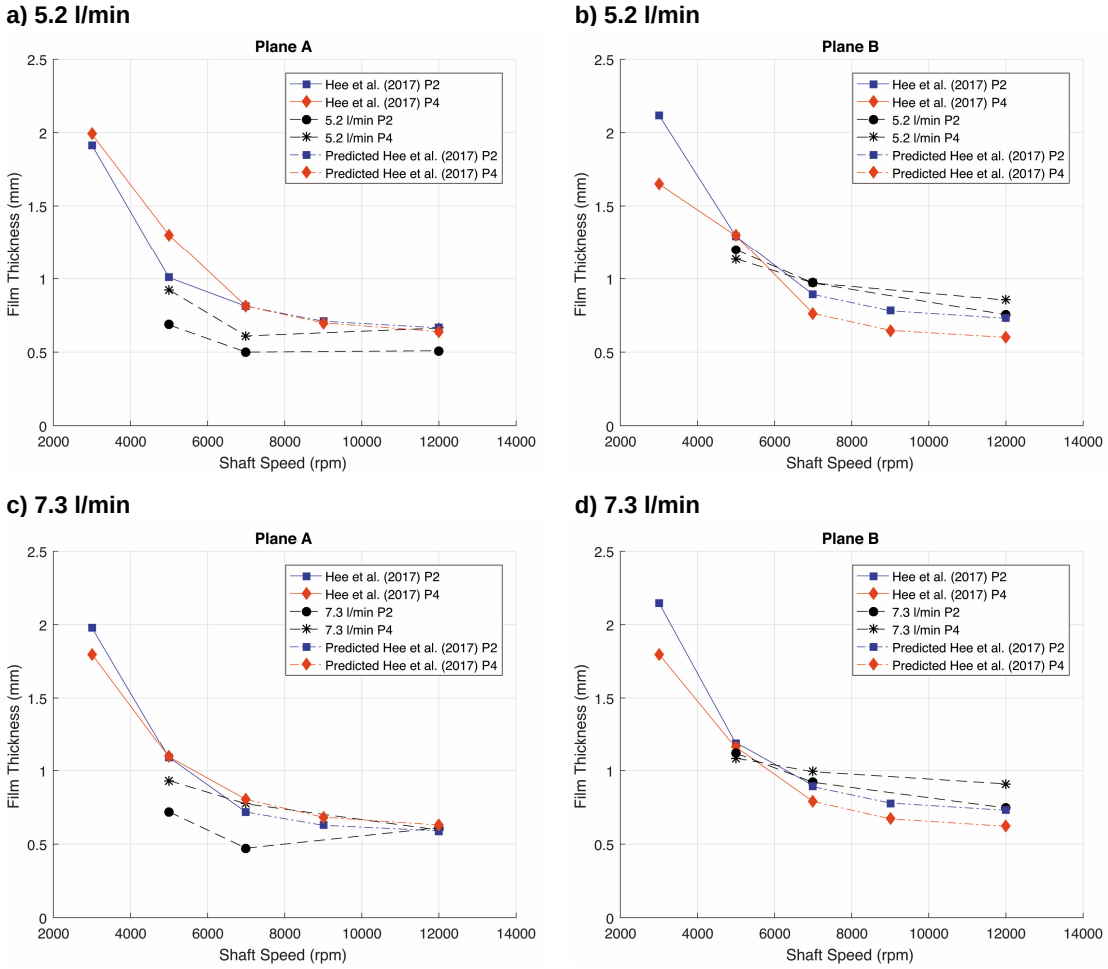


FIGURE 5.11: VARIATION IN OIL FILM THICKNESS WITH ROTATIONAL SHAFT SPEED FOR CO- AND COUNTER-CURRENT REGIONS (P2 AND P4). TOP 5.2 L/MIN AND BOTTOM 7.3 L/MIN.

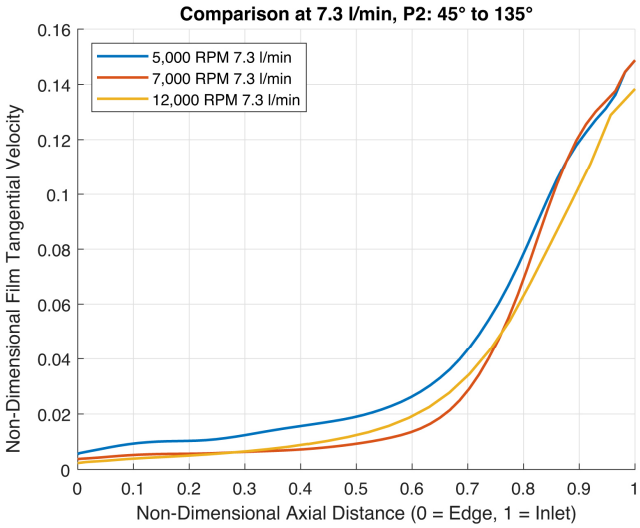
Within Figures 5.11 a) to d), the available computational data is shown in black for the P2 and P4 regions, which are represented by the circles and stars respectively. It is clear that across the data, there is an overall reduction in film thickness with an increase in the rotational shaft speed from 5,000 rpm to 7,000 rpm, in line with the experimental measurements of Hee et al. [54]. Computationally, as an overview and in terms of oil residence volume, moving from 7,000 rpm to 12,000 rpm, we do see an overall reduction in the film thickness within both P2 and P4 regions, although, this is less clear when looking at the individual measurement planes. In Figures 5.11 b) and d), whilst a reduction in film thickness is observed at Plane B, 10mm from the front face-edge; neither a clear increase nor decrease in film thickness is seen at the Plane A location, Figures 5.11 a) and c). This in part can be associated with the inability for both cases at 7,000 rpm and 12,000 rpm never reaching a fully shear dominated smooth flow regime. From Figure 5.8 a) to c), it is apparent that the flow reversal, due to fluid being pulled downward due to gravity, takes place just before the oil film meets the front face-edge before being shed into the bearing chamber. This undulation effect evidently goes through a maximum, i.e. the shock regime, somewhere between both the two shaft speeds and flow rates investigated, hence why the variations are not consistent.

From Figures 5.11 a) to d), for the experimental data points available, the simulations accurately capture the overall trend of decreasing film thickness from 5,000 rpm to 7,000 rpm, especially within plane B. Even though at plane A, the simulations under predict the film thickness, a good agreement is observed especially without knowing the experimental measurement errors. When the measurements of Hee et al. are extrapolated to 9,000 rpm and ultimately 12,000 rpm, it is clear that the simulations all predict a very similar film thickness. The excellent agreement between the predicted and computational results suggests that there is indeed a diminishing reduction in film thickness with an increase in shaft speed.

5.3.3 Oil Residence Time

Over each shaft speed, Figures 5.12 a) and b) show the axial variation of the mean film tangential velocity at the discrete P2 and P4 locations, non-dimensionalised by the linear shaft speed, for the oil flow rate of 7.3 l/min. The same trends are observed at the flow rate of 5.2 l/min. It is clear that for all cases, a significant reduction of film velocity is observed over the first third of the film, reducing from 15% of the shaft speed down to approximately 2.5%, beyond which the film steadily decreases in velocity down to less than 0.5% of the shaft speed. For reference, there was very little variation in the axial velocity of the film along the slot, and for all of the shaft speeds investigated, the mean axial velocity was approximately 0.1 m/s. From Figure 5.12 b), the flow reversal that takes place within the P4, counter-current region, is apparent by the change in tangential velocity from a positive to a negative value. As the shaft speed increases, the flow reversal begins to recover and at 12,000 rpm, the tangential velocity is almost zero, suggesting a pure axial outflow, which is clear from the velocity vectors presented in Figure 5.8 c).

a)



b)

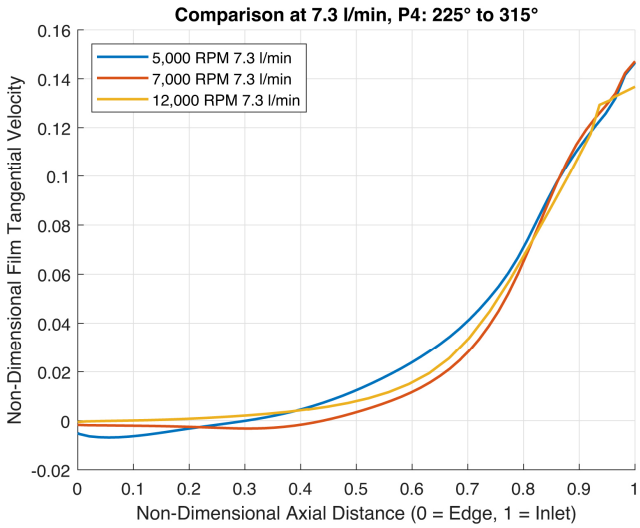


FIGURE 5.12: NON-DIMENSIONALISED FILM VELOCITY AT THE a) P2 SECTOR AND b) P4 SECTOR FOR EACH SHAFT SPEED AT 7.3 L/MIN

Using the result of the mean film velocity, Figures 5.13 a) to c) show plots of streamlines generated and released at both P2 and P4 discrete locations, coloured in red and green respectively. Figure 5.13 a) shows streamlines for the shaft speed at 5,000 rpm, for both sides, the film travels approximately the length of one full revolution around the cylinder annulus before exiting into the main chamber. The difference being, that the fluid from the P2 region travels around the annulus eventually undergoing flow reversal within the P4, gravity dominant side. Increasing the shaft speed to 7,000 rpm, as in Figure 5.13 b), as the film velocity increases, the distance travelled around the annulus also increases; such that the film now makes over one and a half full revolutions. Finally, at 12,000 rpm, the film travels up two times around the annulus, although all of the distance covered in the initial revolution occurs over the first third of the film where the velocity is at its highest. This is apparent from Figures 5.12 a) and b), whereby the greatest film velocity is observed closest to the bearing, which subsequently significantly reduces after the non-dimensional axial distance of 0.6.

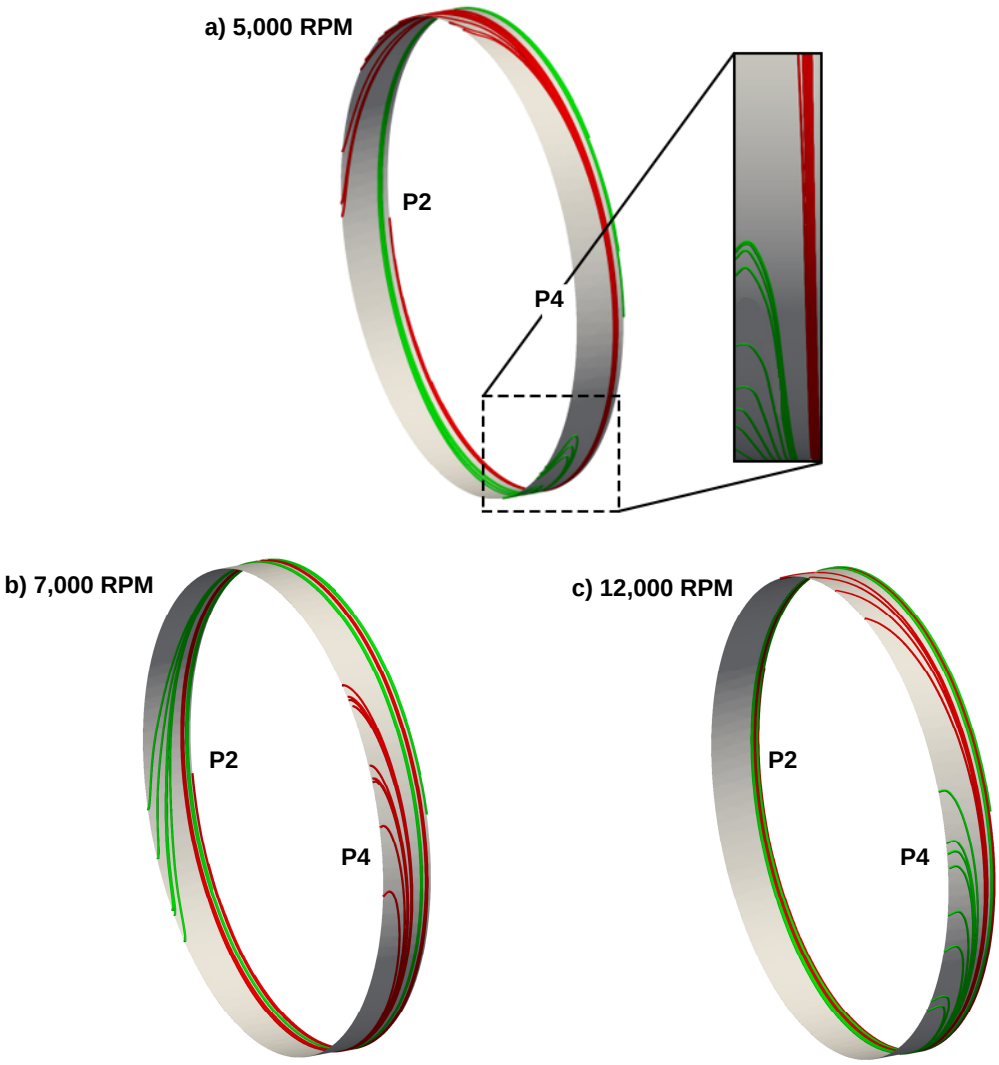


FIGURE 5.13: MEAN STREAMLINE PLOTS GENERATED FOR P2 (RED) AND P4 (GREEN) LOCATIONS AT EACH SHAFT SPEED (7.3 L/MIN)

It is possible to compare the average oil residence times for each of the three shaft speeds, i.e. the amount of time the oil takes to travel around the annulus before exiting into the chamber. At 7.3 l/min and 5,000 rpm it takes approximately 0.345s for the oil to exit, by 7,000 rpm this reduces to 0.285s and finally 0.275s at 12,000 rpm. Very similar results are observed for the flow rate at 5.2 l/min, with times of 0.335s, 0.27s and 0.26s respectively.

It is expected that for the 5.2 l/min case, the oil residence time will be smaller, since at a fixed shaft speed, with less oil, a thinner and hence faster film will form. However, between the two flow rates a very small difference in oil residence times is observed. This is apparent, since for a given shaft speed, the oil film trends toward the same film thickness at both flow rates, as observed from Figures 5.10 a) to f). The main differences occur within the first third of the film development, where the velocity is at its highest. Therefore, it is unsurprising that only a small difference in oil residence time is observed between the two flow rates.

Once again, it is clear that there is a diminishing return on the oil residence time as the shaft speed increases. It is unclear whether a more appropriate film inlet boundary condition, which would account for the momentum exchange of droplets from the cage-edge, would result in a faster oil film and hence a shorter oil residence time. In general, the results show that there is a maximum residence time of approximately 0.35s, occurring at the slowest shaft speed. This suggests that for bearing chamber design, there needs to be accountability for a minimum oil residence time of at least 0.35s when considering heat transfer effects to prevent oil degradation or coking. In a similar manner, from Figures 5.11 a) to d), it is apparent that over both flow rates, due to this diminishing return effect, there is also a minimum average film thickness of roughly 0.4mm, which becomes independent of the shaft rotational speed. For example, with every step in shaft speed of 2,000 rpm, the amount that the film thickness reduced by, each time, was roughly halved. Signifying that even beyond shaft speeds of 12,000 rpm and for this flow regime, a dry-out region will not be observed.

5.4 Comprehensive Film Inlet Boundary Condition

A concern of the previous work is the modelling assumptions of the film inlet condition. As discussed previously, there are two mechanisms for oil formation on the static outer casing wall, namely: oil shed from the cage-edge and the axial displacement of oil from the bearing at the outer-race. However, there is very limited experimental knowledge surrounding the droplets flung from the cage-edge, either regarding the amount of oil shed, the droplet size distribution or the droplet trajectories. Whilst the oil flow may be analogous to the flow over a rotating cup, due to the relatively smaller size of the cage, there is still considerable uncertainty. As such, originally, a representative film inlet boundary condition was proposed, as outlined below, however as explained it is unclear whether a more comprehensive boundary condition is required.

Representative Film Inlet Boundary Condition: for the initial modelling, it was assumed that all of the oil exiting from the cage-edge impinges on the film surface. As such, all of the oil was supplied axially into the domain at the outer-race location, as depicted in Figure 5.3. However, the momentum exchange of droplets impinging on the film surface, shed from the cage-edge, are effectively ignored. It is suspected that this may have a significant impact on the overall film velocity, which could potentially lead to a thinner film but also be a factor in achieving a fully shear driven flow regime. As such, a more comprehensive film inlet boundary condition is investigated to assess the effects of including droplets shed from the cage-edge.

Comprehensive Film Inlet Boundary Condition: here, the oil exiting from the bearing is modelled by including both the oil displaced axially from the bearing at the outer-race and also droplets shed from the bearing cage-edge. Firstly, the film developing as a result of oil exiting at the outer-race is generated in the same way as the representative film inlet boundary condition. However, to simulate droplets produced around the periphery of the cage-edge, a DPM injection condition is implemented, to capture the momentum exchange of droplets with the oil film. As such, the volume flow rate of oil needs to be split accordingly between the two oil inlets.

However, there is no experimental data reporting the proportion of oil shed from the cage-edge compared to that axially displaced at the outer-race location. From visual analysis of the experimental results of Santhosh et al. [53] and Hee et al. [54], the cage-edge produces a much smaller fraction of the total amount of oil. As such, three different oil flow rate splits are investigated, a 10/90 percent split of oil from the cage-edge vs outer-race axial displacement and both a respective 20/80 and 50/50 percent split.

Initially, for this comprehensive film inlet boundary condition, the case setup only considered a shaft speed of 7,000 rpm and an oil flow rate of 7.3 l/min. At the cage-edge, oil is supplied via a DPM injection around the full annulus of the cage-edge. In this, the droplets are given a mass

flow rate based on the derived percentage split. Analogous to flow past the edge of a rotating cup [53], it is assumed that droplets are dispersed tangentially outward with a velocity equivalent to the cage speed, with no radial or axial velocity component. Since no information is available regarding the size and distribution of the droplets, it is assumed to be equivalent to the droplet distribution stripped from the film surface. This is derived based on the initial simulations using the representative boundary condition. As such, a droplet size distribution is provided based on a log-normal Rosin-Rammler distribution; specifying an average diameter of 55μm and a maximum droplet diameter of 100μm. Using this information, the DPM injection is fully prescribed; and, to account for the reduced volume flow rate of oil at the outer-race, the film inlet velocity is adjusted accordingly.

5.4.1 Results: Comprehensive Boundary Condition

To begin with, results were unobtainable for the simulation run with a 50/50 percent split, due to severe numerical instabilities faced as a result of the large proportion of mass injected into the system. However, results were obtained for the 10/90 and 20/80 percent splits and the axial variation in the mean film thickness is shown for the P2 and P4 locations depicted in Figure 5.4. For Figure 5.14, only the axial extent over the last 20mm of the film is shown, whereby 0 corresponds to the front-face edge. Comparison is made to the film thickness measurements presented by Hee et al. [54], as well as the results obtained using the representative film inlet boundary condition presented in Figure 5.10 b), i.e. a 0/100 split of oil. Immediately it is clear that over both oil splits, poor agreement is found between the experimental measurements of Hee et al., and overall, no significant improvement is found over the representative film inlet boundary condition. However, it should be noted that good agreement is observed for the 10/90 percent split within the P2, co-current region. Furthermore, within the P4, counter-current region good agreement is observed up towards Plane B, at 10mm, but beyond which, there is a significant spike in film thickness. As the split is increased to 20/80 percent, the errors that were noticeable in the 10/90 split are multiplied even further, and therefore, it is unsurprising that at a 50/50 percent split numerical instabilities were faced.

Through injecting oil at the cage-edge, with a speed equivalent to the cage, i.e. half the shaft speed, the particles are carried by the turbulent airflow and impact immediately after the injection location. These particles rapidly accelerate the oil film which leads to a sudden thinning and a trough of oil, resulting in a minimum film thickness of 0.4mm. Downstream of this location, at the 20mm position, the film begins to recover and overall there is no comparable difference between the film velocity profiles observed for the two different film inlet conditions. In general, comparison of the mean oil mass over the outer cylinder annulus also showed negligible

differences between the two film inlet boundary conditions. In general, the main difference being, that this initial acceleration of the oil causes a much more unstable film to develop downstream, resulting in short waves of oil travelling around the annulus. These short waves of oil are analogous to capillary waves, which as demonstrated by Kakimpa et al. [83] can be very sensitive to both the numerical grid spacing and timestep, leading to instabilities unless adequately resolved. Suggesting that further work may be required in refining the grid spacing within this region, in order to achieve a stable solution.

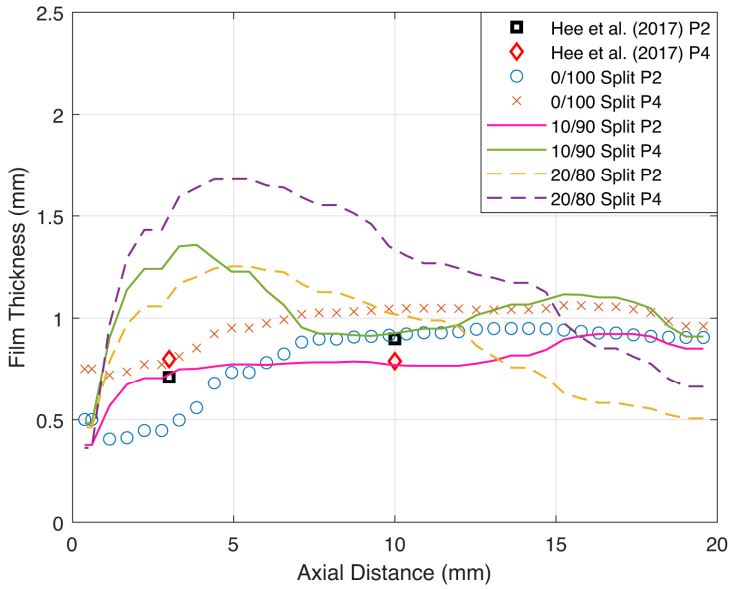


FIGURE 5.14: AXIAL VARIATION OF FILM THICKNESS FOR THE TWO OIL INLET SPLITS AT BOTH P2 AND P4 REGIONS. COMPARISON WITH REPRESENTATIVE FILM INLET BOUNDARY CONDITION, 0/100 SPLIT

For the more comprehensive film inlet condition, over both oil splits investigated, within the P4 region, a shear dominated flow regime is observable at Plane B, similar to the experimental investigations of Hee et al. [54]. However, beyond this, the presence of a gravity dominated flow regime is found moving axially towards Plane A; the same is true for the representative film inlet boundary condition previously evaluated in Section 5.3. Whilst a 5/95 percent split might be viable in achieving a more stable solution, there is an overall negligible difference in velocity observed with the DPM injection cases. Therefore, it is suspected that the same gravity dominated flow regime will still be found, since a 5/95 percent split will have a reduced amount of momentum exchange from droplets relative to the 10/90 split. This suggests that the lack of droplets impinging on the thin film from the cage-edge does not influence the flow regime as originally expected. Due to the very limited information surrounding the oil exiting from the cage-edge, it is difficult to assess a more appropriate film inlet boundary condition. However, these results and the outcomes of Section 5.3, indicate that for future bearing chamber design it is not

necessary to distribute oil from the cage-edge in order to prevent a dry-out region, although it may still be a necessary requirement for the heat management process over these surfaces.

Overall, the originally proposed, representative film inlet boundary condition is therefore deemed the most suitable approach available. Future experimental work is recommended in providing more detailed measurements to support the development of a more suitable DPM inlet condition.

5.5 DPM Results

5.5.1 Oil Residence Mass

Upon reaching a steady state solution of the particulate cloud, DPM particle properties were temporally averaged. Table 5.4 summarises the average particle cloud properties for each rotational shaft speed at a flow rate of 7.3 l/min, distinguishing between both stripped and edge separated particles. For reference, the results at a shaft speed of 7,000 rpm and an oil flow rate of 5.2 l/min are also included. At 5,000 rpm the average total cloud mass, i.e. the sum of both stripped and edge separated particles, is 21.2g, this increases to 27.0g at 7,000 rpm but reduces significantly at 12,000 rpm to just 13.8g. Furthermore, Table 5.5 shows the mass flow rate of oil that is separated as droplets at the front-face edge, compared to the amount of oil supplied into the domain at the film inlet boundary condition. This is then presented as percentage, to therefore demonstrate the proportion of oil that is separated at the edge as droplets. As such, the remainder of oil is either stripped as droplets upstream of the front-face edge or remains attached to the surface and flows down the front-plate.

From Table 5.5, it is clear that with an increase in shaft speed from 5,000 rpm to 7,000 rpm, the amount of mass separated at the edge subsequently increases from 51.6% to 88.0%. This results in a greater particulate cloud mass at 7,000 rpm, as evident from Table 5.4. At 5,000 rpm, there are on average a greater number of edge separate particles within the dispersed phase when compared to 7,000 rpm, however this can be accounted for, since these particles are travelling relatively slower due to the reduced gas velocity and therefore have an increased residence time. With an increase in shaft speed to 7,000 rpm, the momentum of the film at the front-face edge increases, hence the amount of edge separation also increases, resulting in a greater proportion of the film height being separated over the edge. An increase in particle diameter can also be associated with the undulation effect observed within the P4 film region, which goes through a maximum at 7,000 rpm, as the flow transitions through the shock regime. Therefore, an overall increase in droplet diameter is observed, evident from the shift in average diameter from 365μm to 402μm. Whilst there are fewer edge separated droplets at 7,000 rpm, this greater droplet diameter, in combination with the large ligaments produced, results in an increased cloud mass.

Interestingly, a further increase to 12,000 rpm sees a decrease in particulate mass, Table 5.4. Here, the increase in shaft speed from 7,000 rpm results in a reduced undulation effect as the film tends to a more uniform smooth shear dominated flow regime, as a result of the higher gas velocity. Whilst a similar proportion of mass is separated at the edge, as evident from Table 5.5, these particles are travelling relatively faster and therefore have a shorter residence time, hence, the reduced number of particles produces a smaller cloud mass.

As the shaft speed increases, the amount of film shear stripping that takes place also increases. At a shaft speed of 5,000 rpm, only a very minimal amount of stripping is observed, which is almost negligible in proportion to the total cloud mass. However, even at 7,000 and 12,000 rpm the ratio of mass stripped from the film versus that separated at the edge is still very small, accounting for only 0.8% and 1.5% of the total mass respectively. Whilst there are over an order of magnitude more stripped particles than edge separated particles, at both 7,000 and 12,000 rpm, their average diameter is considerably smaller and therefore only represent a smaller fraction of mass.

TABLE 5.4: AVERAGE CLOUD PROPERTIES AT EACH ROTATIONAL SPEED

	Shear Stripped Particles			*Edge Separated Particles*		
Shaft Speed (rpm)	***Average No. Particles***	***Average d (μm)***	***Cloud Mass (kg)***	***Average No. Particles***	***Average d (μm)***	***Cloud Mass (kg)***
5,000	42,100	52.6	2.89×10^{-6}	579,200	630	21.2×10^{-3}
7,000	2,082,500	58.8	2.12×10^{-4}	292,400	830	26.8×10^{-3}
12,000	2,916,200	53.4	2.12×10^{-4}	115,100	780	13.6×10^{-3}
7,000 (5.2 l/min)	496,100	59.8	1.02×10^{-4}	330,348	830	19.4×10^{-3}

TABLE 5.5: PROPORTION OF EDGE SEPARATED MASS AT EACH ROTATIONAL SPEED

Shaft Speed (rpm)	$\dot{m}_{Supplied}$ ***(kg/s)***	$\dot{m}_{Separated}$ ***(kg/s)***	***Percentage***
5,000	0.0965	0.0498	51.6%
7,000	0.0965	0.0849	88.0%
12,000	0.0965	0.0876	90.8%
7,000 (5.2 l/min)	0.0683	0.0610	89.3%

Within Table 5.4, comparing the two oil flow rates at 7,000 rpm the most noticeable difference occurs within the number of stripped particles present. At 7,000 rpm, stripping predominately occurs within the P4 counter-current region, as a result of the undulation effect, whereas as 12,000 rpm stripping takes place more uniformly around the annulus. Therefore, the reduced number of stripped particles at 5.2 l/min suggests that the undulation effects are not as strong. Table 5.5 demonstrates that similar amounts of edge separation occurs at both oil flow rates, however, at the flow rate of 5.2 l/min a smaller average diameter is found, which in combination with the reduced undulation effect, overall, results in a reduced cloud mass.

5.5.2 Qualitative Oil Distribution

Figure 5.15 shows a sample of the instantaneous particle trajectories coloured by their particle diameter at a shaft speed of 7,000 rpm and a flow rate of 7.3 l/min. The snapshot is taken after one complete film cycle to best visualise the particle trajectories.

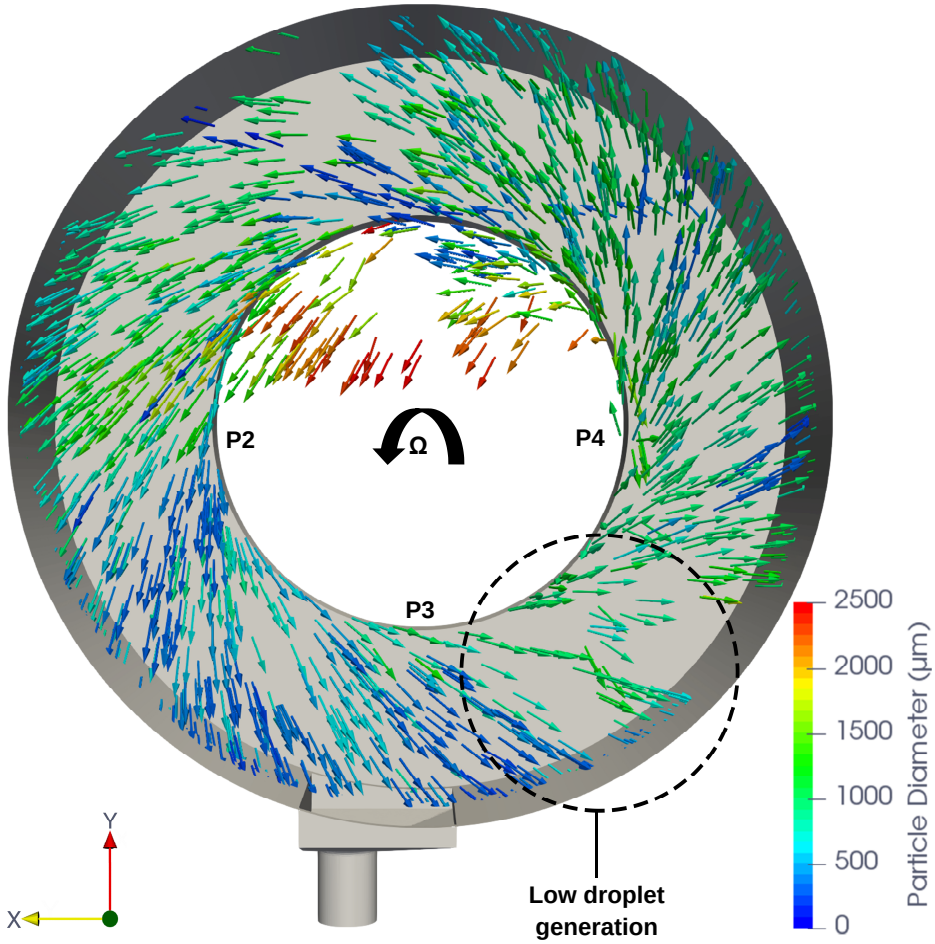


FIGURE 5.15: INSTANTANEOUS PARTICLE TRAJECTORIES WITHIN THE MAIN CHAMBER COLOURED BY DIAMETER FOR 7000 RPM 7.3 L/MIN (FILM NOT SHOWN)

Moving around the chamber annulus, in Figure 5.15, it is immediately clear that the droplet diameter distribution changes significantly as a function of the angular coordinate. To understand the effects more clearly, it is important to analyse the underlying flow physics within each quadrant. Therefore, in in Figure 5.15, if we consider the P2 region and move anticlockwise with the direction of shaft rotation. Firstly, within this co-current section, the film velocity at the front-face edge becomes the greatest, as can be seen from Figure 5.16; which shows the mean film velocity as a function of the angular coordinate for the three shaft speeds investigated at 7.3 l/min. The results within Figure 5.16 are presented at the front-face edge, i.e. the DPM Plane C in Figure 5.3, this is the location at which the film separates into the main chamber. For the P2 sector within

Figure 5.16, as we increase the shaft speed from 5,000 rpm to 12,000 rpm, this local maximum in film velocity shifts further around the annulus from 70° to 135°. Here, the film velocity travels in the direction of gravity and subsequently gains sufficient momentum for it to fully separate over the edge into the bearing chamber, as observed from the instantaneous film thickness measurements on the front-face wall previously presented in Section 5.3.1. With respect to the rest of the oil film around the chamber annulus, the higher film velocity produces a relatively thinner film. At the point of edge separation, based on the formulation of Friedrich's separation model, these edge separated droplets are given a diameter equivalent to the film thickness removed from the surface. As a result, droplets are seen to shed from the edge with an average particle diameter close to 500µm and a minimum of 200µm; this is in good agreement with the most recent, unpublished, experimental results observed within the bearing shedding rig [134], for which both particle diameters and velocities have been quantified.

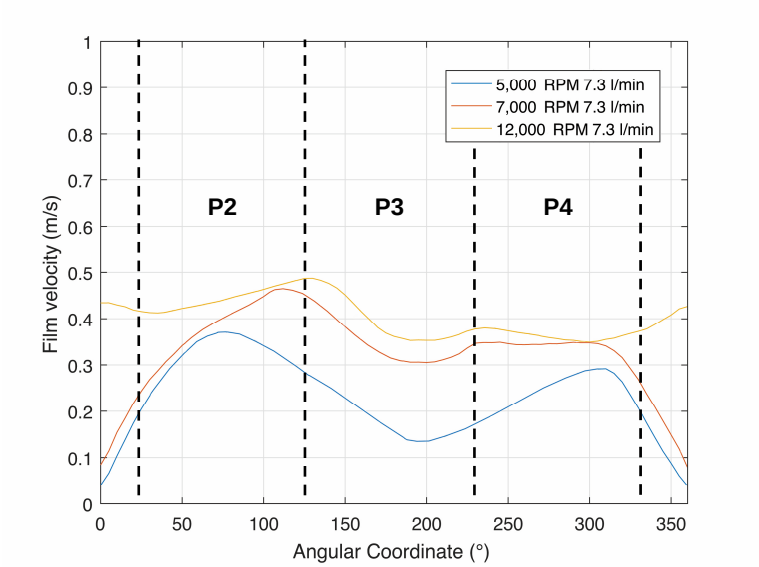


FIGURE 5.16: MEAN FILM VELOCITY WITH ANGULAR COORDINATE AT THE FRONT-FACE EDGE (7.3 L/MIN)

Within Figure 5.15, this trend continues as we move from the P2 region towards the bottom of the chamber at 180°, the P3 quadrant. The film velocity begins to slow, leading to a gradual increase in film thickness and hence an increase in particle diameters separated over the edge. However, as the film velocity slows, its momentum reduces and hence the amount of edge separation decreases resulting in a proportion of the film starting to remain attached as it flows over the edge. For all of the shaft speeds investigated, this effect becomes the greatest, just after the bottom dead centre location, at around 190°, where the film velocity reaches a local minimum, as evident in Figure 5.16. The smooth shear dominated flow regime starts to transition into a gravity dominated flow, whereby the film begins to pool at this location. At the 190° position,

virtually all of the mass remains attached as it turns the corner, with a small number of droplets being periodically separated, apparent by the lack of particles captured in this region within the instantaneous particle trajectories of Figure 5.15.

As discussed previously in Section 5.3.1, moving into the P4, counter-current region, upstream of the edge, at the axial distance of 10mm from the front-face edge, Plane B, the film travels in the opposing direction of gravity, representative of a smooth shear dominated flow regime. This follows the experimental observations of Hee et al. [54] at this Plane B location. However, as we move closer to the edge, the effects of gravity begin to dominate as the fluid slows, changing in direction, as it is pulled back downward; this phenomena mildly persists even up to a shaft speed of 12,000 rpm. The film begins to accelerate downward, intermittently undulating, due to the axial displacement of the incoming upstream fluid. This effect causes a build-up of oil, increasing the film thickness, and as a result, relatively larger particles are seen to shed from this rising side of the chamber in Figure 5.15. This results in an average particle diameter of approximately 1000μm. At this front-face edge, the undulating effect observed computationally reaches a maximum at a shaft speed of 7,000 rpm.

Finally for Figure 5.15, progressing towards the top of the chamber, the P1 region, the film begins to transition back towards a smooth shear dominated flow regime as the angle of the film with respect to gravity changes. From Figure 5.16, it is clear that at the two shaft speeds of 5,000 and 7,000 rpm, the mean film velocity reduces significantly, reaching a minimum at the top dead centre, 0° coordinate. The film momentum decreases accordingly and as such, the amount of edge separation consequently reduces, becoming zero at the 0° location. Here, at the edge, the film remains attached, flowing radially outward over the front-face surface. The reduced velocity and further influence of gravity causes the film to quickly build-up at this location. Eventually, as the film accumulates and the relative velocity between the thin film and high shearing airflow increases, the critical conditions for shear stripping at this location become satisfied. As a result, a small number of large diameter particles are seen to be stripped from this location, with diameters up to a maximum of 2,500μm. This is evident from the lack of oil present within the instantaneous film thickness measurements of Figure 5.6. These large diameter droplets are analogous to the ligaments measured experimentally [134] and that observed by Hee [55] as shown in Figure 5.17. However, computationally, as a result of the DPM limitations, these ligaments are instead represented as droplets. Figure 5.17, highlights the experimental P1 region at a shaft speed of 7,000 rpm and an oil flow rate of 7.3 l/min. Here, the bulk trajectory of the oil, consisting of relatively smaller diameter droplets, Frame 30, is seen to be travelling up and to the right in a similar fashion to that observed computationally within Figure 5.15. It is important to note, that the experimental and computational viewing positions are flipped, Section 5.2. However, the formation of a large three-dimensional ligament structure can also be identified in

Frame 1, instead, this moves down and to the right, which is again in agreement with the large diameter droplets observed computationally within Figure 5.15. Furthermore, Figure 5.6 suggests that within the P1 region, there is no oil travelling radially outward over the front-face plate, this is also consistent with the images presented Figure 5.17, here, demonstrating an absence of oil film over this region.

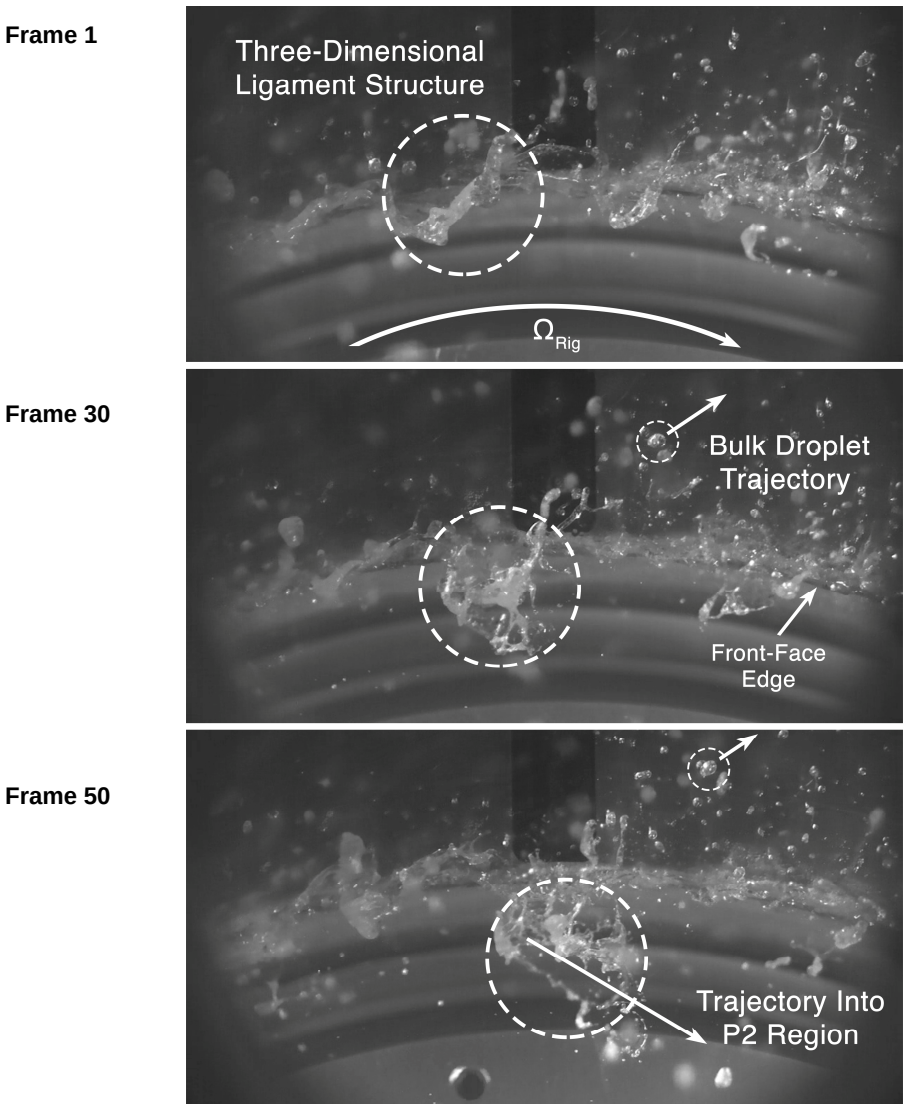


FIGURE 5.17: EXPERIMENTAL OIL STRUCTURE AT P1 [55], 7,000 RPM & 7.3 L/MIN (6,000 fps)

Due to the formulation of the stripping criteria, these large diameter droplets within the P1 region in Figure 5.15 are prescribed an initial velocity and trajectory equivalent to that of film from where they are stripped from, hence, they have a small velocity component. These heavier particles are therefore seen to fall under the effects of gravity into the P2 region, instead of being transported by the gas flow, much like Figure 5.17. An equivalent effect is also observed computationally within the P4 side, whereby a very small number of particles are seen to be moving with a negative tangential velocity with respect to the bulk flow. Similarly, these are

particles stripped from the front-face surface due to the accumulation of film as it flows around the edge, although this occurs much less frequently. At the top of the chamber, for a shaft speed of 12,000 rpm this stripping phenomena still occurs, but with a much reduced frequency; since a greater proportion of the fluid is able to separate over the front-face edge. This occurs from the film being able to reach a more uniform smooth shear dominated flow regime beyond the 270° angular location as previously discussed, which is evident by the faster velocity profile captured within Figure 5.16. Similarly, beyond the 0° location, at the 5,000 rpm and 7,000 rpm shaft speeds, the film velocity begins to increase again, and edge separation resumes as we move back towards the P2 region.

Within Figure 5.15, toward the top of the chamber, there are also a small fraction of particles with a diameter less than 100μm. These particles differ to the previously mentioned edge separated particles, which have a minimum diameter of 150μm. At the top of the chamber, these particles originate further upstream of the front-face edge, resulting from the shear stripping of the thin film. In fact, at a shaft speed of 7,000 rpm, these particles emerge as a result of the undulation effect observed within the P4 counter-current region. The undulation effect causes a thickening of the film toward the edge and the critical conditions for shear stripping take place. These particles are heavily influenced by the core airflow and by the time they reach the main chamber are seen travelling through the P1 region in Figure 5.15. At a shaft speed of 7,000 rpm, shear stripping of the film is only observed to take place within the P4 region. At the slower shaft speed of 5,000 rpm, virtually no shear stripping takes place, as is apparent from the particle cloud statistics reported in Table 5.4. This is in part, due to the lower shaft speed, but more importantly due to the undulation effect approaching a maximum around a shaft speed of 7,000 rpm. As we progress to the higher shaft speed of 12,000 rpm, shear stripping takes place more uniformly around the bearing chamber annulus as the relative velocity between the thin film and gas flow increases. This results in a more uniform dispersion of stripped particles around the annulus of the main chamber compartment.

Since the origin of these stripped particles is located upstream of the front-face edge, experimentally, it may be possible to introduce a baffle in order to block these stripped particles. This is analogous to the work of Flouros [51] who used porous screens to capture droplets shed from the bearing in an effort to reduce power losses. Whilst at 7,000 rpm, the stripped particles represent a small fraction of the total cloud mass, the number of droplets tracked is very high, Table 5.4. At high shaft speeds, these droplets may therefore result in the formation of a fine mist of oil. This may present a problem experimentally, causing difficulties during visualisation and furthermore these droplets may become entrained within the vent pipes. Therefore, the introduction of a baffle may promote a more efficient scavenging process, but also, provide an opportunity to further distinguish between the edge separated and stripped particles.

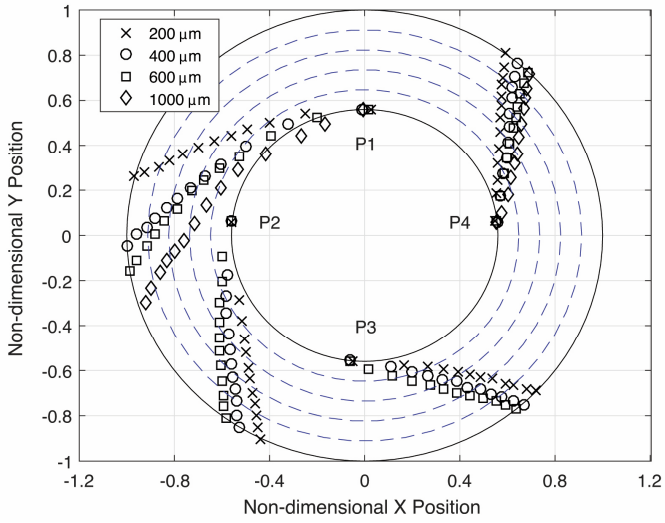
5.5.3 Quantified Particle Trajectories

Figures 5.18 a) to c) shows a more detailed break-down of the particle trajectories in the tangential/radial plane. The front-face edge, where separation occurs is shown by the inner black circle, whilst the chamber outer casing is depicted by the outer black circle; the space is further subdivided by blue dashed lines for viewing clarification. Figure 5.18 a) shows the trajectories for 5,000 rpm and the following images b) and c) are for 7,000 rpm and 12,000 rpm respectively. For each rotational shaft speed, particle trajectories are considered at 4 discrete locations around the annulus to better assess the trajectory dependence on both angular coordinate and particle diameter. For simplification, only the edge separated particles are shown. Therefore, not highlighting the previously discussed stripped particles over the front-face surface, which can range in diameters up to 2,500μm as shown in Figure 5.15

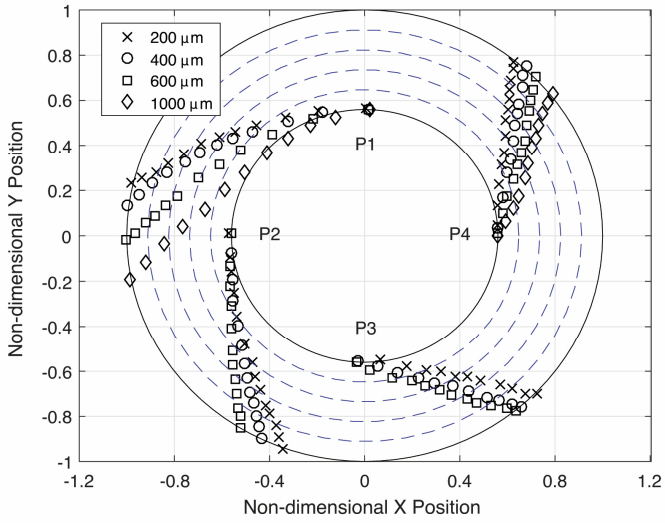
Moving around the chamber annulus, starting at the P2 position for 5,000 rpm, the smaller particles are seen to be more deflected by the gas flow compared with the larger diameter particles. Increasing the shaft speed to 7,000 rpm, the same effect is observed, however, upon reaching 12,000 rpm little deflection is seen, as particles separate with a very high tangential component. A similar trend is observed at the P3 location, however compared to the smaller particles, the larger diameters have a greater radial component due to film velocity slowing and the effect of gravity beginning to dominate. This again carries forward to the P4 location, whereby within the film, the gravity dominated flow regime occurs. As the film is pulled back downward, due to gravity, the film tangential component reduces below zero as demonstrated in Figure 5.12 b). This is most notable at 7,000 rpm where the undulation effect reaches its maximum, this subsequently diminishes with an increase in speed up to 12,000 rpm.

The most notable difference in particle trajectories occurs within the P1 region. At the top of the chamber the spread in particle trajectories is the greatest. For the two slower shaft speeds, the larger particles are seen to deflect downwards with a reduced tangential velocity component. This is associated with the film velocity rapidly reducing towards the 0° location on the front-face edge, as discussed in Figure 5.16. These particles are subsequently carried by the gas flow but are heavily influenced by the effect of gravity, ultimately causing them to arc downwards into the P2 sector. At 12,000 rpm, as a more uniform smooth shear dominated flow regime is achieved, this phenomenon ceases and, in general, around the chamber annulus the particle trajectories are consistent.

a) 5,000 RPM



b) 7,000 RPM



c) 12,000 RPM

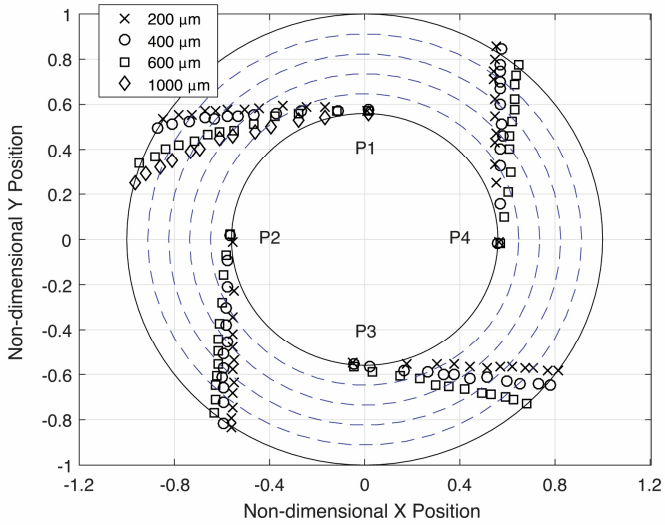


FIGURE 5.18: EDGE SEPARATED PARTICLE MEAN TANGENTIAL TRAJECTORIES FOR EACH SHAFT SPEED (7.3 L/MIN)

The classification of particles shed from the P1 region has an important impact on interpretations of experimental proceedings. It has been identified that these large diameter particles, either edge separated or stripped, will have trajectories passing through the P2, counter-current region. Computationally, this occurs at shafts speeds below 7,000 rpm and therefore falls within the experimental parameter scope. Within the experiment, the high-speed imaging configuration can only consider one quadrant at a time. Therefore, experimentally, when assessing the P2 region it is important to recognise that some of the larger, heavier, particles may originate from the P1 section. This will become critical when trying to assess either particle diameter histograms within a specific quadrant, or when using image processing to determine particle trajectories; since these particles will not be travelling with the bulk of the flow and their subsequent interactions should be carefully considered.

This phenomenon starts to become apparent when considering Figure 5.19, which shows the visualisation results obtained within the P2 region at 7,000 rpm and an oil flow rate of 7.3 l/min, from the most recent, unpublished, G2TRC investigations [134]. Here, in Frame 1, a large droplet enters from the left-hand side of the frame, travelling in a south-eastern heading, originating from the top of the chamber in the P1 region. This droplet is impacted by several subsequent droplets shed from the P2 co-current side, seen in Frame 15. This ultimately causes the droplet to shatter into many smaller droplets, as seen in Frame 25. Finally, as a result of the momentum exchange from the collision of droplets, in combination with the shearing gas forces, these secondary droplets begin to travel with the core of the flow. Overall, experimentally and for the P2 region, this highlights why it may become important to distinguish between droplets emerging from the P1 region and their subsequent interactions, when producing quadrant specific droplet diameter or velocity histograms.

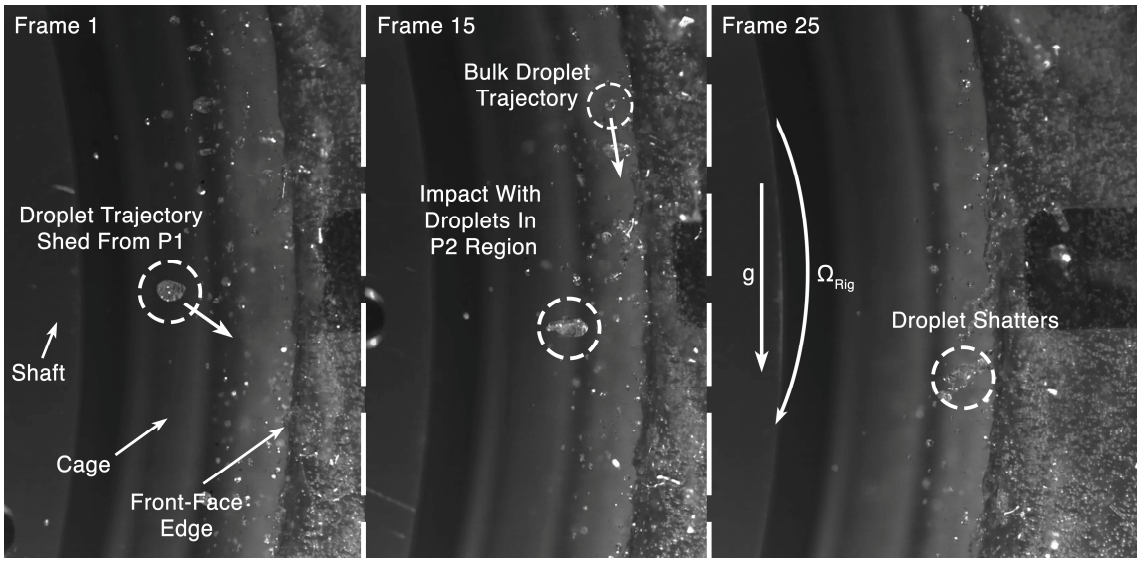


FIGURE 5.19: PARTICLE TRAJECTORIES PASSING FROM P1 THROUGH P2 OBSERVED EXPERIMENTALLY AT THE P2 REGION [134], 7,000 RPM & 7.3 L/MIN

Figure 5.20 shows the averaged particle trajectories in the radial/axial plane for each shaft speed, at 7.3 l/min, it should be noted that only the trajectories for the P2 and P4 regions are shown. The P1 and P3 trajectories are not shown for simplification, although both sectors have very similar trajectories and lie approximately half-way in between the P2 and P4 paths shown in Figure 5.20. Within the non-dimensionalised radial plane, particles start at the front-face edge and terminate on the main chamber outer wall; and within the non-dimensionalised axial plane, the 0 location corresponds to the front-face edge and extends the whole axial length of the domain.

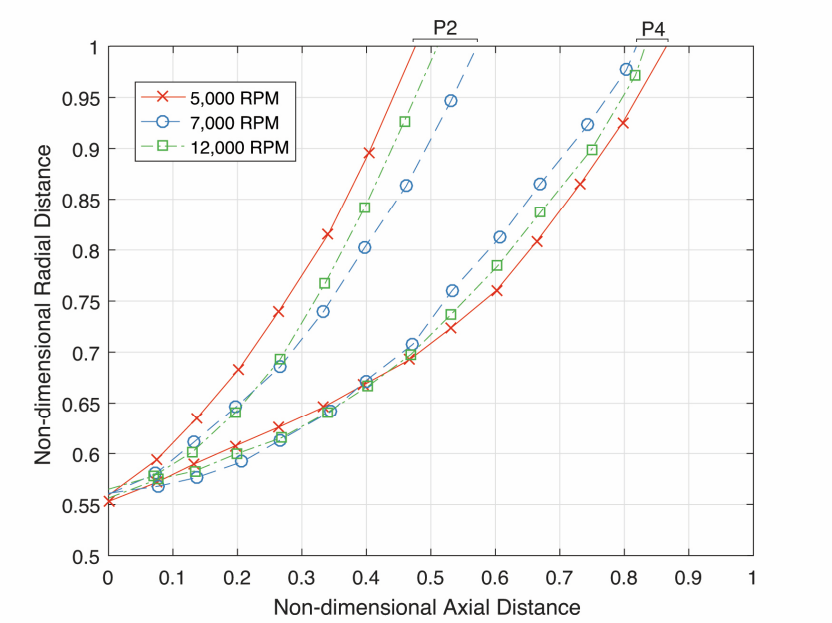


FIGURE 5.20: RADIAL/AXIAL EDGE SEPARATED PARTICLE TRAJECTORIES BASED ON AVERAGE PARTICLE DIAMETER

Within Figure 5.20, considering the P2 or P4 particles trajectories independently, for all of the shaft speeds investigated, there is neither a clear increase or decrease in the axial trajectory of particles with the shaft speed. All of the particles around the chamber annulus, impinge directly on the outer cylinder chamber wall, never reaching as far as the front-facing viewport windows, as seen in Figure 5.10; this is also evident experimentally, due to lack of an oil film on these optical windows [54]. On the outer chamber annulus, the majority of the oil film therefore resides between a non-dimensional axial distance of 0.45 to 0.85. After sufficient time, within the lower half of the chamber, oil fills the space up within the initial non-dimensional distance of 0.45, due to the attached film flowing over the front-face edge as previously reported in Section 5.3.1. On the outer cylinder wall, as the film begins to accumulate, the shearing airflow and gravity causes it to pool towards the sump, where it is eventually gravity scavenged. Clearly outside of this axial extent there exists a dry-out region, namely after a non-dimensional axial distance of 0.85 and for the initial 0.45 within the top half of the outer chamber annulus. Figure 5.21 shows a simplified

representation of this dry-out region, where the wetted chamber walls are depicted in blue. In terms of heat transfer, for an aeroengine bearing chamber application, this may present a significant problem leading to extremely hot regions. Subsequently, any small amounts of oil impinging on these regions could rapidly degrade leading to effects such as coking.

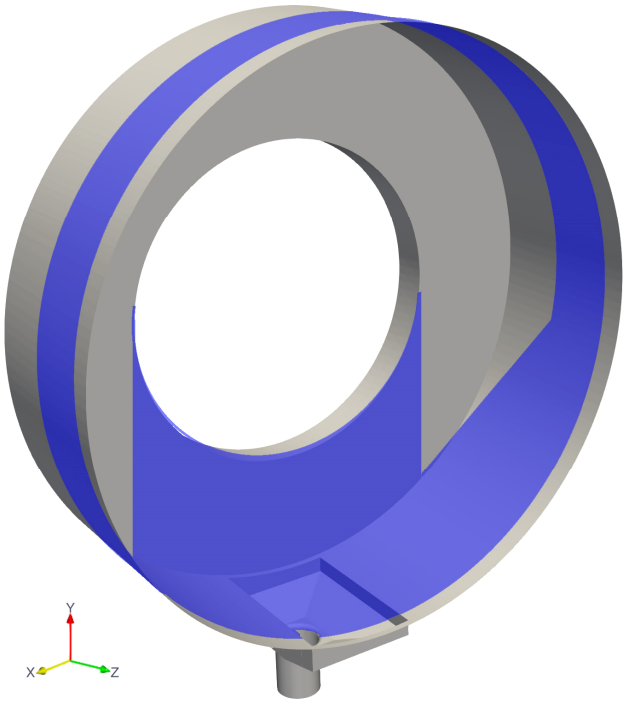


FIGURE 5.21: SIMPLIFIED REPRESENTATION OF WETTED AREA (BLUE) ON OUTER CASING WALLS AFTER DROPLET IMPINGEMENT

Using this information, a more comprehensive parametric study of the bearing chamber is therefore recommended within the future work in order to generate a better system. *sprayParcelFilmFoam* can be used as a design optimisation tool to develop upon the current capability and improve the knowledge surrounding the heat and oil management process. This can be achieved though geometrical changes to the system, such as the addition of struts, bolts, and spring bars; these will influence the two-phase distribution through introducing additional windage and blockage effects. Furthermore, the overall bearing chamber dimensions, such as the axial length or diameter can be varied, to greater understand the effects on the oil distribution. Finally, the axial length of the slot over which the film forms should be modified, to determine the consequences on the film development and ultimately the droplet generation process.

5.5.4 Particle Diameters

The following sections consider a quantitative analysis of the particle statistics into the main chamber. Figure 5.22 shows the particle diameters resulting from the shear stripping effect which takes place upstream of the expansion edge. Results are shown for a shaft speed of 7,000 rpm at 7.3 l/min, however very similar diameter distributions are observed over all cases in which shear stripping takes place. A bin width of 2µm is chosen and the data is presented as a normalised probability distribution, such that the sum of all the bins is equal to a probability of one. The stripped particles are sampled as they pass through the DPM Plane C at 0mm, Figure 5.3.

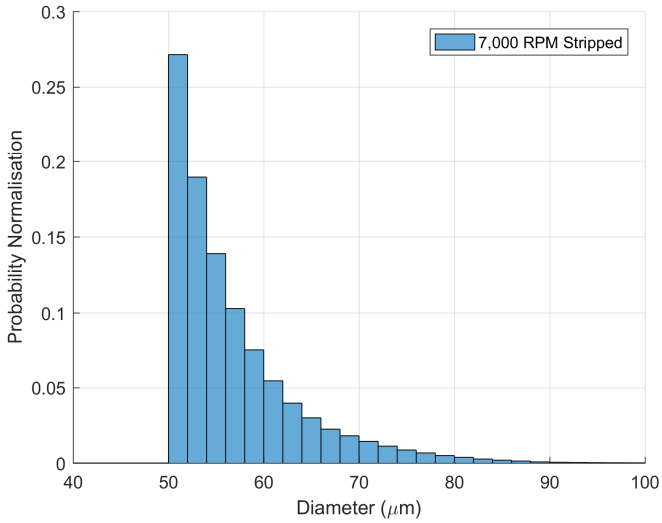


FIGURE 5.22: NORMALISED STRIPPED PARTICLE DIAMETERS AT 7,000 RPM AND 7.3 L/MIN

The stripped particle diameters follow a log-Rosin-Rammler distribution, otherwise known as a Gumbel distribution, which typically favours an extreme value. For a log-Rosin-Rammler distribution, the probability density function usually takes the following formula:

$$F(x;\varphi,\beta,k) = \frac{k}{\beta} e^{-(z+e^{-z})} \tag{5.1}$$

Where, $z = \frac{x-\varphi}{\beta}$, such that φ is the location parameter, β is the scaling factor and k is a constant. For the stripping histogram, shown in Figure 5.22, these constants are φ = 51, β = 4 and k = 3, for x = 0:100. The minimum diameters observed within Figure 5.22, are 50µm up to a maximum diameter of 90µm, resulting in an average particle diameter of 55µm. However, it should be noted that, for the cases investigated at shaft speeds where sufficient stripping takes place, the smallest diameter actually stripped from the surface of the film was as low as 40µm. These smaller diameters followed the same log-Rosin-Rammler distribution, i.e. extrapolating backwards, there are exponentially more particles at 45µm than 50µm and the same again at 40µm. However, the

sheer quantity of particles less than 50μm caused severe numerical difficulties, resulting in an extremely slow DPM calculation per time-step, ultimately causing the simulation to stall. At a shaft speed of 7,000 rpm, the average cloud mass represented by the stripped particles accounts for less than 1% of the total cloud mass. Subsequently, even though there are significantly more particles less than 50μm, due to the smaller diameter, their mass makes up a small proportion of the total stripped mass and an even smaller percentage of the overall cloud mass. Therefore, in order for simulations to run efficiently, without stalling, it was discerned that a limit on the minimum stripped particle diameter was required and set to 50μm. In an effort to conserve mass, stripping is still able to take place below this limit, although particles are immediately transferred to the gas phase using an in-built density correlation available within OpenFOAM. As such, the gas phase density is adjusted accordingly, effectively treating these particles as a fine oil mist. However, due to the very small mass associated with these droplets, the overall change in gas density is almost negligible and is immediately dissipated.

Figures 5.23 a) to d), show the normalised probability distributions for edge separated particle diameters at each shaft speed and an oil flow rate of 7.3 l/min; for comparison the 7,000 rpm 5.2 l/min case is also included. The particle statistics are recorded at the point of edge separation, i.e. along plane A at 0mm, in order to provide accurate data surrounding the particle initial conditions. For simplification, due to their relatively larger diameters, the previously discussed particles that are stripped from the P1 front-face surface are also included in the following particle diameter histograms; since, these can effectively be treated as edge separated particles. The histograms within Figures 5.23 a) to d), have a bin width of 50μm.

At a shaft speed of 5,000 rpm, as in Figure 5.23 a), a similar log-Rosin-Rammler distribution is also observed for the edge separated particles. Much like the stripped particle diameters, the distribution is positively skewed but with less weight towards the extreme value. Following Equation (5.1), this results in the constants $\varphi = 475$, $\beta = 225$ and $k = 45$, for $x = 0{:}2000$. At 5,000 rpm these edge separated particles, have a minimum diameter of 150μm up to a maximum of 1,800μm resulting in an average diameter of 630μm. The particles close to the maximum diameter range are representative of the ligaments observed experimentally [54], which is true for all shaft speeds investigated computationally. Interestingly, across all of the shaft speeds and flow rates investigated, the smallest edge separated particles observed are never less than 150μm. This shows that there is a distinct region in which there is no overlap between edge separated and stripped particle diameters. As the rotational shaft speed is increased to 7,000 rpm, Figure 5.23 b), the log-Rosin-Rammler distribution shifts to a positively skewed bimodal distribution, with clear peaks at both 300μm and 900μm. The same is true at the lower oil flow rate of 5.2 l/min, within Figure 5.23 d), although in contrast, the distribution is negatively skewed with distinct peaks at 450μm and 900μm. However, both oil flow rates at 7,000 rpm share the same average

particle diameter of 830µm, with a maximum size of 2,500µm. Moving to the highest shaft speed, Figure 5.23 c), the bimodal distribution shifts back towards the log-Rosin-Rammler distribution, although this time, slightly skewed to the extreme value, which peaks at a diameter of 600µm. The resultant average particle diameter is 780µm with a maximum diameter 2,150µm. A reasonable fit to the probability distribution described in Equation (5.1) can be achieved using the constants φ = 600, β = 250 and k = 45, for x = 0:2000.

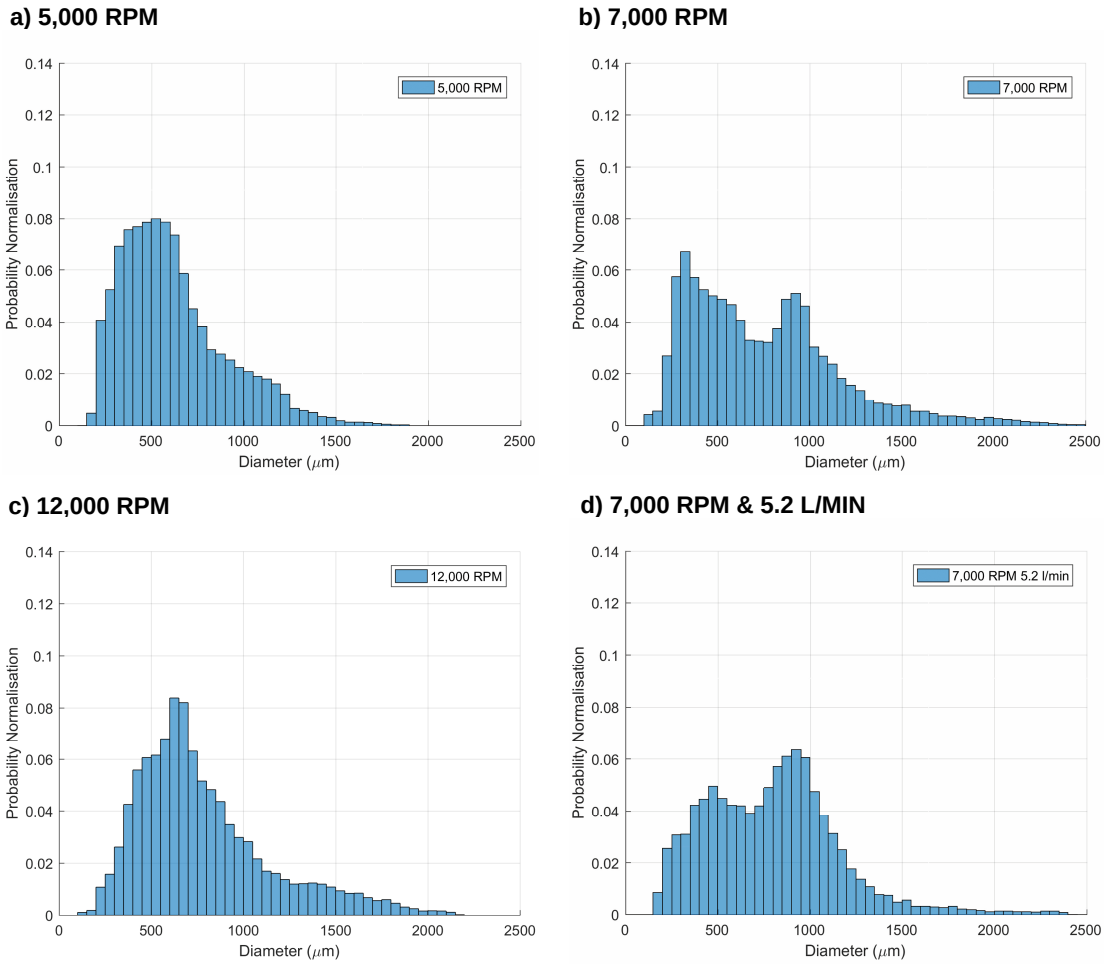


FIGURE 5.23: NORMALISED EDGE SEPARATED PARTICLE DIAMETERS AT EACH SHAFT SPEED

Interestingly, the only cases to experience any secondary breakup of the particulate cloud were for the two oil flow rates at the shaft speed of 12,000 rpm. Figure 5.24 shows a comparison of the original particle diameters at the 0mm plane versus the result of secondary breakup within the particulate cloud at DPM plane E, 12mm away from the front-face edge. A similar result is also observed for the second flow rate at 5.2 l/min. Beyond the 12mm plane, the amount of secondary breakup reduces significantly, and little change is seen. From Figure 5.24, it is clear that only minimal secondary breakup occurs, mainly due to the Kelvin-Helmholtz instabilities formed by the droplet slip velocities. Whereas, it appears that there is not sufficient time or acceleration for

the Rayleigh-Taylor instabilities to fully develop, which ultimately act to shatter the droplet into many smaller ones. The main shift in diameters is observed for the largest particles greater than 1250µm and also for particles with the range of 700µm to 900µm; ultimately this results a greater number of particles within the 450µm to 650µm range. Based on the previous observations presented Section 5.3.1, it is unsurprising that within the main chamber there is minimal particulate breakup, especially beyond the 12mm plane. Within the experimental test rig configuration, it is suspected that the presence of a truncated shaft leads to a reduced shearing velocity within the airflow and the lack of a sealing airflow further compounds this issue. As such, the shearing velocity within the main chamber will be reduced in comparison to that of a real aeroengine bearing chamber where significant breakup of the particulate cloud might be expected.

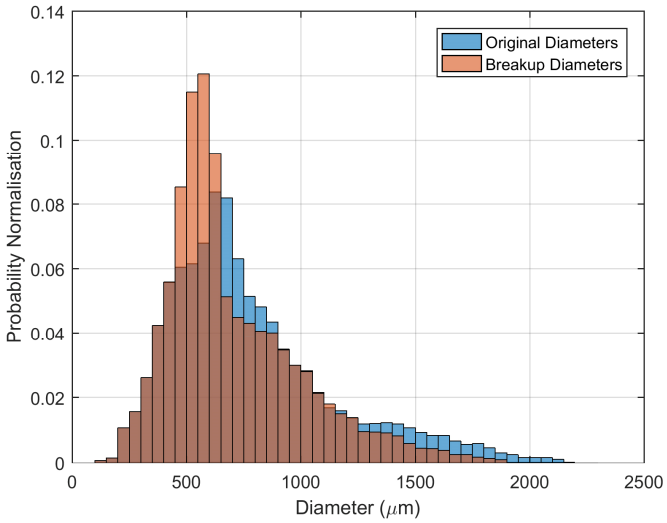


FIGURE 5.24: COMPARISON OF SECONDARY BREAKUP FOR THE PARTICULATE FLOW AT 12,000 RPM (7.3 L/MIN)

In an effort to better understand the bimodal diameter distributions seen at 7,000 rpm, in Figures 5.23 b) and d), Figures 5.25 a) to d) present a detailed break-down of the different diameter distributions for each quadrant around the annulus at a flow rate of 7.3 l/min. Figures 5.25 a) to d) highlight the diameter distributions in terms of particle count, at the 0mm plane, instead of a normalised probability, to enable a more direct comparison between each region; highlighting the difference in frequency of edge separation moving around the annulus. As such, the number of particles shown represents all of the particles sampled at each shaft revolution over the 1.5 seconds of time-averaging. Figure 5.25 b) shows the diameter distribution for the P2 co-current region whereas Figure 5.25 d) represents the counter-current P4 region, respectively these account for 23.0% and 30.7% of the total particle distribution. The P1 sector, in Figure 5.25 a), accounts for 28.9% of the distribution and in turn Figure 5.25 c), the P3 side, represents 17.4%.

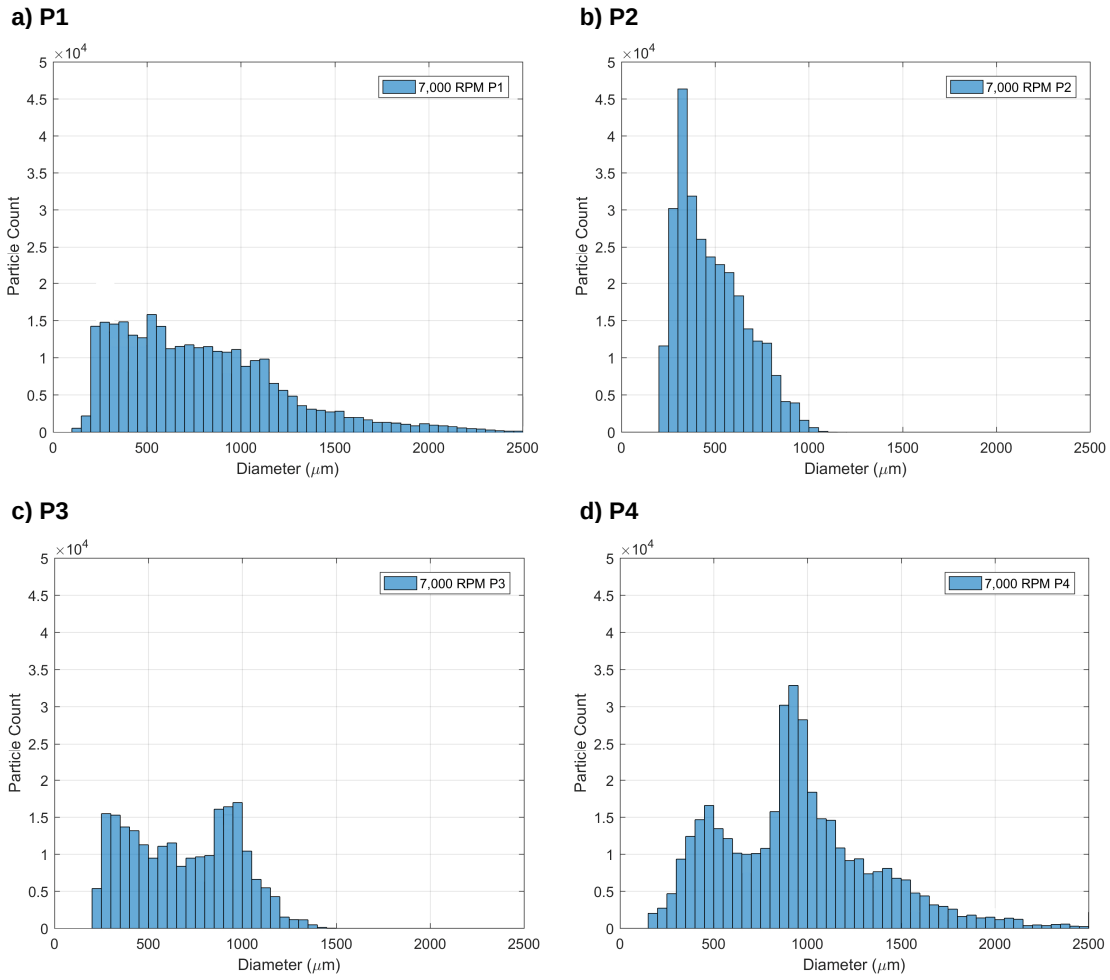


FIGURE 5.25: NORMALISED EDGE SEPARATED PARTICLE DIAMETERS AT EACH QUADRANT

From visualising the break-down of particle diameter histograms around the annulus it starts to become understandable, as to why, a bimodal particle distribution is present within Figure 5.24 b). Within the P2, co-current section, the fully smooth shear dominated flow regime at the front-face edge produces a relatively faster and hence thinner film. This is represented by the diameters shed into the main chamber, due to the positively skewed distribution that peaks with a diameter of 300μm, with a mean of 480μm. Moving around the annulus to the counter-current, P4, region the undulation effect, which reaches a maximum around 7,000 rpm, results in a comparatively thicker film. The undulation effect causes significant variance within the particle diameters observed, yet a distinct peak is identifiable at 900μm, with an average diameter of 830μm. With Figures 5.25 a) and c) having a fairly uniform distribution, combining the co- and counter-current regions, it becomes apparent as to why a bimodal distribution is observed within Figure 5.24 b); the same is also true for within Figure 5.24 d).

5.5.5 Particle Velocities

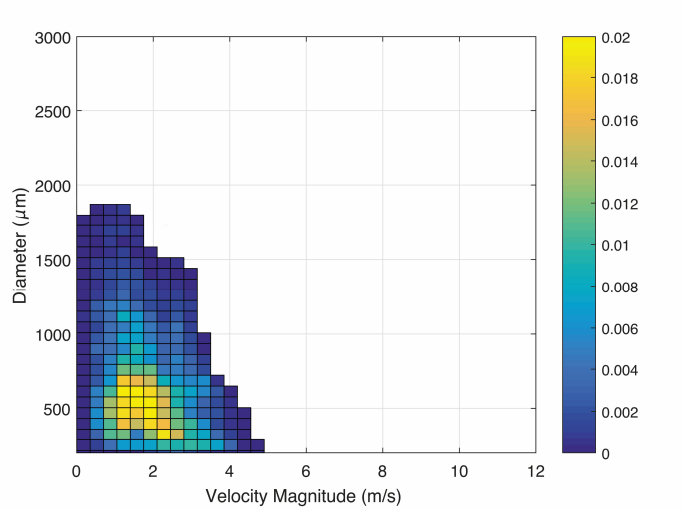
Figures 5.26 a) to c) show contour maps of edge separated particle diameters against the particle average velocity magnitude, for shaft speeds at 5,000 rpm, 7,000 rpm and 12,000 rpm respectively, and an oil flow rate of 7.3 l/min. The contour maps are separated into individual bins, coloured by the normalised probability distribution, such that all of the bins sum to a probability of one. Results are recorded at plane E, 12mm from the front-face edge, although similar results are observed for planes closer to the edge.

Within Figure 5.26 a), at 5,000 rpm, it is clear that the maximum edge separated diameter peaks at 1,800μm in line with the diameter distribution presented in Figure 5.23 a). It is also clear that, the highest frequency of particles resides within the diameter range between 350μm to 650μm. The bulk of these particles separate with a mean velocity magnitude in the range of 1.0 to 2.5 m/s. At 5,000 rpm, the fastest moving particles observed have a velocity magnitude no greater than 4.5 m/s. Overall, there is a clear correlation between the smaller diameter particles having a greater velocity magnitude, compared with the larger diameter particles which move at a relatively slower velocity; this trend applies for all of the shaft speeds investigated. With an increase in shaft speed to 7,000 rpm, Figure 5.26 b), a notable increase in the maximum particle diameter is seen, as a result of the increasing undulation effect within the P4 region. Two distinct peaks are identifiable within the contour map of Figure 5.26 b), for particle diameters at 900μm and 300μm, characteristic of the bimodal distribution presented in Figure 5.23 b). At these two points, particles reach a velocity magnitude of approximately 2 m/s and 3.5 m/s respectively. The smaller, faster moving particles are representative of the fluid separated within the P2 region, as in Figure 5.25 b), and conversely the larger, slower particles for the counter-current P4 section. Overall, at 7,000 rpm the maximum velocity of the particles is around 6 m/s. This is in good agreement with, the most recent, unpublished experimental measurements [134], reporting a maximum particle velocity of 5 m/s at Plane E and a shaft speed of 7,000 rpm. Finally, at a shaft speed of 12,000 rpm, Figure 5.26 c), the maximum diameter reduces back down to a value of 1950μm, as the undulation effect reduces and secondary breakup begins. An overall increase in particle velocity magnitude is observed, with the highest frequency of particles clustered at a diameter of 500μm and a velocity magnitude of approximately 6 m/s. At 12,000 rpm the maximum recorded velocity magnitude is 10 m/s.

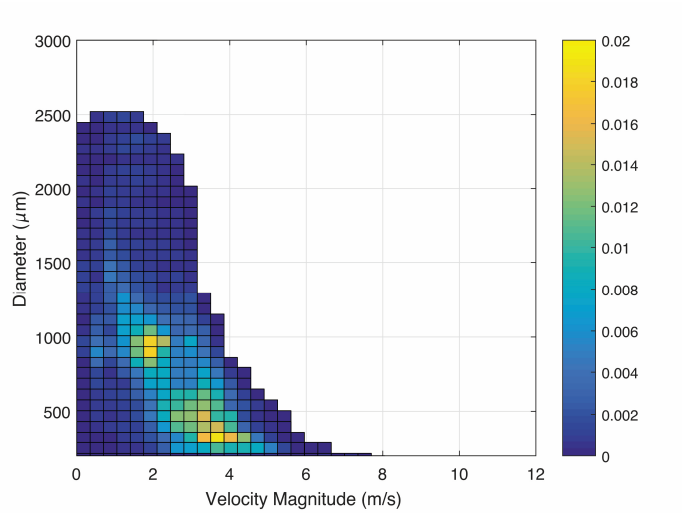
Considering Figures 5.26 a) to c), a general trend of increasing average particle velocity with an increase in the rotational shaft speed can be observed. However, it is important to note that this is also a function of the angular location around the chamber, which can heavily influence both the size and velocity of the edge separated particles. This is particularly true of the P4, counter-current region, where a gravity dominated flow regime is observed close to the front-face edge. This is

most noticeable around 7,000 rpm, whereby the undulation effect reaches a maximum and then subsequently decreases moving towards the smooth shear dominated flow regime at 12,000 rpm.

a) 5,000 RPM



b) 7,000 RPM



c) 12,000 RPM

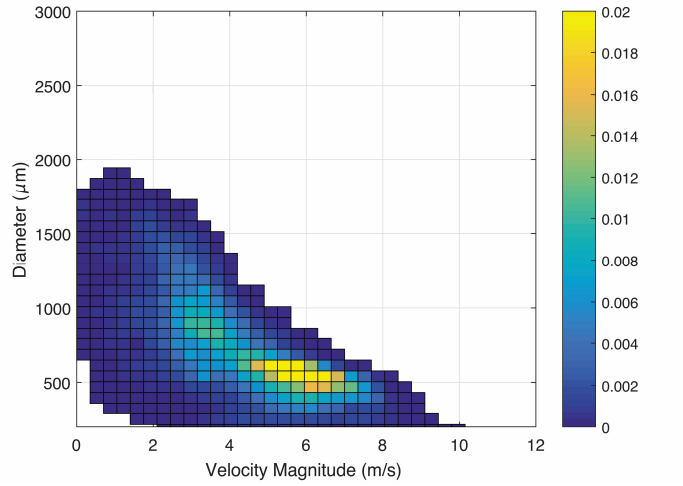


FIGURE 5.26: CONTOUR MAP OF PARTICLE DIAMETER VERSUS VELOCITY COLOURED BY NORMALISED PROBABILITY

5.5.6 Particle Residence Time

Figure 5.27 shows the average residence time recorded for particles immediately before impingement on the outer chamber wall at shaft speeds: 5,000 rpm, 7,000 rpm and 12,000 rpm and a flow rate of 7.3 l/min. Results are only shown for the flow rate of 7.3 l/min, however very similar trends and values are also observed at the lower oil flow rate. Diameters are included for both stripped and edge separated particles.

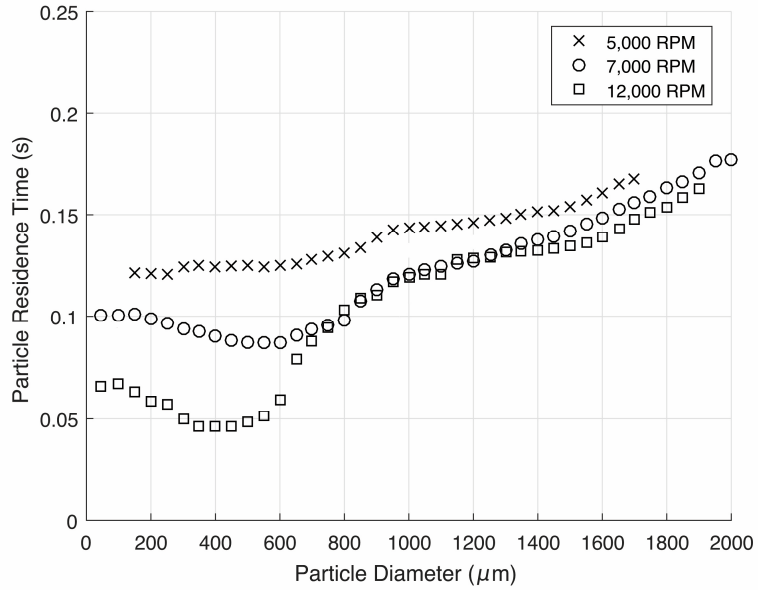


FIGURE 5.27: AVERAGE PARTICLE RESIDENCE TIME IMMEDIATELY BEFORE IMPINGEMENT ON THE OUTER CASING WALL (7.3 L/MIN)

For all of the shaft speeds investigated, it is immediately clear that with an increase in particle diameter, the final residence time of the particles increases. Furthermore, within this flow regime observed, there are no particles exceeding a residence time of 0.2s, with a minimum residence time of at least 0.05s. At 7,000 rpm and 12,000 rpm, within Figure 5.27, the residence time for stripped particles, i.e. less than 100μm, are also shown. Interestingly, the stripped particles experience a very similar residence time compared with the small diameter edge separated particles at 150μm. It is suspected that since these stripped particles, which originate within the film upstream of the front-face edge, travel with a faster velocity. This, in combination with being relatively smaller in size, should result in a shorter residence time. However, these particles are influenced more strongly by the gas flow, resulting in longer particle trajectories and hence residence time. From the stripped particle residence time, it is also clear that these particles are not captured within regions of recirculation, as indicated by the lack of a noticeable increase in residence times. This suggests that there is not a concern for oil degradation due to smaller droplets undergoing significant heating whilst being entrained within the airflow.

For the edge separated particles, at the two higher shaft speeds, initially there is a clear decrease in residence time with an increase in particle diameter up to approximately 400μm, especially at 12,000 rpm, although this is not observed for a shaft speed of 5,000 rpm. Beyond this diameter range, over all shaft speeds investigated, the residence time is seen to increase with the particle diameter. For diameters exceeding 700μm, almost identical residence times are observed for the shaft speeds at both 7,000 rpm and 12,000 rpm.

When considering diameters below 700μm, as expected, there is a decrease in particle residence time with an increase in shaft speed; however, beyond this diameter range, it is clear that increasing the shaft speed starts to have a less significant impact on the residence time. It is also important to consider the particle residence time as a function of the angular location. As observed in Figure 5.20, particles shed from the P4, counter-current region, travel a greater axial distance compared with the co-current P2 sector. Furthermore, at slower shaft speeds, particle trajectories towards the top of the chamber, experience a greater influence of gravity, resulting in a reduced tangential trajectory, as they travel through the P2 region in Figure 5.18. For Figure 5.15, it is also witnessed that particles are stripped from the front-face surface within the P1 region, these tend to fall slowly under the influence of gravity. In addition, within Figures 5.26 a) to c), the relative increase in particle velocity with speed is small for the larger diameter particles, above 1000μm. As such, when incorporating all of the different flow physics observed around the chamber annulus, the reasons for the increase in particle residence time with diameter start to become apparent, highlighting the vast complexity of the problem.

For future bearing chamber simulations, it would be ideal to provide a DPM inlet boundary condition at the front-face edge, to account for both the edge separated and film stripped particles exiting into the main chamber compartment. This would remove the need for modelling the thin film formation which develops as a result of oil exiting from the ball bearing; hence significantly reducing the computational cost associated with resolving the mesh within this region and the associated two-way ETFM-DPM coupling required, such as either film stripping or edge separation. However, from the DPM analysis presented here, it is clear that the mechanisms for both edge separation and film shear stripping are influenced by many different parameters around the chamber annulus. As such, due to the detailed flow physics observed within the present computational investigation, it may become extremely difficult to successfully represent this type of boundary condition and care should be taken to provide both accurate particle and thin film statistics.

5.6 ETFM/DPM Conclusions

The two-way coupled ETFM-DPM solver, *sprayParcelFilmFoam*, has been successfully applied to a bearing chamber geometry, including the effects of both a film stripping and an edge separation criteria. Numerical studies are conducted over three different shaft speeds and two oil volume flow rates. A qualitative and quantitative analysis of the oil film is carried out and compared to the experimental data of Hee et al. [54]. Extending upon this, a detailed analysis of the particles shed into the bearing chamber is performed, providing insight into new flow physics for aeroengine bearing chamber modelling.

ETFM: Qualitatively, results are found to be in excellent agreement with Hee et al. [54]. A shear dominated flow regime is observable at the Plane B location, however downstream of this location, due to the lack of experimental data, uncertainty arises as a gravity dominated flow regime is detected within the counter-current side. In general, close to the front-face edge, a smooth shear dominated flow regime is observed within the P2 region, whereas a gravity dominated flow regime is detected in the P4 region, which mildly persists even up to a shaft speed of 12,000 rpm. Quantitatively, within the co- and counter-current regions, the results are able to accurately capture the axial variation in mean film thickness, compared to the experimental measurements. As the rotational shaft speed is increased, the reduction in film thickness follows a diminishing return. In general, across all shaft speeds, a minimum average film thicknesses of 0.4mm was observed. As such, the film thickness eventually becomes independent of the shaft speed at 12,000 rpm. An investigation into a more comprehensive film inlet boundary condition was unsuccessful, resulting in a worse agreement with the experimental film thickness measurements of Hee et al. [54]. Through injecting DPM particles at the cage-edge location, there is a sudden acceleration of the film, although as a whole, there is a negligible increase in the film velocity. As a result, the film momentum is still not sufficient to over-come the gravity shear dominated flow regime at the edge, and instead, the sudden acceleration causes a more unstable film to develop. Overall, this suggests that the geometrical chamber configuration, with a truncated shaft and the lack of a sealing airflow, leads to a reduced shearing velocity and hence a reduced shearing force towards the front of the chamber, resulting in a P4 gravity dominated flow regime.

Further experimental work is required to determine the flow regime state toward the front of the annulus, in order to determine whether a gravity dominated flow regime is indeed evident. Additionally, a detailed breakdown of the oil exiting the cage-edge is also required to determine if a more complex film inlet boundary condition is needed. However, at present the original, representative, film inlet boundary condition is deemed appropriate for all future ETFM-DPM computational investigations.

DPM: Accurate particle statistics are provided surrounding the droplet conditions as they are shed into the main chamber compartment and an understanding of solution sensitivity is provided. Qualitatively, the distribution of oil resulting from the mechanisms of edge separation and film shear stripping are presented and analysed; giving insight into the dependence on both shaft speed and angular location around the chamber annulus. It is observed that particles separated within the P2, co-current region, are relatively smaller and faster than the P4, counter-current region, due to the differences in flow regimes observed for the thin film.

At slower shaft speeds, the effect of a gravity driven flow regime continues towards the top of the chamber at P1. This causes a significant reduction in film velocity and particles are shed with a reduced tangential trajectory. Subsequently, these particles are observed travelling through the P2 region and can therefore have a significant impact on experimental results if not accounted for. At 12,000 rpm, as the gravity driven flow regime diminishes, this effect also reduces. Furthermore, toward the top of the chamber the fluid can remain attached, flowing over the front-face edge. Subsequently, the film accumulates before being stripped as large diameter particles, up to a maximum of 2,500μm, which consequently fall under the influence of gravity.

A quantitative analysis of particle diameters is presented. A distinct split between edge separated and stripped particles is observed. Stripping only occurs at shaft speeds greater than 7,000 rpm, for which their distribution follows a log-Rosin-Rammler profile, resulting in an average particle diameter of 55μm and a maximum of 90μm. At both 5,000 rpm and 12,000 rpm, a log-Rosin-Rammler distribution is also observed for the edge separated particles. In general, the edge separated particles have a minimum diameter of 150μm, with a maximum of size of 2,500μm, representative of the ligaments reported experimentally. For the oil flow rates at 7,000 rpm, a bimodal diameter distribution is instead observed, with two distinct peaks around 300μm and 900μm. Analysis of diameter distributions within each quadrant revealed this to be a result of the difference in the film between the P2 and P4 co-/counter-current regions; whereby at 7,000 rpm, the undulation effect reaches a maximum. Minimal secondary breakup of the particulate cloud is only experienced at 12,000 rpm, suspected to be as a result of the presence of a truncated shaft and the lack of a sealing airflow throughout the chamber, in comparison to a more traditional aeroengine bearing chamber. A general trend of increasing particle velocities with shaft speed is also observed. Particle residence times are seen to initially decrease with the particle diameter, down to a minimum time of 0.05s. However, beyond a diameter of 700μm, an increase in residence time with diameter is observed, with very similar values are obtained across all shaft speeds; never exceeding a maximum time of 0.2s. Overall, it is clear that there are several different parameters around the chamber annulus that influence the mechanisms for particle formation, predominantly: the shaft speed, angular location and the film flow regime.

Overall, the developed modelling methodology achieved within the OpenFOAM solver, *sprayParcelFilmFoam*, has demonstrated a significant improvement in bearing chamber modelling capability. The results presented within this chapter has illustrated the capacity of *sprayParcelFilmFoam* to capture the complex flow behaviour observed within the bearing oil shedding rig. The computational results exhibit good agreement, both quantitatively and qualitatively, with previously published experimental results as well as the ongoing, unpublished, measurements characterising the edge separated droplets. The computational results are able to provide useful insight into areas that are not feasible to explore experimentally and provide the possibility to further expand into the parameter space through different geometrical configurations. As a result, *sprayParcelFilmFoam*, can effectively be used as a design tool to improve knowledge and better inform experimental investigations, not only for the bearing oil shedding rig, but also for future more complex and representative bearing chamber geometries.

Chapter 6

Conclusions

The work presented in this thesis has, for the first time, demonstrated a fully coupled two-way ETFM-DPM investigation into the droplet generation process within a simplified aeroengine bearing chamber. The aim of the research was to develop and extend the existing state-of-the-art bearing chamber modelling capability. Through providing a deeper understanding of the underlying mechanisms and new flow physics, a greater insight into the heat and oil management process can be established. Ultimately, this work will assist in the design optimisation of aeroengine bearing chambers based on required functionality. Overall, this thesis has demonstrated a significant improvement in aeroengine bearing chamber modelling capability, establishing a firm foundation for future bearing chamber simulations. The following summarises the main conclusions from the research carried out, including the contributions to knowledge and recommendations for future work.

6.1 Summary

An URANS turbulence modelling study was performed within a Taylor-Couette system, to better inform the selection of a turbulence model within bearing chamber simulations. For the Taylor-Couette device under consideration, it was necessary to model the whole computational domain and to achieve the correct final state of the Taylor vortex flow field, careful consideration of the initial conditions is required. The recommended Taylor-Couette methodology proposed that either the standard k-ω or RSM stress-BSL turbulence models were suitable choices for the following bearing chamber modelling. However, the subsequent single-phase bearing chamber investigations revealed that, instead, the SST k-ω turbulence model was the most appropriate choice, providing good agreement to the experimental measurements and was therefore recommended for all future simulations. Overall, it is clear that the comparison of a bearing chamber geometry to that of a Taylor-Couette system is not a simple as originally proposed. Due to the more complex bearing chamber environment, even under single-phase conditions, the study has demonstrated that the required turbulence modelling approach is not entirely transferable and hence requires an alternative turbulence model selection.

From the literature reviewed, it was clear that there was a need for a more accurate and appropriate two-phase modelling approach applicable to aeroengine bearing chamber simulations. Recent moderate-speed experimental bearing chamber investigations have revealed how oil is shed from a ball bearing, into the chamber, as a combination of either droplets, ligaments and/or sheets; causing the formation of a thin film on the stationary outer walls. Within the scope of this work, this resulted in the development of the fully coupled two-way ETFM-DPM solver, *sprayParcelFilmFoam*. As a requirement for bearing chamber simulations, within OpenFOAM, two new thin film sub-models were implemented, these are based on empirical models for both a film stripping and an edge separation criteria. The *sprayParcelFilmFoam* solver is validated against an experimental study for an impinging jet in a high velocity crossflow. Overall, good agreement is achieved for both film thickness measurements and particle statistics, demonstrating a significant improvement over the existing state-of-the-art techniques.

Finally, the newly developed in-house solver, *sprayParcelFilmFoam*, is extended and applied to a simplified aeroengine bearing chamber, specifically the G2TRC bearing oil shedding rig. Qualitatively and quantitatively computational results are compared to the available experimental high-speed imaging and film thickness data. Numerically, a good agreement is observed, demonstrating capability within both the gravity dominated and smooth shear flow regimes. Upstream of the expansion edge, the film flow regime is found to be in good agreement with the experimental observations, predicting a smooth shear dominated flow regime. However, closer to the expansion edge, across all operating conditions, a gravity dominated flow regime is identified

within the counter-current side of the film. Whilst not reported on experimentally, this is suspected to be as a result of the presence of a truncated shaft and the absence of a sealing airflow within the test rig, compared to a more representative aeroengine bearing chamber. Computationally, a minimum average film thickness of 0.4mm was predicted across all shaft speeds, in agreement with the experimentally derived values. The amount that film thickness reduces by with each increase in rotational shaft speed follows a diminishing return; for every step in shaft speed of 2,000 rpm, the amount that the film thickness reduced by was halved. Under these operating conditions and flow regime, the film thickness eventually becomes independent of the shaft speed around 12,000 rpm, reaching a minimum thickness of 0.4mm.

Following the film results, a comprehensive study is performed for the oil shed into the bearing chamber, reporting on droplet statistics, including: particle trajectories, diameters, velocities and residence times. For these droplets and the subsequent film formation, an understanding of solution sensitivity to both operational parameters and initial conditions is provided. At the two lower rotational shaft speeds, the effects of a gravity driven flow regime, within the thin film, significantly influences the particle trajectories shed from the rising side of the chamber. Droplets separated from the top of the annulus can have trajectories passing through the co-current region, this will have consequences during experimental investigations and should be accounted for accordingly. At the highest shaft speed of 12,000 rpm, these effects are no longer observed. Stripped particles follow a log-Rosin-Rammler diameter distribution, never exceeding a maximum size of 90μm. Significant stripping only occurs at 12,000 rpm, with only minor stripping present at 7,000 rpm within the P4 region; finally, at 5,000 rpm, stripping is almost non-existent. At 5,000 and 12,000 rpm, edge separated particles also demonstrate a log-Rosin-Rammler diameter distribution; however, at 7,000 rpm, a bi-modal distribution is observed as a result of the undulation effects observed within the film counter-current region. In general, edge separated droplets range from a minimum of 150μm up to a maximum of 2,500μm, characteristic of the ligaments observed experimentally. Overall, there are several different parameters that influence the droplet generation processes, namely: the rotational shaft speed, angular location and the film flow regime.

sprayParcelFilmFoam, has demonstrated a significant improvement in bearing chamber modelling capability, demonstrating the ability to capture the complex flow behaviour observed within the bearing oil shedding rig. As a result, *sprayParcelFilmFoam*, can be used to better inform experimental investigations not only for the bearing oil shedding rig, but also for future more complex bearing chamber geometries. Through providing knowledge into the underlying mechanisms and flow behaviours, *sprayParcelFilmFoam* can act as a design tool by expanding upon the parameter space in areas that are not feasible or too expensive to explore experimentally.

6.2 Contributions to Knowledge

The unique contributions to knowledge as a result of this thesis are presented:

- The development of the fully coupled two-way ETFM-DPM OpenFOAM solver: *sprayParcelFilmFoam*
- Capability within OpenFOAM for an ETFM-DPM approach that incorporates both primary atomisation and secondary breakup of the particulate cloud
- Within OpenFOAM, the statistical accuracy of particle injections has been improved, this is now fully integrated within all OpenFOAM versions 6.0 and above
- The incorporation of two new ETFM sub-models within OpenFOAM, accounting for both film stripping behaviour and an edge separation criteria
- A recommendation of the SST k-ω turbulence model for all future bearing chamber simulations, based on the single-phase bearing chamber validation study
- The application of a fully coupled two-way ETFM-DPM approach to a simplified aeroengine bearing chamber, reporting on droplet shedding behaviour for the first time
- An improved understanding of the film flow regimes within the bearing oil shedding rig has been developed
- A detailed assessment of the droplet shedding characteristics has been achieved through the CFD analysis
- Knowledge of the solution sensitivity to the operational parameters and initial conditions has been provided

Within bearing chamber applications, these contributions to knowledge represent the first of their kind, collectively demonstrating a major improvement to bearing chamber modelling capability. As such, recommendations for future work are now suggested, as a result of the research carried out and the experience acquired.

6.3 Recommendations for Future Work

With the newly developed fully coupled two-way ETFM-DPM solver, *sprayParcelFilmFoam*, the potential for future aeroengine bearing chamber simulations is large. These numerical investigations are also able to inform future experimental research. As such, the following provides a summary of recommended future work.

6.3.1 Computational Investigations

Computationally, work can now focus toward recreating a DPM inlet boundary condition at the front-face edge of the bearing chamber. This would be achieved through modelling both the edge separated and film stripped droplets entering into the main chamber compartment as a DPM injection. Ideally, this should also be coupled with a film inlet boundary condition, in order to capture the mass flow rate of oil that is not separated over the edge, which in turn flows down the front-face plate. Such an approach would significantly reduce the computational cost of simulations as a result of not having to model the initial film formation for every simulation. By removing the ETFM-DPM coupled approach required upstream of the front-face edge, such as either the need for a film stripping or an edge separation criteria, the requirement of a very fine grid spacing within this region is removed. For this approach, careful consideration needs to be provided for the droplet initial conditions, such as for the particle diameter distributions and velocity trajectories, both of which are a function of the angular coordinate around the annulus. This becomes even more difficult when considering that the particle formation heavily relies on the rotational shaft speed and film flow regime. The work within this thesis and further initial calculations in order to establish the boundary condition, would therefore, inform the inlet for subsequent whole bearing chamber investigations.

The DPM inlet boundary condition can further expanded upon, through the use of a DPM-VOF coupled approach. Historically, such simulations have been limited by the lack of an appropriate oil inlet boundary condition within the DPM approach. Ultimately, this methodology would be advantageous for bearing chamber investigations into areas such as the scavenge performance. Furthermore, the larger diameter droplets that are predicted computationally, which are representative of the ligaments observed experimentally, could feasible be resolved within the VOF reference frame, allowing for more complex oil interactions and collisions to be captured.

The film formation on the static outer casing walls, as a result of the subsequent droplet impingement, should also be further investigated computationally. The film thickness and velocities on these surfaces must be evaluated accordingly, with careful consideration for any dry-out regions that may occur. Validation data for such simulations will soon be provided for the

bearing shedding rig. These simulations can be coupled with a heat transfer model, to better inform the heat transfer process on these outer chamber walls, and where relevant, highlight potential areas of localised heating. These results will help to provide greater insight into the heat and oil management process and ultimately improve design optimisation.

Furthermore, a more comprehensive parametric study of the bearing chamber can now be carried out. The overall dimensions of the bearing chamber, such as axial length or diameter, should be modified to provide a greater understanding of the flow behaviour on the underlying mechanisms. However, more specifically, the axial extent of the stationary wall over which the film first develops, should be varied accordingly. Within this section, the axial length will have consequences on the film development, including quantities for both the film thickness and velocity. Subsequently, this will impact the droplet generation process caused by the edge separation phenomena at the front-face edge. Further geometric complexity can be introduced to domain such as, but not limited to, struts, bolts and spring bars since these will introduce additional windage and blockage effects and therefore influence the two-phase environment. In addition, a wider range of oil properties should also be considered. Experimentally, a significant proportion of bubbles are retained within the oil film, these bubbles will influence the fluid properties and hence the overall film behaviour. It may also be possible to incorporate a thin film sub-model to account this bubbly flow present.

6.3.2 Experimental Investigations

Experimentally, it is necessary to provide a greater level of both qualitative visualisation and quantifiable oil film measurements in order to supplement the computational validation process, but also the engine design perspective. Currently within the bearing oil shedding rig, there are no measurements of the film velocity, however this is planned for future experiments. Furthermore, work should aim to provide a greater understanding of the droplet generation process at the point of edge separation, including measurements of the droplet diameter distributions, together with droplet trajectories, both as a function of rotational shaft speed and oil flow rate. In order to inform a more comprehensive numerical film inlet boundary condition, measurements should also be performed to quantify the proportion of oil shed from the cage-edge. Additionally, the split of oil supplied to the bearing should be modified to determine the influence of oil shed from the cage-edge on the subsequent film formation and ultimately the droplets separated at the front-face edge. Moreover, there is considerable uncertainty regarding the oil flow regime found within the counter-current side of the film development. Computationally, upstream of the front-face edge, a smooth shear dominated flow regime is observed within this region, although, moving toward the front-face edge, the flow transitions to a gravity dominated pool regime, which mildly persists

even at 12,000 rpm. Moreover, as it stands, experimental measurements are predominantly performed within the co- and counter-current regions of the bearing chamber; however, as demonstrated computationally, there is also significant interest within the P1 and P3 sectors and more detailed experimental measurements should be made accordingly, these experiments have been planned within the future work to be carried out in the G2TRC.

Where possible, further geometrical modifications to the bearing oil shedding rig should be made. In order to achieve a more realistic engine operating condition, a sealing airflow rate should be introduced and therefore a pressure differential across the bearing. Additionally, the truncated shaft should extend along the whole axial extent of the domain, to achieve a more representative aeroengine bearing chamber configuration. Such modifications will have a significant impact on the overall droplet disintegration process. Finally, to distinguish between edge separated and stripped particles, a baffle could be introduced upstream of the front-face edge in order to capture and identify the droplets stripped from the film surface.

References

[1] IATA, “Vision 2050,” 2011.

[2] IATA, “Fact Sheet Climate Change,” 2018.

[3] M. Darecki *et al.*, “Flightpath 2050 Europe’s Vision for Aviation,” *Flightpath 2050 Eur. Vis. Aviat.*, p. 28, 2011.

[4] P. Arguelles *et al.*, “European Aeronautics: A vision for 2020,” Report of the Group of Personalities, The European Commission, 2001.

[5] Exxon Mobil, “Jet Engine Oil System, Part 1,” 2016. [Online]. Available: https://www.exxonmobil.com/en/aviation/knowledge-library/resources/jet-engine-oil-system-1.

[6] European Commission, “Final Report Summart - ELUBSYS (Engine LUBrication SYStem technologies),” 2014.

[7] Rolls Royce, *The Jet Engine*. John Wiley & Sons, Ltd., 2015.

[8] D. Peduto, “Oil Droplet Impact Dynamics in Aero-Engine Bearing Chambers-Correlations derived from Direct Numerical Simulations,” PhD Thesis, Karlsruhe Institute of Technology, 2015.

[9] W. Kurz and H.-J. Bauer, “An Approach for Predicting the Flow Regime in an Aero Engine Bearing Chamber,” *Proc. ASME Turbo Expo*, pp. 1–8, 2014.

[10] S. Wittig, A. Glahn, and J. Himmelsbach, “Influence of High Rotational Speeds on Heat Transfer and Oil Film Thickness in Aero-Engine Bearing Chambers,” *J. Eng. Gas Turbines Power*, vol. 116, no. 2, pp. 395–401, 1994.

[11] G. I. Taylor, “Stability of a viscous liquid contained between two rotating cylinders,” *Philos. Trans. R. Soc. A*, vol. 223, no. 605–615, pp. 289–343, 1922.

[12] K. W. Moser *et al.*, “Visualization of Taylor-Couette and spiral Poiseuille flows using a snapshot FLASH spatial tagging sequence,” *Magn. Reson. Imaging*, 2000.

[13] G. P. Smith and A. A. Townsend, “Turbulent Couette flow between concentric cylinders at large Taylor numbers,” *J. Fluid Mech.*, vol. 123, pp. 187–217, 1982.

[14] S. I. Pai, “Turbulent flow between rotating cylinders,” *NACA, Tech. Rep.*, vol. TN 892, 1943.

[15] R. J. Donnelly, K. W. Schwarz, and P. H. Roberts, “Experiments on the stability of viscous flow between rotating cylinders,” *Proc. R. Soc. A*, vol. 283, no. 1395, pp. 531–556, 1964.

[16] J. E. Burkhalter and E. L. Koschmieder, “Steady supercritical Taylor vortices after sudden starts,” *Phys. Fluids*, vol. 17, no. 11, pp. 1929–1935, 1974.

[17] D. Coles, “Transition in cicular Couette flow,” *J. Fluid Mech.*, vol. 21, no. part 3, pp. 385–425, 1965.

[18] E. L. Koschmieder, “Turbulent Taylor vortex flow,” *J. Fluid Mech.*, vol. 93, no. 3, pp. 515–527, 1978.

[19] A. Barcilon, J. Brindley, M. Lessen, and F. R. Mobbs, “Marginal instability in Taylor-Couette flows at a very high Taylor number,” *J. Fluid Mech.*, vol. 94, no. 3, pp. 453–463, 1979.

[20] S. Grossmann, D. Lohse, and C. Sun, “Velocity profiles in strongly tubulent Taylor-Couette flow,” *Phys. Fluids*, vol. 26, pp. 1–20, 2014.

[21] R. Ostilla-Mónico *et al.*, “Optimal Taylor-Couette flow: radius ratio dependence,” *J. Fluid Mech.*, vol. 747, pp. 1–29, 2014.

[22] L. Wang, “Computational fluid dynamics simulation of precipitation processes,” PhD Thesis, Iowa State Univesity, 2004.

[23] S. T. Wereley and R. M. Lueptow, “Spatio-temporal character of non-wavy and wavy Taylor-Couette flow,” *J. Fluid Mech.*, vol. 364, pp. 59–80, 1998.

[24] R. Ostilla-Mónico, E. P. van der Poel, R. Verzicco, S. Grossmann, and D. Lohse, “Exploring the phase diagram of fully turbulent Taylor–Couette flow,” *J. Fluid Mech.*, vol. 761, pp. 1–26, 2014.

[25] P. M. Wild, N. Djilali, and G. W. Vickers, “Experimental and Computational Assessment of Windage Losses in Rotating Machinery,” *J. Fluids Eng.*, vol. 118, no. 1, pp. 116–122, 1996.

[26] W. M. J. Batten, N. W. Bressloff, and S. R. Turnock, “Transition from vortex to wall driven turbulence production in the Taylor–Couette system with a rotating inner cylinder,” *Int. J. Numer. Methods Fluids*, vol. 38, no. 3, pp. 207–226, 2002.

[27] D. S. Adebayo and A. Rona, “The three-dimensional velocity distribution of wide gap Taylor-Couette flow modelled by CFD,” *Int. J. Rotating Mach.*, 2016.

[28] D. S. Adebayo and A. Rona, “Numerical Investigation of the Three-Dimensional Pressure Distribution in Taylor Couette Flow,” *J. Fluids Eng.*, vol. 139, no. 11, pp. 111201–111210, 2017.

[29] S. Poncet, R. Soghe, C. Bianchini, S. Viazzo, and A. Aubert, “Turbulent Coutte-Taylor flows with endwall effects: A numerical benchmark,” *Int. J. Heat Fluid Flow*, vol. 44, pp. 229–238, 2013.

[30] M. Bilson and K. Bremhorst, “Direct numerical simulation of turbulent Taylor–Couette flow,” *J. Fluid Mech.*, vol. 579, pp. 227–270, 2007.

[31] S. Dong, “Direct numerical simulation of turbulent Taylor–Couette flow,” *J. Fluid Mech.*, vol. 587, pp. 373–393, 2007.

[32] D. Pirrò and M. Quadrio, “Direct numerical simulation of turbulent Taylor–Couette flow,” *Eur. J. Mech. - B/Fluids*, vol. 27, no. 5, pp. 552–566, 2008.

[33] P. Gorse, K. Willenborg, S. Busam, J. Ebner, K. Dullenkopf, and S. Wittig, “3D-LDA

Measurements in an Aero-Engine Bearing Chamber," *Proc. ASME Turbo Expo*, no. 36886, pp. 257–265, 2003.

[34] O. Czarny, E. Serre, P. Bontoux, and R. M. Lueptow, "Ekman vortices and the centrifugal instability in counter-rotating cylindrical Couette flow," *Theor. Comput. Fluid Dyn.*, vol. 18, no. 2, pp. 151–168, 2004.

[35] J. A. Cole, "Taylor-vortex instability and annulus-length effects," *J. Fluid Mech.*, 1976.

[36] M. J. Burin, E. Schartman, and H. Ji, "Local measurements of turbulent angular momentum transport in circular Couette flow," *Exp Fluids*, vol. 48, pp. 763–769, 2010.

[37] A. Glahn and S. Wittig, "Two-Phase Air/Oil Flow in Aero Engine Bearing Chambers: Characterization of Oil Film Flows," *J. Eng. Gas Turbines Power*, vol. 118, p. 578, 1996.

[38] C. W. Lee, "Air and Oil Flow Investigations in an Aeroengine Bearing Chamber," PhD Thesis, University of Nottingham, 2004.

[39] J. Aidarinis, D. Missirlis, K. Yakinthos, and A. Goulas, "CFD Modeling and LDA Measurements for the Air-Flow in an Aero Engine Front Bearing Chamber," *J. Eng. Gas Turbines Power*, vol. 133, no. 8, pp. 82504–82508, 2011.

[40] P. Gorse, S. Busam, and K. Dullenkopf, "Influence of Operating Condition and Geometry on the Oil Film Thickness in Aeroengine Bearing Chambers," *J. Eng. Gas Turbines Power*, vol. 128, no. 1, pp. 103–110, Mar. 2004.

[41] C. Eastwick, K. Huebner, B. Azzopardi, K. Simmons, C. Young, and R. Morrison, "Film Flow Around Bearing Chamber Support Structures," no. 47268. pp. 1267–1272, 2005.

[42] W. Kurz, K. Dullenkopf, and H. J. Bauer, "Influences on the oil split between the offtakes of an aero-engine bearing chamber," *Proc. ASME Turbo Expo*, 2012.

[43] B. Chandra, K. Simmons, S. Pickering, and M. Tittel, "Factors Affecting Oil Removal From an Aeroengine Bearing Chamber," *Proc. ASME Turbo Expo*, pp. 219–228, 2011.

[44] B. Chandra, K. Simmons, S. Pickering, S. H. Collicott, and N. Wiedemann, "Study of Gas/Liquid Behavior Within an Aeroengine Bearing Chamber," *J. Eng. Gas Turbines Power*, vol. 135, no. 5, p. 051201, 2013.

[45] A. Glahn, M. Kurreck, M. Willmann, and S. Wittig, "Feasibility Study on Oil Droplet Flow Investigations Inside Aero Engine Bearing Chambers—PDPA Techniques in Combination With Numerical Approaches," *J. Eng. Gas Turbines Power*, vol. 118, no. 4, p. 749, 1996.

[46] A. Glahn, S. Busam, M. F. Blair, K. L. Allard, and S. Wittig, "Droplet generation by disintegration of oil films at the rim of a rotating disk," *J. Eng. Gas Turbines Power*, 2002.

[47] A. Glahn, M. F. Blair, K. L. Allard, S. Busam, O. Schäfer, and S. Wittig, "Disintegration of oil films emerging from radial holes in a rotating cylinder," *J. Eng. Gas Turbines Power*, 2003.

[48] A. Glahn, M. F. Blair, K. L. Allard, S. Busam, O. Schäfer, and S. Wittig, "Disintegration of oil jets emerging from axial passages at the face of a rotating cylinder," *J. Eng. Gas Turbines Power*, 2003.

[49] P. Gorse, K. Dullenkopf, H.-J. Bauer, and S. Wittig, "An Experimental Study on Droplet Generation in Bearing Chambers Caused by Roller Bearings," *Proc. ASME Turbo Expo*, no. 43147, pp. 1681–1692, 2008.

[50] M. Flouros, “The impact of oil and sealing air flow, chamber pressure, rotor speed, and axial load on the power consumption in an aeroengine bearing chamber,” *J. Eng. Gas Turbines Power*, 2005.

[51] M. Flouros, “Reduction of power losses in bearing chambers using porous screens surrounding a ball bearing,” *J. Eng. Gas Turbines Power*, 2006.

[52] K. Willenborg, S. Busam, H. Roßkamp, and S. Wittig, “Experimental studies of the boundary conditions leading to oil fire in the bearing chamber and in the secondary air system of aeroengines,” *Proc. ASME Turbo Expo*, 2002.

[53] R. Santhosh, J. L. Hee, K. Simmons, G. Johnson, D. Hann, and M. Walsh, “Experimental Investigation of Oil Shedding From an Aero-Engine Ball Bearing at Moderate Speeds,” *Proc. ASME Turbo Expo*, 2017.

[54] J. L. Hee, R. Santhosh, K. Simmons, G. Johnson, D. Hann, and M. Walsh, “Oil Film Thickness Measurements on Surfaces Close to an Aero-Engine Ball Bearing Using Optical Techniques,” *Proc. ASME Turbo Expo*, 2017.

[55] J. L. Hee, “Experimental and Computational Investigation into Oil Shedding from an Aeroengine Ball Bearing,” PhD Thesis in Progress, University of Nottingham, 2019.

[56] J. L. Hee, K. Simmons, D. Hann, and M. Walsh, “Characterisation of Waves and Ligaments in Films Close to an Aeroengine Ball Bearing,” 2019.

[57] P. Paleo Cageao, K. Simmons, A. Prabhakar, and B. Chandra, “Assessment of the oil scoop capture efficiency in high speed rotors,” *J. Eng. Gas Turbines Power*, 2019.

[58] C. W. Lee, G. R. Johnson, P. C. Palma, K. Simmons, and S. J. Pickering, “Factors affecting the behaviour and efficiency of a targetted jet delivering oil to a bearing lubrication system,” *Proc. ASME Turbo Expo*, 2004.

[59] M. B. Krug, D. Peduto, W. Kurz, and H. J. Bauer, “Experimental investigation into the efficiency of an aero-engine oil jet supply system,” *J. Eng. Gas Turbines Power*, 2015.

[60] A. A. Hashmi, K. Dullenkopf, H. J. Bauer, and M. Klingsporn, “Experimental investigation of lubrication oil film dynamics in a typical aero-engine bearing chamber environment,” *Proc. ASME Turbo Expo*, 2011.

[61] S. K. Alghoul, C. N. Eastwick, and D. B. Hann, “Normal droplet impact on horizontal moving films: An investigation of impact behaviour and regimes,” *Exp. Fluids*, 2011.

[62] A. J. Mitchell, K. Simmons, and D. Hann, “Experimental investigation into droplet impingement upon moving films using high speed video and thermal imaging,” *Proc. ASME IMECE*, 2015.

[63] A. J. Mitchell, D. Hann, and K. Simmons, “Experimental investigation into crater morphology for droplets impinging on a moving film,” *Proc. ASME Turbo Expo*, 2017.

[64] J. Vasques, A. Ibrahim, D. Hann, K. Simmons, and M. Walsh, “The Effect of Surface Tension on Bubble Generation in Gas-Sheared Liquid Films,” *Proc. ASME Turbo Expo*, 2019.

[65] B. Kakimpa, H. P. Morvan, and S. Hibberd, “The numerical simulation of multi-scale oil films using coupled VOF and Eulerian thin-film models,” *Proc. ASME Turbo Expo*, 2016.

[66] D. Peduto, A. A. Hashmi, K. Dullenkopf, H.-J. Bauer, and H. Morvan, “Modelling of an Aero-Engine Bearing Chamber Using Enhanced CFD Technique,” *Vol. 5 Heat Transf.*

Parts A B, no. 54655, pp. 809–819, 2011.

[67] M. Krug, “Evaluation of the Volume of Fluid Method for the Numerical Modelling of an Aero Engine Bearing Chamber,” PhD Thesis, Karlsruhe Institute of Technology, 2012.

[68] A. Bristot, “Application of the Volume of Fluid Method with Heat Transfer to a Two Shaft Aero-Engine Bearing Chamber,” PhD Thesis, University of Nottingham, 2017.

[69] Z. Jingyu, L. Yaguo, L. Zhenxia, and R. Guozhe, “Numerical Study on the Improvement of Oil Return Structure in Aero-Engine Bearing Chambers,” *Int. J. Turbo Jet Engines*, 2018.

[70] D. G. Arcila, H. Morvan, K. Simmons, S. Ambrose, M. Walsh, and B. Kakimpa, “Modelling Droplet Heat and Mass Transfer in Aero-Engine Bearing Chambers,” *Proc. ASME Turbo Expo*, 2019.

[71] A. Crouchez-Pillot and H. P. Morvan, “CFD Simulation of an Aeroengine Bearing Chamber Using an Enhanced Volume of Fluid (VOF) Method: An Evaluation Using Adaptive Meshing,” *Proc. ASME Turbo Expo*, 2014.

[72] M. Krug, C. Höfler, H.-J. Bauer, and W. Kurz, “Evaluation of the Volume-of-Fluid Method for the Numerical Modelling of an Aero Engine Bearing Chamber,” *22nd Int. Symp. Air Breath. Engines*, 2015.

[73] M. Berthold, H. Morvan, C. Young, and R. Jefferson-Loveday, “Toward Investigation of External Oil Flow from a Journal Bearing in an Epicyclic Gearbox,” *J. Eng. Gas Turbines Power*, 2018.

[74] M. Berthold, H. Morvan, R. Jefferson-Loveday, C. Young, B. C. Rothwell, and S. Ambrose, “Multiphase computational fluid dynamics modeling of external oil flow from a journal bearing,” *J. Eng. Gas Turbines Power*, 2018.

[75] A. Prabhakar, Y. A. Abakr, and K. Simmons, “Numerical investigations to assess the impact of shaft speed on the performance of scoop devices,” *Proc. ASME Turbo Expo*, 2018.

[76] K. Simmons, L. Harrison, E. Korsukova, and P. P. Cageao, “CFD study exploring jet configurations and jet pulsing for an aeroengine scoop-based oil delivery system,” *Proc. ASME Turbo Expo*, 2018.

[77] L. Jiang, Y. Lyu, Z. Liu, and Z. Pengfel, “Numerical Study on Flow Characteristics of Liquid Jet in Airflows,” *Proc. ASME Turbo Expo*, 2017.

[78] A. Prabhakar, S. Ambrose, and H. Morvan, “Numerical Investigation of Two Phase Flow in a Dual Drive Booster (DDB),” *Proc. ASME Turbo Expo*, 2019.

[79] P. Vita, B. F. W. Gschaider, D. Prieling, and H. Steiner, “Thin film flow simulation on a rotating disc,” in *ECCOMAS 2012 - European Congress on Computational Methods in Applied Sciences and Engineering*, 2012.

[80] B. Kakimpa, H. P. Morvan, and S. Hibberd, “Thin-Film Flow Over a Rotating Plate: An Assessment of the Suitability of VOF and Eulerian Thin-Film Methods for the Numerical Simulation of Isothermal Thin-Film Flows,” *Proc. ASME Turbo Expo*, 2015.

[81] M. Farrall, K. Simmons, and S. Hibberd, “A Numerical Model For Oil Film Flow in an Aero-Engine Bearing Chamber and Comparison with Experimental Data,” *Proc. ASME Turbo Expo*, 2004.

[82] C. Wang, H. P. Morvan, S. Hibberd, and K. A. Cliffe, “Thin Film Modelling for Aero-Engine Bearing Chambers,” *Proc. ASME Turbo Expo*, 2011.

[83] B. Kakimpa, H. Morvan, and S. Hibberd, “The Depth-Averaged Numerical Simulation of Laminar Thin-Film Flows With Capillary Waves,” *J. Eng. Gas Turbines Power*, vol. 138, 2016.

[84] C. Wang, H. P. Morvan, S. Hibberd, K. A. Cliffe, A. Anderson, and A. Jacobs, “Specifying and benchmarking a thin film model for oil systems applications in ansys fluent,” *Proc. ASME Turbo Expo*, 2012.

[85] J. Ashmore, A. E. Hosoi, and H. A. Stone, “The effect of surface tension on rimming flows in a partially filled rotating cylinder,” *J. Fluid Mech.*, vol. 479, pp. 65–98, 2003.

[86] E. S. Benilov, V. N. Lapin, and S. B. G. O’Brien, “On rimming flows with shocks,” *J. Eng. Math.*, pp. 49–62, 2012.

[87] M. Villegas-Diaz, H. Power, and D. S. Riley, “Analytical and numerical studies of the stability of thin-film rimming flow subject to surface shear,” *J. Fluid Mech.*, vol. 541, pp. 317–344, 2005.

[88] E. D. Kay, S. Hibberd, and H. Power, “A depth-averaged model for non-isothermal thin-film rimming flow,” *Int. J. Heat Mass Transf.*, vol. 70, pp. 1003–1015, 2014.

[89] R. A. Cook and R. H. Clark, “The experimental determination of velocity profiles in smooth falling liquid films,” *Can. J. Chem. Eng.*, 1971.

[90] N. A. Malamataris, M. Vlachogiannis, and V. Bontozoglou, “Solitary waves on inclined films: Flow structure and binary interactions,” *Phys. Fluids*, 2002.

[91] B. Kakimpa, H. P. Morvan, and S. Hibberd, “Solution Strategies For Thin Film Rimming Flow Modelling,” *Proc. ASME Turbo Expo*, 2015.

[92] K. Singh, M. Sharabi, S. Ambrose, C. Eastwick, and R. Jefferson-loveday, “Prediction of Film Thickness of an Aero-Engine Bearing Chamber Using Coupled VOF and Thin Film Model,” *Proc. ASME Turbo Expo*, 2019.

[93] K. Singh, M. Sharabi, S. Ambrose, C. Eastwick, R. Jefferson-loveday, and J. Cao, “Assessment of an Enhanced Thin Film Model to Capture Wetting and Drying,” *Proc. ASME Turbo Expo*, 2019.

[94] A. A. Adeniyi, “A coupled Lagrangian-Eulerian framework to model droplet to film interaction with heat transfer,” PhD Thesis, University of Nottingham, 2015.

[95] A. A. Adeniyi, H. P. Morvan, and K. A. Simmons, “A Transient CFD Simulation of the Flow in a Test Rig of an Aeroengine Bearing Chamber,” *Proc. ASME Turbo Expo*, 2014.

[96] A. A. Adeniyi, H. P. Morvan, and K. A. Simmons, “A Multiphase Computational Study of Oil-Air Flow Within the Bearing Sector of Aeroengines,” *Proc. ASME Turbo Expo*, 2015.

[97] T. Pringuey, “Large Eddy Simulation of Primary Liquid-Sheet Breakup,” PhD Thesis, Universtiy of Cambridge, 2012.

[98] J. Dick, V. Kumar, N. Pravin, and F. Montanari, “Simulation Of An Aero-Engine Bearing Compartment Using Two-Way Transition Between Lagrangian Droplets And A Three-Dimensional Eulerian Liquid Film,” *Proc. ASME Turbo Expo*, 2019.

[99] J. Williams, “Thin Film Rimming Flow Subject To Droplet Impact at the Surface,” PhD Thesis, University of Nottingham, 2008.

[100] M. Farrall, S. Hibberd, and K. Simmons, “The Effect of Initial Injection Conditions on the Oil Droplet Motion in a Simplified Bearing Chamber,” *J. Eng. Gas Turbines Power*, vol. 130, no. 1, pp. 1–7, 2008.

[101] B. Chen, G. D. Chen, H. C. Sun, and Y. H. Zhang, “Effect of oil droplet deformation on its deposited characteristics in an aeroengine bearing chamber,” *Proc. Inst. Mech. Eng. Part G J. Aerosp. Eng.*, 2014.

[102] H. Sun, G. Chen, Y. Zhang, and L. Wang, “Theoretical and experimental studies on the motion and thermal states of oil droplet in a bearing chamber,” *Proc. Inst. Mech. Eng. Part G J. Aerosp. Eng.*, 2016.

[103] Z. Jingyu, Z. X. Liu, J. P. Hu, and Y. Lu, “Numerical Modelling of Unsteady Oil Film Motion Characteristics in Bearing Chambers,” *Int. J. Turbo Jet Engines*, vol. 32(3), pp. 233–245, 2015.

[104] Z. Jingyu and L. Zhenxia, “Numerical and experimental study for unsteady oil film thickness of the rotating cylinder chamber wall,” *J. Eng. Gas Turbines Power*, vol. 137, no. 12, pp. 1–9, 2015.

[105] J. L. Hee, K. Simmons, B. Kakimpa, and D. Hann, “Computationally Efficient Modelling of Oil Jet-Breakup and Film Formation for Bearing Chamber Applications,” *Proc. ASME Turbo Expo*, 2018.

[106] J. Aidarinis and A. Goulas, “Enhanced Computational Fluid Dynamics Modeling and Laser Doppler Anemometer Measurements for the Air-Flow in an Aero-engine Front Bearing Chamber—Part I,” *J. Eng. Gas Turbines Power*, vol. 137, no. 8, 2015.

[107] H. K, Versteeg and W. Malalasekera, *Introduction: Computational Fluid Dynamics The Finite Volume Method*. 2006.

[108] ANSYS, *ANSYS FLUENT Theory Guide Release 17.1*. Canonsburg: ANSYS, 2016.

[109] H. Brauckmann and B. Eckhardt, “Direct numerical simulations of local and global torque in Taylor-Couette flow,” *J. Fluid Mech.*, vol. 718, pp. 398–427, 2013.

[110] R. Ostilla-Mónico, R. Verzicco, and D. Lohse, “Effects of the computational domain size on direct numerical simulations of Taylor-Couette turbulence with stationary outer cylinder,” *Phys. Fluids*, vol. 27, no. 2, p. 25110, 2015.

[111] R. Ostilla-Mónico, E. P. van der Poel, R. Verzicco, S. Grossmann, and D. Lohse, “Boundary layer dynamics at the transition between the classical and the ultimate regime of Taylor-Couette flow,” *Phys. Fluids*, vol. 26, no. 1, p. 15114, 2014.

[112] T. A. Shedd, M. L. Corn, J. M. Cohen, M. Arienti, and M. C. Soteriou, “Liquid film formation by an impinging jet in a high-velocity air stream,” in *47th AIAA Aerospace Sciences Meeting including the New Horizons Forum and Aerospace Exposition*, 2009.

[113] M. Arienti, L. Wang, M. C. Soteriou, T. A. Shedd, and M. Herrmann, “Modeling wall film formation and breakup using an integrated interface-tracking/discrete-phase approach,” *J. Eng. Gas Turbines Power*, 2011.

[114] The OpenFOAM Foundation, “OpenFOAM Source Code Guide Ver: 6.0,” 2018. [Online]. Available: https://cpp.openfoam.org/v6/.

[115] K. V. Meredith, A. Heather, J. de Vries, and Y. Xin, “A numerical model for partially-wetted flow of thin liquid films,” in *WIT Transactions on Engineering Sciences*, 2011.

[116] K. Meredith, Y. Xin, and J. De Vries, “A numerical model for simulation of thin-film water transport over solid fuel surfaces,” in *Fire Safety Science*, 2011.

[117] P. T. Brun, A. Damiano, P. Rieu, G. Balestra, and F. Gallaire, “Rayleigh-Taylor instability under an inclined plane,” *Phys. Fluids*, 2015.

[118] I. Owen and D. J. Ryley, “The flow of thin liquid films around corners,” *Int. J. Multiph. Flow*, 1985.

[119] K. Meredith, J. De Vries, Y. Wang, and Y. Xin, “A comprehensive model for simulating the interaction of water with solid surfaces in fire suppression environments,” *Proc. Combust. Inst.*, 2013.

[120] K. V. Meredith, P. Chatterjee, Y. Wang, and Y. Xin, “Simulating Sprinkler Based Rack Storage Fire Suppression Under Uniform Water Application,” *Proc. Seventh Int. Semin. Fire Explos. Hazards*, 2013.

[121] W. Yi, Z. Xiangyang, X. Yibing, R. Ning, and K. V. Meredith, “Numerical simulation of sprinkler suppression of rack storage fires,” in *Fire Safety Science*, 2014.

[122] N. Ren, J. de Vries, X. Zhou, M. Chaos, K. V. Meredith, and Y. Wang, “Large-scale fire suppression modeling of corrugated cardboard boxes on wood pallets in rack-storage configurations,” *Fire Saf. J.*, 2017.

[123] A. B. Liu, D. Mather, and R. D. Reitz, “Modeling the effects of drop drag and breakup on fuel sprays,” *SAE Tech. Pap.*, no. May, 1993.

[124] M. Yousefifard, P. Ghadimi, and M. Mirsalim, “Numerical simulation of biodiesel spray under ultra-high injection pressure using OpenFOAM,” *J. Brazilian Soc. Mech. Sci. Eng.*, 2015.

[125] P. Ghadimi, M. Yousefifard, and H. Nowruzi, “Applying different strategies within OpenFOAM to investigate the effects of breakup and collision model on the spray and in-cylinder gas mixture attribute,” *J. Appl. Fluid Mech.*, 2016.

[126] S. Teclllwlvgy and R. D. Reitz, “Modeling Atomization Processes in High-Pressure Vaporizing Sprays,” *Science.*, vol. 3, pp. 309–337, 1987.

[127] S. Mayer, “Theory of Liquid Atomization in High Velocity Gas Streams,” *ARS J.*, vol. 31, pp. 467–473, 1961.

[128] M. A. Friedrich, H. Lan, J. L. Wegener, J. A. Drallmeier, and B. F. Armaly, “A separation criterion with experimental validation for shear-driven films in separated flows,” *J. Fluids Eng. Trans. ASME*, 2008.

[129] T. Arai and H. Hashimoto, “Disintegration of Thin Liquid Sheet in Cocurrent Gas Stream: (Wave Motion of Thin Liquid Sheet and Breakup Patterns),” *Trans. Japan Soc. Mech. Eng. Ser. B*, 1985.

[130] C. Bai and A. D. Gosman, “Mathematical Modelling of Wall Films Formed by Impinging Sprays,” *SAE Trans.*, vol. 105, pp. 782–796, 1996.

[131] M. Iqbal and A. Chan, “A Study of the Effect of Element Types on Flow and Turbulence Characteristics Around an Isolated High-Rise Building,” in *11th International Conference on CFD in the Minerals and Process Industries*, 2015.

[132] M. Peric and S. Ferguson, “The Advantage of Polyhedral Meshes,” *CD-adapco*.

[133] E. Goodarzi, J. Farhoudi, and N. Shokri, “Flow characteristics of rectangular broad-crested weirs with sloped upstream face,” *J. Hydrol. Hydromechanics*, 2012.

[134] M. Walsh and K. Miller, “Experimental Bearing Shedding Rig Internal Report,” Gas Turbine and Transmissions Research Centre (G2TRC), 2019.